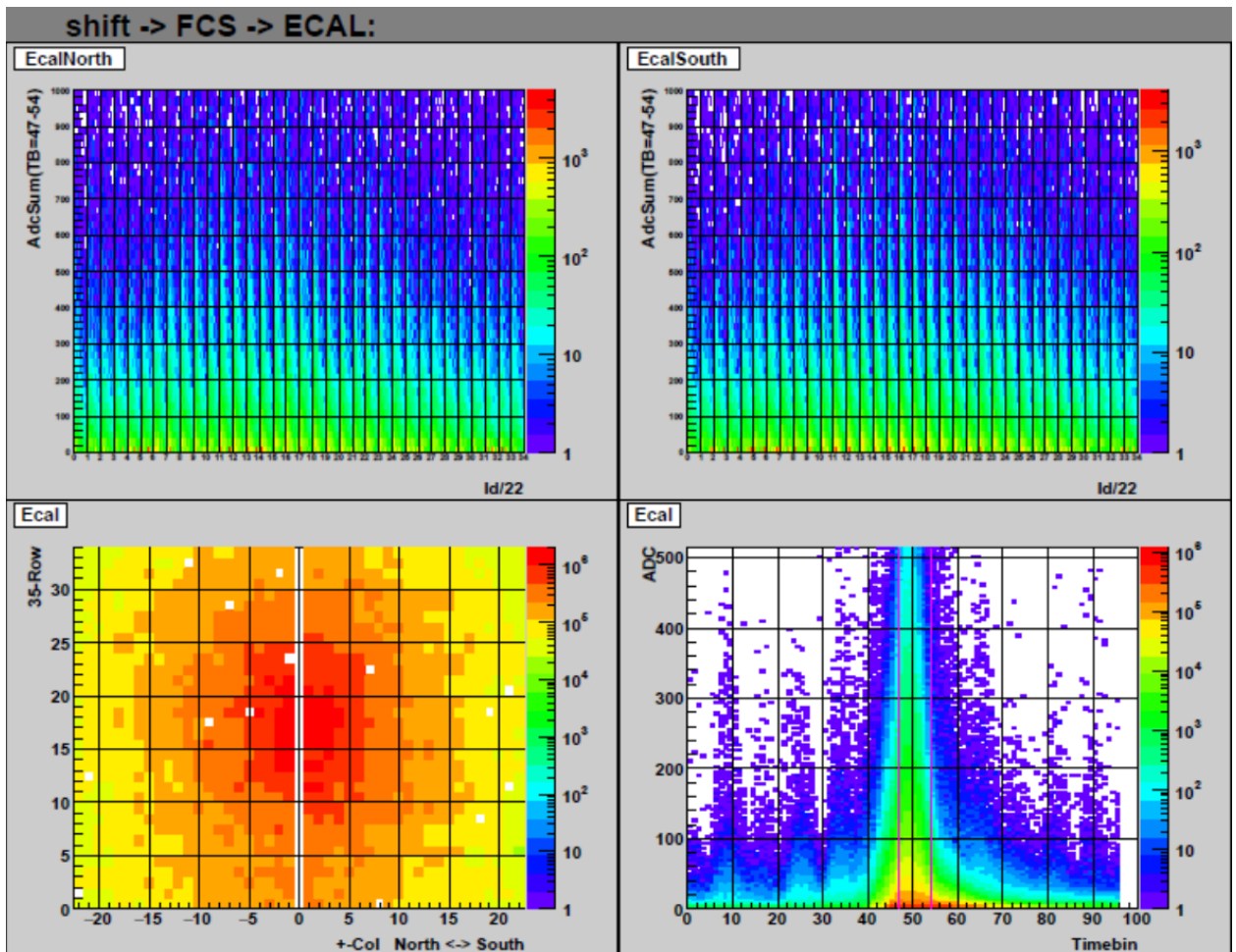


The STAR Beam Use Request for Run-22 and data taking in 2023-25

The STAR Collaboration



FCS EMCAL plots from online monitoring during Run-21.

Bottom left: distribution of hits across all the EMCAL modules.

Bottom right: energy deposition as a function of time bin in the electronics readout.

Top: Energy deposition vs module ID.

1 Executive Summary

2 This Beam Use Request outlines the strong physics programs proposed by STAR collabora-
3 tion for data taking during Run-22 and 2023-2025.

4 STAR's **highest scientific priority** is to initiate the "must-do" Cold QCD forward
5 physics program enabled by the newly completed suite of forward detectors via the collection
6 of transversely polarized pp data at 510 GeV in Run-22. A combination of soft and hard
7 probes collected during 2023-25 will be used to probe the QGP's microstructure and continue
8 our unique forward physics program via the collection of high statistics Au+Au, p +Au, and
9 pp data at $\sqrt{s_{NN}} = 200$ GeV.

10 Run-22 takes full advantage of STAR's new forward detection capabilities, consisting of a
11 Forward Calorimeter System (FCS) and a Forward Tracking System (FTS) located between
12 $2.5 < \eta < 4$, while also capitalizing on the recent BES-II detector upgrades. As shown
13 in Table 1, we propose **a dedicated 20 cryo-week transversely polarized pp run**
14 **at $\sqrt{s} = 510$ GeV**. We note that an 18 cryo-week run would very detrimental to STAR
15 achieving all our physics goals. Due to the need to commission the new detectors in the first
16 weeks of running, a reduction of two weeks will result in more than a $\sim 15\%$ reduction in
17 our sampled luminosity estimates; the loss will occur once the detectors and RHIC will be
18 operating at their most efficient.

Table 1: Proposed Run-22 assuming 20 cryo-weeks, including an initial one week of cool-down and a two weeks set-up time.

\sqrt{s} (GeV)	Species	Polarization	Run Time	Sampled Luminosity	Priority
510	pp	Transverse	16 weeks	400 pb ⁻¹	1

19 These data will enable STAR to explore, with unprecedented precision, forward jet
20 physics that probe both the high-x (largely valence quark) and low-x (primarily gluon)
21 partonic regimes.

22 The STAR collaboration has also identified a number of topics that together make a
23 compelling case to take data during Runs 23-25 alongside sPHENIX, and successfully com-
24 plete RHIC's scientific mission. This scientific program is enabled by the first opportunity
25 to capitalize on the combination of the BES-II and Forward Upgrades in the data collected
26 from Au+Au, p +Au, and pp collisions at $\sqrt{s_{NN}} = 200$ GeV as outlined in Table 2.

27 Significantly increased luminosities, the extended acceptance at mid-rapidity due to the
28 iTPC, improved event plane and triggering capabilities of the EPD, and the ability to probe
29 the previously inaccessible forward region are all exploited in our Hot QCD program, that
30 informs on the microstructure of the QGP, and our Cold QCD program that will utilize
31 transverse polarization setting the stage for related future measurements at the EIC.

32 By combining the data collected via Au+Au collisions at 200 GeV in Run-23 and Run-
33 25 we will be able to address important questions about the inner workings of the QGP,

34 including the temperature dependence of the shear and bulk viscosities, the 3-D nature of
 35 the initial state, how global vorticity is transferred to the spin angular momentum of particles
 36 on such short time scales and the chiral properties of the medium.

37 In Run-24 STAR considers it critical that we collect approximately equal nucleon-nucleon
 38 luminosities for pp and $p+Au$ at 200 GeV. In this way we can optimize the statistical precision
 39 of several critical observables that require comparisons between results in both pp and $p+Au$.
 40 We request transversely polarized protons for both datasets. Assuming 28 cryo-weeks in Run-
 41 24 we expect to record samples that represent a factor 4.5 times the luminosity that STAR
 42 sampled during transversely polarized pp collisions in Run-15 and 3 times the luminosity
 43 sampled during transversely polarized $p+Au$ collisions in Run-15.

Table 2: Proposed Run-23 - Run-25 assuming 28 cryo-weeks of running every year, and 6 weeks set-up time to switch species in 2024. Sampled luminosities assume a "take all" triggers.

$\sqrt{s_{NN}}$ (GeV)	Species	Number Events/ Sampled Luminosity	Year
200	Au+Au	10B / 31 nb ⁻¹	2023
200	pp	235 pb ⁻¹	2024
200	$p+Au$	1.3 pb ⁻¹	2024
200	Au+Au	10B / 31 nb ⁻¹	2025

44 As requested, we also considered the scenario that each run is reduced to only 20 cryo-
 45 weeks in 2023-25. The dramatic decrease in sampled luminosity resulting from this scenario
 46 will have a serious negative impact on us achieving all of our physics goals outlined in this
 47 BUR.

48 If such a negative scenario unfolds, the STAR collaboration would continue to request
 49 Au+Au, $p+Au$, and pp running as outlined in Table 3 to take the best possible advantage
 50 of our recent upgrades. The ordering of this running could be optimized to minimize time
 51 lost to moving the magnets for $p+Au$ running. This scenario would result in a significant
 52 increase in both the statistical and systematic uncertainties of all the data. The hard probe,
 53 thermal di-lepton, and photon-induced di-lepton and J/ψ Au+Au programs would be very
 54 detrimentally hit. The impact of the nuclear PDFs, fragmentation functions, and gluon
 55 saturation measurements would also be affected; these require comparisons of the same
 56 observables measured in both pp and $p+Au$ collisions.

57 Finally in Section 5 we propose the collection of two datasets as the opportunity arises.
 58 One proposal enables the determination of nuclear deformation parameters of heavy-ion
 59 nuclei which are important to improve our modeling and subsequent understanding of the
 60 hydrodynamical response of the medium. Information on these deformation parameters are
 61 of significant interest to the nuclear structure physics community, and heavy ion collisions
 62 have very different sensitivity on and might probe different aspects of these parameters.

63 The other proposal expands our fixed-target program to include other light beam and
 64 target combinations. These data will help clarify the role and mechanisms of nucleon stop-

Table 3: Proposed Run-23 - Run-25 assuming 20 cryo-weeks of running every year, and 6 weeks set-up time to switch species in 2024. Sampled luminosities assume a "take all" triggers.

$\sqrt{s_{\text{NN}}}$ (GeV)	Species	Number Events/ Sampled Luminosity
200	Au+Au	12B / 37 nb ⁻¹
200	<i>pp</i>	214 pb ⁻¹
200	<i>p</i> +Au	1.2 pb ⁻¹

65 ping. In addition, light nucleus cross sections in the target/projectile regions using beams
 66 of 3-50 GeV/n are of great interest to the NASA Space Radiation community.

67 Contents

68	1 Highlights from the STAR Program	1
69	1.1 Highlights from the Heavy Ion Program	1
70	1.1.1 Bulk Correlations	1
71	1.1.2 pp and Heavy-Ion Jet Measurements	7
72	1.1.3 Heavy-flavor	14
73	1.1.4 Light Flavor and Ultra-peripheral Collisions	15
74	1.2 CME Search and Isobar Run	19
75	1.2.1 Introduction	19
76	1.2.2 Modality of Isobar Running at RHIC	19
77	1.2.3 Blinding of Data Sets and Preparation for Analyses	20
78	1.2.4 Methods for the Isobar Blind Analyses	21
79	1.2.5 Observables for Isobar Blind Analyses	22
80	1.2.6 Benchmarking CME Observables Against EBE-AVFD Model	26
81	1.2.7 Prospect of CME Search Beyond the Isobar-era	29
82	1.3 Cold QCD Highlights	33
83	1.3.1 Introduction	33
84	1.3.2 Longitudinal Program	34
85	1.3.3 Transverse Program	35
86	1.3.4 Unpolarized Program	39
87	1.4 Run-21 Performance	42
88	1.4.1 Performance to Date	42
89	1.4.2 Projections to Complete the Run-21 Physics Priorities	45
90	1.5 Additional Physics Opportunity for Run-21	47
91	2 Physics with $p^\uparrow p^\uparrow$ and $p^\uparrow + A$ Collisions at 510 and 200 GeV	49
92	2.1 Run-22 Request for $p^\uparrow p^\uparrow$ Collisions at 510 GeV	50
93	2.1.1 Inclusive Transverse Spin Asymmetries at Forward Rapidities	50
94	2.1.2 Sivers and Efremov-Teryaev-Qiu-Sterman Functions	53
95	2.1.3 Transversity, Collins Function and Interference Fragmentation Function	59
96	2.1.4 Probing Unpolarized Distributions in the Proton	65
97	2.1.5 Spatial Imaging of the Nucleon	66
98	2.2 Run-24 Request for Polarized pp and $p+A$ Collisions at 200 GeV	69
99	2.2.1 Spin Physics with Polarized pp and $p+A$ Collisions at 200 GeV	69
100	2.2.2 Physics Opportunities with Unpolarized proton-Nucleus Collisions	74
101	2.2.3 Novel QGP Droplet Substructure in $p+A$ Collisions	87
102	3 Exploring the Microstructure of the QGP (Run-23 and Run-25 Au+Au)	91
103	3.1 Correlation Measurements Utilizing Extended Acceptance	93
104	3.2 Correlation Measurements Utilizing the Enhanced Statistics	101
105	3.3 Hard Probes: Jets and Heavy Flavor	106
106	3.3.1 Precision Jet Measurements to Study the QGP Micro-Structure	108

107	3.3.2	Deconfinement and Thermalization With Charmonia Measurements .	111
108	3.4	Electromagnetic Probes and Ultra-peripheral collisions	114
109	3.4.1	Probing the degrees of freedom of the medium and its transport prop-	
110		erties:	114
111	3.4.2	Studying the Photon Wigner Function and Final-state Magnetic Fields	
112		in the QGP	116
113	3.4.3	Ultra-peripheral Au+Au Collisions: Probe Gluon Distribution Inside	
114		the Nucleus	117
115	4	Forward Upgrade	119
116	4.1	Status	120
117	4.2	Forward Calorimeter System	120
118	4.3	Forward Silicon Tracker	121
119	4.4	Forward sTGC Tracker	122
120	4.5	Software	123
121	5	Future Opportunities	126
122	5.1	Fixed-target Measurements Using Light Beam and Target Combinations . .	126
123	5.2	Shape Tomography of Atomic Nuclei Using Collective Flow Measurements .	127
124	6	Charge for 2021 NPP PAC	132

1 Highlights from the STAR Program

1.1 Highlights from the Heavy Ion Program

1.1.1 Bulk Correlations

Over the past years, the STAR collaboration has performed a series of correlation measurements directed towards a comprehensive understanding of the QCD phase diagram and the bulk properties of the QGP phase. Here we highlight the most recent STAR results on bulk correlations, which are expected to shed light on the QCD phase diagram as well as on the transport properties of the QGP.

Net-proton Number Fluctuations and a Crossover Search

One of the main goals in heavy-ion collision experiments is to understand a phase diagram of QCD matter with respect to temperature (T) and baryon chemical potential (μ_B). In the Beam Energy Scan program (BES-I), heavy-ion collision experiments were carried out by varying the collision energy in order to scan a wide region of the baryon chemical potential, $30 < \mu_B$ (MeV) < 400 . The STAR experiment has measured higher-order fluctuations up to the fourth-order of net-proton multiplicity distributions from the BES-I. The fourth-order fluctuations were found to have a non-monotonic beam energy dependence within 3.1σ significance [1], which could indicate a critical point exists at $\sqrt{s_{NN}} \approx 7.7$ GeV. More precise measurements with enhanced statistics at low collision energies of $3.0 < \sqrt{s_{NN}}$ (GeV) < 19.6 will be performed with data from the Beam Energy Scan program phase II (BES-II) and the Fixed-Target program (FXT).

On the other hand, it is also important to establish the nature of the phase transition experimentally at small μ_B region. A smooth crossover is predicted at $\mu_B = 0$ by first principle lattice-QCD calculations [2], however, there is currently no direct experimental evidence. Theoretically, the sixth-order fluctuations of baryon numbers are expected to be negative near the phase transition temperature [3–5]. The STAR experiment has measured the sixth-order fluctuations, C_6/C_2 , of net-proton distributions using high statistics datasets at $\sqrt{s_{NN}}=27$, 54.4, and 200 GeV. Figure 1 shows net-proton C_6/C_2 as a function of collision centrality. Most of the data points for 27 and 54.4 GeV are consistent within uncertainties with a statistical baseline ($C_6/C_2 = 1$). On the other hand, the C_6/C_2 values at 200 GeV are negative systematically from peripheral to central collisions. The experimental results are compared with lattice QCD and UrQMD calculations. Results for 27 and 54.4 GeV are consistent with UrQMD calculations, while for 200 GeV results are below the UrQMD calculations. The negative values observed in central collisions are qualitatively consistent with QCD-based model and lattice QCD calculations within large uncertainties. The current results are dominated by large statistical uncertainties, which makes it difficult to extract definitive physics messages. The statistical accuracy for 200 GeV will be significantly improved by Au+Au collisions in Run-23 and Run-25.

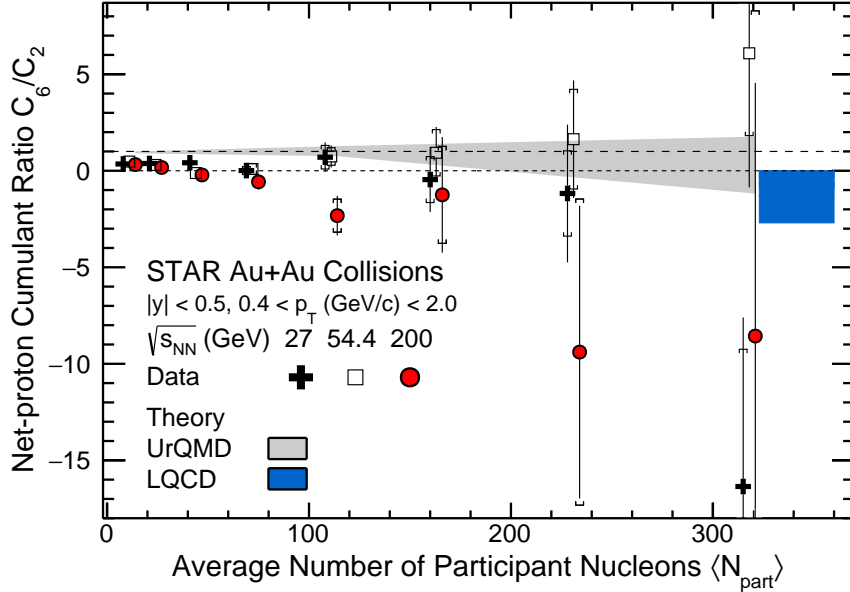


Figure 1: Collision centrality dependence of net-proton C_6/C_2 in Au+Au collisions for $\sqrt{s_{NN}} = 27, 54.4,$ and 200 GeV within $|y| < 0.5$ and $0.4 < p_T$ (GeV/c) < 2.0 . Points for different beam energies are staggered horizontally to improve clarity. A shaded band show the results from UrQMD model calculations. The lattice QCD calculations for $T = 160$ MeV and $\mu_B < 110$ MeV are shown as a blue band at $\langle N_{part} \rangle \approx 340$.

162 Global Polarization of Ξ and Ω Hyperons in Au+Au collisions at 200 GeV:

163 The phenomenon of global polarization in heavy-ion collisions results from the partial
 164 transformation of the orbital angular momentum of colliding nuclei into the spin angular
 165 momentum of the particles produced in the collision [6, 7]. Consequently, these particles
 166 display global polarization along the direction of the initial orbital momentum of the nuclei.
 167 Global polarization was first measured by the STAR Collaboration in the beam energy scan
 168 Au+Au collisions [8].

169 Although the energy dependence of the Λ polarization can be reasonable described by
 170 theoretical models [9–12], several questions remain open, and a detailed modeling of global
 171 polarization and a dynamical approach of spin is under development. Therefore, further
 172 experimental inputs are crucial for understanding vorticity and polarization phenomena in
 173 heavy-ion collisions. Recently STAR reported the first measurements of the global polariza-
 174 tion of spin $s = 1/2$ Ξ^- and Ξ^+ hyperons, as well as spin $s = 3/2$ Ω hyperons in Au+Au
 175 collisions at 200 GeV.

176 Figure 2 shows the collision energy dependence of the Λ hyperon global polarization
 177 previously measured [8, 14] along with the new Ξ and Ω global polarizations measurements
 178 at $\sqrt{s_{NN}} = 200$ GeV. For Ξ and Ω , to reduce the statistical uncertainty, we averaged over
 179 particle and antiparticle, 20%-80% centrality range, transverse momentum $p_T > 0.5$ GeV/c,
 180 and rapidity $|y| < 1$. Global polarization of Ξ^- and Ξ^+ measurements determined via the
 181 daughter Λ polarization show positive values, with no significant difference between Ξ^- and

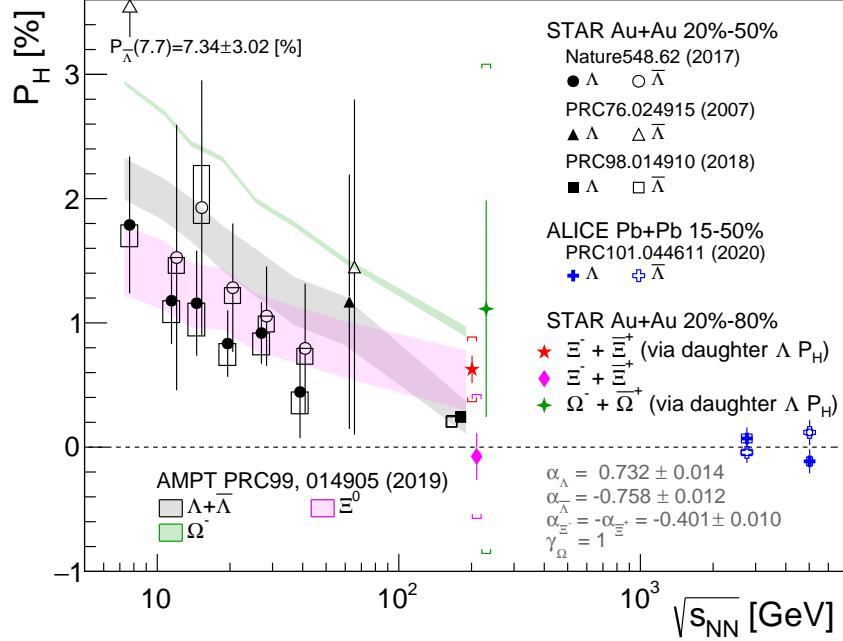


Figure 2: The energy dependence of the hyperon global polarization measurements. The points corresponding to Λ and $\bar{\Lambda}$ polarizations, as well as Ξ and Ω points in Au+Au collisions at $\sqrt{s_{NN}} = 200$ GeV are slightly shifted for clarity. Previous results from the STAR [8, 13] and ALICE [14] experiments compared here are rescaled by new decay parameter indicated inside the figure. The data point for $\bar{\Lambda}$ at 7.7 GeV is out of the axis range and indicated by an arrow with the value. The results of the AMPT model calculations [15] for 20%-50% centrality are shown by shaded bands where the band width corresponds to the uncertainty of the calculations.

182 $\bar{\Xi}^+$ (P_{Ξ^-} (%) = 0.77 ± 0.16 (stat.) ± 0.49 (syst.) and $P_{\bar{\Xi}^+}$ (%) = 0.49 ± 0.16 (stat.) ± 0.20 (syst.)).
183 The average polarization value obtained by this method is $\langle P_{\Xi^-} \rangle$ (%) = 0.63 ± 0.11 (stat.) \pm
184 0.26 (syst.). The $\Xi^- + \bar{\Xi}^+$ polarization was also measured via analysis of the angular distribution
185 of daughter Λ in Ξ^- rest frame. This result, $\langle P_{\Xi^-} \rangle$ (%) = -0.07 ± 0.19 (stat.) ± 0.50 (syst.),
186 has larger uncertainty in part due to a smaller value of α_{Ξ^-} compared to α_Λ , which leads
187 to smaller sensitivity of the measurement. The weighted average of the two measurements
188 is $\langle P_{\Xi^-} \rangle$ (%) = 0.47 ± 0.10 (stat.) ± 0.23 (syst.), which is larger than the polarization of
189 inclusive $\Lambda + \bar{\Lambda}$ measured at the same energy for 20%-80% centrality, $\langle P_\Lambda \rangle$ (%) = $0.24 \pm$
190 0.03 ± 0.03 [8], although the difference is still not significant considering the statistical and
191 systematic uncertainties of both measurements. The Ω^- global polarization, presented in
192 Fig. 2, is $\langle P_\Omega \rangle$ (%) = 1.11 ± 0.87 (stat.) ± 1.97 (syst.) for 20%-80% centrality events, more
193 precise measurements will be needed to make a definitive statement. Future measurements
194 with higher precision will shed light on the uncertainty of the decay parameter γ_Ω , as well
195 as experimental results on the global polarization of spin-3/2 particles, providing critical
196 information about spin dynamics in heavy-ion collisions.

197 Nuclear Deformation Measurements

198 Deformation is a fundamental property of atomic nuclei that reflects the correlated nature
 199 of the dynamics of nucleons within a quantum many-body system. The majority of atomic
 200 nuclei possess an intrinsic deformation, most of which are an axial quadrupole, or ellipsoidal,
 201 deformation.

202 Prior relativistic heavy-ion collision measurements from STAR reported strong signatures
 203 of nuclear deformation using detailed comparisons between Au+Au collisions and U+U col-
 204 lisions [16]. These measurements suggest that U+U collisions are much more deformed in
 205 their ground state. Consequently, we can say that detailed comparisons between different
 206 nuclei enabled us to examine the geometry of the colliding ions.

207 Recently it has been suggested to examine the geometry of the colliding nuclei using the
 208 correlation coefficient, $\rho(v_n^2, [p_T])$ [17–22];

$$\rho(v_n^2, [p_T]) = \frac{\text{cov}(v_n^2, [p_T])}{\sqrt{\text{Var}(v_n^2)}\sqrt{\text{Var}([p_T])}}, \quad (1)$$

209 which might be more sensitive to the initial-state geometry, because it leverages the correla-
 210 tion between the eccentricity-driven flow harmonics v_n and the average transverse momentum
 211 of particles in an event $[p_T]$. The latter is related to the transverse size of the overlap region,
 212 so events that have similar energy-density but smaller initial-state transverse size should
 213 have a larger radial expansion and consequently larger mean transverse momentum [23]. It
 214 has also been proposed that the $\rho(v_n^2, [p_T])$ correlator is sensitive to the correlations between
 215 the initial size and the initial-state deformation of colliding nuclei [24, 25].

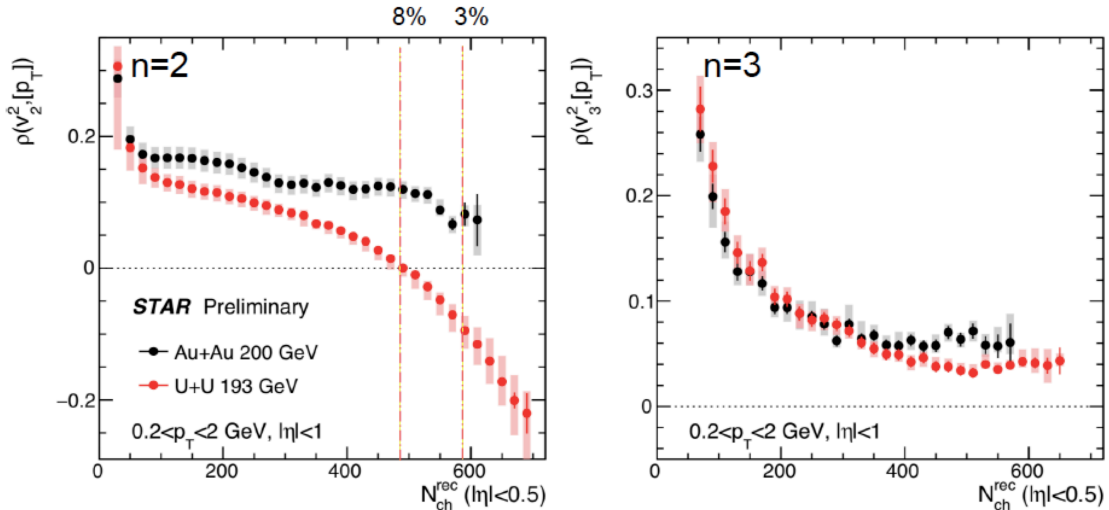


Figure 3: The N_{ch} dependence of the $\rho(v_2^2, [p_T])$ correlator panel (a) and $\rho(v_3^2, [p_T])$ correlator panel (b) for U+U at 193 GeV and Au+Au at 200 GeV.

216 Figure 3 presents the N_{ch} dependence of the $\rho(v_2^2, [p_T])$ correlator, left panel, and $\rho(v_3^2, [p_T])$
 217 correlator, right panel, for U+U at 193 GeV and Au+Au at 200 GeV. Data are shown for

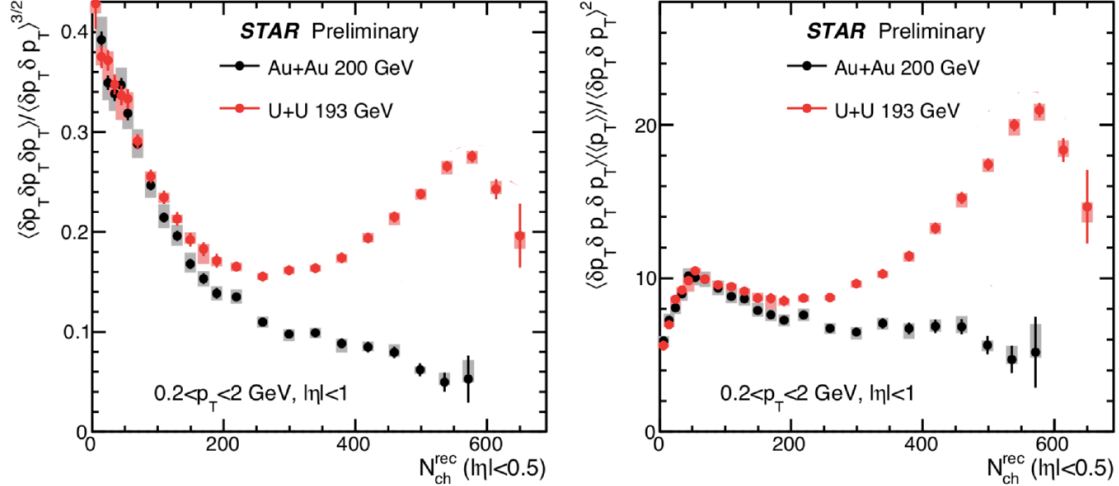


Figure 4: The N_{ch} dependence of the standard skewness left panel and intensive skewness right panel for U+U at 193 GeV and Au+Au at 200 GeV.

218 $0.2 < p_T < 2.0$ GeV/ c and $|\eta| < 1.0$. The presented $\rho(v_2^2, [p_T])$ measurement is shown to
 219 be negative in central U+U collisions, while it is positive in central Au+Au collisions. Such
 220 an effect is compatible with the theoretical expectations [25], and is caused by the prolate
 221 deformation of ^{238}U nuclei. Also the $\rho(v_2^2, [p_T])$ in U+U collisions is lower than in Au+Au
 222 collisions across essentially the full N_{ch} range. In the right panel we present $\rho(v_3^2, [p_T])$ that
 223 shows minor difference between Au+Au and U+U collisions.

224 Also, it had been argued that the p_T dimensionless skewness depends on the system size
 225 and shape [26]. The standardized and *intensive* skewness are shown in Fig. 4 for U+U at
 226 193 GeV and Au+Au at 200 GeV. The presented dimensionless skewness measurement shows
 227 a nonmonotonic trend for U+U at central collisions. This large difference between U+U and
 228 Au+Au could be attributed to the deformation of ^{238}U nuclei.

229 Azimuthal Anisotropy Measurements of Strange and Multi-strange Hadrons in 230 U+U collisions at 193 GeV

231 Stronger constraints on transport and hydrodynamic model simulations can be achieved
 232 via investigating the azimuthal anisotropy of identified particles as a function of transverse
 233 momentum and collision centrality. Also, one can understand the initial conditions in heavy-
 234 ion collisions via varying the collision system size. This could be achieved by performing
 235 collisions of Uranium nuclei which have a deformed shape. Uranium nuclei possess a prolate
 236 shape [27], consequently, there are collision configurations (body-body collisions) in which the
 237 initial overlap region is not spherical even in central collisions. Moreover, depending on the
 238 angles of the two colliding Uranium nuclei relative to the reaction plane, several other collision
 239 configurations of U+U collisions are possible [28–30]. Studying these various collision shapes
 240 will provide an additional constraint for the initial conditions in models [31–33].

241 Recently we reported the results on flow coefficients v_n ($n = 2, 3$, and 4) of K_s^0 , ϕ , Λ , Ξ ,

and Ω at mid-rapidity ($|y| < 1.0$) in U+U collisions at $\sqrt{s_{NN}} = 193$ GeV.

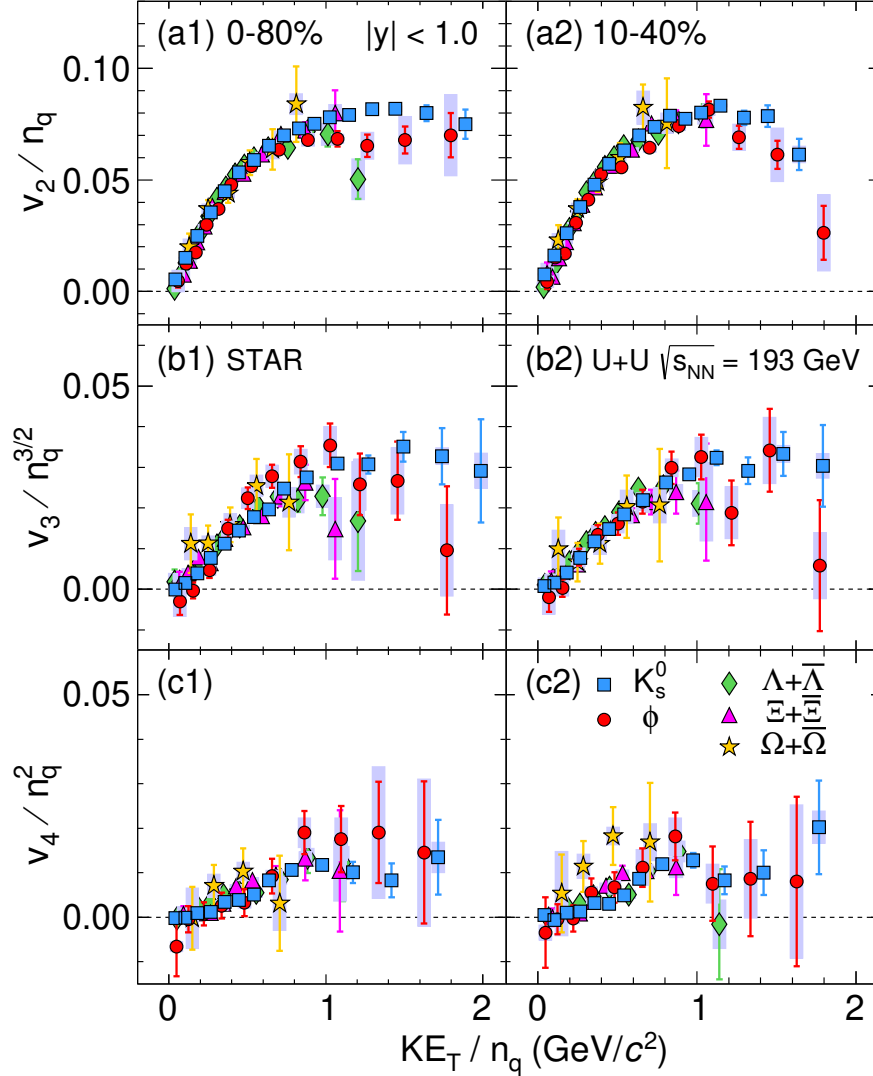


Figure 5: Flow coefficients v_2 , v_3 , and v_4 as a function of transverse kinetic energy KE_T/n_q for various particles at mid-rapidity ($|y| < 1$) in U+U collisions at $\sqrt{s_{NN}} = 193$ GeV, scaled by the number of constituent quarks (n_q) to the power $n/2$. Left panels represent results for minimum bias (0-80%) and right panels for centrality class (10-40%). The error bars represent statistical uncertainties. The bands represent point-by-point systematic uncertainties.

242

243

244

245

246

247

248

Figure 5 presents the measurements of v_n coefficients scaled by $n_q^{n/2}$ as a function of KE_T/n_q , for strange and multi-strange hadrons in U+U collisions at $\sqrt{s_{NN}} = 193$ GeV. Our measurements show that the NCQ scaling holds within experimental uncertainties for each harmonic order $n = 2, 3$ and 4. The $v_n/n_q^{n/2}$ vs. KE_T/n_q values lie on a single curve for all the particle species within $\pm 15\%$. The measured NCQ scaling of v_n coefficients indicates the evolution of partonic collectivity during the QGP phase in heavy-ion collisions. This observed

249 scaling also suggests the formation of hadrons through quark coalescence in the intermediate
 250 p_T range ($2.0 < p_T(\text{GeV}/c) < 4.0$) [34, 35]. Although there are considerable differences
 251 between U+U and Au+Au in the collision geometry, the hydrodynamical evolution and the
 252 coalescence mechanism for hadron formation persist-key features of QGP drops formed in
 253 nucleus-nucleus collisions.

254 **Studies of Strong Interactions**

255 The study of nucleon-nucleon (NN), nucleon-hyperon (NY), and hyperon-hyperon (YY)
 256 interactions are fundamental to understanding the physics of relativistic heavy-ion colli-
 257 sions, neutron stars, and the existence of various exotic hadrons. A significant amount of
 258 NN scattering data allows us to construct precise NN potential models. However, the lim-
 259 ited availability of NY scattering data and no scattering data for the YY systems creates
 260 understanding the NY and YY potentials complicated and challenging. It has become pos-
 261 sible to study with Lattice QCD constraints of the strong interactions [36]. Commonly, the
 262 experimental information on the bound states of strange baryons and nucleons (hypernuclei)
 263 are used to provide information on YY interactions [37]. However, the extraction of strong
 264 interactions' parameters becomes difficult due to, e.g., contamination by many-body effects.

265 High-energy heavy-ion collisions provide a significant number of hyperons in each colli-
 266 sion, which provides an excellent opportunity to study strong interactions. Measurement of
 267 two-particle correlations at low relative momentum, with the femtoscopy method, has been
 268 used to study the space-time dynamics of the source created in heavy-ion collisions [39], [40].
 269 In addition to this, the measurement of two-particle correlations at low relative momentum
 270 can also be used to measure final state interactions (FSI) between nucleons and hyperons.
 271 A recent study of lattice QCD calculations for heavy quark masses shows that the $N\Omega$ in-
 272 teraction is attractive at all distances [41]; the shape of the two-particle correlation function
 273 at low relative momentum changes significantly with the strength of the $N\Omega$ attraction [42].
 274 However, the Coulomb interaction in the $p\Omega$ channel makes it challenging to access the strong
 275 interaction parameters directly from the measured two-particle correlation function. There-
 276 fore, a new measurement, namely the ratio of the correlation functions of peripheral (small)
 277 to central (large) collision systems, has been proposed in [42]. This ratio provides direct
 278 access to the strong interaction between proton and omega, independent of the model used
 279 for the emission source. The attractive nature of an $N\Omega$ interaction leads to the possible
 280 existence of the $N\Omega$ dibaryon. Such an $N\Omega$ dibaryon is the most interesting candidate after
 281 the H-dibaryon [43]. Several attempts have been made to estimate the binding energy of the
 282 $N\Omega$ state in different QCD-motivated models [41]. The $N\Omega$ dibaryon can be produced in
 283 high-energy heavy-ion collisions through the coalescence mechanism [44]. The measurement
 284 of the $p\Omega$ correlation function for peripheral and central Au+Au collisions at $\sqrt{s_{NN}} = 200$
 285 GeV, presented in Fig.6, provides insight into the existence of an $N\Omega$ dibaryon.

286 **1.1.2 pp and Heavy-Ion Jet Measurements**

287 The STAR jet program has recently focused on a new generation of measurements that
 288 are aimed at differentially studying jet production and fragmentation mechanisms in pp

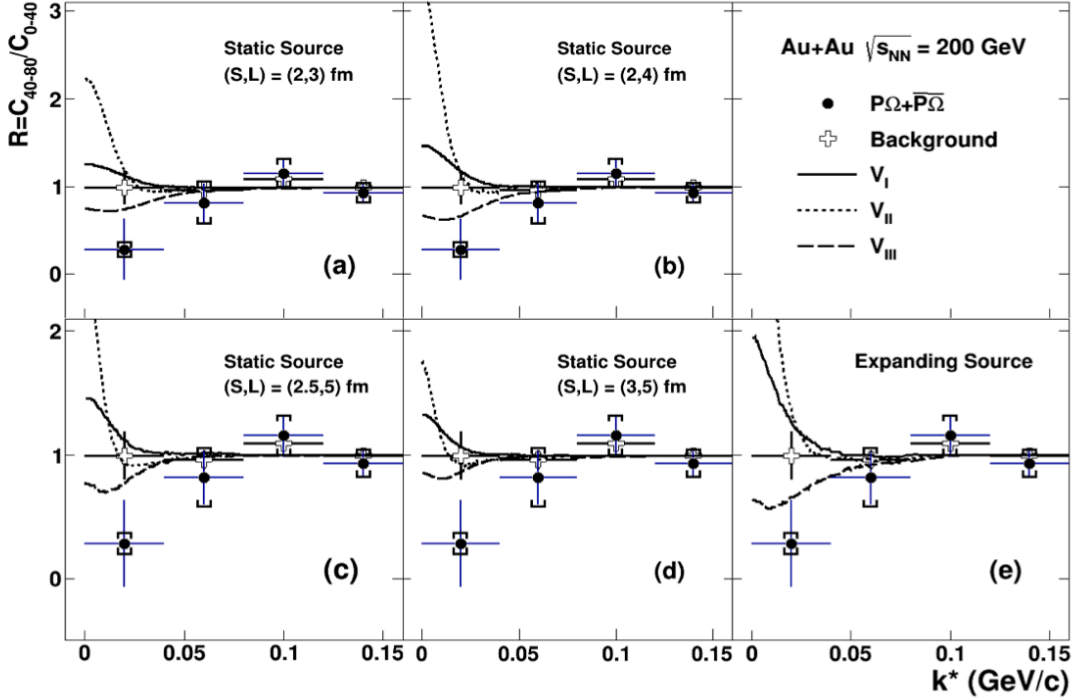


Figure 6: The solid circle represents the ratio (R) of the small system (40-80% collisions) to the large system (0-40% collisions) for $p\Omega$ and $\bar{p}\Omega$. The error bars correspond to statistical uncertainties, and caps correspond to systematic uncertainties. The open crosses represent the ratio for background candidates from the side-band of the Ω invariant mass. Predictions for the ratio of the small system to the large system for $p\Omega$ interaction potentials V_I , V_{II} and V_{III} for static sources with different source sizes $(S, L) = (2,3)$, $(2,4)$, $(2.5, 5)$ and $(3,5)$ fm, where S and L are corresponding to small and large systems, are shown in (a), (b), (c) and (d) respectively. In addition, the prediction for an expanding source is shown in (e) [38].

289 and heavy-ion collisions. In this section, we highlight recent results on jet substructure
 290 in pp collisions along with a measurement of correlations between jet production and the
 291 underlying event (UE) in p +Au collisions. These measurements serve a dual purpose in
 292 that they help us with studies of fundamental QCD in comparison with Monte Carlo (MC)
 293 models and theoretical calculations and as a reference for hot/cold nuclear matter effects in
 294 heavy-ion collisions.

295 Differential Measurements of Jet Substructure in pp Collisions

296 As jets are composite objects built from a parton shower and its fragmentation, they
 297 contain rich substructure information that can be exploited via jet finding algorithms [45].
 298 These algorithms typically employ an iterative clustering procedure that generates a tree-
 299 like structure, which upon an inversion, gives access to a jet's substructure at different
 300 steps along the cluster tree. The most common toolkit for such measurements is SoftDrop
 301 grooming [46] which employs a Cambridge/Aachen re-clustering of a jet's constituents and

302 imposes a criterion at each step as we walk backwards in the de-clustered tree

$$z_g = \frac{\min(p_{T,1}, p_{T,2})}{p_{T,1} + p_{T,2}} > z_{\text{cut}} \left(\frac{R_g}{R_{\text{jet}}} \right)^\beta ; R_g = \Delta R(1,2) \quad (2)$$

303 where $z_{\text{cut}} = 0.1$ is a momentum fraction threshold and β is the angular exponent which in
 304 our analysis is set to zero [47]. These default values for the parameters make the SoftDrop
 305 observable comparable to theoretical calculations, and at the infinite momentum limit they
 306 converge to the DGLAP splitting functions.

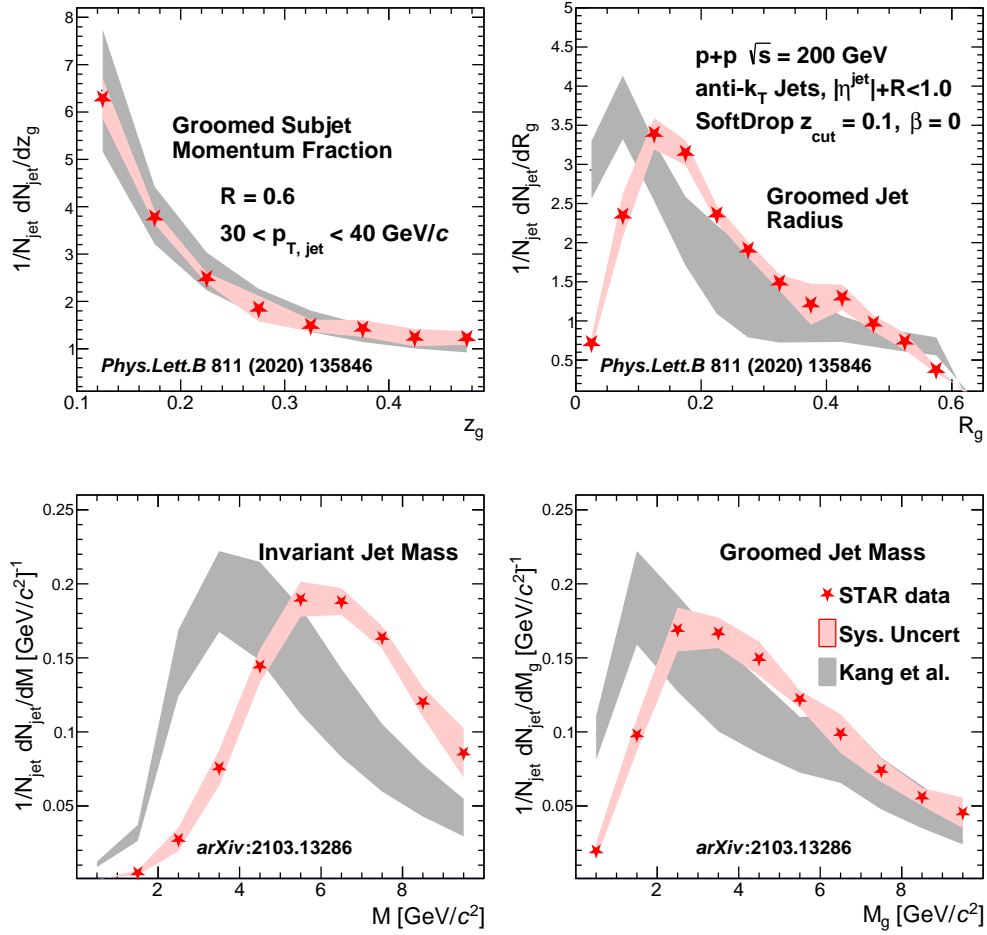


Figure 7: Comparisons of the first split SoftDrop groomed subjet momentum fraction z_g (top left), groomed jet radius R_g (top right), invariant jet mass M (bottom left) and the groomed jet mass M_g (bottom right) shown in the red markers to theoretical calculations in the shaded back regions.

307 STAR has recently published jet substructure measurements at the first split [48, 49]
 308 for jets of varying transverse momenta (p_T) and jet radius in pp collisions at $\sqrt{s} = 200$
 309 GeV. A compilation of the different observables are shown in Fig. 7 for $R = 0.6$ jets with
 310 $30 < p_{T,\text{jet}} < 40$ GeV/ c where the data are shown in the filled red star markers compared

311 to theoretical calculations [50] in the shaded gray bands. The red band represents the total
 312 systematic uncertainty resulting from variation of the tracking efficiency, tower energy scale,
 313 hadronic correction due to tracks matched with towers and the unfolding procedure. The top
 314 panels show the SoftDrop groomed momentum fraction (z_g , top left) and the groomed jet
 315 radius (R_g , top right); we see a relatively good comparison with theory predictions which do
 316 not include any non-perturbative corrections. The calculations reproduce the z_g distribution
 317 in data for high p_T , large-radius jets (the publication [48] includes jets of various momenta
 318 and radii, and the calculations do not reproduce the distributions at lower jet momenta and
 319 smaller jet radii) whereas the R_g shows significant quantitative differences with the data
 320 which can be characterized as a shape function due to non-perturbative corrections. The
 321 bottom two panels of Fig. 7 shows the first measurements of the invariant and groomed
 322 jet mass for the same jet selections as the top panels. The jet mass is sensitive to the
 323 virtuality of the jet [51] and is related to both the momentum and the angular scales [52].
 324 The same theoretical calculation severely under-predicts the jet mass distributions primarily
 325 due to the lack of hadronization corrections and the overall small jet scales which lead to
 326 large theoretical uncertainties. The grooming procedure overall helps in reducing these non-
 327 perturbative effects and as a result, the groomed jet mass data exhibits a similar level of
 328 disagreement as that of the groomed jet radius.

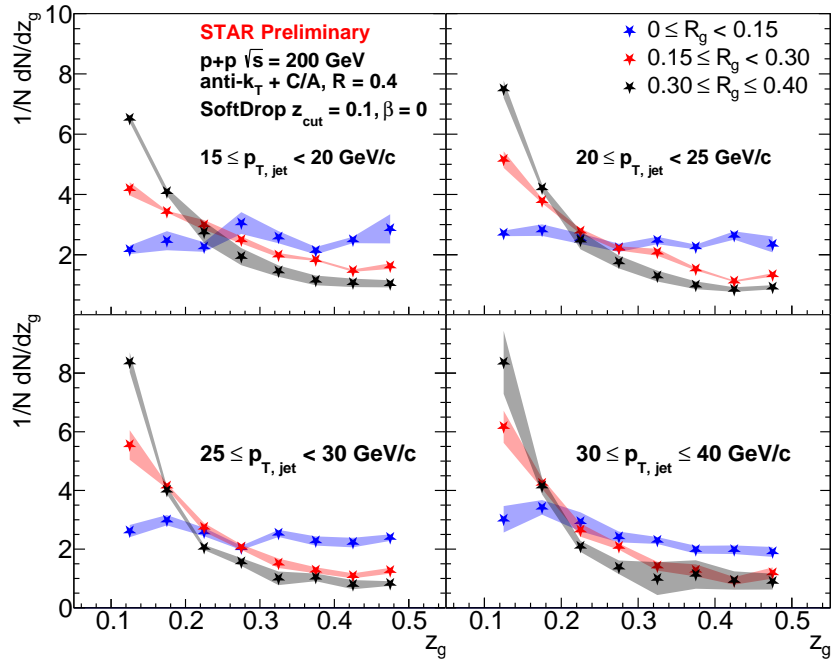


Figure 8: Differential measurements of the first split SoftDrop groomed subjet momentum fraction for jets of varying opening angle ($0 < R_g < 0.15$, $0.15 < R_g < 0.3$, $0.3 < R_g < 0.4$ in the blue, red and black markers) and transverse momenta ($15 < p_T < 20$ GeV/c in the top left to $30 < p_T < 40$ GeV/c in the bottom right).

329 These double differential measurements were corrected in both jet p_T and z_g/R_g simul-

330 taneously and show quite a significant variation in substructure for jets of a particular p_T .
 331 STAR has recently measured the correlations between the momentum and angular scales of
 332 jet substructure at the first split as shown in Fig. 8. The jet p_T increases from the top left to
 333 the bottom right with each panel containing three sets of data markers representing a selec-
 334 tion on the groomed jet radius, $0 < R_g < 0.15$ (blue), $0.15 < R_g < 0.3$ (red), $0.3 < R_g < 0.4$
 335 (black). The correlations between $z_g - R_g$ are unfolded via an 2-D iterative Bayesian proce-
 336 dure as implemented in the RooUnfold package [53] and followed by a boot-strap correction
 337 for the jet energy scale. The final results are the first in jet substructure that are corrected
 338 and presented in 3-D i.e, z_g vs R_g vs $p_{\text{jet},T}$.

339 The data show a stark modification in the shape of the splitting z_g as R_g is varied from
 340 small to large angle. Narrow, or collinear, splits are found to have a symmetric distribution
 341 implying a near equal probability for soft or hard splittings. Wide angle splits on the contrary
 342 are strongly peaked at small values of z_g resulting in those splits containing softer emissions.
 343 The dependence on the jet p_T is observed to be weak compared to the R_g which essentially
 344 drives the z_g distribution for jets in our kinematics. These measurements signify the need of
 345 all three observables if one aims to tag jets with a unique substructure.

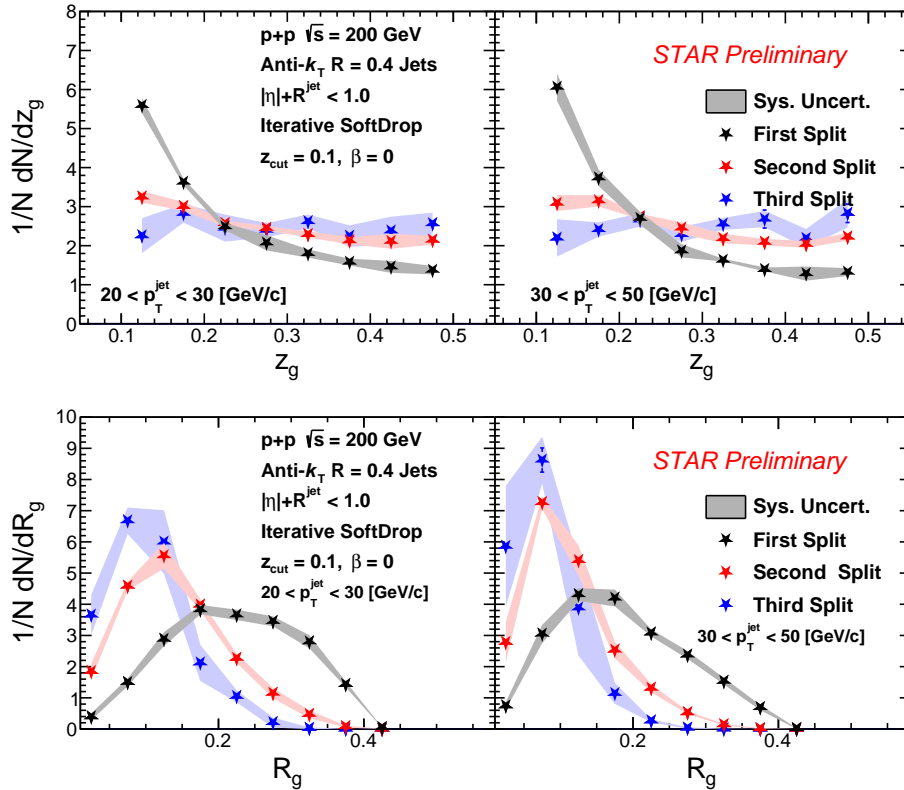


Figure 9: Measurements of the iterative SoftDrop splitting observable for the first (black markers), second (red markers) and third (blue markers) splits shown for the z_g (top panels) and R_g (bottom panels) observables for two jet momenta selections (left - $20 < p_T^{\text{jet}} < 30$ and right - $30 < p_T^{\text{jet}} < 50$ GeV/c).

346 Since the jet cluster tree extends beyond a first split, one can iteratively apply the Soft-
 347 Drop procedure on the hardest surviving branch and measure the jet substructure at each
 348 split along the de-clustered tree [54]. Such measurements enable a study of the parton shower
 349 and evolution of both the momentum and angular scales within a jet. Upon applying the
 350 iterative SoftDrop procedure to the jets studied in this measurements, we reconstruct a col-
 351 lection of observables corresponding to the total number of splittings n and z_g^n and R_g^n at
 352 each split. We limit our measurement to the first three surviving splits within the jets and
 353 present the results fully corrected in 3-D corresponding to the jet p_T , z_g/R_g , and the split
 354 number n . The detector smearing effects on the $z_g/R_g, p_T^{\text{jet}}$ are corrected via a 2-D Bayesian
 355 iterative unfolding via RooUnfold and the splitting hierarchy is corrected by matching the
 356 splits based on the prong that initiates that particular split at both the particle and detector
 357 level $\Delta R_{\text{initiator}} < 0.1$.

358 The data are shown in Fig. 9 for the first, second and third splits in the black, red and
 359 blue colored markers, respectively. The corresponding colored shaded regions behind the
 360 data markers represent total systematic uncertainty resulting from variations in the similar
 361 sources as shown in Fig. 7 with the addition of an extra systematic to the corrected data
 362 shape based on the split matching criterion varied by 0.1 ± 0.025 . These first measurements
 363 detail a remarkable feature of substructure evolution along the jet shower where we observe
 364 a gradual variation in moving from the first to the third splits. The R_g at a split can also be
 365 interpreted as the available phase space for subsequent emissions/splits and is also related
 366 to the virtuality at the split. As R_g gets progressively narrower with increasing split n ,
 367 the shape of z_g also changes from being peaked at smaller values i.e asymmetric splitting,
 368 to a flatter distribution with increased probability for symmetric splits. By comparing the
 369 left and right panels of Fig. 9, a weak dependence on the jet p_T is observed, phase space
 370 restrictions, via selecting a split, significantly impact the substructure observables.

371 These novel multi-dimensional measurements of jet substructure enable a critical compar-
 372 ison with MC event generators and quantitatively assess the impact of perturbative (parton
 373 showers) and non-perturbative (hadronization, multi-parton interactions) models and theo-
 374 retical calculations with small jet and subjet scales that are close to Λ_{QCD} . With a corrected
 375 split hierarchy, we now have a measurement separated in the split formation time along a jet
 376 shower. This technique will be utilized in an upcoming heavy-ion measurements in Au+Au
 377 collisions resulting in a space-time tomography of jet quenching and parton energy loss by
 378 tagging on jets of a specific substructure.

379 **Correlations of the UE and Jet Production in p+Au collisions**

380 Jets are originated from high- Q^2 parton scatterings very early in hadronic collisions. Beside
 381 this high- Q^2 process, particles are also produced from the elastic and inelastic scatterings of
 382 multiple partons from each of the colliding beams. These processes are often described as
 383 non-perturbative and non-factorizable in comparison with the jet production, and a recent
 384 STAR measurement [55] of the canonical underlying event vs the jet momenta in pp collisions
 385 shows an anti-correlation where the particle multiplicity in the off-axis region away from the
 386 jet decreases as the jet momentum increases. This slight negative correlation is understood

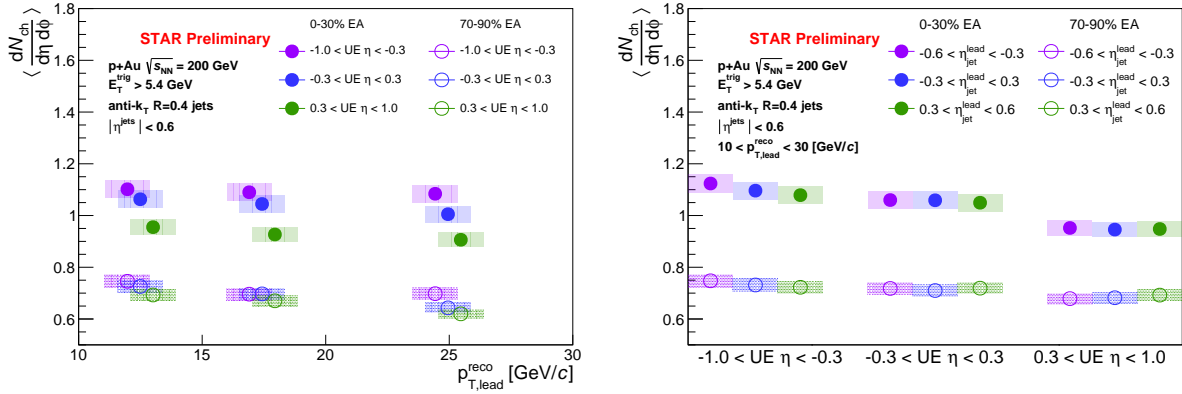


Figure 10: Average corrected charged particle multiplicity in the UE in low/high (open/filled symbols) activity p +Au collisions measured differentially as a function of the reconstructed jet momenta (left panel) and the forward, mid and backward rapidity (right panel).

387 to be consistent with energy conservation restricting particle production in the transverse
388 region as the leading jet becomes more energetic.

389 Asymmetric p +Au collisions offer a natural extension of such measurements where one
390 can study the dependence of this anti-correlation on the event activity and the jet rapidity,
391 i.e. if the jet is perceived to have come from the Au or p beam. The event activity (EA)
392 is defined as the sum of ADC hits in the Au-going inner Beam Beam Counter (east iBBC)
393 located at $\eta \in [-5, -2]$. The EA deciles are defined from the EA distribution in minimum
394 bias events and high/low EA events are selected as 0 – 30%/70 – 90%. Preliminary results
395 are shown in Fig. 10 where the UE average charged particle multiplicity $\langle dN_{ch}/d\eta d\phi \rangle$ for
396 high/low EA events (filled/open markers) are measured as a function of the leading jet p_T
397 (left panel) and the UE η (right panel). The multiplicity is corrected for detector effects
398 and the shaded regions represent the systematic uncertainty on the tracking efficiency. Each
399 panel also has three different colored markers corresponding to UE η in the left and jet η in
400 the right panel. These results are not yet corrected for the jet energy scale and resolution
401 which will be included in the final published results. The UE mean multiplicity in p +Au
402 collisions have a significant dependence on the EA as expected, with high EA events having
403 large multiplicity. We also observe a slight anti-correlation on the jet momenta for the
404 proton going direction ($0.3 < \eta < 1.0$), similar to pp collisions, along with a significant
405 dependence on the UE η , especially in high EA events. The Au-going side has relatively
406 similar $\langle dN_{ch}/d\eta d\phi \rangle$ within uncertainties and meaning the UE multiplicity is independent
407 on the leading jet η .

408 These results, along with recent STAR preliminary measurements on semi-inclusive jet
409 yield in high/low EA p +Au collisions, point to an early time correlation between the high Q^2
410 scattering leading to jet production and the low energy processes which result in the forward
411 activity. The UE multiplicity shows very little anti-correlation with the jet momenta and is
412 currently explored as a selection of event EA for future measurements to reduce the early
413 time or long range effects which nominally result from selecting on forward activity.

414 Isobar Collisions

415 The isobar data collected by STAR during Run-18 is a high statistics minimum bias
416 dataset where the primary goal was to study potential differences in chiral magnetic effects
417 between the two colliding species, Ru and Zr, as detailed in Sec 1.2. The jet working group
418 in STAR is involved in ongoing measurements of energy loss via inclusive charged hadrons
419 suppression and semi-inclusive hadron-jet measurements exploiting these high statistics and
420 low pile-up data. Isobar data provides a motivation to study energy loss for various system
421 sizes in comparison with Au+Au collisions and dependencies on the system geometry.

422 1.1.3 Heavy-flavor

423 Heavy-flavor (HF) quarks are produced predominately via hard scatterings of partons in
424 p(A)+p(A) collisions. Kinematic distributions and hadronization probabilities of HF quarks
425 in A collisions can be different than those in pp collisions due to interactions of HF quarks
426 with the QGP medium. Understanding these differences allows us to determine properties
427 of the QGP. STAR has recently published two papers on heavy flavor production: 1) the
428 measurement of inclusive J/ψ polarization in pp collisions at $\sqrt{s_{NN}} = 200$ GeV [56] and 2)
429 observation of D_s/D^0 enhancement in Au+Au collisions at $\sqrt{s_{NN}} = 200$ GeV [57]. The former
430 measures the J/ψ polarization in pp collisions with improved precision and over a wider
431 p_T range, and thus provides a stricter constraint on quarkonium production mechanisms.
432 The latter reveals that the strange-charm meson (D_s) yield is significantly enhanced in
433 Au+Au collisions with respect to that in elementary pp / $e+p$ / $e+e$ collisions and confirms
434 that coalescence is an important hadronization mechanism also for charm quarks in heavy-
435 ion collisions. Below we describe new results from STAR on inclusive J/ψ production in
436 p +Au collisions at $\sqrt{s_{NN}} = 200$ GeV and in Au+Au collisions at $\sqrt{s_{NN}} = 54.4$ GeV.

437 J/ψ production has been found to be suppressed in Au+Au collisions at RHIC top
438 energies [58, 59]. Such a suppression can be produced from color screening of the $c\bar{c}$ potential
439 by the QGP medium, and by cold nuclear matter (CNM) effects from e.g., nuclear parton
440 distribution functions, energy loss or absorption in the nucleus, and interaction with co-
441 moving hadrons. Moreover, in heavy-ion collisions J/ψ can be produced from recombination
442 of uncorrelated c and \bar{c} in the QGP. Therefore, in order to precisely determine the suppression
443 due to the color screening effect alone, it is important to quantify the CNM effects, and be
444 able to disentangle the color-screening and recombination effects.

445 STAR has reported a preliminary result on the nuclear modification factor R_{pA} for in-
446 clusive J/ψ with $p_T > 4$ GeV/c and $|y| < 1$, as shown in Fig. 11. The result is extracted
447 in the dielectron channel from the data collected from pp and p +Au collisions at $\sqrt{s_{NN}} =$
448 200 GeV in 2015. Compared to previous measurements, this result presents a more precise
449 determination of the CNM effects for high- p_T inclusive J/ψ at the RHIC top energy. The
450 measured R_{pAu} is consistent with unity, suggesting little suppression in this kinematic region
451 due to the CNM effects. The result confirms that the color-screen effect is the main cause
452 of the large suppression of high- p_T inclusive J/ψ observed in Au+Au collisions at $\sqrt{s_{NN}} =$
453 200 GeV. These data points provide a stronger constraint on theoretical calculations for J/ψ
454 suppression due to the CNM effects and J/ψ production mechanisms in heavy-ion collisions.

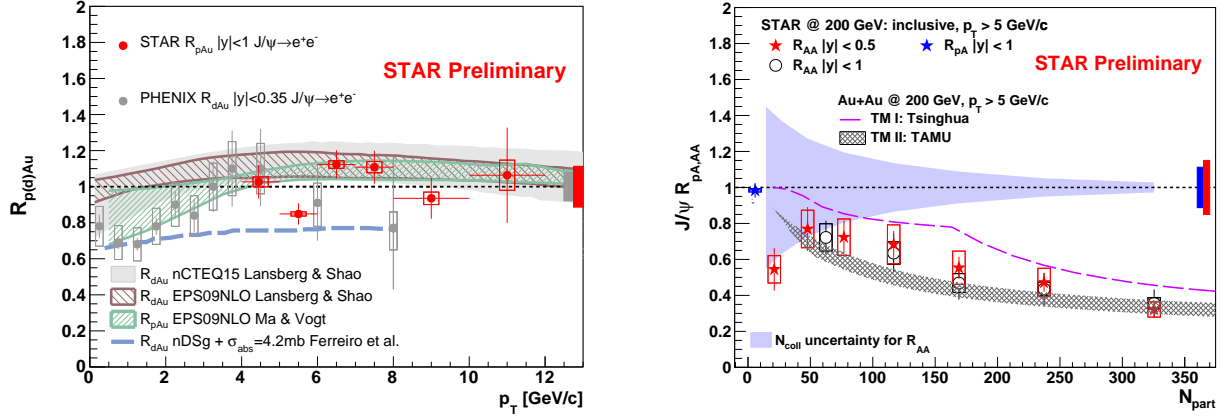


Figure 11: Left: $R_{p(d)Au}$ vs. p_T for inclusive J/ψ in p(d)+Au collisions at $\sqrt{s_{NN}} = 200$ GeV. Red circle: this analysis; grey circle: PHENIX R_{dAu} in $|y| < 0.35$ [60]; grey band: R_{dAu} from nCTEQ15 nuclear PDF sets [61]; brown shadowed: R_{dAu} from EPS09 NLO nuclear PDF sets [61]; green shadowed: R_{pAu} from EPS09 NLO nuclear PDF sets [62]; blue dashed line: R_{dAu} nDSg + $\sigma_{abs} = 4.2$ mb [63]. Right: R_{pAu} and R_{AA} vs. N_{part} . Blue star: this analysis; red star: STAR R_{AA} $|y| < 0.5$ [59]; violet dashed line: Tsinghua model [64]; black shadowed: TAMU model [65].

455 STAR has also released at the 2021 Strangeness in Quark Matter conference a new pre-
 456 liminary result on the nuclear modification factor R_{AA} for inclusive J/ψ in Au+Au collisions
 457 at $\sqrt{s_{NN}} = 54.4$ GeV. The result is extracted in the dielectron channel from BES-II data
 458 collected in 2017. As can be seen in Fig. 12, the measured R_{AA} at $\sqrt{s_{NN}} = 54.4$ GeV is
 459 consistent with those measured at $\sqrt{s_{NN}} = 39, 62.4$ and 200 GeV [58], suggesting a partial
 460 cancellation of J/ψ suppression due to the color-screen effect by J/ψ produced from recom-
 461 bination. Indeed, the J/ψ yields in heavy-ion collisions from SPS [66, 67], RHIC [58, 59] and
 462 LHC experiments [68, 69] at $\sqrt{s_{NN}}$ ranging from 17.2 GeV to 5.02 TeV can be described by
 463 model calculations that incorporate both the color-screening and recombination effects [65].

464 1.1.4 Light Flavor and Ultra-peripheral Collisions

465 The Light Flavor Spectra and Ultra-peripheral Collisions (LFSUPC) physics working group
 466 is responsible for the measurements of calibrated production yields and spectra in inclusive
 467 ion-ion collisions, ultra-peripheral collisions, and exclusive pp collisions.

468 Elastic scattering plays an important role in proton-proton scattering at high energies.
 469 At the the LHC, for example, it makes up 20% of the total cross section. The pp elastic and
 470 total cross sections have been measured at pp colliders, however there exists a large energy
 471 gap between the measurements at the ISR and the LHC. The are proton-antiproton data
 472 from the Tevatron, however these are expected to have differences to the pp cross sections.
 473 It is important to fill the gap between the ISR and LHC to constrain the phenomenological
 474 models and to better understand the differences to the proton-antiproton data. The STAR
 475 detector was upgrades to include far-forward Roman Pots which were previously used by the

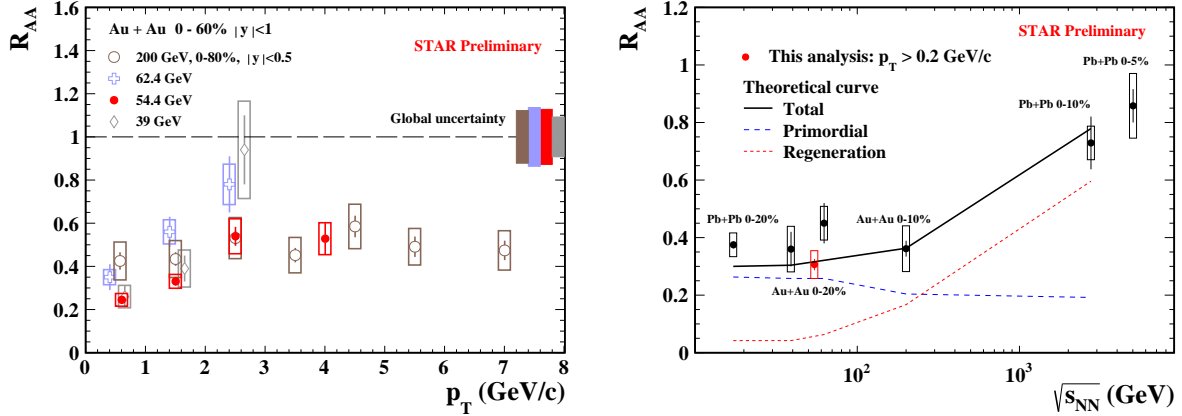


Figure 12: Left: R_{AA} vs. p_T for inclusive J/ψ in Au+Au collisions at $\sqrt{s_{NN}} = 54.4$ GeV (this analysis) and at 39, 62.4 and 200 GeV [58]. Right: R_{AA} vs. $\sqrt{s_{NN}}$ for inclusive J/ψ in Pb+Pb collisions at $\sqrt{s_{NN}} = 17.2$ GeV [66, 67], 2.76 [68] and 5.02 TeV [69], and in Au+Au collisions at 39, 62.4 and 200 GeV [58, 59].

476 PP2PP experiment. Figure 13 shows the STAR results for the elastic, inelastic, and total
 477 cross sections compared to the world data for both proton-proton and proton-antiproton
 478 collisions. The STAR results at 200 GeV are in good agreement with the trends of the
 479 world data and with the COMPETE predictions [70]

480 The first results from the STAR fixed-target program for Au+Au collisions at $\sqrt{s_{NN}} =$
 481 3.0 GeV are now becoming available. Figure 14 shows the most advanced analyses from these
 482 data. The left panel of Fig. 14 shows the ϕ/K^- ratio as a function of collision energy. A
 483 significant enhancement of the ϕ yield as compared to that of the charge kaons is striking. The
 484 Grand Canonical Ensemble, which assumes a system of infinite extent, predicts significantly
 485 lower relative yields for the ϕ . However in the finite and ephemeral systems created in heavy-
 486 ion collisions near the nucleon-nucleon production threshold, there is a strong tendency for
 487 the strange quarks and anti-quarks to coalesce into a ϕ . This tendency had been previously
 488 noted in experiments at the GSI. The recent STAR results provide data for three different
 489 centrality ranges, which allows comparison to the lighter beam-target combinations from the
 490 GSI, to better constrain the strange quark coalescence radius. Microscopic transport models,
 491 UrQMD and SMASH, which include both resonance decays and the finite size effects, can
 492 reasonably describe the ϕ/K^- ratio at this energy (but not the K^- and ϕ yields). These
 493 results suggest a significant change in the strangeness production mechanisms at $\sqrt{s_{NN}} =$
 494 3.0 GeV as compared to that in higher energy collisions. This could shed new light on the
 495 understanding of the QCD Equation of State in the high baryon density regime.

496 The STAR fixed-target program covers the collision energy range where the yields of
 497 hyper-nuclei are expected to be maximized. Hyper-nuclei are understood to be created via
 498 the coalescence of hyperons with neutrons and protons. Although the hyperon yields in-
 499 crease approximately linearly with $\ln(\sqrt{s_{NN}})$, due to the stopping of participant baryons,
 500 the density of neutrons and protons is significantly higher at these lower energies. Thus,

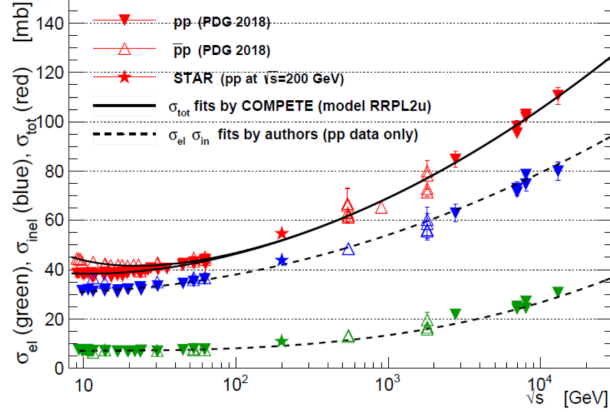


Figure 13: Comparison of STAR results on σ_{tot} , σ_{inel} , and σ_{el} with the world data for data below 1.8 TeV, the Tevatron and the LHC experiments. The COMPETE prediction for σ_{tot} is also shown (solid curve). The dashed curves represent STAR fits to σ_{inel} and σ_{el} using the same function at COMPETE. STAR data were not used in the fit.

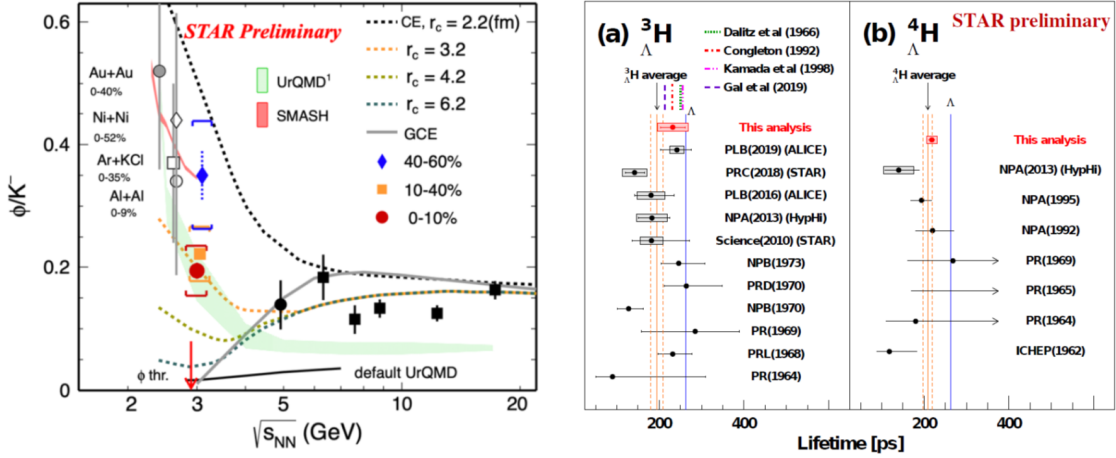


Figure 14: (Left) ϕ/K^- ratio as a function of collisions energy. The colored data points show the recent STAR measurements in centrality bins. The red arrow depicts the ϕ -meson production threshold in proton-proton collisions. The grey solid line represents a thermal model based the the Grand Canonical Ensemble (GCE) while the dashed lines represent calculations based on the Canonical Ensemble (CE) with four different parameters of strangeness correlation radius (r_c). The blue and red bands show transport model calculations using UrQMD and SMASH respectively. (Right) ${}^3_\Lambda\text{H}$ (a) and ${}^4_\Lambda\text{H}$ (b) measured lifetime compared to previous measurements, model calculations and the free Λ lifetime. The experimental average lifetimes and the corresponding uncertainties of ${}^3_\Lambda\text{H}$ (a) and ${}^4_\Lambda\text{H}$ are also shown as orange bands.

501 hyper-nucleus production is expected to be maximized at $\sqrt{s_{\text{NN}}} = 5$ GeV. The acceptance
502 for hyper-nucleus detection is maximized at the lowest fixed-target energies making this
503 lowest energy fixed-target data set an ideal laboratory for the study of hyper-nuclei. Even
504 with only a few hundred million Au+Au collisions at $\sqrt{s_{\text{NN}}} = 3$ GeV, as compared to the
505 few billion at 200 GeV, we are able to achieve far more significant yields of hyper-nuclei
506 and reduce the uncertainty on measurements of their properties. One of the first properties
507 of interest is the lifetimes of hyper-nuclei. The question being addressed is whether incor-
508 porating a hyperon within a nucleus stabilizes or de-stabilizes the hyperon; one notes that
509 neutrons are stabilized when bound within a nucleus. This question has been addressed both
510 theoretically and experimentally for several decades, as seen in the right panel of Fig. 14.
511 The preliminary results from the STAR fixed-target data for the lifetimes of ${}^3_{\Lambda}\text{H}$ (a) and ${}^4_{\Lambda}\text{H}$
512 have the highest precision of any measurement to date conclusively demonstrating the the
513 lifetimes are significantly smaller than the free Λ lifetime. The ${}^3_{\Lambda}\text{H}$ lifetime is consistent with
514 theoretical calculations assuming the ${}^3_{\Lambda}\text{H}$ is weakly bound state and including pion final state
515 interactions.

516 1.2 CME Search and Isobar Run

517 1.2.1 Introduction

518 A decisive experimental test of the Chiral Magnetic Effect (CME) has become one of the
 519 major scientific goals of the heavy-ion physics program at RHIC. The existence of CME
 520 will be a leap towards an understanding of the QCD vacuum, establishing a picture of
 521 the formation of a deconfined medium where chiral symmetry is restored, and will also
 522 provide unique evidence of the strongest known electromagnetic fields created in relativistic
 523 heavy-ion collisions [71, 72]. The impact of such a discovery goes beyond the community of
 524 heavy-ion collisions and will possibly be a milestone in physics. The remaining few years
 525 of RHIC running and analyses of already collected data probably provide the only chance
 526 for dedicated CME searches in heavy-ion collisions in the foreseeable future. Significant
 527 efforts from STAR, as well as other collaborations, have been dedicated towards developing
 528 methods and observables to isolate possible CME-driven signals from non-CME background
 529 contributions in measurements of charge separation across the reaction plane. Many clever
 530 ideas have been proposed and applied to existing data. However, a general consensus is that
 531 measurements from isobar collisions, Ruthenium+Ruthenium (Ru+Ru) that has 5 – 9%
 532 higher B-field than Zirconium+Zirconium (Zr+Zr), thus a 10 – 18% larger CME correlation
 533 signal because of its B^2 dependence, provide the best solution. At the time of writing this
 534 BUR document, STAR has already produced all the data for the final step of the analysis,
 535 the two species are separated and the analyzers are running their codes to produce the final
 536 results. We discuss the steps of blind analysis in the following sections.

537 1.2.2 Modality of Isobar Running at RHIC

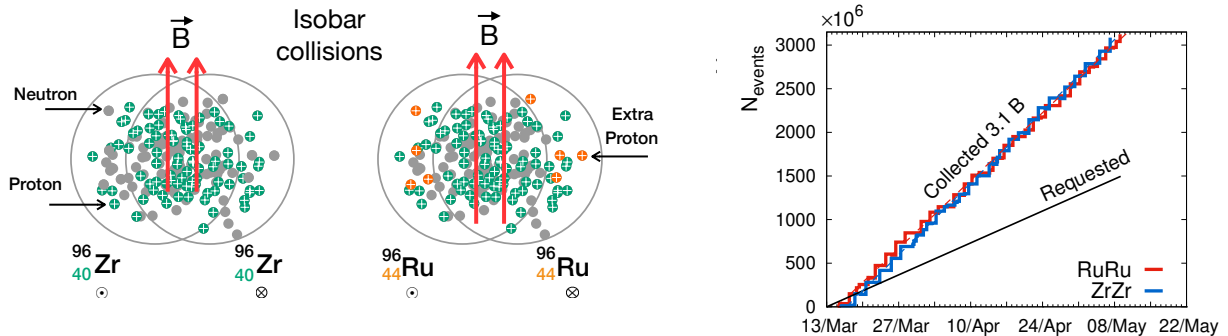


Figure 15: Left: Cartoon of the isobar collisions, about 10 – 18% stronger B-field squared is expected in Ru+Ru collisions as compared to Zr+Zr. Right: Summary of the Isobar data collected during Run-18.

538 Colliding isobars, particularly Ru+Ru and Zr+Zr, to make a decisive test of CME was
 539 proposed by Voloshin in Ref [73], the same paper also proposed to use Uranium collisions to

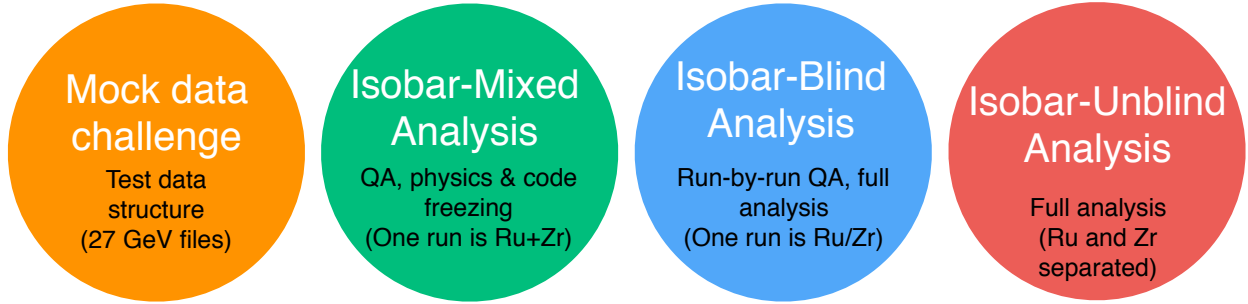


Figure 16: Cartoon taken from Ref [79], showing the steps of analysis consisting of the mock-data challenge and the three-step isobar blind analysis. This cartoon is based on the procedure for the blind analysis of isobar data that have been outlined in Ref [80]. At the time of writing of this document the two species are separated and analyzers in STAR are running their codes as a part of the last step (shown in red).

540 disentangle signal and background of CME. The possible difference in the signals relies on
 541 the 10–18% higher B-field squared in Ru+Ru compared to Zr+Zr, due to four extra protons
 542 in each Ru nucleus [74], in contrast to about 4% difference in flow driven background [75].
 543 Such estimates are sensitive to details of the shape, charge distribution and neutron skin
 544 thickness of the two isobar nuclei [74, 76, 77].

545 In the 2017-18 RHIC BUR [78] STAR proposed to collect data for two 3.5 week periods
 546 in Run-18. The projection was based on the prospect of achieving five-sigma significance in
 547 a scenario where the measurement of $\Delta\gamma$ has 80% non-CME background. This, however,
 548 relies on the assumption that the systematic uncertainties of the measurements are only a
 549 few percent, and much smaller than the statistical uncertainty. This started a large scale
 550 collaboration wide effort in synergy with the RHIC collider accelerator department to plan
 551 for the isobar running in 2018. Based on the studies of previous years of data from Au+Au
 552 and U+U collisions several major sources of systematics in the measurement of $\Delta\gamma$ were
 553 identified. The major sources include: run-to-run variation of detector response due to loss
 554 of acceptance, change in efficiency and variation in luminosity that affects the number of
 555 reconstructed tracks in the TPC. This eventually leads to uncorrectable systematic uncer-
 556 tainties in $\Delta\gamma$, the main observable to measure charge separation across the event plane. In
 557 order to minimize such systematics a running proposal was developed to: 1) switch species
 558 between each store and, 2) keep long stores with a level luminosity; aiming for specific rates
 559 in the coincidence measurements of beam fragments via zero-degree calorimeters. The aim
 560 was to maintain exact balance of run and detector conditions for the two species so that
 561 observations in the two systems are equally affected and can later on be largely eliminated
 562 in the ratios of observables.

563 1.2.3 Blinding of Data Sets and Preparation for Analyses

564 The procedure to blind the isobar data was already in place well ahead of the actual data
 565 taking to limit the access of the data to the analysts to eliminate possible unconscious biases.

566 At the successful conclusion of the isobar run in 2018 STAR had collected more than 3 billion
567 minimum-bias events for each isobar species. A total of five institutional groups agreed to
568 perform blind analyses on the data. The analysts from each group will focus on a specific
569 analysis described in the following section. The substantial overlap of some analyses will
570 help cross check the results.

571 The details of the blinding procedure and data structure were decided by an analysis
572 blinding committee (ABC) who are not part of the team of analysts but work in close
573 collaboration with STAR experts who are part of the production team. The idea is to provide
574 the analysts access to data where species-specific information are disguised or removed prior
575 to the final step, shown in red in Fig. 16. Careful consideration was taken by the ABC
576 to make sure only the essential information to do the analysis-specific quality assurance of
577 the data was available to the analysts, to ensure the integrity of the CME Isobar analyses.
578 The quality assurance, calibration and centrality determination work, that require species
579 information, were done only by STAR experts who were not a part of the blind analysis
580 team.

581 1.2.4 Methods for the Isobar Blind Analyses

582 The detailed procedure for the blind analyses of isobar data have been outlined in Ref [80].
583 Figure 16 is a cartoon that summarizes the mock-data challenge and three steps of the blind
584 analysis.

585 The zeroth step shown, in the extreme left of Fig. 16 (orange circle), was the mock-
586 data challenge; a crucial step to familiarize the analysts with the technicalities of the data
587 structures that have been specifically designed for blind analysis, and ensure the blinding
588 worked.

589 The first step shown in Fig. 16 (green circle) as the “isobar-mixed analysis” was truly the
590 first step of the blind analysis. This was also the most challenging step from the point of
591 view of the analysts. In this step they were provided with a data sample where each “run”
592 comprised of events that were a mixed sample of the two species. In this step the analysts
593 performed the full quality assurance (QA) and physics analysis of the data, documented
594 every detail of their procedures and froze the codes. After the completion of this step, no
595 changes to the analysis code or procedures were permissible. The only permissible change
596 in the following step was to reject bad runs or pile-up events. However, in order to avoid
597 unconscious bias, such rejections could not be done arbitrarily. Instead, an automated
598 algorithm for bad run rejection was developed and corresponding codes frozen. The stability
599 of the automated QA algorithm was tested on existing Au+Au and U+U data.

600 The second step shown in Fig. 16 (blue circle) is referred to as the “isobar-blind analysis”.
601 For this the analysts were provided with files each of which contained data from a single,
602 but blinded, species. From this step on-wards, the analysts were only allowed to run their
603 previously frozen codes. The main purpose of this step was to perform run-by-run QA of
604 the data. The files each contained a limited number of events that could not lead to any
605 statistically significant result. Although a pseudo-run-number was used for each file, the
606 time ordering was preserved with a unique mapping that was unknown to the analysts. It

607 was important to maintain the time ordering to identify time-dependent changes in detectors
 608 and run conditions as a part of the run-by-run QA. A similar automated algorithm was also
 609 used for identifying and rejecting bad runs. After this step no more changes are allowed in
 610 terms of QA.

611 The final step of isobar blind analysis shown by red circle in Fig. 16 is referred to as
 612 “isobar-unblind” analysis. In this step, the species information will be revealed and the
 613 physics results will be produced by the analysts using the previously frozen codes. However,
 614 one important step is as follows. No analyzer is allowed to run his/her own code. The frozen
 615 codes should be run by a independent person. The findings from this step will be directly
 616 submitted for publication without alteration. If a mistake is found in the analysis code, the
 617 erroneous results will also accompany the corrected results.

618 1.2.5 Observables for Isobar Blind Analyses

619 The general strategy is to compare two isobar species to search for a significant difference
 620 in whatever observable used. The following sections briefly describe the procedures agreed
 621 upon as the focus of the Isobar blind analysis with comments on the outlook for isobar blind
 622 analysis: 1) measurement of higher order harmonics of γ -correlator, 2) exploiting the relative
 623 charge separation across participant and spectator planes, 3) differential measurements of
 624 $\Delta\gamma$ to identify and quantify backgrounds, 4) the use of the R-observable to measure charge
 625 separation. The first three approaches are based on the aforementioned three-particle corre-
 626 lator, and the last employs slightly different approaches to quantify charge separation. There
 627 is also another analysis which will be performed using the signed balance function, but this
 628 is not part of the blind analyses.

629 Mixed Harmonics Measurements with Second and Third Order Event Planes

630 In order to proceed, it is better to rewrite the conventional γ -correlator in a more general
 631 notation as $\gamma_{112} = \langle \cos(\phi_a^\alpha + \phi_b^\beta - 2\Psi_2) \rangle$. The idea is to measure charge separations across the
 632 third harmonic event plane by constructing a new correlator $\Delta\gamma_{123} = \gamma_{123}(OS) - \gamma_{123}(SS)$,
 633 where $\gamma_{123} = \langle \cos(\phi_a^\alpha + 2\phi_b^\beta - 3\Psi_3) \rangle$ was introduced by CMS collaboration in Ref [82]. Since
 634 the Ψ_3 plane is random and not correlated to B-field direction (see Fig. 17), γ_{123} is purely
 635 driven by non-CME background, the contribution of which should go as v_3/N . This is very
 636 useful to contrast signal and background scenarios by comparing measurements in the two
 637 isobaric collision systems. Since Ru+Ru has larger B-field than Zr+Zr but comparable back-
 638 ground, the case for CME would be as follows: $(\Delta\gamma_{112}/v_2)^{\text{Ru+Ru}}/(\Delta\gamma_{112}/v_2)^{\text{Zr+Zr}} > 1$ and
 639 $(\Delta\gamma_{112}/v_2)^{\text{Ru+Ru}}/(\Delta\gamma_{112}/v_2)^{\text{Zr+Zr}} > (\Delta\gamma_{123}/v_3)^{\text{Ru+Ru}}/(\Delta\gamma_{123}/v_3)^{\text{Zr+Zr}}$. Figure 17 (left) shows
 640 the measurement of these observables in U+U and Au+Au collisions. Within the uncertain-
 641 ties of the measurements, no significant difference in the trend of $\Delta\gamma_{112}/v_2$ and $\Delta\gamma_{123}/v_3$ is
 642 observed for the two collision systems except for the very central events. Predictions from
 643 hydrodynamic model calculations with maximum possible strength of local charge conserva-
 644 tion [75] is shown on the same plot. Overall observation indicates the backgrounds dominate
 645 the measurements and a similar analysis of the isobar data is highly anticipated.

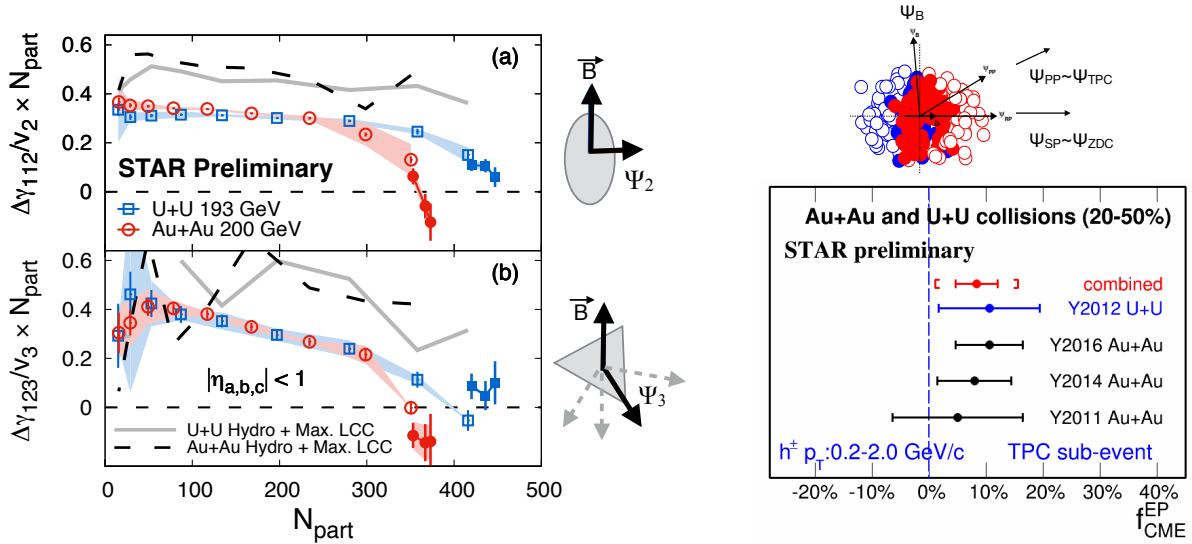


Figure 17: (Left) Measurement of charge separation along second and third order event planes in Au+Au and U+U collisions. (Right) Fraction of possible CME signal in the measurement of $\Delta\gamma$ with respect to spectator and participant planes [81].

Charge Separation Along Participant and Spectator Planes

This analysis makes use of the fact that the B-field driven signal is more correlated to the spectator plane, in contrast to flow-driven backgrounds which are maximal along the participant plane. The idea was first introduced in Ref. [83] and later on followed up in Ref. [84]. It requires measurement of $\Delta\gamma$ with respect to the plane of produced particles, a proxy for the participant plane, as well as with respect to the plane of spectators. In STAR, the two measurements can be done by using Ψ_2 from the TPC and Ψ_1 from the ZDCs, respectively. The approach is based on three main assumptions: 1) the measured $\Delta\gamma$ has contributions from signal and background, which can be decomposed as $\Delta\gamma = \Delta\gamma^{\text{bkg}} + \Delta\gamma^{\text{sig}}$, 2) the background contribution to $\Delta\gamma$ should follow the scaling $\Delta\gamma^{\text{bkg}}(\text{TPC})/\Delta\gamma^{\text{bkg}}(\text{ZDC}) = v_2(\text{TPC})/v_2(\text{ZDC})$ and, 3) the signal contribution to $\Delta\gamma$ should follow the scaling $\Delta\gamma^{\text{sig}}(\text{TPC})/\Delta\gamma^{\text{sig}}(\text{ZDC}) = v_2(\text{ZDC})/v_2(\text{TPC})$. The first two have been known to be working assumptions, widely used for a long time and can be used to test the case of CME [84] if $(\Delta\gamma/v_2)(\text{ZDC})/(\Delta\gamma/v_2)(\text{TPC}) > 1$. The validity of the last one was studied and demonstrated in Ref. [83]. Using all three equations one can extract [81] the fraction of possible CME signal $f_{\text{CME}} = \Delta\gamma^{\text{sig}}/\Delta\gamma$ in a fully data-driven way as shown in Fig. 17(right). This analysis will be done with the isobar data and the case for CME will be

$$f_{\text{CME}}^{\text{Ru+Ru}} > f_{\text{CME}}^{\text{Zr+Zr}} > 0.$$

Differential Measurements of $\Delta\gamma$ to Identify and Quantify Background

Invariant mass dependence of charge separation: Differential measurements of $\Delta\gamma$ with invariant mass and relative pseudorapidity provide interesting prospects to identify and quantify the sources of flow and non-flow driven backgrounds. The idea to use invariant mass is

668 simple and was first introduced in Ref. [85]. Resonances are widely identified by observing
669 structures in the invariant mass spectra of the decay daughters. Consider a pair of opposite
670 sign pions for example, it is known that a large fraction of them come from the neutral
671 resonances that show up in the invariant mass spectrum of $m_{inv}(\pi^+ + \pi^-)$. If we restrict
672 the analysis to pairs of pions, differential measurements of $\Delta\gamma$ with $m_{inv}(\pi^+ + \pi^-)$ should
673 also show similar peak like structures if background from neutral resonances dominate the
674 charge separation. Indeed similar peak structures are observed and an analysis has been per-
675 formed to extract the possible fraction of CME signals from the current measurements [86].
676 This analysis relies on the assumption that CME signals do not show peak like structures
677 in $m_{inv}(\pi^+ + \pi^-)$ and also requires an assumption of m_{inv} dependence of the CME signal,
678 therefore calls for more theoretical insight in this direction have been made.

679 *Relative pseudorapidity dependence:* The relative pseudorapidity dependence of azimuthal
680 correlations are widely studied to identify sources of long-range components that are domi-
681 nated by early time dynamics as compared to late time correlations that are prevented by
682 causality to appear as short-range correlations. The same can be extended to charge depen-
683 dent correlations which provide the impetus to explore the dependence of $\Delta\gamma$ on the pseudo-
684 rapidity gap between the charge carrying particles $\Delta\eta_{ab} = |\eta_a - \eta_b|$ in $\langle \cos(\phi_a^\alpha + \phi_b^\beta - 2\Psi_{RP}) \rangle$.
685 Such measurements have been performed in STAR with Au+Au and U+U data. It turns
686 out that the possible sources of short-range correlations due to photon conversion to $e^+ - e^-$,
687 HBT and Coulomb effects can be identified and described as Gaussian peaks at small $\Delta\eta_{ab}$,
688 the width and magnitude of which strongly depend on centrality and system size. Going to
689 more peripheral centrality bins, it becomes harder and harder to identify such components
690 as they overlap with sources of di-jets fragmentation that dominates both same-sign and
691 opposite sign correlations. An effort to decompose different components of $\Delta\gamma$ via study of
692 $\Delta\eta_{ab}$ can be challenging although a clear sign of different sources of correlations are visible in
693 change of shape of individual same-sign and opposite sign measurements of γ -correlator [87].

694 In any case, these differential measurements of $\Delta\gamma$ in isobar collisions provide the prospect
695 to extract the $m_{inv}(\pi^+ + \pi^-)$ and $\Delta\eta$ dependence of CME signals that will provide much
696 deeper insights on the origin of the effect. Comparing the differential measurements in
697 Ru+Ru and Zr+Zr it will be possible to extract the invariant mass and the relative pseu-
698 dorapidity distribution of the CME signal that will provide deeper insight into the origin of
699 the phenomenon.

700 **Alternate Measure: The Novel R-observable**

701 The R -observable is actually a distribution, introduced in Ref. [90], and defined as the
702 ratio of two distribution functions of the quantity ΔS parallel and perpendicular to B-field
703 direction defined as $R_{\Psi_m}(\Delta S) = C_{\Psi_m}(\Delta S)/C_{\Psi_m}^\perp(\Delta S)$. Here ΔS measures the difference in
704 the dipole moment of the positive and negative charge in an event (see Ref. [90] for details).
705 The shape of $R_{\Psi_2}(\Delta S)$ will be sensitive to CME as well as non-CME background. Model
706 calculations have established several unique features of this observable: 1) presence of CME
707 signal will lead to a concave shape of the $R_{\Psi_2}(\Delta S)$, 2) increasing strength of CME signal will
708 increase the concavity of $R_{\Psi_2}(\Delta S)$. In the original paper [90] a second correlator $R_{\Psi_3}(\Delta S)$

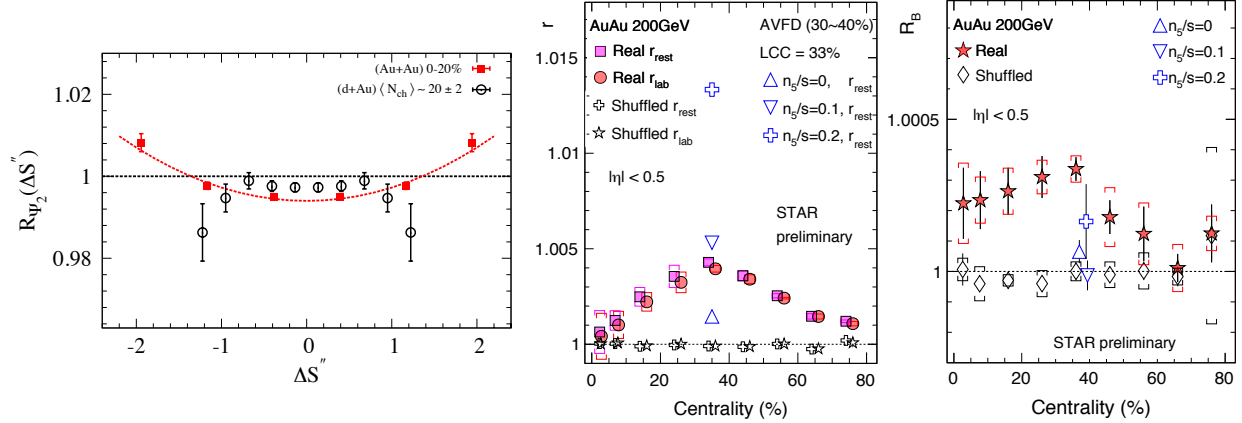


Figure 18: (Left) The R-observable shown for different collision systems, a concave shape is consistent with CME expectation [88]. (Right) The two main quantities r and R_B derived from the signed balance function, deviation from unity is consistent with CME expectations [89].

709 was proposed which will measure charge separation purely driven by non-CME background
 710 and may serve as a baseline. However, recent investigation has shown that due to symmetry
 711 properties of harmonics in R-variable, the results for $R_{\Psi_3}(\Delta S)$ correlator may be difficult
 712 to interpret and require further studies. Therefore, ongoing and future experimental studies
 713 from STAR will focus only on R_{Ψ_2}

714 The measurement of R_{Ψ_2} is shown in Fig.18. The quantity $\Delta S''$ shown is a slight variant of
 715 (ΔS) that incorporates correction for particle number fluctuations and event plane resolution.
 716 The observation of Fig.18 indicates more concave shape for R_{Ψ_2} in Au+Au whereas flat or
 717 convex shapes for p/d+Au indicates that the measurements are consistent with expectations
 718 of CME [88]. For isobar collisions, the case of CME requires an observation of a concave
 719 shape for the ratio of the observables $R_{\Psi_2}(\Delta S)^{\text{Ru+Ru}}/R_{\Psi_2}(\Delta S)^{\text{Zr+Zr}}$.

720 Alternate Measure: The Signed Balance Function

721 A very recently proposed observable to search for CME is via the signed balance function
 722 (SBF) [91]. The idea is to account for the ordering of the momentum of charged pairs
 723 measured by the width of SBF that is expected to be different for out-of-plane as compared
 724 to in-plane measurements captured in the ratio r_{lab} . In addition, one can also account for
 725 the boost due to collective expansion of the system that forces all pairs to move in the same
 726 direction and measure the ratio in the pair rest frame r_{rest} . In the presence of CME, the
 727 individual ratios, as well as the double ratio $R_B = r_{\text{rest}}/r_{\text{lab}}$, are expected to be greater
 728 than unity. Preliminary measurements, shown in Fig. 18 (right), from STAR in Au+Au 200
 729 GeV data seem to be consistent with CME expectation. This observable will be studied
 730 with the isobar data but not as a part of the blind analysis. The CME expectation is:
 731 $r(\text{Ru} + \text{Ru}) > r(\text{Zr} + \text{Zr})$.

1.2.6 Benchmarking CME Observables Against EBE-AVFD Model

As the STAR Collaboration is analyzing the data from isobaric collisions with multiple CME observables, it is desirable to have a controlled study on observables so that their relative performance can be understood and calibrated. This will serve as an important reference point when interpreting isobaric data. In this section, we present a benchmark study for three CME observables, namely, the inclusive γ correlator [92], the R correlator [90, 93] and the signed balance functions [91]. The first two observables are included in STAR’s blind-analysis, for which the study was conducted with frozen code that was checked into STAR official repository as part of blinding procedure. Aforementioned, the last one is not a part of blind-analysis, but has intrinsic connections [94] with the other two thus it is also presented here for completeness. For a full version of this study, please refer to [94].

The model used in this study is event-by-event anomalous-viscous fluid dynamics (EBE-AVFD) model [95–97]. It implements the anomalous transport current from CME into fluid dynamics framework to simulate the evolution of fermion currents on an event-by-event basis and to evaluate the resulting charge separation in the QGP, on top of the neutral bulk background described by the VISH2+1 hydrodynamic simulations [98] with Monte-Carlo Glauber initial conditions, followed by a URQMD hadron cascade stage [99, 100]. This new tool allows one to quantitatively and systematically investigate the various proposed measurements’ responses to the CME signal and account for the resonance contributions.

For each of the two isobaric collision systems, Ru+Ru and Zr+Zr at $\sqrt{s_{NN}} = 200$ GeV, four cases of the EBE-AVFD events have been generated, with $n_5/s = 0, 0.05, 0.1, \text{ and } 0.2$, respectively. Here n_5 is the initial axial charge density and s is the entropy density. A strong CME effect is expected when n_5/s is large. The centrality selection for all the cases focuses on 30-40% central collisions, where the potential CME signal is relatively easy to detect owing to good event plane resolutions. 200 million events were produced for each case of $n_5/s = 0$ and $n_5/s = 0.2$, and 400 million events for the each of the other two cases. To mimic the detection performance of the STAR Time Projection Chamber, simulated particles in the EBE-AVFD events are randomly rejected according to a transverse-momentum dependent tracking efficiency.

Figure 19 presents the EBE-AVFD calculations of $\gamma_{112}^{\text{OS(SS)}}$ (a) and $\Delta\gamma_{112}$ (b) as functions of n_5/s for 30-40% isobaric collisions at $\sqrt{s_{NN}} = 200$ GeV. The ratios of $\Delta\gamma_{112}$ between Ru+Ru and Zr+Zr is delineated in panels (c). At each n_5/s value, γ_{112}^{OS} remains positive and γ_{112}^{SS} stays negative, both with larger magnitudes at higher n_5/s . Although the CME expects γ_{112}^{OS} and γ_{112}^{SS} to be symmetric around zero, there exist some charge-independent backgrounds such as momentum conservation and elliptic flow that shift both γ_{112}^{OS} and γ_{112}^{SS} up or down. Therefore, we shall focus on $\Delta\gamma_{112}$, which shows a finite background contribution at $n_5/s = 0$ and increases with the CME signal. The difference between Ru+Ru and Zr+Zr is better viewed with the ratio of $\Delta\gamma_{112}^{\text{Ru+Ru}}/\Delta\gamma_{112}^{\text{Zr+Zr}}$. This ratio is consistent with unity at $n_5/s = 0$, and increases quadratically with n_5/s as demonstrated by the 2nd-order-polynomial fit function that passes (0, 1) (dashed line). The quadratically-increasing trend is expected, because this ratio is a linear function of the CME signal fraction in $\Delta\gamma_{112}$ in a two-component perturbative framework [101], and the latter is proportional to $(n_5/s)^2$ or a_1^2 . The significance

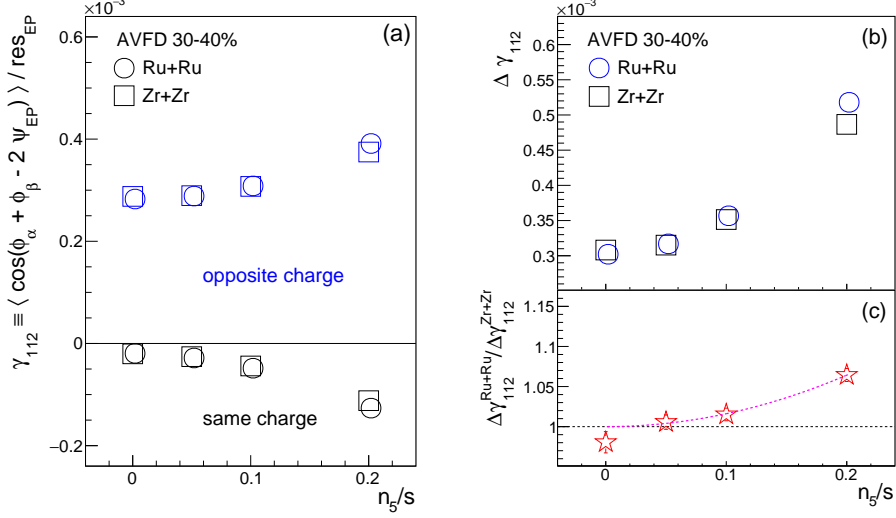


Figure 19: EBE-AVFD calculations of $\gamma_{112}^{\text{OS(SS)}}$ (a) and $\Delta\gamma_{112}$ (b) as functions of n_5/s for 30-40% isobaric collisions at $\sqrt{s_{\text{NN}}} = 200$ GeV, together with the ratio of $\Delta\gamma_{112}$ (c) between Ru+Ru and Zr+Zr. In panel (c), the 2nd-order-polynomial fit function illustrates the rising trend starting from (0, 1).

774 values of the $\Delta\gamma_{112}^{\text{Ru+Ru}} / \Delta\gamma_{112}^{\text{Zr+Zr}}$ ratio, along with other ratios to be discussed, are stored in
 775 Table 4.

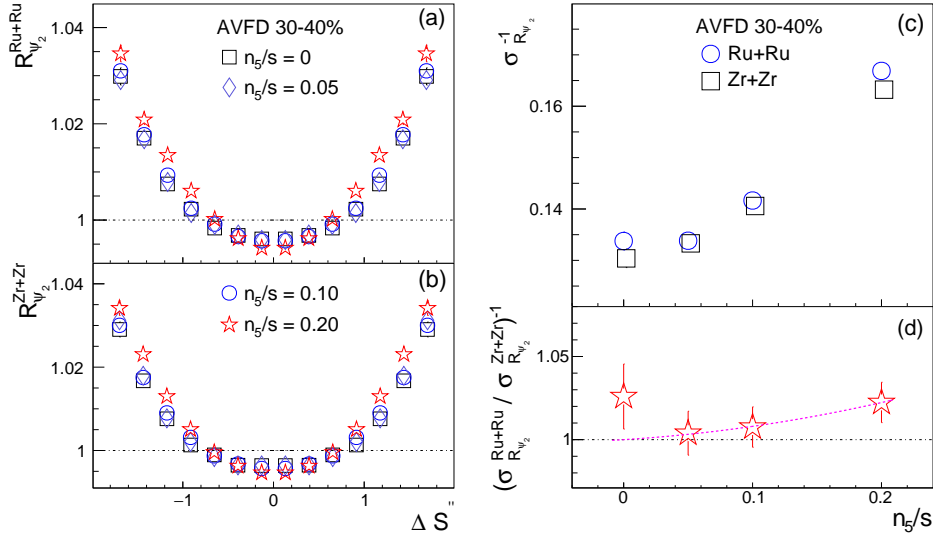


Figure 20: Distributions of $R(\Delta S_2'')$ from EBE-AVFD events of 30-40% Ru+Ru (a) and Zr+Zr (b) at 200 GeV with different n_5/s inputs. Panel (c) depicts $\sigma_{R_2}^{-1}$ vs n_5/s , extracted from panels (a) and (b), and the $\sigma_{R_2}^{-1}$ ratios between Ru+Ru and Zr+Zr are shown in panel (d), where the 2nd-order-polynomial fit function shows the rising trend starting from (0, 1).

Table 4: The statistical significance of $(O^{\text{Ru+Ru}}/O^{\text{Zr+Zr}} - 1)$ for different experimental observables. N_{event} is the number of events used for each isobaric system of 30-40% centrality in the simulation. See [94] for discussions on observables that are listed but not discussed in this document.

n_5/s	N_{event}	$\Delta\gamma_{112}$	$\Delta\delta$	κ_{112}	r_{lab}	σ_{R2}^{-1}
0	2×10^8	-1.50	-2.89	-1.21	-0.77	1.33
0.05	4×10^8	0.62	-6.16	1.37	0.47	0.29
0.10	4×10^8	1.91	-16.81	3.43	3.11	0.62
0.20	2×10^8	7.73	-42.96	14.07	5.96	1.84

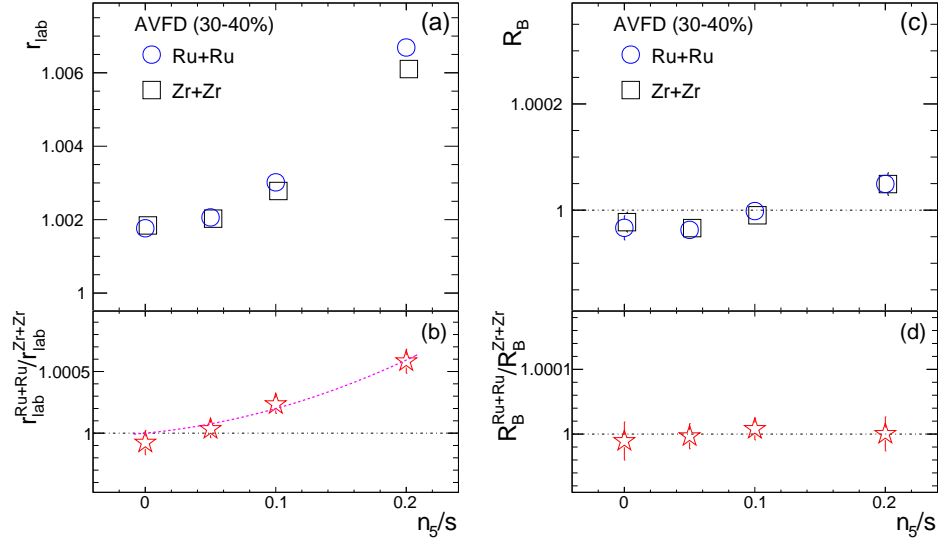


Figure 21: r_{lab} (a) and R_{B} (c) as function of n_5/s from the EBE-AVFD model for 30-40% Ru+Ru and Zr+Zr collisions at $\sqrt{s_{\text{NN}}} = 200$ GeV, with their ratios between Ru+Ru and Zr+Zr in panels (b) and (d), respectively. In panel (b), the 2nd-order-polynomial fit function demonstrates the rising trend starting from (0, 1).

776

777 A similar frozen-code analysis is performed for the $R(\Delta S_2)$ correlator, and the results
778 are presented in Figure 20. Panels (a) and (b) show the $R(\Delta S_2)$ [90] distributions from
779 EBE-AVFD events of 30-40% Ru+Ru and Zr+Zr collisions, respectively, at $\sqrt{s_{\text{NN}}} = 200$
780 GeV with different n_5/s inputs. As n_5/s increases, the $R(\Delta S_2)$ distribution becomes more
781 concave, qualitatively representing more CME contributions. To quantify the distribution
782 shape, the Gaussian width (σ_{R2}) is obtained by fitting each $R(\Delta S_2)$ distribution with an
783 inverse Gaussian function, and the resultant σ_{R2}^{-1} values are depicted in panel (c), increasing
784 with n_5/s . The σ_{R2}^{-1} ratios between Ru+Ru and Zr+Zr are shown in panel (d). We fit the
785 σ_{R2}^{-1} ratios with a 2nd-order polynomial function starting from (0, 1).

786 Figure 21 presents the sensitivity study for the signed balance functions. This approach
787 is not part of the STAR blind analysis, but follows the same procedure as used in the Quark
788 Matter 2019 Conference proceedings [89]. The observables r_{lab} and R_{B} [91] are exhibited

789 in panels (a) and (c) as function of n_5/s from the EBE-AVFD model for 30-40% Ru+Ru
790 and Zr+Zr collisions at $\sqrt{s_{\text{NN}}} = 200$ GeV. The corresponding ratios between Ru+Ru and
791 Zr+Zr are shown in panels (b) and (d), respectively. r_{lab} increases with the CME signal
792 in each isobaric collision. The r_{lab} ratio between the two systems should roughly obey a
793 2nd-order polynomial function that starts from (0, 1). This relation is demonstrated with
794 the corresponding fit in Fig. 21(b). Panel (d) does not show a clear trend for the ratio of
795 $R_B^{\text{Ru+Ru}}/R_B^{\text{Zr+Zr}}$, which is not a complete surprise: R_B looks for a higher-order effect in the
796 difference between r_{lab} and r_{rest} , and thus requires much more statistics than r_{lab} .

797 To summarize, in this study [94], we have established the relation between these methods
798 via analytical derivation, and employed both simple Monte Carlo simulations and the EBE-
799 AVFD model to verify the equivalence between the kernel components of these observables
800 (not shown in this document). Our study supports the assumption that the CME signal
801 and the background contributions can be linearly added up in such kernel components. We
802 have extracted their sensitivities to the difference between Ru+Ru and Zr+Zr collisions
803 at $\sqrt{s_{\text{NN}}} = 200$ GeV from 30-40% central events generated by EBE-AVFD. $\Delta\delta$ and κ_{112}
804 may render better sensitivities than other observables, which could be a model-dependent
805 feature instead of a universal truth, and needs to be further scrutinized by data. The same
806 significance level has been corroborated for $\Delta\gamma_{112}$, r_{lab} and σ_{R2}^{-1} , if put on an equal footing. In
807 the implementation of the STAR frozen codes, slight differences in the kinematic cuts cause
808 the apparently worse sensitivity of σ_{R2}^{-1} than the other observables. This study provides a
809 reference point to gauge the STAR isobaric-collision data.

810 1.2.7 Prospect of CME Search Beyond the Isobar-era

811 It is important to discuss the strategy for CME search beyond the isobar-era. While it is true
812 that such a strategy needs to be finalized based on the outcome of the isobar program, we
813 would like to get started by considering two possible scenarios at top RHIC energy: 1) isobar
814 program results in a significance of 3σ and below, 2) isobar program results in a significance
815 of 3σ and above.

816 In the first scenario one can infer from the projection plot of Fig. 22 that the upper limit
817 of the fraction of CME signal should be less than or equal to 8%. Under such a scenario can
818 STAR perform a follow up measurement to achieve a decisive 5σ significance and establish
819 a conclusive evidence of CME? It turns out such a measurement is possible even with a
820 single Au+Au 200 GeV data set during the year 2023-25 running of STAR concurrently with
821 sPHENIX. Current CME related analyses of the aforementioned Au+Au 200 GeV extraction
822 using elliptic flow and charge separation with respect to spectator and participant planes
823 yields 4% statistical uncertainty with 2.4 B events ($2 - 3\sigma$ significance). In order to get 5σ
824 significance with the same analysis one needs to have a statistical uncertainty of order 1.6%
825 which would require about $(4/1.6)^2 \times 2.4 = 15$ Billion events. Therefore, as per the previous
826 estimates of anticipated 20 Billion events that can be collected by STAR during Run-23
827 and 25, one can achieve more than 5σ significance on the upper limit of a possible CME
828 signal fraction in the measurement of charge separation. This estimate does not account for
829 two important facts that can lead to higher significance and a decisive measurement. The

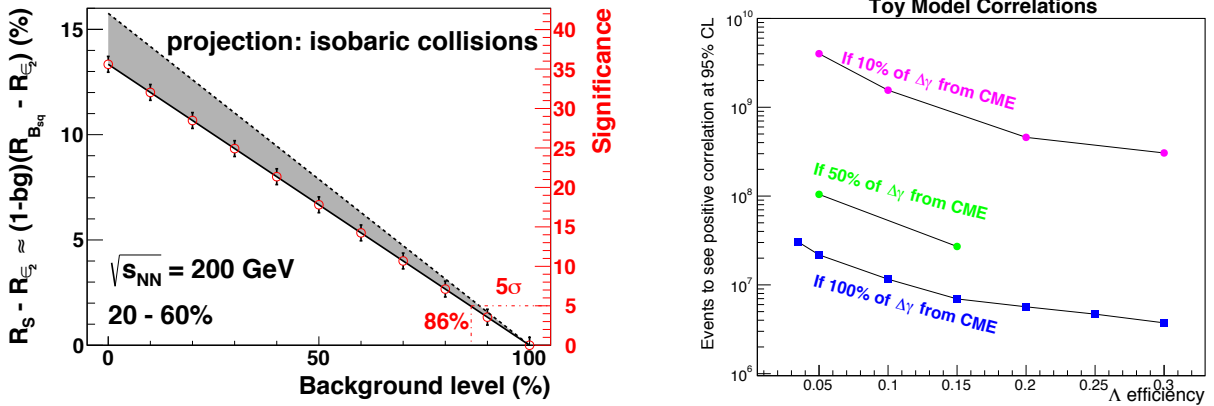


Figure 22: (Left) Projection plot taken from a previous beam user request document [78] indicating the anticipated significance in the measurement of charge separation as a function of the CME signal fraction prepared using 2.5 B simulated events. (Right) Estimation of the number of events required to see positive correlation between net Λ helicity with out-of-plane charge separation sensitive to local parity violation at 95% confidence level, plotted against the efficiency of $\Lambda(\bar{\Lambda})$ reconstruction (see [102] for details).

830 first is that the magnitude of the projected B-field on the reaction plane is higher in Au+Au
 831 collisions as compared to isobar collisions. The second one is that the iTPC upgrade enhances
 832 the charge particle multiplicity by 50% and therefore triplet ($\sim dN/d\eta^3$) (pair $\sim dN/d\eta^2$)
 833 statistics by a factor of 3.4 (2.3). So the final conclusion is that even if isobar program results
 834 in a 3σ measurement running STAR in 2023-25 will result in a $> 5\sigma$ measurement if about
 835 20 Billion events are collected. This conclusion assumes that the systematic uncertainty
 836 can be controlled to be smaller than the statistical uncertainty, i.e. below 2%. Also, this
 837 estimation does not include the systematics due to effect of sub-event gap which is being
 838 studied in STAR.

839 For the second scenario ($> 3\sigma$ measurement from isobar program) we will also be able to
 840 establish an upper limit of the fraction of CME signal. For example, in Fig. 22 we see that
 841 a 5σ significance will establish 13% CME signal and a discovery of the CME phenomenon
 842 in heavy-ion collisions. The impact of such a discovery will be a significant milestone. Run-
 843 ning STAR in 2023-25 concurrently with sPHENIX would be essential to perform dedicated
 844 precision measurements to further investigate and characterize the phenomenon.

845 A topic that may be addressed with future data is event-by-event correlations between
 846 CME charge separation and other parity-odd features of the event. One such analysis is
 847 motivated by the idea that the local parity violation (characterized in each event by a net
 848 topological charge Q) that is expected to work with the spectator-produced magnetic field
 849 to given the CME should also cause a net helicity of $\Lambda(\bar{\Lambda})$ with the same handedness in each
 850 event as the charge separation relative to the B-field.

851 We are looking for evidence of an event-by-event correlation between these two parity-
 852 odd effects as suggested in [102]. To do this, we first need to measure the charge separation

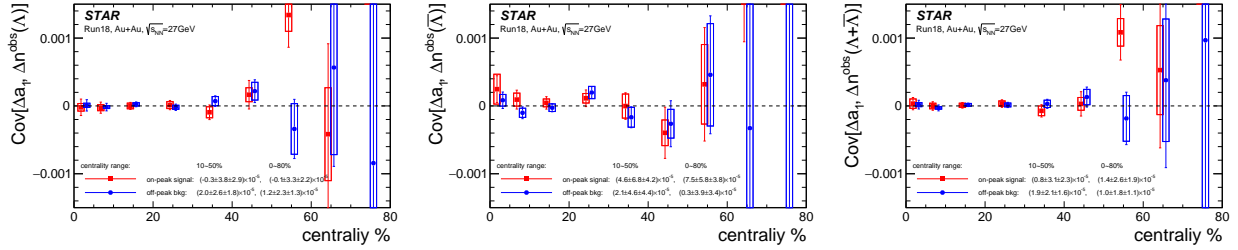


Figure 23: The covariance between Δa_1 and measured Δn for Λ (Left), $\bar{\Lambda}$ (Middle), and the sum of them (Right) as functions of centrality. The red markers come from the $\Lambda(\bar{\Lambda})$ mass peak region with purity correction and blue markers come from the side bands for pure background.

853 with respect to the first-order reaction plane in each event which we can characterize by the
 854 azimuthal correlator ($\Delta a_1 \equiv \langle \sin(\phi^+ - \Psi_{RP}) \rangle - \langle \sin(\phi^- - \Psi_{RP}) \rangle$). We next need to determine
 855 the imbalance in the handedness of $\Lambda(\bar{\Lambda})$, $\Delta N = N_L - N_R$. A measured correlation between
 856 Δa_1 and ΔN would be strong evidence for the CME and underlying local parity violation,
 857 and would extend the measurement into other parity-odd effects. Note also that the flow-
 858 related backgrounds that plague charge-separation measurements are not expected to affect
 859 ΔN or this correlation measurement. We use a similar toy model to that used in [102] to
 860 estimate the number of events required to see non-zero correlations between Δa_1 and ΔN
 861 at the 95% confidence level as a function of the efficiency of $\Lambda(\bar{\Lambda})$ reconstruction for various
 862 cases with different CME signal fraction in the $\Delta\gamma$ measurement (see Fig. 22(right)). The
 863 chief unknown in this estimate is the extent to which strange quarks may be counted as light
 864 quarks and so will have a net handedness imparted by the parity-odd domain.

865 Although Fig. 22(right) suggests that this will be a topic that may require the large data
 866 sets of future runs, these event number estimates have a large uncertainty, making it very
 867 useful to perform such an analysis with existing data both to search for a correlation signal
 868 and as an exercise of the analysis method.

869 To explore this correlation, we have analyzed the Run-18 Au+Au collision data at
 870 $\sqrt{s_{NN}} = 27$ GeV. The $\Lambda(\bar{\Lambda})$ baryons are reconstructed by their decay daughter tracks and
 871 identified by topological cuts. Each Λ handedness is estimated by decay kinematics. After
 872 a purity correction, N_L and N_R are calculated for both Λ and $\bar{\Lambda}$ in each event, and then
 873 Δn (normalized ΔN , $\Delta n = \frac{N_L - N_R}{\langle N_L + N_R \rangle}$) is calculated. The observable Δa_1 can be calculated
 874 from primordial particles' azimuthal angles w.r.t. the first-order EP measured by the Event
 875 Plane Detector (EPD). The covariance between Δn and Δa_1 is then calculated for the event
 876 sample. In this exploratory measurement, the covariance is consistent with zero, and so no
 877 correlations have been observed beyond statistical fluctuations (see Fig. 23).

878 Regardless of the outcome of the measurements with the isobar program, that will be
 879 performed at the top RHIC energy, one question will remain. What happens at lower collision
 880 energy? In this context a new idea has emerged. The newly installed event-plane detector
 881 (EPD) upgrade provides a new capability at STAR towards CME search at lower collision
 882 energy and for the BES-II program [103]. The idea is simple, at lower energies the EPD

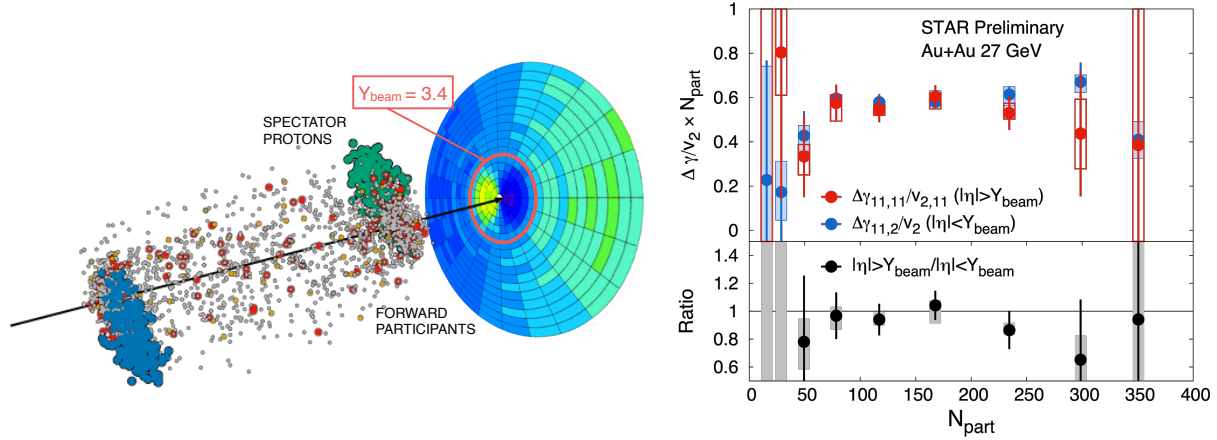


Figure 24: Prospect of CME search with the BES-II data. (Left) Single simulated UrQMD event and EPD detector acceptance that covers beam rapidity and detects both forward participants and spectators in 27 GeV Au+Au collisions that have large directed flow which changes sign at $\eta = Y_{\text{beam}} = 3.4$. (Right) γ -correlators scaled by v_2 across different event-planes and double ratio of spectator/participant event plane results which would be above unity for finite CME scenario.

883 acceptance ($2.1 < |\eta| < 5.1$) falls in the region of beam rapidity (Y_{beam}) and can measure
 884 the plane of strong directed flow (Ψ_1) of spectator protons, beam fragments and stopped
 885 protons, therefore strongly correlated to the B-field direction (See Fig. 24). The next step
 886 is to measure $\Delta\gamma$ with respect to Ψ_1 and compare it with the measurement of $\Delta\gamma$ along Ψ_2
 887 planes from outer regions of EPD and TPC at mid-rapidity that are relatively more weakly
 888 correlated to the B-field directions. A test of CME scenario will be to see if a large difference
 889 is observed in the measurements. First preliminary measurements from STAR as shown in
 890 Fig, 24 are dominated by uncertainty, but seem to show good prospects for the CME search
 891 at lower energies. With the higher statistics data from the BES-II (7.7-19.6 GeV) and fixed
 892 target programs more precise measurements are possible.

1.3 Cold QCD Highlights

1.3.1 Introduction

The goal of the STAR Cold QCD program is to probe the spin and flavor structure of the proton and understand the role of spin in Quantum Chromodynamics, exploiting the unique capability of RHIC to provide longitudinally and transversely polarized pp collisions at multiple energies. Measurements with longitudinal beam polarizations have given new insights into the helicity structure of the proton, while measurements with transverse polarizations have provided new ways to probe polarized parton distribution functions in the collinear and transverse momentum dependent frameworks. This program is complemented by studies of polarized pp elastic scattering and central exclusive production, in which a far-forward proton is detected intact.

Since 2009, RHIC STAR has completed several highly successful polarized pp runs both at $\sqrt{s} = 200$ GeV and $\sqrt{s} = 500/510$ GeV. Moreover, p +Au and p +Al datasets with a transversely polarized proton beam have been recorded in 2015 at $\sqrt{s} = 200$ GeV to address important physics problems, including the underlying non-perturbative mechanism responsible for large forward transverse single spin asymmetries, the ridge phenomenon and the possible onset of gluon saturation effects. Table 5 summarizes the STAR sampled luminosity and the luminosity averaged beam polarization as measured by the hydrogen jet (H-jet) polarimeter.

Table 5: Summary of polarized pp and p +A running periods at RHIC since 2009, including center-of-mass energy, STAR’s integrated luminosity and the average beam polarization for blue (B) and yellow (Y) beams from the H-jet polarimeter.

Year	System	\sqrt{s} (GeV)	Recorded Lumi. (pb^{-1})	Polarization Orientation	B/Y $\langle P \rangle$ (%)
2009	pp	200	25	Longitudinal	55/55
2009	pp	500	10	Longitudinal	39/39
2011	pp	500	12	Longitudinal	48/48
2011	pp	500	25	Transverse	48/48
2012	pp	200	22	Transverse	61/56
2012	pp	510	82	Longitudinal	50/53
2013	pp	510	300	Longitudinal	51/52
2015	pp	200	52	Transverse	53/57
2015	pp	200	52	Longitudinal	53/57
2015	p Au	200	0.45	Transverse	60/–
2015	p Al	200	1	Transverse	54/–
2017	pp	510	320	Transverse	55/55

Since the last PAC meeting, there have been four publications in Phys. Rev. D and nine new preliminary releases that are highlighted in the following section. Additionally, STAR

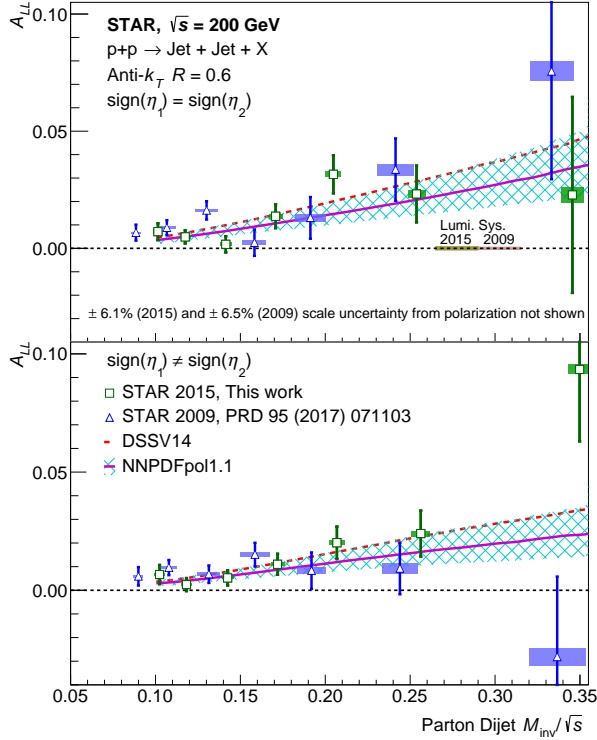


Figure 25: A_{LL} versus M_{inv}/\sqrt{s} for dijets with the $\text{sign}(\eta_1) = \text{sign}(\eta_2)$ (top) and $\text{sign}(\eta_1) \neq \text{sign}(\eta_2)$ (bottom) event topologies [104]. The square markers show the present data, whereas the triangle markers show the data of Ref. [105]. The results are compared to theoretical predictions for dijets from DSSV14 [106] and NNPDF-pol1.1 [107] with its uncertainty.

914 has one analysis, Run-13 inclusive jet and dijet A_{LL} at mid-rapidity, that just formed its
 915 God Parent Committee.

916 1.3.2 Longitudinal Program

917 STAR has recently completed and published in PRD Letters its results for the high precision
 918 inclusive jet and dijet longitudinal double-spin asymmetries, A_{LL} , from Run-15 pp collisions
 919 at $\sqrt{s} = 200$ GeV [104], which was selected for an *Editors' Suggestion*. These results are
 920 sensitive to the gluon helicity distribution in the proton, especially for the medium gluon
 921 momentum fractions in the range from $x \simeq 0.05$ to $x \simeq 0.5$. Figure 25 shows the new
 922 results of dijet A_{LL} together with the Run-9 results of Ref. [105] and the expected A_{LL}
 923 values for the DSSV14 [106] and NNPDFpol1.1 [107] parton distributions. The results are
 924 in good agreement with previous measurements at $\sqrt{s} = 200$ GeV and with the theoretical
 925 evaluations of prior world data. They have better precision and thus provide further evidence
 926 that $\Delta G(x, Q^2)$ is positive for $x > 0.05$.

927 Dijet measurements at larger pseudorapidity and higher center-of-mass energy probe
 928 lower values of partonic momentum fraction x , a region where the gluon helicity distribution
 929 is still poorly constrained. The first measurement of A_{LL} for intermediate pseudorapidity
 930 dijets [108] used Run-9 data at $\sqrt{s} = 200$ GeV. Figure 26 shows preliminary results for
 931 intermediate pseudorapidity dijet A_{LL} using Run-12 STAR pp data at $\sqrt{s} = 510$ GeV. The
 932 higher collision energy of the Run-12 preliminary results will provide lower kinematic reach
 933 in partonic momentum fraction x relative to the Run-9 results, and further constrain the

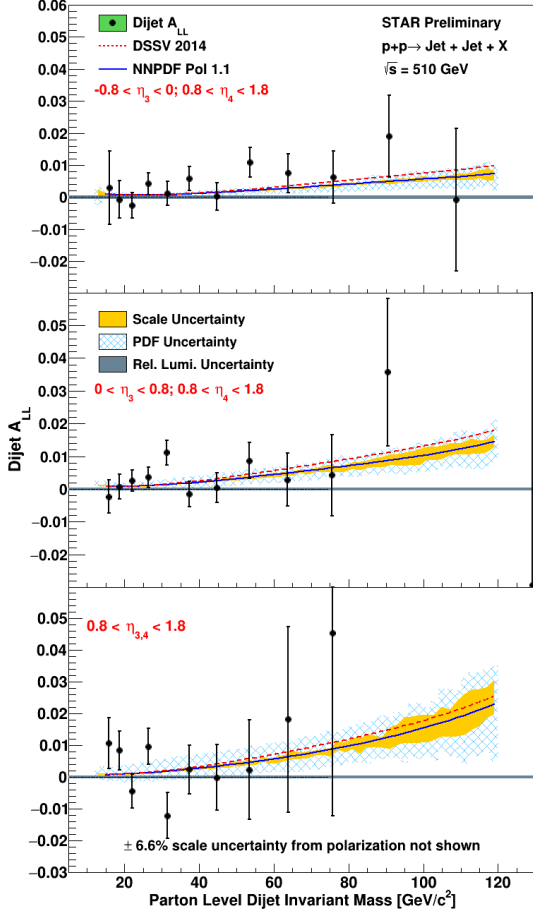


Figure 26: Preliminary results of A_{LL} as a function of parton-level invariant mass for dijets from Run-12 data at 510 GeV with the East Barrel-Endcap (top), West Barrel-Endcap (middle) and Endcap-Endcap (bottom) event topologies [109]. The curves represent theoretical predictions of A_{LL} for the DSSV14 [106] and NNPDFpol1.1 [107] parton distributions.

934 low- x behavior of $\Delta G(x, Q^2)$.

935 The longitudinal spin transfer, D_{LL} , of Λ and $\bar{\Lambda}$ are expected to be sensitive to the
 936 helicity distributions of the strange quark and anti-quark and the longitudinal polarized
 937 fragmentation functions. The left panel of Fig. 27 shows new D_{LL} preliminary results based
 938 on the Run-15 dataset at 200 GeV [110], which have about two times larger statistics than
 939 previously published results from the Run-9 dataset [111]. The new results cover transverse
 940 momenta up to 8.0 GeV/ c , and are consistent with zero within uncertainty.

941 1.3.3 Transverse Program

942 There have been three new preliminary results released and two publications from the trans-
 943 verse spin program since the last PAC meeting. The highlights include new preliminary
 944 results for the Collins asymmetries for a charge hadron in a jet [112], interference fragmenta-
 945 tion function (IFF) asymmetries for di-pion [113], and hyperon transverse spin transfer [110]
 946 in $\sqrt{s} = 200$ GeV pp collisions. Moreover, the A -dependence of transverse single spin asym-
 947 metries (TSSA) for π^0 at forward rapidity in pp p +Au and p +Al at 200 GeV, and isolated
 948 π^0 & EM-jet TSSA in pp collisions at 200 GeV and 500 GeV are now both published in Phys.

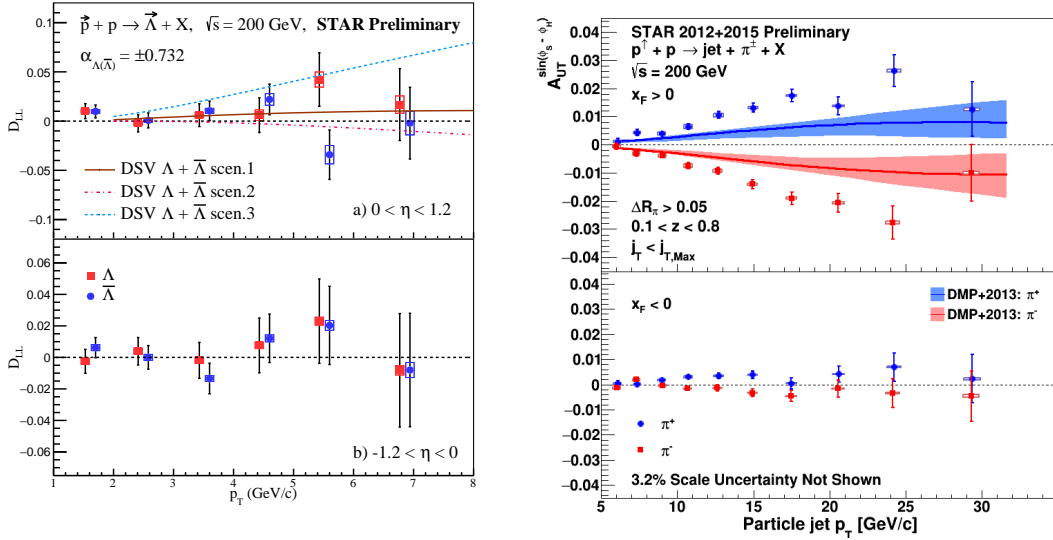


Figure 27: Left: Preliminary results of longitudinal spin transfer, D_{LL} , of Λ (red) and $\bar{\Lambda}$ (blue) from Run-15 pp data set [110]. The top and bottom panels are for the positive and negative η with respect to the polarized beam, respectively. The results for the $\bar{\Lambda}$ have been shifted to larger p_T slightly for clarity. Right: Preliminary results for the the combined Run-12 and Run-15 Collins asymmetry plotted for identified π^+ (blue) and π^- (red) particles as a function of jet p_T for jets that scatter forward relative to the polarized beam ($x_F > 0$) on top panel and those scatter backward ($x_F < 0$) on lower panel [112]. The full range of both z and j_T are integrated over. Theoretical evaluations from [116] with their uncertainties are presented for π^+ (blue) and π^- (red).

950 In the soft-collinear-effective theory framework, the Collins asymmetry combines the
 951 collinear quark transversity in the proton with the transverse momentum dependent Collins
 952 fragmentation function [117–119], and thus provides a cleaner probe of the Collins fragmenta-
 953 tion function than that in semi-inclusive deep inelastic scattering (SIDIS). This also enables
 954 tests of evolution, universality and factorization breaking in the TMD formalism. The right
 955 panel of Fig. 27 shows the combined Run-12 and Run-15 preliminary Collins asymmetries for
 956 charged pions within jets with jet p_T dependence. The measured asymmetries at positive x_F
 957 are larger than theoretical predictions [119] which are based on the transversity and Collins
 958 fragmentation function from SIDIS and e^+e^- processes with TMD approach.

959 In transversely polarized proton collisions, di-hadron production is also sensitive to
 960 transversity. The coupling of transversity to the di-hadron fragmentation function creates
 961 azimuthal modulations which leads to observed asymmetries. STAR has released new pre-
 962 liminary results on di-pion ($\pi^+\pi^-$) correlation asymmetry [113] based on the Run-15 $\sqrt{s} =$
 963 200 GeV dataset, as shown in Fig. 28, as $A_{UT}^{sin(\phi_{RS})}$ versus the di-pion invariant mass, $M_{inv}^{\pi^+\pi^-}$,
 964 in the forward pseudorapidity region ($\eta^{\pi^+\pi^-} > 0$). The asymmetry signal is enhanced near
 965 the ρ mass ($M_{inv}^{\pi^+\pi^-} \approx 0.78 GeV/c^2$), consistent with the theory prediction. The statisti-

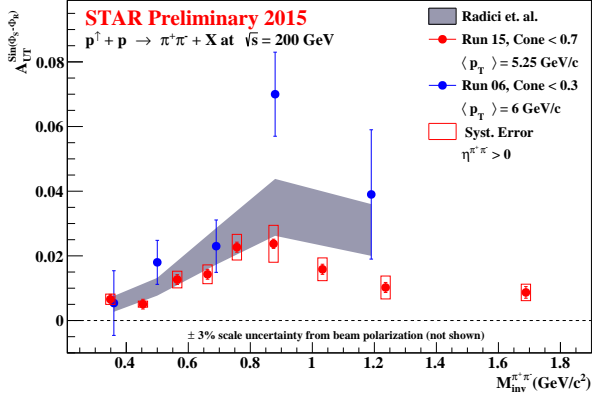


Figure 28: Preliminary results of di-hadron asymmetry $A_{UT}^{sin(\phi_{RS})}$ as a function of $M_{inv}^{\pi^+\pi^-}$, integrated over $p_T^{\pi^+\pi^-}$ in forward pseudo-rapidity region ($\eta^{\pi^+\pi^-} > 0$) at $\sqrt{s} = 200$ GeV from Run-15 together with previously published Run-6 data. The error bars represent the statistical uncertainty, while the boxes represent the systematic uncertainty.

966 cal precision of the 2015 result is significantly improved compared to the previous Run-6
 967 measurement.

968 Transverse Spin transfer, D_{TT} , of hyperons in pp collisions can provide a connection to
 969 the transversity distribution of the $s(\bar{s})$ quark in the proton and the polarized fragmentation
 970 functions. STAR has published its first measurement of the transverse spin transfer of Λ and
 971 $\bar{\Lambda}$ hyperons at $\sqrt{s} = 200$ GeV based on the Run-12 pp data set [120]. A new D_{TT} preliminary
 972 result using the Run-15 pp dataset has been released [110]. The Run-15 dataset is about
 973 twice as large as the Run-12 dataset, allowing for better statistical precision. Figure 29 shows
 974 the preliminary Run-15 results for D_{TT} versus $\Lambda(\bar{\Lambda}) p_T$. The new results are consistent with
 975 zero within uncertainties, and also are consistent with model predictions.

976 A new STAR publication reports on the transverse single spin asymmetry (TSSA) for
 977 forward neutral pions produced in polarized proton collisions with protons (pp), aluminum
 978 nuclei ($p+Al$) and gold nuclei ($p+Au$) at $\sqrt{s} = 200$ GeV are measured with the FMS in Run-
 979 15 [114]. The measured asymmetries, presented in Fig. 30, are found to rise with transverse
 980 momentum at $x_F < 0.5$, while they flatten or fall at larger x_F . The results are consistent
 981 with a weak nuclear A dependence. Moreover, a further observation is that the TSSA is
 982 significantly larger for isolated π^0 s than for non-isolated π^0 s, which are accompanied by
 983 additional jet-like fragments.

984 The TSSA of neutral pions in pp collisions at both $\sqrt{s} = 200$ GeV and 500 GeV from
 985 FMS data are shown in Fig. 31. The 200 GeV data are from Run-15, while the 500 GeV data
 986 are from the Run-11. The results have been accepted for publication [115]. A continuous
 987 increase of the TSSA with Feynman- x indicates a weak dependence on the center-of-mass
 988 energy. Pions with no nearby particles ("isolated"), which may not arise from conventional
 989 parton fragmentation, tend to have a higher TSSA than non-isolated pions, which suggests
 990 that a different mechanism (i.e., diffractive) other than the Sivers or Collins effects is required
 991 to explain these results. The theoretical calculations presented in the plot are based on the
 992 TMD and collinear twist-3 functions from a recent global analysis [122], which also includes
 993 previous forward π^0 and charged hadron TSSA data from RHIC in the fit. The theoretical
 994 calculation differs from our measurement and only provides a reasonable description of the
 995 non-isolated π^0 in the low- x_F region.

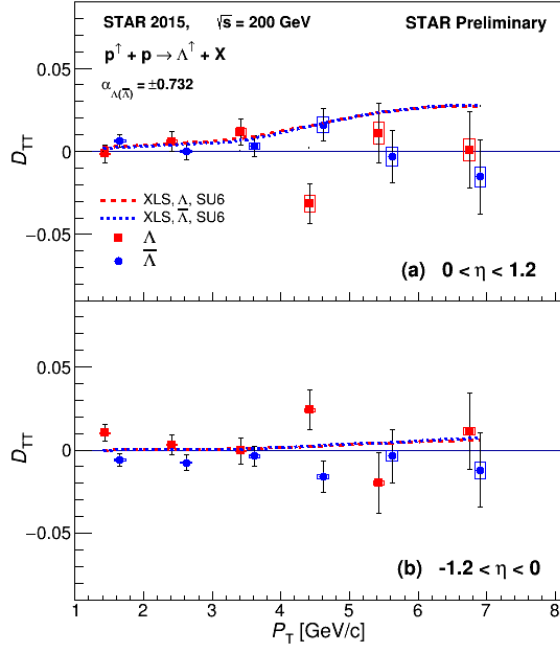


Figure 29: Preliminary results of D_{TT} versus $\Lambda(\bar{\Lambda})$ p_T from STAR Run-15 pp dataset at $\sqrt{s} = 200$ GeV [110]. The upper panel is for positive η with respect to the polarized beam and the lower panel is for negative η . The results are compared with a model calculation [121]. The Λ results have been offset to slightly smaller p_T values for clarity.

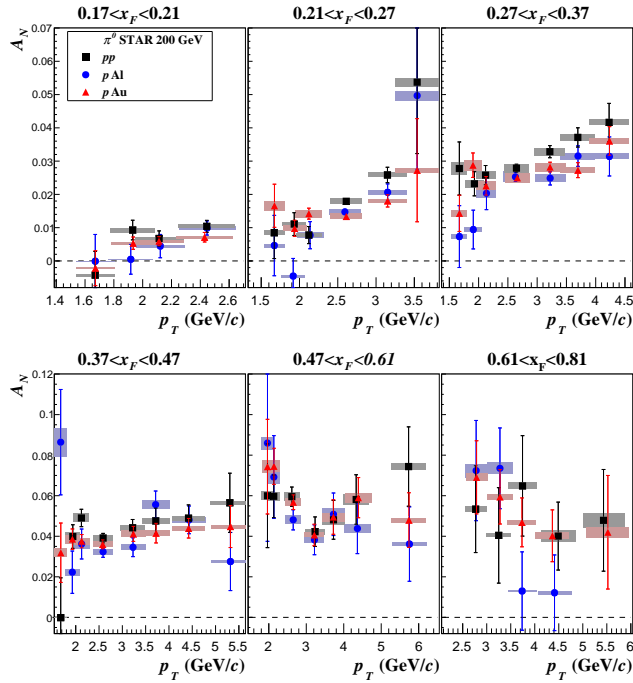


Figure 30: Transverse single spin asymmetry for forward π^0 production as a function of transverse momentum for six Feynman x_T regions [114]. The results for three collisions systems are shown, the black squares are for pp blue circles for $p+Al$ and red triangles for $p+Au$ collisions. The statistical uncertainties are shown with vertical error bars and the filled boxes indicate the horizontal and vertical systematic uncertainties.

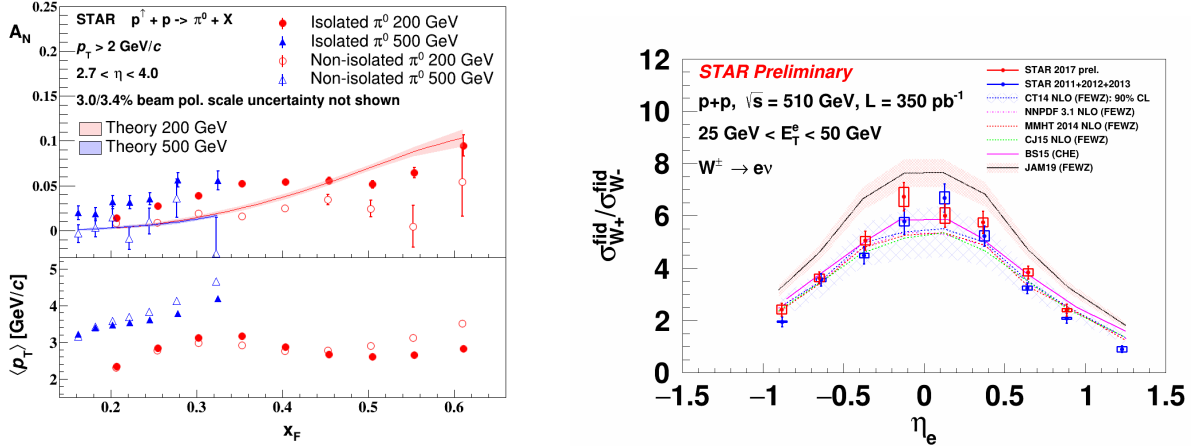


Figure 31: Left: Results for the transverse single-spin asymmetry as function of Feynman- x for the isolated and non-isolated π^0 in transversely polarized pp collisions at $\sqrt{s} = 200$ and 500 GeV [115]. Theory curves based on a recent global fit [122] are also shown. The average transverse momentum of the π^0 for each x_F bin is shown in the lower panel. Right: Comparison of W^+ and W^- cross-section ratio as a function of lepton pseudorapidity for the Run-17 dataset to the recently published combined Runs-11, 12 and 13 datasets [123]. The central values correspond to the mean value of η_e distribution for that bin. The error bars represent the statistical uncertainty, whereas the rectangular boxes represent the systematic uncertainty for the respective data point. These measurements are compared to various theory frameworks, which use several different PDF inputs.

1.3.4 Unpolarized Program

Since the last PAC meeting STAR has published one paper on the W and Z cross sections and their ratios for the combined Run-11, Run-12, and Run-13 $\sqrt{s} = 500/510$ GeV pp datasets [123]. The W^+/W^- cross-section ratio is a unique measurement that is sensitive to the unpolarized \bar{d}/\bar{u} quark distribution and will provide insight and constraints to its x dependent distribution. This STAR measurement is complementary to the Drell-Yan results from NuSea [124] and SeaQuest [125], covering the overlapping x region of about $0.1 - 0.35$ at higher $Q^2 (= M_W^2)$. The W^+/W^- cross-section ratio measured with Run-17 dataset at $\sqrt{s} = 510$ GeV has been released as preliminary [126]. Figure 31 shows the ratio plotted as a function of lepton pseudorapidity for the combined Run-11, 12 and 13 published results and the Run-17 preliminary result.

Measurements of the differential inclusive jet cross section in pp collisions can be incorporated into global fits to provide constraints on the unpolarized gluon PDFs. Differential inclusive jet cross section results at $\sqrt{s} = 200$ GeV and 510 GeV from STAR's Run-12 dataset have been released as preliminary [127, 128]. The measurement at $\sqrt{s} = 200$ GeV, as seen in Fig. 32, corresponds to a range of $x_T \equiv \frac{2p_T^{\text{jet}}}{\sqrt{s}}$ from 0.067 up to 0.5 , allowing for the possibility of constraining the unpolarized gluon PDF at high- x . The measurement at $\sqrt{s} = 510$ GeV, shown in Fig. 33, is sensitive to lower x values of the gluon PDF compared to the 200 GeV measurement.

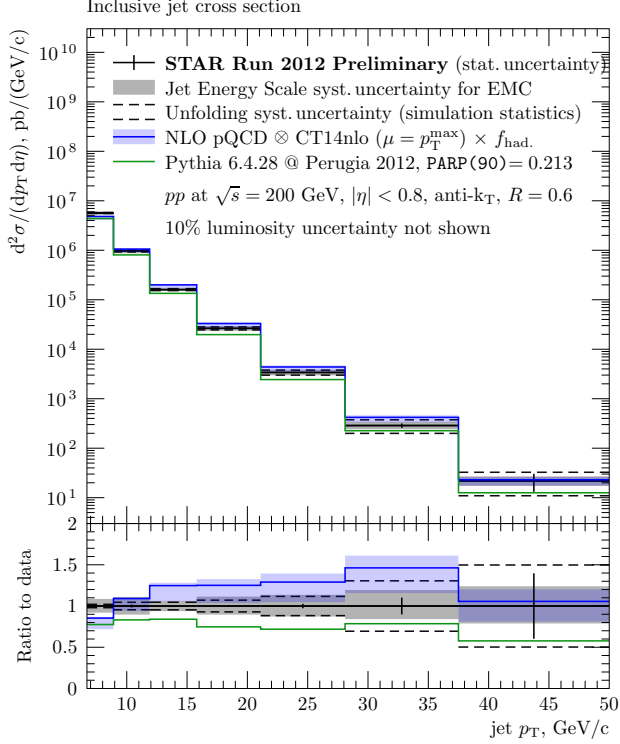


Figure 32: Differential inclusive jet cross section for pp collisions at $\sqrt{s} = 200$ GeV as a function of jet p_T corrected for underlying event. The measurement is compared to a prediction from the PYTHIA Monte Carlo generator. Another comparison is to a prediction of the NLO pQCD theory with a bin-by-bin correction for effects of the hadronization estimated using the same PYTHIA generator.

1015 The azimuthal correlation of forward di-hadrons produced in pp and $p+A$ collisions pro-
 1016 vides an essential tool to access the underlying gluon dynamics in the nonlinear evolution
 1017 region. STAR has released preliminary results for the measurement of azimuthal correlations
 1018 of di- π^0 produced in the forward direction ($2.6 < \eta < 4.0$) in pp , $p+Al$ and $p+Au$ collisions at
 1019 $\sqrt{s} = 200$ GeV from the Run-15 data set [129]. A clear suppression of the correlated yields of
 1020 back-to-back pairs is observed in $p+Al$ and $p+Au$ compared with the reference pp collisions.
 1021 The larger suppression found in $p+Au$ than $p+Al$ collisions exhibits the saturation scale,
 1022 Q_s^2 , dependence on A . The observed suppression of back-to-back pairs as a function of event
 1023 activity and p_T from Fig. 34 points to the non-linear gluon dynamics arising at high parton
 1024 densities.

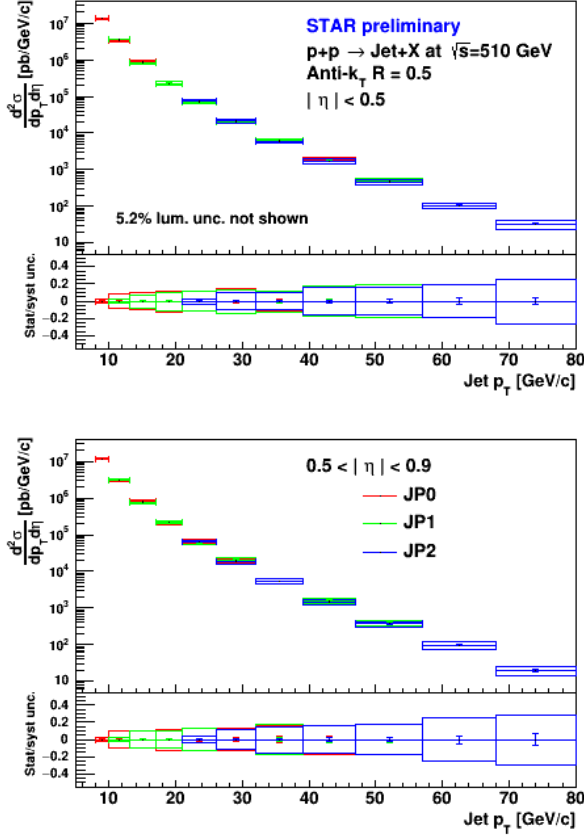


Figure 33: Differential inclusive jet cross section, $\frac{d^2\sigma}{dp_T d\eta}$, as a function of particle jet transverse momentum p_T for JP0, JP1 and JP2 triggered samples within two η regions, $|\eta| < 0.5$ and $0.5 < |\eta| < 0.9$. The results show excellent agreement between triggers, which indicates an accurate simulation of the trigger efficiency used in detector effect unfolding.

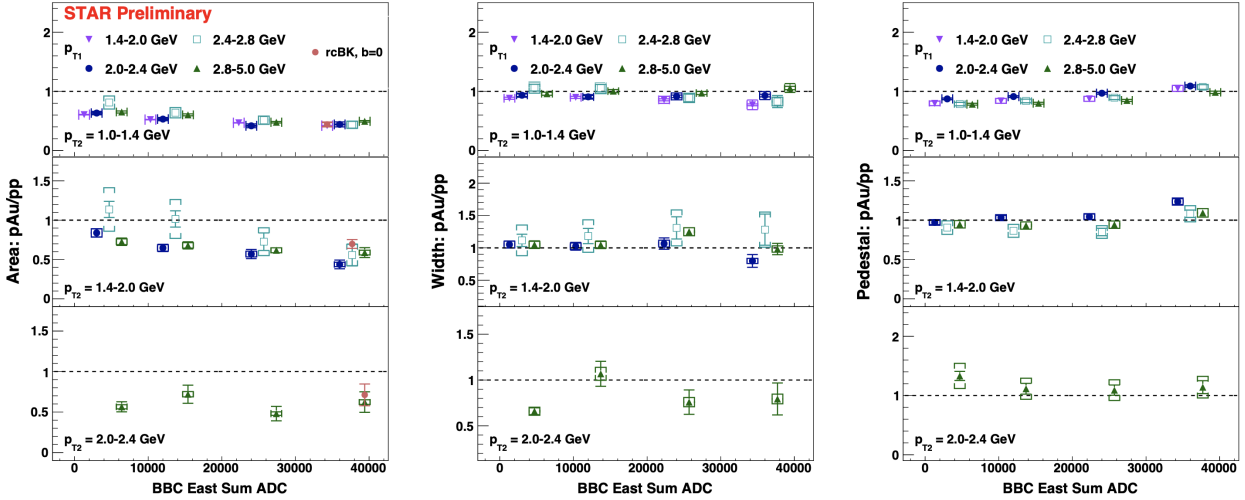


Figure 34: Comparison of back-to-back di- π^0 ratios of pair yields, the width, and the level of pedestal in p +Au and minBias pp collisions as a function of di- π^0 's p_T and event activity. Energy deposited at east Beam-Beam Counter (BBC) quantifies the “event activity”. The measured area ratio is compared with theory predictions based on rcBK model [130].

1025 **1.4 Run-21 Performance**

1026 In this section, we review the BES-II collider and fixed-target performance to date, detailing
 1027 which of the Run-21 physics priorities have been completed. Careful study of these perfor-
 1028 mance metrics will be used to make projections about the required time to complete the
 1029 remaining Run-21 physics priorities. As our projections indicate that we are highly likely
 1030 to complete the Run-21 priorities within the allotted run-time, we also propose an addi-
 1031 tional physics topic which could be addressed if time is available toward the end of Run-21
 1032 operations.

1033 The highest priority for Run-21 was to complete the BES-II physics program. Most of
 1034 the BES-II collider and fixed-target systems had been completed during 2018-2020. The only
 1035 remaining dataset to be collected was the 7.7 GeV collider system. This had been chosen
 1036 to be run last as it was expected to be the most difficult from an operations point of view.
 1037 Tests of the 7.7 GeV collider program had been performed in 2019 (without electron cooling)
 1038 and in 2020 (with electron cooling), and projections using the best performance from 2020
 1039 suggested that, conservatively, it would require 28 weeks to complete the 7.7 GeV collider
 1040 system. STAR optimistically projected that the 7.7 GeV collider system would be completed
 1041 in 11-20 weeks, and proposed a prioritized physics program that could make use of additional
 1042 beam-time if available (see Table 6).

Table 6: Physics Priorities for Run-21

Priority	Beam Energy	$\sqrt{s_{NN}}$	System	Events	Weeks	Goals
1	3.85	7.7	Au+Au	100 M	11-20	Complete BES-II
2a	3.85	3.0	Au+Au	300 M	3 days	Fluctuations
2b	44.5	9.1	Au+Au	50 M	1 day	Stopping
2b	70	11.5	Au+Au	50 M	1 day	Stopping
2b	100	13.7	Au+Au	50 M	1 day	Stopping
3a	100	200	O+O	400 M	4 days	Small systems (min bias)
3a	100	200	O+O	200 M	4 days	Small systems (central)
3b	8.65	17.3	Au+Au	250 M	2.5	Additional BES-II energy
3c	3.85	3.0	Au+Au	2 B	3	Double hyper-nucleus search

1043 **1.4.1 Performance to Date**

1044 Priority 1:
 1045 STAR started taking physics data for the 7.7 GeV collider program on January 31st, and
 1046 completed the event statistics goal on May 1st. This was a total of 90 days (or 12.8 weeks)
 1047 of data taking. The 7.7 GeV run did prove to be very technically challenging. At the start
 1048 of data taking in early February, the good event rates were only half of those that had been
 1049 achieved the year before. Optimizations and improvements included: using the Tandem (as
 1050 opposed to EBIS) to achieve the maximum intensity at injection, including a beta-squeeze

1051 ten minutes into the fill (made possible by the reduction of the beam emittance due to the
 1052 electron cooling), optimizing the longitudinal matching for injection from the AGS to RHIC,
 1053 developing a new "low tune" for RHIC, and implementing dampers. After this month of
 1054 optimizations, the store-average good event rate reached 30 Hz, which was a factor of five
 1055 better than was achieved in 2010, and a factor of two better than the best rates achieved
 1056 in the 2020 tests. The key run-averaged performance metrics are detailed in Table 7, and
 1057 compared to those achieved for the other BES-II collider energies. Although the store-average
 1058 good event rate reached 30 Hz in the later half of the run, the run-averaged value was 22 Hz,
 1059 which was close to the most optimistic projection. The second most significant performance
 1060 metric is the average hours of data taking per day. This metric is influenced by the store
 1061 length, the up-time of the collider, the up-time of the experiment, and the fraction of time
 1062 dedicated to other programs (CeC and APEX) and maintenance. STAR had estimated 12-15
 1063 hours per day of data taking. Over the course of the run, an average of 13 hours per day
 1064 was achieved, however, it should be noted that an average of 1.5 hours per day had been
 1065 dedicated to CeC and APEX during the 90 days of 7.7 GeV running; therefore the average
 1066 hours per day was also close to the most optimistic projection. Data quality assurance is
 1067 performed on a run-by-run basis by the shift crews, on a daily basis by remote QA shifters
 1068 using fast offline production, and on a weekly basis by the physics working groups.

Table 7: Achieved and projected experiment performance criteria for the BES-II Au+Au collider program.

Collision Energy (GeV)	7.7	9.2	11.5	14.6	17.1	19.6	27
Performance in BES-I	2010	NA	2010	2014	NA	2011	2011
Good Events (M)	4.3	NA	11.7	12.6	NA	36	70
Days running	19	NA	10	21	NA	9	8
Data Hours per day	11	NA	12	10	NA	9	10
Fill Length (min)	10	NA	20	60	NA	30	60
Good Event Rate (Hz)	7	NA	30	23	NA	100	190
Max DAQ Rate (Hz)	80	NA	140	1000	NA	500	1200
Performance in BES-II (achieved)	2021	2020	2020	2019	2021	2019	2018
Required Number of Events	100	160	230	300	250	400	NA
Achieved Number of Events	101	162	235	324	TBD	582	560
fill length (min)	30	45	25	45	50	60	120
Good Event Rate (Hz)	22	33	80	170	265	400	620
Max DAQ rate (Hz)	600	700	550	800	1300	1800	2200
Data Hours per day	13	13	13	9	15	10	9
Projected number of weeks	11-20	8.5-14	7.6-10	5.5	2.5	4.5	NA
weeks to reach goals	12.8	14.6	8.9	8.6	TBD	5.1	4.0

1069 Priority 2:

1070 The second priority really breaks down in two distinct fixed-target physics programs. The
1071 first (indicated as Priority 2a in Table 6) required 300 M minimum bias events from fixed-
1072 target collisions using the 3.85 GeV Au beam. This study used the same beam energy as
1073 the 7.7 GeV collider program, therefore it was efficient to run immediately after the 7.7 GeV
1074 program was completed as the reconfiguration of the collider was minimal. The fixed-target
1075 program did need a long beta star lattice and used only twelve bunches in the yellow ring,
1076 and STAR needed to reconfigure its trigger. All of these changes were completed efficiently,
1077 and within three hours of the completion of the 7.7 GeV collider run, STAR was taking
1078 physics data for the 3.85 GeV fixed-target run. The key physics goals for this 3.85 GeV run
1079 are fluctuation measurements, therefore, strict requirements were placed in consistency of
1080 operations and minimization of pile-up. These operational requirements limited the store
1081 length to two hours, shorter than the expected four hours, which resulted in the 3.3 days
1082 instead of the expected 3.0 days. On a positive note, the eTOF detector system, which is
1083 critical for this energy, was live for 99.6% of all events recorded.

1084 The second part of the priority 2 fixed-target program (indicated as Priority 2b in Ta-
1085 ble 6) required 50 M events at three higher energies (44.5, 70, and 100 GeV). Changing
1086 the collider from low-energy to high-energy operations required reconfiguring the injection
1087 kickers, the abort kickers, conditioning the RHIC magnets to run at full current, and devel-
1088 oping three new energies with 5 m beta star lattices. Developing the high rigidity 100 GeV
1089 beam for fixed-target operations proved especially challenging as the 1.8 mm vertical shift
1090 in the beam necessary to graze the target was at the limit of the capabilities of the collider
1091 and maintaining the optimal luminosity required maximum use of the BBQ kicker, injection
1092 mismatch, and IBS scattering to produce the largest emittance 100 GeV Au beam ever seen.
1093 In total, the reconfiguration, beam development, and data taking took a little over three
1094 days (with data taking times of 12, 12, and 10 hours for each of the three beams). Each
1095 of these three energies completed data taking with a single store. Overall performance was
1096 exactly as expected. A summary of the Run-21 fixed-target performance is compared to the
1097 expected metrics and to previous years runs in Table 8

1098
1099 Priority 3a:

1100 The O+O system at $\sqrt{s_{NN}} = 200$ GeV provides a small system for flow and correlation studies.
1101 The events request was divided into a 400 M events request for minimum bias data and a 200
1102 M event request for central collisions (top 5%). There is ample luminosity for O+O collisions
1103 at full energy to fill the STAR DAQ bandwidth, therefore a few operational choices were
1104 made to increase the quality of the recorded data. First, the beams were collided with a
1105 1.65 mrad angle, which helps by limiting the vertex distribution to ± 30 cm in z . Second,
1106 the luminosity was limited by slightly adjusting the offsets of the beams in y to limit the
1107 minimum bias trigger rate to 4 kHz to minimize the pile-up. This program was started
1108 on May 8th. For the minimum bias part of the program achieved an average of 14 hours
1109 per day of data taking, and good events rates of 7.5 M events per hour, as expected for a
1110 program that efficiently filled the STAR DAQ bandwidth. We finished the minimum bias
1111 event statistics requirements on Sunday May 16th with 404 M good events. For the central

Table 8: Achieved and projected experiment performance criteria for the BES-II Au+Au fixed-target program.

Beam Energy	$\sqrt{s_{NN}}$ (GeV)	Expected Duration	Actual Duration	Proposed Events	Recorded Events	Year
3.85	3.0	4 days	3.5 days	100 M	258 M	2018
3.85	3.0	3 days	3.3 days	300 M	307 M	2021
3.85	3.0	3 weeks	TBD	2 B	TBD	2021
4.59	3.2	2 days	46 hours	200 M	200.6 M	2019
5.75	3.5	1 day	23 hours	100 M	115.6 M	2020
7.3	3.9	0.5 days	12 hours	50 M	52.7 M	2019
7.3	3.9	1 day	29 hours	100 M	117 M	2020
9.8	4.5	1 day	31 hours	100 M	108 M	2020
13.5	5.2	1 days	21 hours	100 M	103 M	2020
19.5	6.2	1 days	22 hours	100 M	118 M	2020
26.5	7.2	parasitic	2 days	none	155 M	2018
26.5	7.2	parasitic	3.5 days	none	317 M	2020
26.5	7.2	parasitic	TBD	none	TBD	2021
31.2	7.7	0.5 days	11.5 hours	50 M	50.6 M	2019
31.2	7.7	1 day	26 hours	100 M	112 M	2020
44.5	9.1	0.5 days	12 hours	50 M	53.9 M	2021
70	11.5	0.5 days	12 hours	50 M	51.7 M	2021
100	13.7	0.5 days	10 hours	50 M	50.7 M	2021

1112 collisions, the luminosity was increased by a factor of five by reducing the vertical offset of
1113 the beams. There was still sufficient luminosity to fill the STAR DAQ bandwidth. As it was
1114 important the hardware trigger did not bias the top 5% of centrality events, which will be
1115 selected in offline analysis, the trigger efficiency was only 45%. We completed the central
1116 collision data set on May 21st (5 days) with 212 M good events. It had been expected to
1117 take 4-5 days to complete the central collisions goals. Upon completion of the physics goals
1118 for the O+O system, the field for the STAR solenoid was flipped and another three days
1119 (shared with CeC) of minimum bias were taken. These data are needed to carefully study
1120 the alignment, calibrations, and corrections needed to maximize the tracking accuracy of the
1121 STAR TPC. Data taking for O+O was completed on May 24th.

1122 1.4.2 Projections to Complete the Run-21 Physics Priorities

1123 Priority 3b:

1124 The Au+Au system at $\sqrt{s_{NN}} = 17.3$ GeV adds an energy to the BES-II collider program
1125 where there is a larger than average gap between adjacent energies, and hence μ_B , and where
1126 there is hint of a change in the ratios of the light nuclei which could suggest an increase
1127 in neutron fluctuations. The projections for the key metrics are interpolated from those

1128 achieved to the 14.6 and 19.6 GeV collider systems (see Table 7). RHIC needed less than
1129 one day to reconfigure the injection and abort kickers and to tune the 17.3 GeV collisions.
1130 The collider optimization occurred faster than expected and the RHIC was exceeding the
1131 expected good event rate within a day of starting operations at this energy. Data taking is
1132 expected to take 17-21 days. Four days of CeC, APEX, machine set-up, and maintenance
1133 have been included in the data taking time estimates. It is projected that data for the 17.3
1134 GeV Au+Au system will be completed by June 10-14th.

1135

1136 Priority 3c:

1137 STAR will return to 3.85 GeV fixed target running toward the end of Run-21. The driving
1138 physics goal for this period is the search for the doubly-strange hyper-nucleus. As this is a
1139 rare particle search and not a fluctuations measurement, the conduct of operations will be
1140 optimized for the total number of recorded events and not for reduction of pile-up. Data
1141 taking is expected to take 23-28 days (mostly depending on the weather in June and July).
1142 Two and a half days of CeC, APEX, and maintenance have been included in the data
1143 taking time estimate. It is projected that data for this 3.85 GeV fixed-target system will be
1144 completed by July 3-10th (July 10th would be a hard stop in preparation for warm-up).

1145

1146 Priority X:

1147 In previous years, STAR has recorded 26.5 GeV fixed-target data parasitically while CeC is
1148 running. This typically only occurs once CeC has reached consistent running. This has not
1149 yet happened to date, however it is expected that toward the end of Run-21 operations there
1150 will be several days of stable CeC operations, at which time we are likely to record 26.5 GeV
1151 fixed-target data.

1152 1.5 Additional Physics Opportunity for Run-21

1153 Pinning Down the Precise Role of Geometry on Collectivity with Central d+Au 1154 Collisions

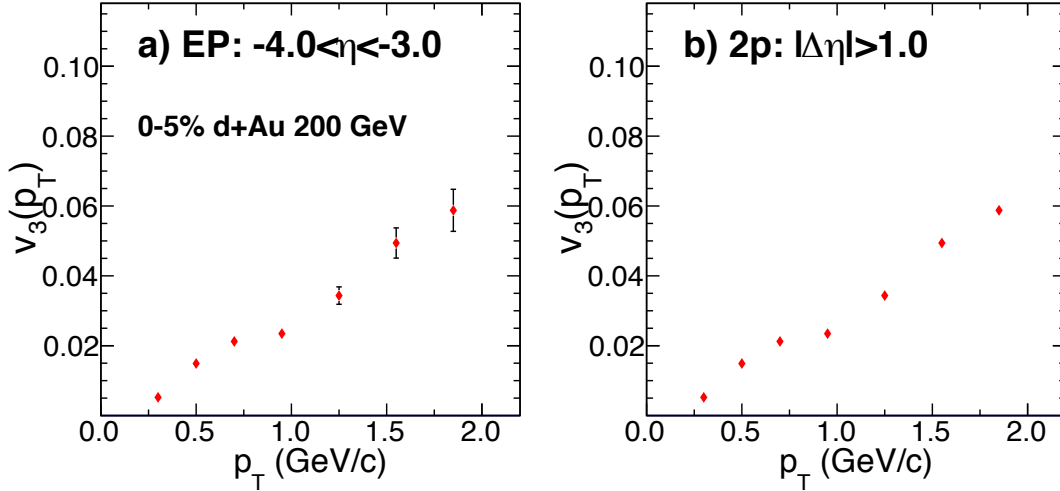


Figure 35: Projection for v_3 with forward and midrapidity acceptance in high multiplicity d+Au collisions utilizing the extended pseudorapidity capability of iTPC and EPDs.

1155

1156 The first striking evidence of collective behavior in small collision systems was observed
1157 in the pattern of anisotropy of particle emissions in rare high activity pp collisions at the
1158 LHC [131]. This, followed by measurements in p +Pb collisions [132–134], started a strong
1159 debate on whether such correlations originate at a very early stages due to collective behavior
1160 of gluons inside colliding protons, or whether they originate at a late stage due to the
1161 formation of a fluid like medium. Measurements of azimuthal anisotropy coefficients (v_n) in
1162 most central (0-5%) small collision systems $^3He + Au$ [135], d+Au [136, 137] and $p + Au$ [138]
1163 with different initial shapes from RHIC have confirmed that even in small collision systems
1164 fluid-dynamic final state effects are essential to drive collectivity [139]. Such results from
1165 the PHENIX experiment using the combination of particles from mid-rapidity ($|\eta| < 0.35$)
1166 and another from forward rapidity ($1 < \eta < 3$, Au-going side) indicate a specific ordering
1167 of triangular harmonic anisotropy $v_3(^3He + Au) > v_3(d + Au) \sim v_3(p + Au)$. This hints at
1168 the possibility that a more triangular initial geometry is produced in $^3He + Au$ collisions
1169 (compared to d+Au and $p + Au$) as expected from a nucleon based initial state model [140].

1170

1171 However, recent STAR preliminary results using two particle correlations with both par-
1172 ticles at mid-rapidity ($|\eta| < 1$) show $v_3(^3He + Au) \sim v_3(d + Au) \sim v_3(p + Au)$ [141]
1173 implying no system dependence of triangularity indicating fluctuations or geometry at the
1174 sub-nucleonic scale drives anisotropy. This qualitative difference of system dependence of
1175 v_3 measurements between STAR and PHENIX kinematics is very striking. With the antici-
1176 pated high statistics d+Au run by triggering on central events at RHIC it will be possible to

1176 perform measurements of v_n using acceptance similar to both previous PHENIX and STAR
1177 measurements and answer:

- 1178 • How will v_3 measurements in d+Au change from mid-rapidity to forward rapidity?
- 1179 • How will forward v_3 measurements in d+Au from STAR compare to the same from
1180 PHENIX?

1181 Figure 35 shows a projection plot for v_3 using particles from forward and midrapidity
1182 acceptance in high multiplicity d+Au collisions utilizing the extended pseudorapidity capa-
1183 bility of STAR. The two panels show estimates for v_3 in two-particle correlation approach by
1184 using : 1) tracks from TPC+iTPC ($|\eta| < 1.5$) and hits from EPDs ($2.1 < |\eta| < 5.1$), 2) pairs
1185 of tracks from TPC+iTPC ($|\eta| < 1.5$) and using a relative pseudorapidity gap of $|\Delta\eta| > 1$.
1186 To start with we assume STAR will collect data at the rate of 2.2 kHz and a combined
1187 RHIC×STAR down time of 50% (12 hour/day) for three days of running during Run-21.
1188 The desired run conditions will be such that the coincidence rate of ZDCs will be about
1189 10 kHz. The idea is to dedicate the first day entirely on collecting minimum bias events.
1190 This will lead to the accumulation of about $1(\text{day}) \times 86400(\text{sec.}) \times 0.5(\text{downtime}) \times 2200(\text{rate})$
1191 $\times 1.0(\text{bandwidth}) \approx 95$ Million events. On the second and the third day, we plan to split
1192 the bandwidth equally into collecting min-bias and high multiplicity events with a dedicated
1193 trigger. Following the same estimates of rate, we can collect 95 million events for the two
1194 case. Therefore over all three days, we will be able to accumulate 190 Million min-bias events
1195 and 95 Million high multiplicity events. With such statistics and aforementioned measure-
1196 ments it will possible to revisit the v_n measurements in STAR and PHENIX kinematics and
1197 understand the apparent discrepancy between the previous measurements.

2 Physics with $p^\uparrow p^\uparrow$ and $p^\uparrow + A$ Collisions at 510 and 200 GeV

The exploration of the fundamental structure of strongly interacting matter has always thrived on the complementarity of lepton scattering and purely hadronic probes. As the community eagerly anticipates the future Electron Ion Collider (EIC), an outstanding scientific opportunity remains to complete “must-do” measurements in pp and $p+A$ physics during the final years of RHIC. These measurements will be essential if we are to fully realize the scientific promise of the EIC, by providing a comprehensive set of measurements in hadronic collisions that, when combined with future data from the EIC, will establish the validity and limits of factorization and universality. Much of the Run-22 and Run-24 physics program outlined here is, on the one hand, unique to proton-proton and proton-nucleus collisions and offers discovery potential on its own. On the other hand, these studies will lay the groundwork for the EIC, both scientifically and in terms of refining the experimental requirements of the physics program, and thus are the natural next steps on the path to the EIC. When combined with data from the EIC these STAR results will provide a broad foundation to a deeper understanding of fundamental QCD.

The separation between the intrinsic properties of hadrons and interaction-dependent dynamics, formalized by the concept of factorization, is a cornerstone of QCD and largely responsible for the predictive power of the theory in many contexts. While this concept and the associated notion of universality of the quantities that describe hadron structure have been successfully tested for unpolarized and, to a lesser extent, longitudinally polarized parton densities, its experimental validation remains an unfinished task for much of what the EIC is designed to study – the three-dimensional structure of the proton and the physics of dense partonic systems in heavy nuclei. To establish the validity and limits of factorization and universality, it is essential to have data from *both* lepton-ion and proton-ion collisions, with experimental accuracy that makes quantitative comparisons meaningful.

Beginning in Run-22, STAR will be in a unique position to provide this essential pp and $p+A$ data. A full suite of forward detectors will be installed this year, providing excellent charged-particle tracking at high pseudorapidity ($2.5 < \eta < 4$) for the first time, coupled with both electromagnetic and hadronic calorimetry. This will enable STAR to explore the interesting regimes of high- x (largely valence quark) and low- x (primarily gluon) partonic physics with unparalleled precision. In addition, mid-rapidity detector upgrades motivated primarily by the BES-II program, in particular the iTPC, will substantially extend STAR’s already excellent kinematic reach and particle identification capabilities beyond those that existed during previous pp and $p+A$ runs.

For the case of pp spin physics, it is important to recognize the complementary roles that will be played by Run-22 at 510 GeV and Run-24 at 200 GeV. The combination of 510 GeV pp collisions and the STAR Forward Upgrade will provide access to forward jet physics at perturbative scales, thereby enabling measurements at the highest and lowest x values. In parallel, mid-rapidity measurements at 510 and, especially, 200 GeV will interpolate between the high and low x values, with significant overlaps to probe evolution effects

1239 and provide cross-checks. Together, the two runs will allow STAR to measure fundamental
1240 proton properties, such as the Sivers and transversity distributions, over nearly the entire
1241 range $0.005 < x < 0.5$.

1242 Run-24 will also provide outstanding opportunities to probe fundamental questions re-
1243 garding QCD in cold nuclear matter. The STAR Forward Upgrade will enable an extensive
1244 suite of measurements probing the quark-gluon structure of heavy nuclei and the regime of
1245 low- x non-linear gluon dynamics, as predicted by saturation models. STAR will also ex-
1246 plore how a nucleus, serving as a color filter, modifies the propagation, attenuation, and
1247 hadronization of colored quarks and gluons.

1248 For these reasons, STAR requests at least 16 weeks of polarized pp data-taking at $\sqrt{s} =$
1249 510 GeV in Run-22. All data-taking will involve proton beams polarized transversely relative
1250 to their momentum direction in order to focus on those observables where factorization,
1251 universality, and/or evolution remain open questions, with spins aligned vertically at the
1252 STAR IR. Based on the latest guidance from CAD, and mindful of ‘lessons learned’ in
1253 previous pp runs at full energy (see Fig. 36), we will ask for luminosity-leveling of the collision
1254 rate to maximize the efficiency of our main tracking detectors. Assuming we will have running
1255 conditions similar to those achieved in Run-17, we expect to sample at least 400 pb^{-1} for
1256 our rare / non-prescaled triggers. Reducing the Run-22 run time from 20 to 18 cryo-weeks
1257 would have a significant impact on our physics program described in section 2.1.1. Along
1258 with the luminosity loss associated with fewer running weeks, STAR will be commissioning
1259 its newly installed, and critical for the proposed program, forward detector suite which will
1260 result in additional luminosity being subtracted from physics running. In total, this would
1261 result in at least 15% less sampled luminosity, as the loss will occur near the end of the run
1262 when the detectors and RHIC will be operating most efficiently.

1263 STAR also requests at least 11 weeks of polarized pp data-taking at $\sqrt{s} = 200 \text{ GeV}$ and 11
1264 weeks of polarized $p+\text{Au}$ data-taking at $\sqrt{s_{NN}} = 200 \text{ GeV}$ during Run-24. All of the running
1265 will involve vertically polarized protons. Based on recent CAD guidance, we expect to sample
1266 at least 235 pb^{-1} of pp collisions and 1.3 pb^{-1} of $p+\text{Au}$ collisions. These totals represent
1267 4.5 times the luminosity that STAR sampled during transversely polarized pp collisions
1268 in Run-15, and 3 times the luminosity that STAR sampled during transversely polarized
1269 $p+\text{Au}$ collisions in Run-15. Effectively, we request approximately equal nucleon-nucleon
1270 luminosities for pp and $p+\text{Au}$ which is essential to optimize several critical, and in many
1271 cases luminosity-demanding, measurements that require comparisons of the same observable
1272 in (polarized or unpolarized) pp and $p+\text{Au}$ collisions, described further in Section 2.2. Any
1273 significant reduction of the available running period, e.g. 20 instead of 28 weeks, would
1274 almost certainly result in the impossibility of fulfilling the unique physics goals in Run-24.

1275 2.1 Run-22 Request for $p^\uparrow p^\uparrow$ Collisions at 510 GeV

1276 2.1.1 Inclusive Transverse Spin Asymmetries at Forward Rapidities

1277 The experimental study of spin phenomena in nuclear and particle physics has a long history
1278 of producing important, and often surprising, results. Attempts to understand such data

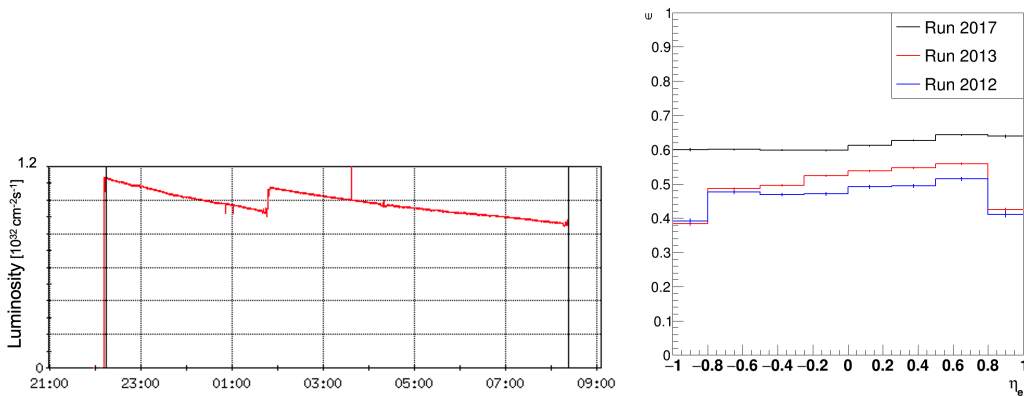


Figure 36: Example of the leveled luminosity profile for a fill from Run-17 at 510 GeV (left). The right panel shows the impact of the luminosity leveling on the W boson reconstruction efficiency. Luminosity leveling was applied during Run-17 but not for Run-12 and Run-13. A higher W efficiency is clearly seen in Run-17 with the luminosity leveling applied. The more uniform efficiency in Run-17 for two outer lepton- η bins is the result of a different cut at $|\eta| < 0.9$ to remove the detector edge effects.

1279 have pushed the field forward, forcing the development of both new theoretical frameworks
 1280 and new experimental techniques. Recent and ongoing detector upgrades at STAR, at mid-
 1281 and forward-rapidity, coupled with the versatility of RHIC, will allow us to gain new insights
 1282 into long-standing puzzles, and to probe more deeply the complexities of emergent behavior
 1283 in QCD.

1284 Results from PHENIX and STAR have shown that large transverse single-spin asymme-
 1285 tries (TSSA) for inclusive hadron production, first seen in pp collisions at fixed-target en-
 1286 ergies and modest p_T , extend to the highest RHIC center-of-mass energies, $\sqrt{s} = 510$ GeV,
 1287 and surprisingly large p_T . Figure 37 summarizes the world data for the inclusive neutral
 1288 pion asymmetries A_N as a function of Feynman- x . The asymmetries are seen to be nearly
 1289 independent of \sqrt{s} over the very wide range of roughly 19 to 500 GeV.

1290 To understand the observed TSSAs, one needs to go beyond the conventional leading-
 1291 twist (twist-2) collinear parton picture for the hard-scattering processes. Two theoretical
 1292 formalisms have been developed to try to explain these sizable asymmetries in the QCD
 1293 framework: transverse-momentum-dependent (TMD) parton distribution and fragmentation
 1294 functions, such as the Sivers and Collins functions; and transverse-momentum-integrated
 1295 (collinear) quark-gluon-quark correlations, which are twist-3 distributions in the initial state
 1296 proton or in the fragmentation process. For many of the experimentally accessible spin
 1297 asymmetries, several of these functions can contribute, and need to be disentangled in order
 1298 to understand the experimental data in detail, in particular the observed p_T dependence.
 1299 These functions manifest their spin dependence either in the initial state—for example, the
 1300 Sivers distribution and its twist-3 analog, the Efremov-Teryaev-Qiu-Sterman (ETQS) func-
 1301 tion [142]—or in the final state via the fragmentation of polarized quarks, such as in the
 1302 Collins function and related twist-3 function $\hat{H}_{FU}(z, z_z)$.

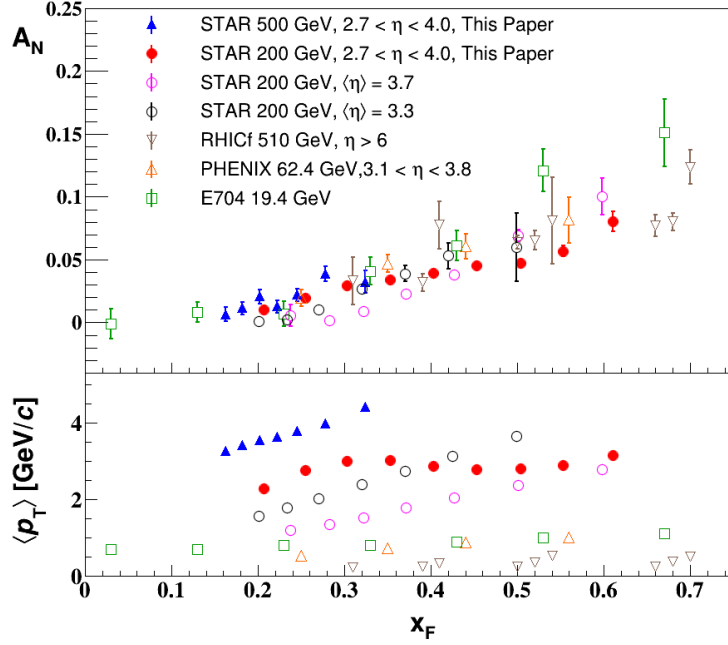


Figure 37: Transverse single-spin asymmetry A_N measurements for neutral pion in pp collisions at different center-of-mass energies as a function of Feynman- x [115].

1303 Incorporating the fragmentation term within the collinear twist-3 approach demonstrated
 1304 the ability of this formalism to describe the large values of A_N for π^0 production observed at
 1305 RHIC [143]. In this work, the relevant (non-pole) 3-parton collinear fragmentation function
 1306 $\hat{H}_{FU}(z, z_z)$ was fit to the RHIC data. The so-called soft-gluon pole term, involving the ETQS
 1307 function $T_{q,F}(x_1, x_2)$, was also included by fixing $T_{q,F}$ through its well-known relation to the
 1308 TMD Sivers function f_{1T}^\perp . The authors obtained a very good description of the data due to
 1309 the inclusion of the non-pole fragmentation function and based on this work they were able
 1310 to make predictions for π^+ and π^- production asymmetries A_N at the forward rapidities
 1311 covered by the STAR upgrades, $2.5 < \eta < 4$. The results are shown in Fig. 38 for $\sqrt{s} = 200$
 1312 and 500 GeV for two rapidity ranges, $2 < \eta < 3$ and $3 < \eta < 4$.

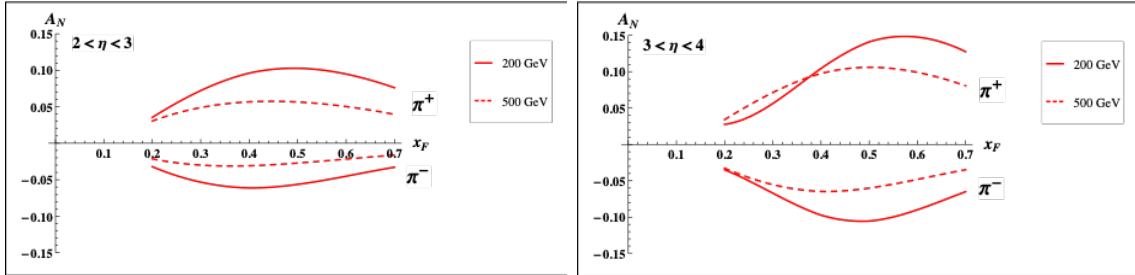


Figure 38: Predictions for A_N for π^+ and π^- production over the ranges $2 < \eta < 3$ (left) and $3 < \eta < 4$ (right) at $\sqrt{s} = 200$ GeV (solid lines) and 500 GeV (dashed lines).

1313 In Run-22, with the full suite of forward tracking detectors and calorimetry installed,
 1314 STAR will for the first time be able to map out inclusive charged-hadron asymmetries up to
 1315 the highest energies achievable at RHIC and at these forward rapidities in the Feynman-x
 1316 region $0.2 < x_F < 0.7$. It would be very interesting to confirm that these asymmetries are
 1317 indeed largely independent of center-of-mass energy. The measurements of A_N for charged
 1318 hadrons, together with analogous data (from Run-22 as well as previous STAR runs) on
 1319 A_N for direct photons and neutral pions, should provide the best data set in the world
 1320 to constrain the evolution and flavor dependence of the twist-3 ETQS distributions and to
 1321 determine if the 3-parton collinear fragmentation function \hat{H}_{FU} is the main driver of the
 1322 large forward inclusive asymmetries. The expected separation power between positively and
 1323 negatively charged hadrons in the pseudorapidity region $2.5 < \eta < 4$ with the STAR forward
 1324 upgrade is presented in Figure 39.

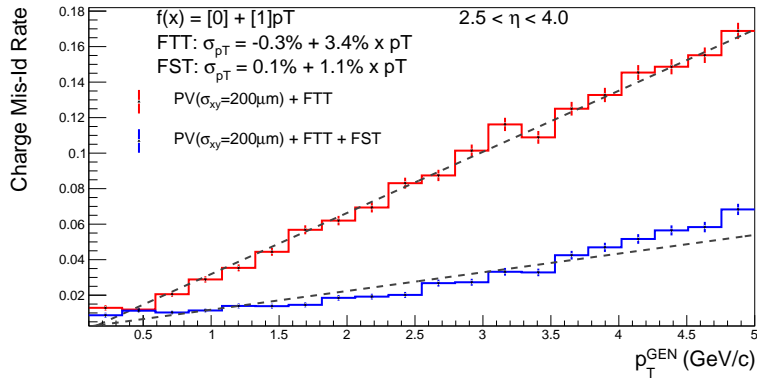


Figure 39: The expected charge mis-identification rate as a function of particle p_T in the pseudo-rapidity region $2.5 < \eta < 4$ with the STAR forward upgrade. The results in blue correspond to full tracking system including both sTGC and silicon detectors and the red ones include sTGC only.

1325 2.1.2 Sivers and Efremov-Teryaev-Qiu-Sterman Functions

1326 There is great theoretical interest in testing the relation between the ETQS correlation
 1327 functions and the Sivers function. As discussed above, both the Sivers and the ETQS
 1328 functions encapsulate partonic spin correlations within the proton, but they are formally
 1329 defined in different frameworks. While the Sivers function is a TMD quantity that depends
 1330 explicitly on spin-dependent transverse partonic motion k_T , the ETQS function is a twist-3
 1331 collinear distribution, in which SSAs are generated through soft collinear gluon radiation.

1332 Measurements of forward jet production from the ANDY collaboration [144] indicated
 1333 rather small asymmetries. This was argued to be consistent with the idea that the twist-3
 1334 parton correlation functions for up and down valence quarks should cancel, because their
 1335 behavior reflects the Sivers functions extracted from fits to the SIDIS data that demonstrate
 1336 opposite sign, but equal magnitude, up and down quark Sivers functions. Preliminary STAR
 1337 results on charge-tagged dijets at mid-rapidity [145] (see Fig. 44) support this interpretation,
 1338 with the caveat that the measured observable (a spin-dependent $\langle k_T \rangle$) is defined in the TMD,

1339 and not the twist-3, framework. Moreover, recently published STAR results for forward
 1340 inclusive electromagnetic jets [115] also show small TSSA as seen in Fig. 40. The results
 1341 have been analyzed with the generalized parton model approach [146], and when incorporated
 1342 in the reweighing procedure of the quark Sivers functions extracted from SIDIS data they
 1343 significantly improved its uncertainty at larger momentum fraction x (see Fig. 41).

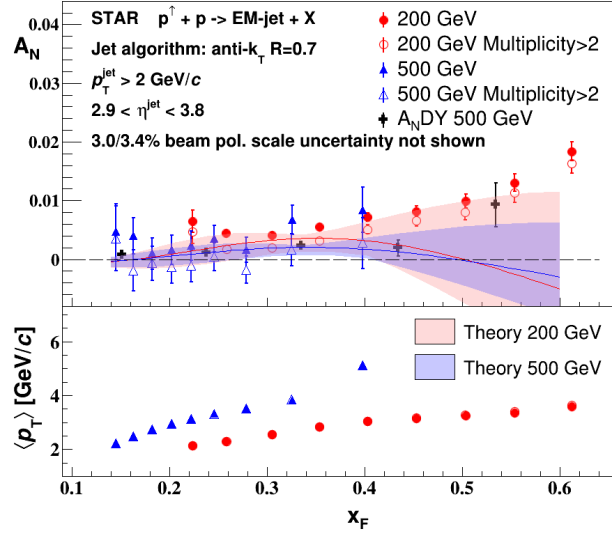


Figure 40: New STAR results on inclusive electromagnetic jets TSSA in pp collisions at both 200 and 500 GeV [115]. The results that require more than two photons observed inside a jet are shown as open symbols. Theory curves [147] for TSSA of full jets at rapidity $\langle y \rangle = 3.25$ for 200 GeV (red) and $\langle y \rangle = 3.57$ for 500 GeV (blue) are also shown. The average p_T of the jet for each x_F bin is shown in the lower panel.

1344 To better test quantitatively the relation between the twist-3 and TMD regimes, one
 1345 can measure spin asymmetries for jets which are *intentionally* biased towards up or down
 1346 quark jets via detection of a high- z charged hadron within the jet. Figure 42 shows the
 1347 flavor of initial partons for positively and negatively charged leading hadrons in the rapidity
 1348 range $2.6 < \eta < 4.1$ for different regions of Feynman- x based on PYTHIA Minimum Bias
 1349 studies for pp at 510 GeV. For $x_F > 0.2$ one can see a significant enhancement of the u -
 1350 quark contribution for positively charged leading hadrons, and the d -quark contribution for
 1351 negatively charged ones.

1352 Higher-twist calculations of jet asymmetries based on the Sivers function predict sizeable
 1353 effects for these flavor-enhanced jets. With the suite of new forward detectors installed
 1354 at STAR, full jet reconstruction, along with identification of a high- z hadron of known
 1355 charge sign (see Fig. 39), will be possible at high pseudorapidity. Using realistic simulation
 1356 of the forward calorimeter, and requiring a charged hadron with $z > 0.5$, the expected
 1357 statistical uncertainties of asymmetries has been extracted and are presented in Fig. 43.
 1358 The simulations have assumed an integrated luminosity of 350 pb^{-1} at $\sqrt{s} = 510 \text{ GeV}$.
 1359 No tracking or hadron reconstruction has been included, and the trigger effects have been

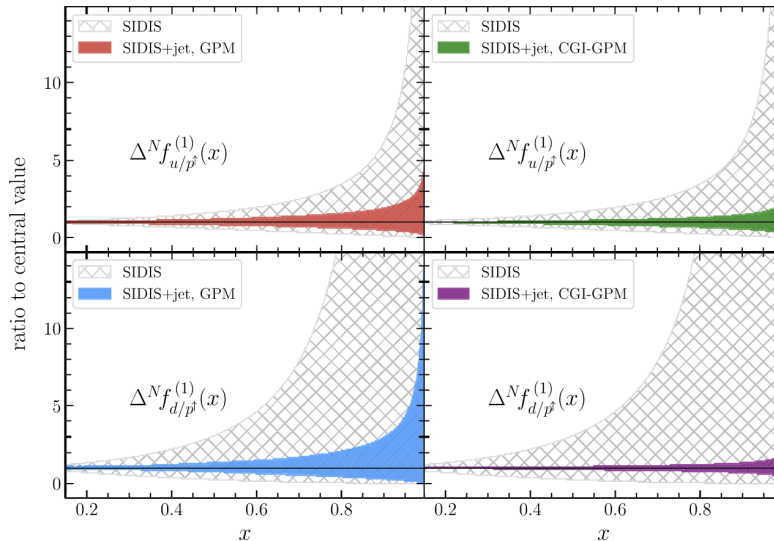


Figure 41: Comparison between the Siverson function first moments normalized to the corresponding central value from SIDIS data and their reweighted counterparts that incorporate new STAR results on electromagnetic jets [115] extracted in [146] in the generalized parton model (left panels) and color gauge invariant generalized parton model (right panels) framework. In both plots, results for u (upper panels) and d (lower panels) quarks are shown.

1360 accounted for by applying jet p_T thresholds (4, 6, 7.5 GeV/ c) for jet-patch triggers in two
 1361 pseudo-rapidity regions spanning $2.5 < \eta < 3.5$ and $3 < \eta < 4$ respectively. A similar
 1362 measurement is also expected at 200 GeV. Figure 43 also compares the Run-22 projections
 1363 to the single spin asymmetries calculated by the ETQS function, based on the SIDIS Siverson
 1364 functions.

1365 In a TMD framework, the Siverson effect manifests itself as a correlation (a triple product)
 1366 between the transverse momentum of a parton (\vec{k}_T) with momentum fraction x , and the
 1367 transverse spin (\vec{S}) of a polarized proton moving in the longitudinal (\vec{p}) direction. Thus,
 1368 for transversely polarized protons, the Siverson effect probes whether the k_T of the constituent
 1369 quarks is preferentially oriented in a direction perpendicular to both the proton momentum
 1370 and its spin. Momentum conservation then implies that the two jets in the final state will
 1371 not emerge back-to-back on average, but instead will ‘tilt’ in the direction of the summed
 1372 k_T of the initial state partons. Moreover, the (average) tilt of interest will reverse direction
 1373 under a ‘flip’ of the proton spin; a spin-dependent $\langle k_T \rangle$ can then be extracted by associating
 1374 the azimuthal opening angle of the jet pair with this tilt.

1375 STAR carried out an earlier measurement of this transverse single-spin asymmetry using
 1376 a dijet dataset with $\sim 1 \text{ pb}^{-1}$ of integrated luminosity [148], and found it to be consistent
 1377 with zero within 2σ . An ongoing and much improved analysis based on Run-12 and Run-15
 1378 has past STAR paper preview process, and the preliminary results can be found in [145].
 1379 Perhaps most significantly, the jets were sorted according to their net charge Q , calculated

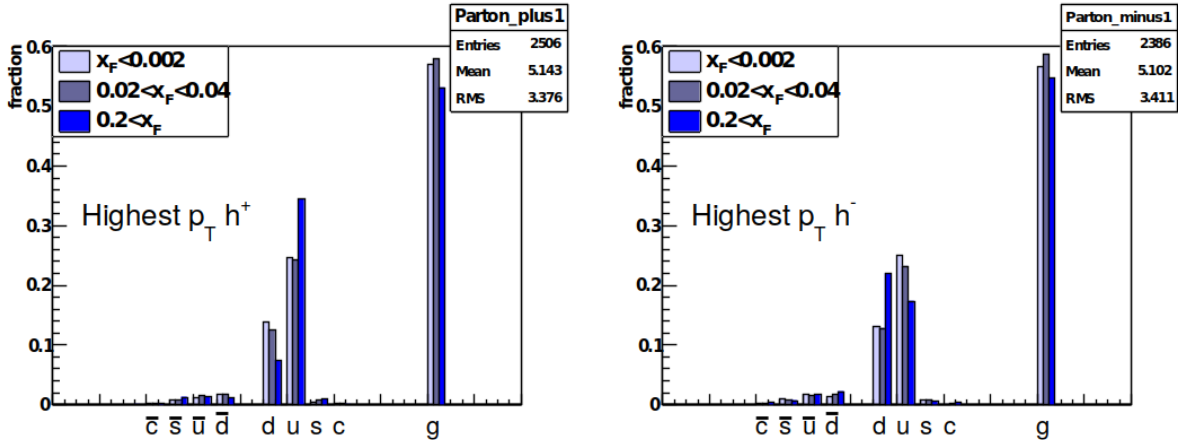


Figure 42: Flavor of initial partons for events with positively (left) and negatively (right) charged leading hadrons in the rapidity range $2.6 < \eta < 4.1$ for different regions of Feynman- x based on PYTHIA Minimum Bias studies for pp at 510 GeV. For $x_F > 0.2$ one can see an enhancement of the u -quark contribution for positively charged leading hadrons, and the d -quark contribution for negatively charged ones.

1380 by summing the signed momentum of all particle tracks with $p > 0.8$ GeV, to minimize
 1381 underlying event contributions, yielding jet samples with enhanced contributions from u
 1382 quarks (positive Q) and d quarks (negative Q), with a large set near $Q = 0$ dominated by
 1383 gluons. Simple kinematics allow for conversion from the spin-dependent ‘tilt’ of the dijet
 1384 pair to a value of k_T on an event-by-event basis; these are then sorted by the Q of the jet
 1385 and binned by the summed pseudorapidities of the outgoing jets, $\eta^{\text{total}} \equiv \eta_3 + \eta_4$. Because
 1386 the contributions of different partons (u , d , all else) to $\langle k_T \rangle$ vary with both Q and also η^{total} ,
 1387 in a way that can be estimated robustly using simulation, the data can be inverted to yield
 1388 values of $\langle k_T \rangle$ for the individual partons, though with coarser binning in η^{total} . Figure 44
 1389 shows the preliminary results for the spin-dependent $\langle k_T \rangle$ values for u , d and $gluon + sea$.

1390 With the new forward detectors in place, along with the enhanced reach in η afforded by
 1391 the iTPC, this technique can be expanded in Run-22 to cover pseudorapidities at STAR from
 1392 roughly -1 to 4 , though with a gap at $1.5 < \eta < 2.5$. Despite this gap, values of $\langle k_T \rangle$ can be
 1393 extracted for u and d quarks for η^{total} ranging from ~ -1.5 to as high as 7 with reasonable
 1394 statistics. This latter regime will probe $2 \rightarrow 2$ hard scattering events in which $x_1 \gg x_2$,
 1395 *i.e.*, a sample enriched in valence quarks interacting with low- x gluons. Such measurements,
 1396 exploiting the full kinematic reach of STAR, will not only allow precise determinations of
 1397 the average transverse partonic motion, $\langle k_T \rangle$, exhibited by individual partonic species in
 1398 the initial state, but will provide important information on the x dependence of the proton
 1399 Sivers functions.

1400 Collisions at $\sqrt{s} = 510$ GeV will also allow STAR to continue our successful program
 1401 to study the evolution and sign change of the Sivers function. By focusing on interactions
 1402 in which the final state involves only weakly interacting particles, and hence the transverse

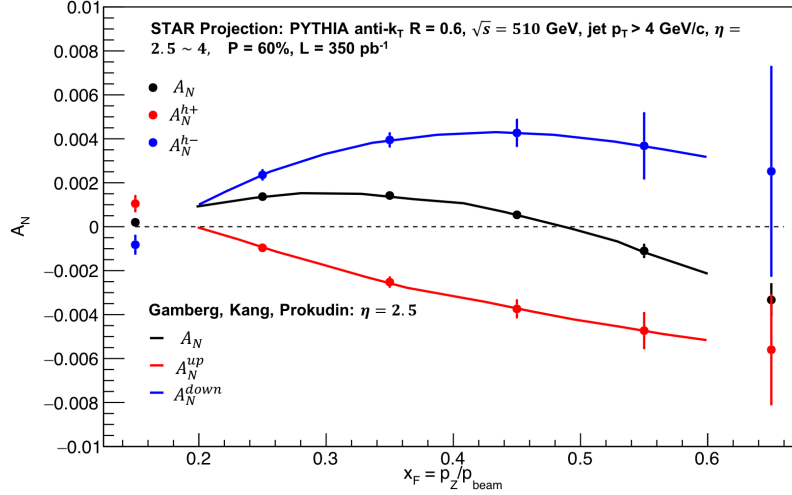


Figure 43: Up quark (red line), down quark (blue line) and all jet (black line) single spin asymmetries as a function of x_F as calculated by the ETQS function, which is based on the SIDIS Sivvers functions, for 200 GeV center-of-mass energy proton collisions – the 510 GeV results are expected to be qualitatively similar. Overlaid on the theory curves are the expected experimental sensitivities for jet asymmetries tagging in addition a positive hadron with z above 0.5 (red points), a negative hadron with z above 0.5 (blue points) or all jets (black) as a function of x_F at 510 GeV.

1403 partonic motion (in a TMD framework) or the collinear gluon radiation (in twist-3) must be
 1404 in the initial state, one can test for the predicted sign change in A_N relative to interactions
 1405 in which these terms must appear in the final state, such as SIDIS measurements. Following
 1406 the low statistics Run-11 proof-of-principle measurement, STAR has measured A_N in W and
 1407 Z in Run-17, which had about 14 times more integrated luminosity than Run-11. Figure 45
 1408 compares the reconstructed Z mass between combined Runs-11+12+13 and Run-17. From
 1409 the comparison one can see a consistent mass spectrum and the clearly visible Z mass peak.
 1410 Additionally, from the number of reconstructed Z events shown, one can see the effect of that
 1411 the higher efficiency in Run-17 (see Fig. 36), due to the luminosity leveling, has on the data.
 1412 The Run-17 preliminary Z and W^\pm A_N results plotted as a function of reconstructed boson
 1413 rapidity are shown in Figs. 46 and 47, respectively. The systematic uncertainties assigned to
 1414 the W A_N preliminary results were estimated by varying the various cut criteria, in particular
 1415 the lepton E_T cut, according to the Barlow criteria. Additionally the contribution from the
 1416 transversal helicity function, g_{1T} , which has a \cos azimuthal modulation was estimated by
 1417 extracting the asymmetry A_N from a simultaneous \sin/\cos fit to the measured azimuthal
 1418 modulations. With the increased precision provided by Run-17 we find smaller asymmetries
 1419 than were suggested by Run-11. As a result it is critical that we increase the statistics of
 1420 our dataset with Run-22 to improve the precision of our asymmetry measurements in order
 1421 to provide a conclusive test of the Sivvers' function sign change.

1422 The improved tracking capabilities provided by the iTPC upgrade will allow us to push
 1423 our mid-rapidity W^\pm and Z measurements to larger rapidity $y_{W/Z}$, a regime where the

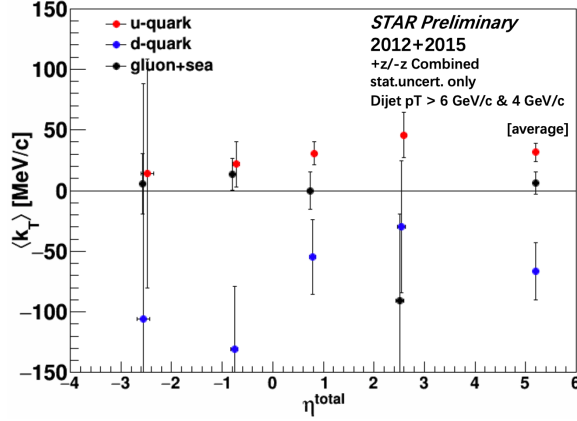


Figure 44: Preliminary results for the spin-dependent $\langle k_T \rangle$ values for u , d and $gluon+sea$ from the dijet Sivers measurement as a function of the sum of dijet pseudorapidities $\eta_1 + \eta_2 \sim \ln(\frac{x_1}{x_2})$ [145].

1424 asymmetries are expected to increase in magnitude and the anti-quark Sivers' functions
 1425 remain largely unconstrained. In addition to the noted extension of our kinematic reach, an
 1426 additional 16 weeks of beam time at $\sqrt{s} = 510$ GeV in Run-22 would increase our dataset by
 1427 about a factor of 2. This experimental accuracy would significantly enhance the quantitative
 1428 reach of testing the limits of factorization and universality in lepton-proton and proton-
 1429 proton collisions.

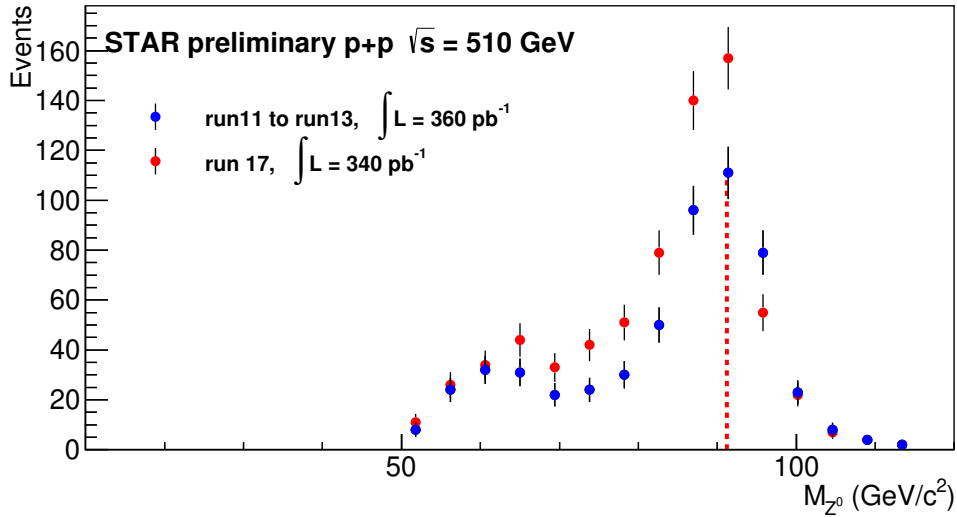


Figure 45: Preliminary results for the reconstructed Z boson mass for Run-11 + 12 +13 (blue markers) and Run-17 (red markers).

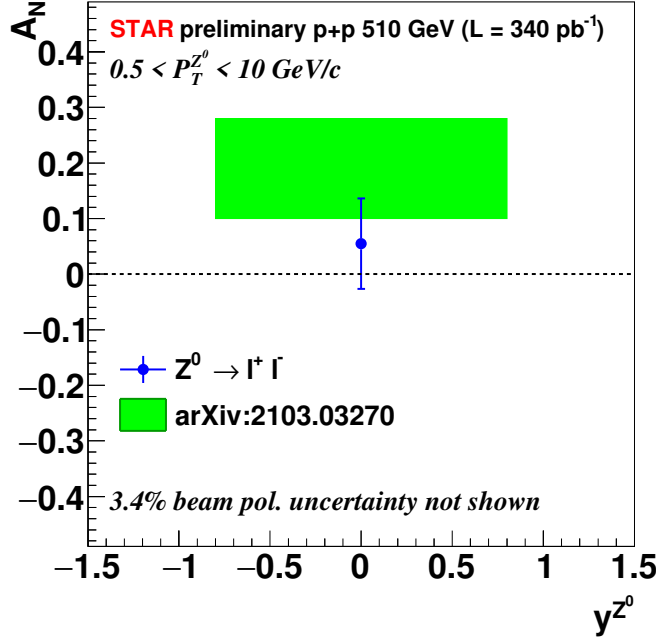


Figure 46: Preliminary results for the transverse single-spin asymmetries of Z boson as a function of rapidity for Run-17. The green band is a theoretical prediction from [149], folding in data on the sea-quark Sivers functions.

1430 2.1.3 Transversity, Collins Function and Interference Fragmentation Function

1431 A complete picture of nucleon spin structure at leading twist must include contributions
 1432 from the unpolarized and helicity distributions, as well as those involving transverse po-
 1433 larization, such as the transversity distribution [151–153]. The transversity distribution
 1434 can be interpreted as the net transverse polarization of quarks within a transversely polar-
 1435 ized proton. The difference between the helicity and transversity distributions for quarks
 1436 and antiquarks provides a direct, x -dependent connection to nonzero orbital angular mo-
 1437 mentum components in the wave function of the proton [154]. Recently, the first lattice
 1438 QCD calculation of the transversity distribution has been performed [155]. In addition,
 1439 the measurement of transversity has received substantial interest as a means to access the
 1440 tensor charge of the nucleon, defined as the integral over the valence quark transversity:
 1441 $\delta q^a = \int_0^1 [\delta q^a(x) - \delta \bar{q}^a(x)] dx$ [152, 156]. Measuring the tensor charge is very important for
 1442 several reasons. First, it is an essential and fundamental quantity to our understanding of
 1443 the spin structure of the nucleon. Also, the tensor charge can be calculated on the lattice
 1444 with comparatively high precision, due to the valence nature of transversity, and hence is
 1445 one of the few quantities that allow us to compare experimental results on the spin structure
 1446 of the nucleon directly to *ab initio* QCD calculations. Finally, the tensor charge describes
 1447 the sensitivity of observables in low-energy hadronic reactions to beyond the standard model

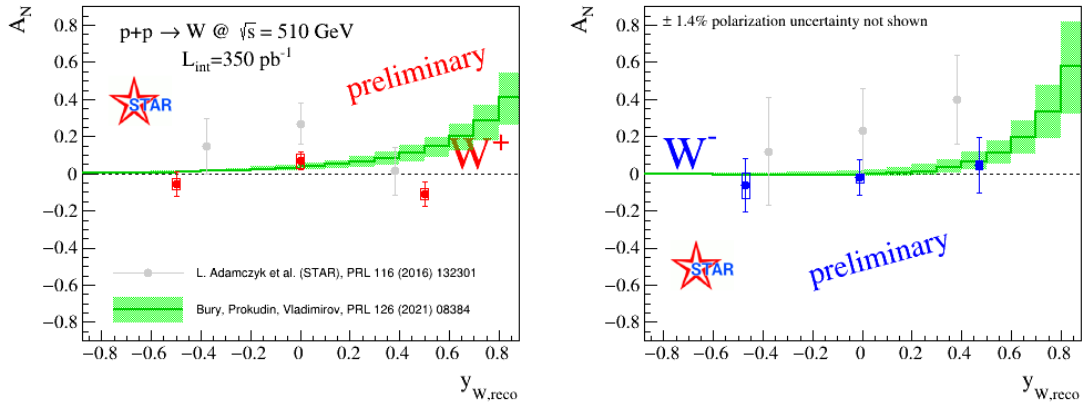


Figure 47: Preliminary results for the transverse single-spin asymmetries of W^\pm bosons as a function of their rapidity for Run-17 compared to the Run-11 results [150]. The green lines and boxes are theoretical predictions from [149] using data from SIDIS, pion-induced polarized Drell-Yan, and $W^{+/-}/Z^0$ -boson A_N STAR measurements from Run-11.

1448 physics processes with tensor couplings to hadrons. Examples are experiments with ultra-
 1449 cold neutrons and nuclei.

1450 Transversity is difficult to access due to its chiral-odd nature, requiring the coupling of
 1451 this distribution to another chiral-odd distribution. Semi-inclusive deep-inelastic scattering
 1452 (SIDIS) experiments have successfully probed transversity through two channels: asym-
 1453 metric distributions of single pions, convoluting the TMD transversity distribution with
 1454 the TMD Collins fragmentation function, and azimuthally asymmetric distributions of di-
 1455 hadrons, coupling transversity to the so-called “interference fragmentation function” (IFF)
 1456 in the framework of collinear factorization. Yet in spite of a wealth of lepton-scattering
 1457 data, the kinematic reach of existing SIDIS experiments limits the precision with which the
 1458 proton’s transversity can be extracted, as the range of Bjorken- x values that can be accessed
 1459 does not extend above $x \sim 0.3$.

1460 In hadronic collisions, the k_T integrated quark transversity distribution may be accessed
 1461 mainly via two channels. The first is the single spin asymmetry of the azimuthal distribution
 1462 of hadrons in high energy jets [117]. In the jet+hadron channel, the collinear transversity
 1463 distribution couples to the TMD Collins function [117, 118]. This makes pp collisions a more
 1464 direct probe of the Collins fragmentation function than Collins asymmetries in SIDIS [117],
 1465 where a convolution with the TMD transversity distribution enters. This also makes the
 1466 Collins asymmetry in pp collisions an ideal tool to explore the fundamental QCD questions
 1467 of TMD factorization, universality, and evolution. The second channel is the single spin
 1468 asymmetry of pion pairs, where transversity couples to the collinear interference fragmen-
 1469 tation function [157]. STAR mid-rapidity IFF data [158] have been included in the first
 1470 extraction of transversity from SIDIS and proton-proton IFF asymmetries [159]. In addi-
 1471 tion, transverse spin transfer, D_{TT} , of Λ hyperons in pp collisions is also expected to be able
 1472 to provide sensitivity for the strange quark transversity through the polarized fragmenta-
 1473 tion functions. The strange quark transversity is not constrained at all currently. The first

1474 D_{TT} measurement of Λ and $\bar{\Lambda}$ hyperons at $\sqrt{s} = 200$ GeV has been performed with the
 1475 Run-12 pp dataset [120], and current results didn't indicate a sizable spin transfer yet. The
 1476 iTPC upgrade will help to reach near-forward pseudo-rapidity $\eta < 1.5$ for the spin transfer
 1477 measurements.

1478 The universality of TMD PDFs and fragmentation functions in pp collisions has been an
 1479 open question. General arguments [160, 161] have shown that factorization can be violated
 1480 in hadron-hadron collisions for TMD PDFs like the Sivers function, though very recent
 1481 calculations indicate the violations might be quite small [162, 163]. In contrast, while there
 1482 is no general proof that the Collins effect in pp collisions is universal to all orders, explicit
 1483 calculations [117, 118, 164, 165] have shown that diagrams like those that violate factorization
 1484 of the Sivers function make no contribution to the Collins effect at the one- or two-gluon
 1485 exchange level, thereby preserving its universality at least to that level.

1486 Comparisons of the transversity distributions extracted from the Collins and IFF channels
 1487 will allow STAR to study the size and nature of any factorization breaking effects for TMD
 1488 observables in hadronic collisions. Likewise, comparisons with the transversity, Collins and
 1489 IFF distributions extracted from SIDIS collisions will shed light on universality and constrain
 1490 evolution effects. The measurement of evolution effects in TMD distributions is particularly
 1491 important because, unlike the collinear case, TMD evolution contains a non-perturbative
 1492 component that cannot be calculated directly. Measurements at \sqrt{s} of 200 and 510 GeV will
 1493 provide additional experimental constraints on evolution effects and provide insights into the
 1494 size and nature of TMD observables at the future Electron-Ion Collider.

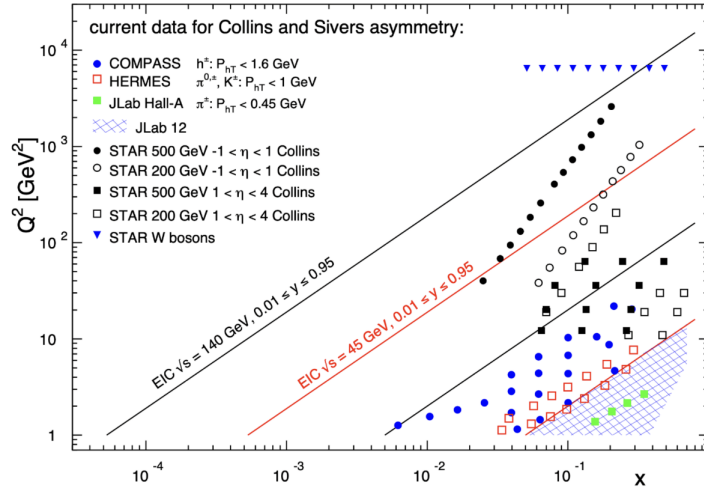


Figure 48: $x - Q^2$ coverage of RHIC measurements compared to existing Collins and Sivers effect measurements in SIDIS and the future coverage of the EIC.

1495 Extending measurements of di-hadron and Collins asymmetries to the forward direction
 1496 during Run-22 will allow access to transversity in the region $x > 0.3$. This valence quark
 1497 region is not currently probed by any experiments and is essential for the determination of
 1498 the tensor charge, which receives 70% of its contributions from $0.1 < x < 1.0$. In addition,

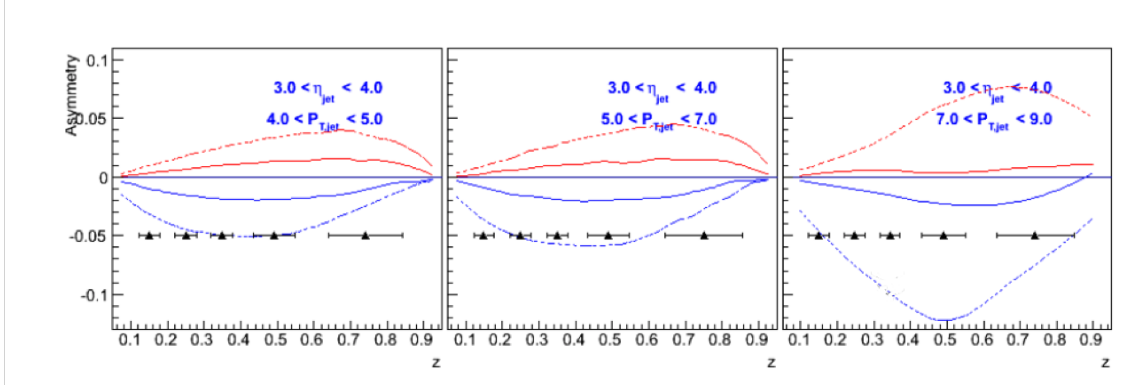


Figure 49: Expected h^- Collins asymmetry uncertainties at $3 < \eta < 4$ (black points) from a sampled luminosity of 350 pb^{-1} at $\sqrt{s} = 510 \text{ GeV}$, compared to positive (red) and negative (blue) pion asymmetries based on the Torino extraction (full lines) and the Soffer bound (dashed lines) as a function of hadron z for bins in jet p_T . Most uncertainties are smaller than the height of the triangles.

1499 probing transversity in pp collisions also provides better access to the d -quark transversity
 1500 than is available in SIDIS, due to the fact that there is no charge weighting in the hard
 1501 scattering QCD $2 \rightarrow 2$ process in pp collisions. This is a fundamental advantage of pp
 1502 collisions, as any SIDIS measurement of the d -quark transversity has to be on a bound
 1503 system, *e.g.* He-3, which ultimately requires nuclear corrections to extract distributions.
 1504 The high scale we can reach in 500 GeV collisions at RHIC has allowed STAR [166] to
 1505 demonstrate, for the first time, that previous SIDIS measurements at low scales are in fact
 1506 accessing the nucleon at leading twist. Figure 48 shows the $x - Q^2$ coverage spanned by
 1507 the RHIC measurements compared to the future EIC, JLab-12, and the current SIDIS world
 1508 data.

1509 Another fundamental advantage of pp collisions is the ability to access gluons directly.
 1510 While gluons cannot be transversely polarized in a transversely polarized spin 1/2 hadron,
 1511 they can be linearly polarized. Similarly, there exists an equivalent of the Collins fragmen-
 1512 tation function for the fragmentation of linearly polarized gluons into unpolarized hadrons
 1513 [167]. The linear polarization of gluons is a largely unexplored phenomenon, but it has been
 1514 a focus of recent theoretical work, in particular due to the relevance of linearly polarized
 1515 gluons in unpolarized hadrons for the p_T spectrum of the Higgs boson measured at the LHC.
 1516 Polarized proton collisions with $\sqrt{s} = 510 \text{ GeV}$ at RHIC, in particular for asymmetric par-
 1517 ton scattering if jets are detected in the backward direction, are an ideal place to study the
 1518 linearly polarized gluon distribution in polarized protons. (Note that the distributions of
 1519 linearly polarized gluons inside an unpolarized and a polarized proton provide independent
 1520 information). A first measurement of the ‘‘Collins-like’’ effect for linearly polarized gluons
 1521 has been done by STAR with data from Run-11 [166], providing constraints on this function
 1522 for the first time.

1523 Figure 49 shows projected h^- Collins asymmetry uncertainties along with $\pi^+/-$ Collins
 1524 asymmetries from theory calculations at 510 GeV with the Forward Upgrade during Run-22.

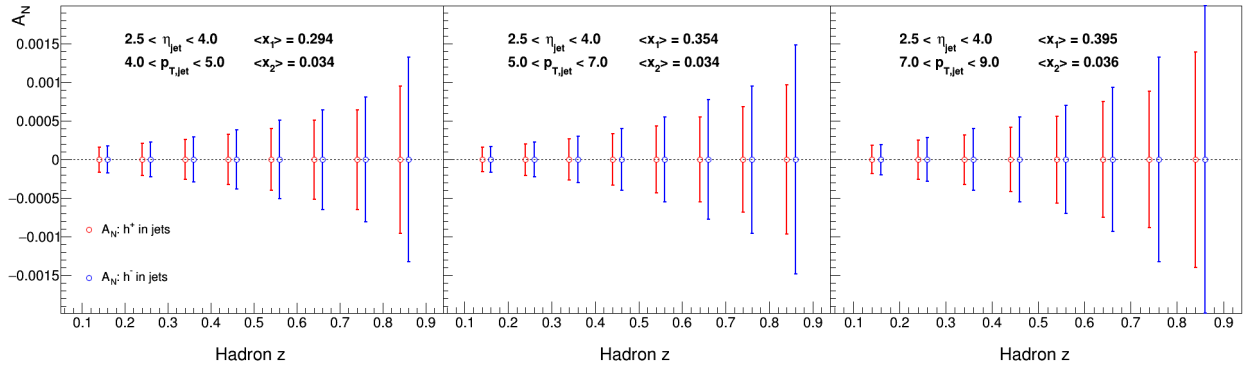


Figure 50: Expected h^\pm Collins asymmetry uncertainties at $2.5 < \eta < 4$ for the three momentum bins shown in Fig. 49, based on a sampled luminosity of 350 pb^{-1} at $\sqrt{s} = 510 \text{ GeV}$.

1525 Figure 50 shows STAR’s expected h^\pm Collins asymmetry corresponding to the kinematic
 1526 regions shown in Fig. 49, but with a zoomed in vertical scale. As indicated on the figure, jets
 1527 with $2.5 < \eta < 4$ and $4 < p_T < 9 \text{ GeV}/c$ will explore transversity in the important region
 1528 $0.3 < x < 0.5$ that has not yet been probed in SIDIS. A realistic momentum smearing of final
 1529 state hadrons as well as jets in this rapidity range was assumed and dilutions due to beam
 1530 remnants (which become substantial at rapidities close to the beam) and underlying event
 1531 contributions have been taken into account. As no dedicated particle identification at forward
 1532 rapidities will be available for these measurements, only charged hadrons were considered.
 1533 This mostly reduces the expected asymmetries due to dilution by protons (10-14%) and a
 1534 moderate amount of kaons (12-13%). As anti-protons are suppressed compared to protons
 1535 in the beam remnants, especially the negative hadrons can be considered a good proxy for
 1536 negative pions ($\sim 78\%$ purity according to PYTHIA6). Given their sensitivity to the down
 1537 quark transversity via favored fragmentation, they are particularly important since SIDIS
 1538 measurements, due to their electromagnetic interaction, are naturally dominated by up-
 1539 quarks. We have estimated our statistical uncertainties based on an accumulated luminosity
 1540 of 350 pb^{-1} , which leaves nearly invisible uncertainties after smearing. These expected
 1541 uncertainties are compared to the asymmetries obtained from the transversity extractions
 1542 based on SIDIS and Belle data [168] as well as from using the Soffer positivity bound for
 1543 the transversity PDF [169]. More recent global fits have slightly different central up and
 1544 down quark transversity distributions. But due to the lack of any SIDIS data for $x > 0.3$,
 1545 the upper uncertainties are compatible with the Soffer bounds. This high- x coverage will
 1546 give important insights into the tensor charge, which is essential to understand the nucleon
 1547 structure at leading twist.

1548 Although the studies presented here are for the Collins asymmetries, the resulting sta-
 1549 tistical uncertainties will be similar for other measurements using azimuthal correlations of
 1550 hadrons in jets. One important example is the measurement of “Collins-like” asymmetries to
 1551 access the distribution of linearly polarized gluons. As described earlier, the best kinematic
 1552 region to access this distribution is at backward angles with respect to the polarized proton
 1553 and at small jet p_T . Figure 49 shows that a high precision measurement of the distribution

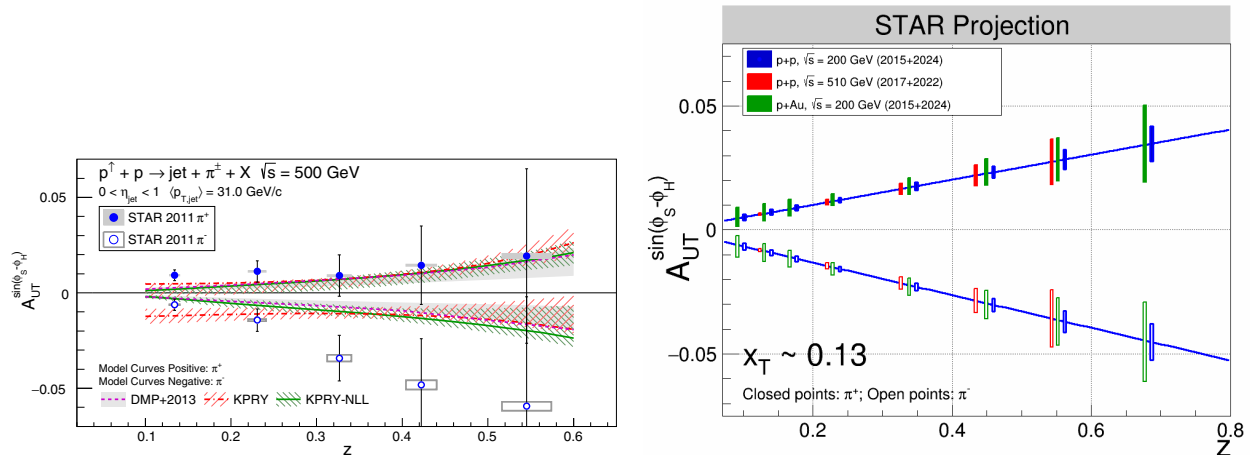


Figure 51: The left panel shows STAR measurements of the Collins asymmetry vs. pion z in 500 GeV pp collisions from Run-11, compared to several model calculations. See [166] for details. The right panel shows projected statistical uncertainties for STAR Collins asymmetry measurements at $0 < \eta < 0.9$ in pp at $\sqrt{s} = 200$ and 510 GeV and p -Au at $\sqrt{s_{NN}} = 200$ GeV. The points have arbitrarily been drawn on the solid lines, which represent simple linear fits to the STAR preliminary 200 GeV pp Collins asymmetry measurements from 2015. (Note that only one bin is shown spanning $0.1 < z < 0.2$ for 510 GeV pp whereas three bins are shown covering the same z range for the 200 GeV measurements).

1554 of linearly polarized gluons down to $x \sim 0.005$ will be performed concurrently.

1555 It is also important to recognize that these hadron-in-jet measurements with the STAR
 1556 Forward Upgrade will provide very valuable experience detecting jets close to beam rapidity
 1557 that will inform the planning for future jet measurements in similar kinematics at the EIC.

1558 While the STAR Forward Upgrade will provide sensitivity to transversity to the high-
 1559 est x , concurrent mid-rapidity measurements (see Fig. 48) will provide the most precise
 1560 information as a function of x , z , j_T , and Q^2 to probe questions of TMD factorization, uni-
 1561 versality, and evolution. The left panel of Fig. 51 shows published STAR measurements of
 1562 the Collins asymmetry vs. pion z in 500 GeV Run-11 pp collisions [166]. The results, which
 1563 represented the first ever observation of the Collins effect in pp collisions, are consistent at
 1564 the 2σ level with model predictions, with and without TMD evolution, derived from fits to
 1565 e^+e^- and SIDIS data [117, 170]. However, greater precision is clearly necessary for a detailed
 1566 universality test, as well as to set the stage for the EIC.

1567 STAR Run-17 sampled about 14 times the luminosity that we recorded in Run-11. In
 1568 Run-22, we propose to record another data set equivalent to 16 times the sampled luminos-
 1569 ity from Run-11. Furthermore, during Run-22 the iTPC will improve the dE/dx particle
 1570 identification compared to the previous years. Studies using the dE/dx distributions seen in
 1571 our 200 GeV pp data from Run-15 and the actual dE/dx resolution improvements that have
 1572 been achieved during BES-II indicate the iTPC will yield a 20 – 25% increase in the effective
 1573 figure-of-merit for pions with $|\eta| < 0.9$. The right-hand panel of Fig. 51 shows the projected
 1574 STAR statistical uncertainties for the Collins asymmetry at $0 < \eta < 0.9$ in 510 GeV pp

1575 collisions once the Run-17 and Run-22 data sets are fully analyzed. It's also important to
 1576 recognize that the iTPC will also enable STAR to measure the Collins asymmetry over the
 1577 region $0.9 < \eta < 1.3$ during Run-22, in addition to the projections that are shown in Fig. 51.

1578 The statistical precision of transversity measured in 510 GeV pp collisions using IFF asym-
 1579 metries are expected to be comparable to the statistical improvements from Run-11 [158] to
 1580 Run-17 + Run-22 shown for the Collins effect data in Fig. 51.

1581 2.1.4 Probing Unpolarized Distributions in the Proton

1582 STAR can also provide important information related to unpolarized quark distributions
 1583 and constrain unpolarized TMD PDFs by measuring the spin integrated W and Z cross
 1584 sections. As discussed in Sec. 1.3, the W^+/W^- cross-section ratio is sensitive to the \bar{d}/\bar{u}
 1585 quark distribution, providing complimentary information to Drell-Yan experiments [124,125].
 1586 Recent results from STAR [123] have been shown to not only have an impact on constraining
 1587 the \bar{d}/\bar{u} quark distribution, but other quark distributions as well [171]. Figure 52 shows the
 1588 uncertainty on PDF distributions where STAR data was included in the global analysis
 1589 relative to the uncertainties where it was not. This global analysis shows about 30% relative
 1590 uncertainty reduction in the region $0.2 < x < 0.3$. An additional 16 weeks of running during
 1591 Run-22 would yield similar statistics as was achieved in Run-17. Combining our already
 1592 measured datasets with what would be collected during Run-22 would provide a precision
 1593 measurement of W^+/W^- consisting of about 1000 pb^{-1} . Furthermore, STAR's Z differential
 1594 cross section as a function of the boson p_T can serve as input to constrain unpolarized TMD
 1595 PDFs. Figure 53 shows preliminary results for the Run-11, 12, 13, and 17 combined datasets.

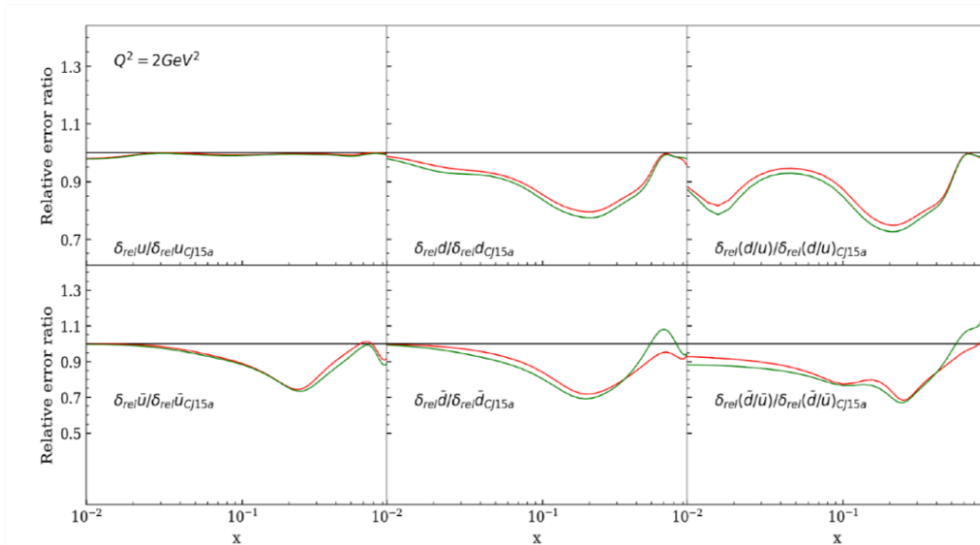


Figure 52: CJ collaboration global analysis comparing the uncertainties on unpolarized PDF distributions where STAR data was included in the analysis relative to the uncertainties where it was not [171].

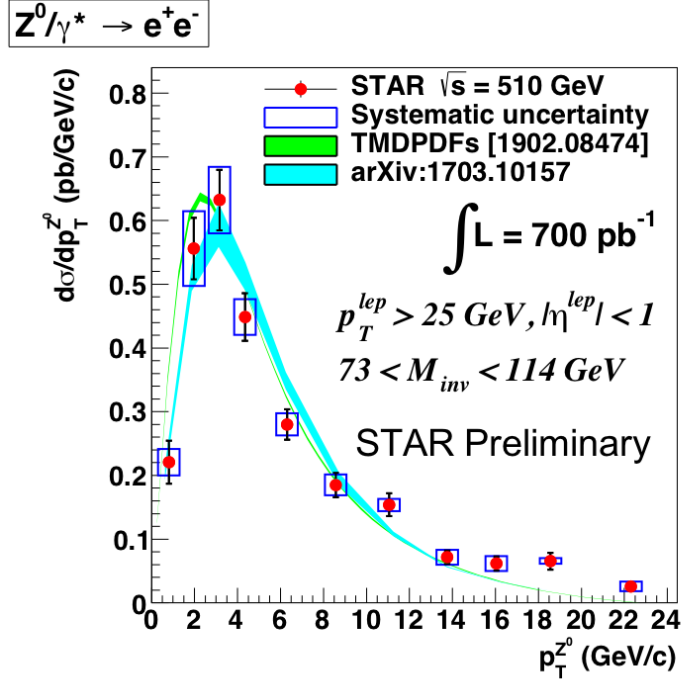


Figure 53: Z differential cross section as a function of boson p_T for combined Run-11,12, 13, and 17 datasets.

1596 2.1.5 Spatial Imaging of the Nucleon

1597 Diffractive and Ultra Peripheral processes at RHIC are an essential tool that can elucidate
 1598 the origin of single-spin asymmetries in polarized pp collisions and access the orbital motion
 1599 of partons inside the proton. Also at the EIC diffractive processes have been identified as
 1600 the golden tool to study several key physics programs

- 1601 • What is the spatial distribution of quarks and gluons inside the nucleon?
- 1602 • What is the role of orbital motion of sea quarks and gluons in building the nucleon
 1603 spin?
- 1604 • Saturation in nuclei.

1605 **Diffractive:** The essential characteristics of diffraction in QCD are summarized by two
 1606 facts:

- 1607 • The event is still called diffractive if there is a rapidity gap. Due to the presence
 1608 of a rapidity gap, the diffractive cross-section can be thought of as arising from an
 1609 exchange of several partons with zero net color between the target and the projectile.
 1610 In high-energy scattering, which is dominated by gluons, this color neutral exchange
 1611 (at the lowest order) consists of at least two exchanged gluons. This color singlet

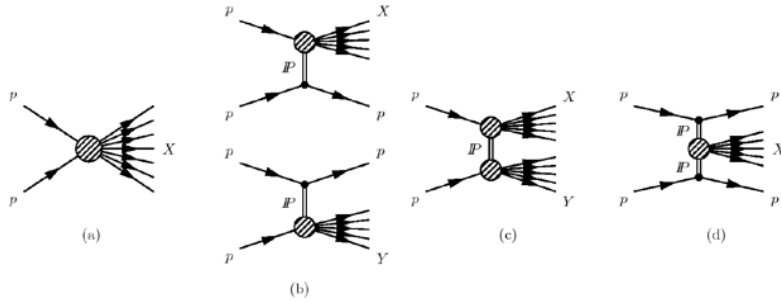


Figure 54: Schematic diagrams of (a) nondiffractive, $pp \rightarrow X$, (b) singly diffractive, $pp \rightarrow Xp$ or $pp \rightarrow pY$, (c) doubly diffractive, $pp \rightarrow XY$, and (d) centrally diffracted, $pp \rightarrow pXp$, events.

1612 exchange has historically been called the pomeron, which had a specific interpretation
 1613 in Regge theory. A crucial question in diffraction is the nature of the color neutral
 1614 exchange between the protons. This interaction probes, in a novel fashion, the nature
 1615 of confining interactions within hadrons.

- 1616 • The proton/nuclear target is not always an opaque “black disk” obstacle of geometric
 1617 optics. A projectile that interacts more weakly due to color-screening and asymptotic
 1618 freedom is likely to produce a different diffractive pattern from a larger, more strongly
 1619 interacting, projectile.

1620 HERA discovered that 15% of the total ep cross-section is given by diffractive events
 1621 (for details see [172] and references therein), basically independent of kinematics. At RHIC
 1622 center-of-mass energies diffractive scattering events constitute $\sim 25\%$ of the total inelastic
 1623 pp cross-section [173]. As described above diffraction is defined as an interaction that is
 1624 mediated by the exchange of the quantum numbers of the vacuum, as shown in Fig. 54.
 1625 Experimentally these events can be characterized by the detection of a very forward scattered
 1626 proton and jet (singly diffractive) or two jets (doubly diffractive) separated by a large rapidity
 1627 gap. Central diffraction, where two protons, separated by rapidity gaps, are reconstructed
 1628 along with a jet at mid-rapidity, is also present, but suppressed compared to singly and
 1629 doubly diffractive events. To date, there have been no data in pp collisions studying spin
 1630 effects in diffractive events at high \sqrt{s} apart from measuring single spin asymmetries in
 1631 elastic pp scattering [174–177].

1632 A discovery of large transverse single spin asymmetries in diffractive processes would
 1633 open a new avenue to study the properties and understand the nature of the diffractive
 1634 exchange in pp collisions. One of the primary observables of STAR to access transverse spin
 1635 phenomena has been forward neutral pion production in transversely polarized pp collisions
 1636 at both $\sqrt{s} = 200$ and 500 GeV. Figure 31 shows the isolated and non-isolated transverse
 1637 single spin asymmetries A_N for π^0 detected in the STAR FMS at $2.5 < \eta < 4.0$ as a function
 1638 of x_F , where the neutral pion A_N is larger for isolated pion than when it is accompanied by
 1639 additional nearby photons [115]. A similar observation was seen in STAR’s 200 GeV $p+A$
 1640 results [114].

1641 All these observations might indicate that the underlying subprocess causing a significant
 1642 fraction of the large transverse single spin asymmetries in the forward direction are not of
 1643 $2 \rightarrow 2$ parton scattering processes but of diffractive nature. PYTHIA-8 [178] was used

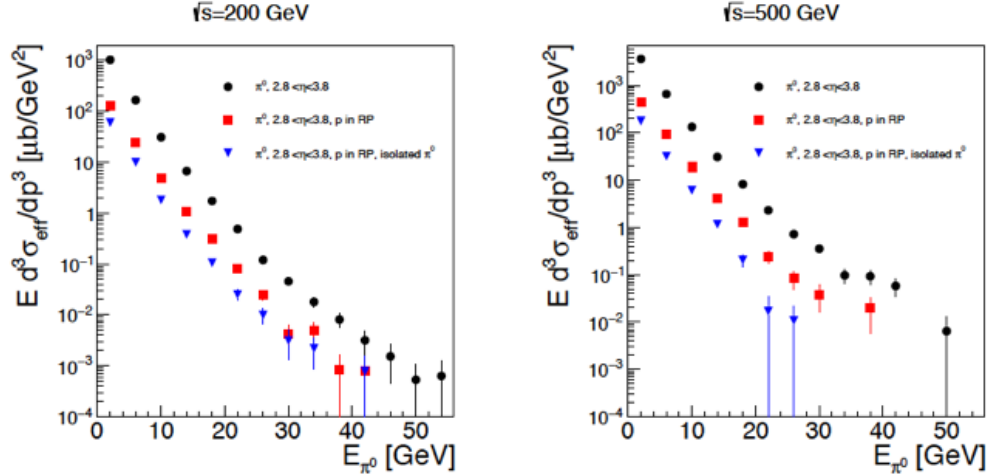


Figure 55: Estimate of the cross-section for hard diffractive processes at $\sqrt{s} = 200$ GeV and 500 GeV using PYTHIA 8. The different points reflect different analysis cuts applied: π^0 in rapidity $2.8 < \eta < 3.8$ (black), one proton is required to be detected in the STAR Roman Pot acceptance (red) and an isolation cut of 35 mrad around the π^0 (blue).

1644 to evaluate the fraction of hard diffractive events [179] contributing to the inclusive π^0
 1645 cross-section at forward rapidities. Figure 55 shows the hard diffractive cross-section for
 1646 π^0 production at $\sqrt{s} = 200$ GeV and 500 GeV for a rapidity range of $2.5 < \eta < 4.0$ with
 1647 and without applying several experimental cuts, i.e. the proton in the STAR Roman Pot
 1648 acceptance. While the information from Roman Pots will not be available in Run-22, the
 1649 diffractive processes will be studied by requiring the rapidity gaps. The prediction from this
 1650 PYTHIA-8 simulation is that 20% of the total inclusive cross-section at forward rapidities is
 1651 of diffractive nature. This result is in agreement with measurements done over a wide range
 1652 of \sqrt{s} (see Fig. 12 in Ref. [172]).

1653 In 2015 STAR collected data in $\sqrt{s} = 200$ GeV transversely polarized pp collisions,
 1654 where an isolated π^0 is detected in the forward pseudorapidity range along with the forward-
 1655 going proton, which scatters with a near-beam forward pseudorapidity into Roman Pot
 1656 detectors. The sum of the π^0 and the scattered proton energies is consistent with the
 1657 incident proton energy of 100 GeV, indicating that no further particles are produced in this
 1658 direction. Correlations between the π^0 and scattered proton have been presented [180], along
 1659 with single-spin asymmetries which depend on the azimuthal angles of both the pion and
 1660 the proton. This is the first time that spin asymmetries have been explored for this process,
 1661 and a model to explain their azimuthal dependence is needed.

1662 The STAR Forward Upgrade will be a game changer for diffractive measurements at
 1663 RHIC. It will allow the reconstruction of full jets both at $\sqrt{s} = 200$ GeV and 510 GeV.
 1664 Measuring spin asymmetries for diffractive events as function of \sqrt{s} might reveal surprises,
 1665 which will inspire new physics opportunities for EIC, i.e SSA in polarized $e+A$ collisions.

2.2 Run-24 Request for Polarized pp and $p+A$ Collisions at 200 GeV

Run-24, with polarized pp and $p+Au$ collisions at $\sqrt{s_{NN}} = 200$ GeV, will likely be the last RHIC spin/cold QCD run. This run will provide STAR with the unique opportunity to investigate these 200 GeV collision systems with the Forward Upgrade providing full tracking and calorimetry coverage over the region $2.5 < \eta < 4$ and the iTPC providing enhanced particle identification and expanded pseudorapidity coverage at mid-rapidity. These powerful detection capabilities, when combined with substantially increased sampled luminosity compared to Run-15, will enable critical measurements to probe universality and factorization in transverse spin phenomena and nuclear PDFs and fragmentation functions, as well as low- x non-linear gluon dynamics characteristic of the onset of saturation. This will provide unique insights into fundamental QCD questions in the near term, and essential baseline information for precision universality tests when combined with measurements from the EIC in the future.

We therefore request at least 11 weeks of polarized pp data-taking at $\sqrt{s} = 200$ GeV and 11 weeks of polarized $p+Au$ data-taking at $\sqrt{s_{NN}} = 200$ GeV during Run-24. Effectively, we request approximately equal nucleon-nucleon luminosities for pp and $p+Au$ which is essential to optimize several critical measurements that require comparisons of the same observable in (polarized or unpolarized) pp and $p+Au$ collisions described in the following sections.

All of the running will involve vertically polarized protons. Based on recent C-AD guidance, we expect to sample at least 235 pb^{-1} of pp collisions and 1.3 pb^{-1} of $p+Au$ collisions. These totals represent 4.5 times the luminosity that STAR sampled during transversely polarized pp collisions in Run-15 and 3 times the luminosity that STAR sampled during transversely polarized $p+Au$ collisions in Run-15.

2.2.1 Spin Physics with Polarized pp and $p+A$ Collisions at 200 GeV

Section 1.3 described several very mature STAR analyses and recent publications that are based on the transversely polarized pp and $p+Au$ data sets that we recorded during 2015. Run-24 will enable STAR to probe these questions with a far more capable detector and much larger data sets than were available during Run-15, thereby allowing us to set the stage for related future measurements at the EIC. Here we give brief descriptions of several of the opportunities presented by Run-24.

Forward Transverse Spin Asymmetries

Section 1.3.3 presents some results that STAR recently published in a pair of papers discussing forward transverse spin asymmetries in pp , $p+Al$ and $p+Au$ collisions measured with the Forward Meson Spectrometer (FMS). One paper focuses on the dynamics that underlie the large asymmetries that have been seen to date. Figure 31 shows that A_N for forward π^0 production in pp collisions at 200 and 500 GeV is substantially larger when the π^0 is isolated than when it is accompanied by additional nearby photons. The same analysis also shows that A_N for inclusive electromagnetic jets (EM-jets) in 200 and 500 GeV collisions

1705 is substantially larger than that for EM-jets that contain three or more photons and that the
 1706 Collins asymmetry for π^0 in EM-jets is very small. The other paper focuses on the nuclear
 1707 dependence of A_N for π^0 in $\sqrt{s_{NN}} = 200$ GeV collisions. It presents a detailed mapping of
 1708 A_N as functions of x_F and p_T for all three collision systems. Figure 30 shows the observed
 1709 nuclear dependence is very weak. The same analysis shows that isolated *vs.* non-isolated π^0
 1710 behave similarly in p +Al and p +Au collisions as they do in pp collisions.

1711 These two papers provide a wealth of new data to inform the ongoing discussion regard-
 1712 ing the origin of the large inclusive hadron transverse spin asymmetries that have been seen
 1713 in pp collisions at forward rapidity over a very broad range of collision energies. Nonetheless,
 1714 the STAR Forward Upgrade will be a game changer for such investigations. It will enable
 1715 measurements of A_N for $h^{+/-}$, in addition to π^0 . It will enable isolation criteria to be ap-
 1716 plied to the $h^{+/-}$ and π^0 that account for nearby charged, as well as neutral, fragments. It
 1717 will enable full jet asymmetry and Collins effect measurements, again for $h^{+/-}$ in addition
 1718 to π^0 , rather than just EM-jet measurements. It will permit all of these measurements to
 1719 be performed at both 510 GeV, as discussed in Sects. 2.1.1 and 2.1.2, and at 200 GeV. In
 1720 addition, all of these observables can be tagged by forward protons detected in the STAR
 1721 Roman pots or by requiring rapidity gaps to identify the diffractive component of the ob-
 1722 served transverse spin asymmetries. For pp there will be considerable overlap between the
 1723 kinematics at the two energies, but the 510 GeV measurements will access higher p_T , while
 1724 the 200 GeV measurements will access higher x_F . Moreover, at 200 GeV we will also perform
 1725 the full suite of measurements in p +Au to identify any nuclear effects. Figure 38 shows one
 1726 set of predictions for the inclusive $\pi^{+/-}$ A_N in 200 and 500 GeV pp collisions, while Fig. 43
 1727 shows the predictions for the one hadron-in-jet measurement that will help to isolate the
 1728 Sivers effect contribution at 200 GeV.

1729 Sivers Effect

1730

1731 Section 2.1.2 describe the first ever observation of the Sivers effect in dijet production.
 1732 Such measurements are crucial to explore questions regarding factorization of the Sivers func-
 1733 tion in dijet hadroproduction [160–163]. Those results were derived from 200 GeV transverse
 1734 spin data that STAR recorded in Run-12 and Run-15 (total sampled luminosity ~ 75 pb $^{-1}$
 1735 for the two years combined). Nonetheless, the uncertainties remain large, as can be seen in
 1736 Fig. 44. Run-24 data will reduce the uncertainties for $|\eta_3 + \eta_4| < 1$ by a factor of two. The
 1737 increased acceptance from the iTPC will reduce the uncertainties at $|\eta_3 + \eta_4| \approx 2.5$ by a
 1738 much larger factor, while the Forward Upgrade will enable the measurements to be extended
 1739 to even larger values of $|\eta_3 + \eta_4|$. When combined with the 510 GeV data from Run-17 and
 1740 Run-22 (see Sect. 2.1.2), the results will provide a detailed mapping *vs.* x for comparison to
 1741 results for Sivers functions extracted from SIDIS, Drell-Yan, and vector boson production.

1742 Transversity and Related Quantities

1743

1744 As described in Sect. 2.1.3, measurements of the Collins asymmetry and IFF in pp colli-

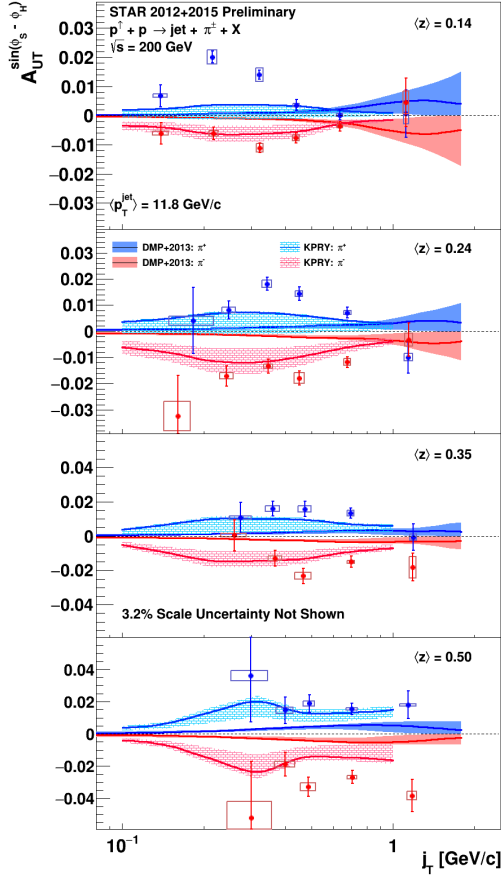


Figure 56: Preliminary Run-12 and Run-15 results for the Collins asymmetry for charged pions in 200 GeV pp collisions as a function of z and j_T , integrated over $9.9 < p_T < 31.6$ GeV/ c and $0 < \eta < 0.9$. Theoretical evaluations from [116] with their uncertainties are presented for π^+ (blue) and π^- (red).

1745 sions at RHIC probe fundamental questions regarding TMD factorization, universality, and
 1746 evolution. Data from 200 GeV pp collisions will play an essential role toward answering these
 1747 questions. Figure 48 shows that 200 GeV pp collisions interpolate between the coverage that
 1748 we will achieve during Run-22 at high- x with the Forward Upgrade and at low- x with the
 1749 STAR mid-rapidity detectors. They will also provide a significant overlapping region of x
 1750 coverage, but at Q^2 values that differ by a factor of 6. This will provide valuable information
 1751 about evolution effects, as well as cross-checks between the two measurements. Furthermore,
 1752 for most of the overlapping x region, 200 GeV pp collisions will also provide the greatest sta-
 1753 tistical precision (see for example Fig. 51), thereby establishing the most precise benchmark
 1754 for future comparisons to ep data from the EIC.

1755 The high statistical precision of the Run-24 data will enable detailed multi-dimensional
 1756 binning for the Collins asymmetry results. This is particularly valuable because, as empha-
 1757 sized in [117, 118], hadron-in-jet measurements in pp collisions provide a direct probe of the
 1758 Collins fragmentation function since they combine it with the *collinear* transversity distri-
 1759 bution. In general, the observed asymmetries are functions of jet (p_T, η), hadron (z, j_T), and
 1760 Q^2 . However, the physics interpretations associated with these variables separate, with p_T
 1761 and η primarily coupling to the incident quark x and the polarization transfer in the hard
 1762 scattering, while z and j_T characterize the fragmentation kinematics. Thus, A_{UT} vs. p_T ,

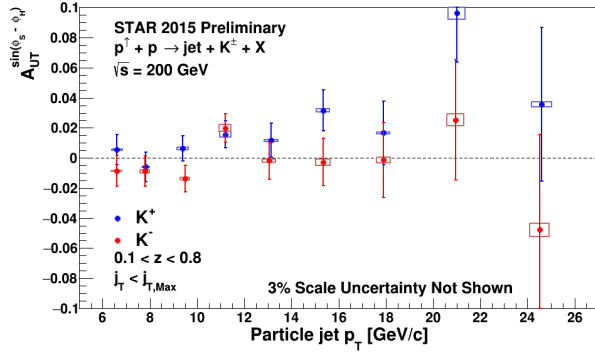


Figure 57: Preliminary Run-15 results for the $K^{+/-}$ Collins asymmetries *vs.* jet p_T for $0 < \eta < 0.9$ in 200 GeV pp collisions.

1763 as shown in Fig. 27 for the preliminary Run-12 and Run-15 analysis, provides information
 1764 about the transversity distribution. In parallel, the (z, j_T) dependence, integrated over a
 1765 wide range of jet p_T , as shown in Fig. 56 for the preliminary Run-12 and Run-15 results,
 1766 provides a detailed look at the Collins fragmentation function. Note that STAR finds the
 1767 maximum value of A_{UT} shift to higher j_T as z increases which is not seen in the current
 1768 theory evaluations [116]. The statistical uncertainties in Figs. 27 and 56 will be reduced by
 1769 a factor of about 2.5 when Run-12, Run-15 and Run-24 data are combined together.

1770 The Run-15 Collins analysis has also, for the first time, measured the Collins effect
 1771 for charged kaons in pp collisions, as shown in Fig. 57. The asymmetries for K^+ , which
 1772 like π^+ have a contribution from favored fragmentation of u quarks, are about 1.5-sigma
 1773 larger than those for π^+ in Fig. 27, while those for K^- , which can only come from unfavored
 1774 fragmentation, are consistent with zero at the 1-sigma level. These trends are similar to those
 1775 found in SIDIS by HERMES [181] and COMPASS [182], and provide additional insight into
 1776 the Collins fragmentation function. This same analysis with Run-24 data will yield statistical
 1777 uncertainties a factor of 3 smaller than those in Fig. 57. This is a much greater improvement
 1778 than would be expected from the increase in sampled luminosity thanks to the improved
 1779 dE/dx resolution provided by the iTPC. In addition, the iTPC will enable the measurements
 1780 in Figs. 27, 56, and 57 to be extended to an additional higher η bin ($0.9 < \eta < 1.3$).

1781 RHIC has the unique opportunity to extend the Collins effect measurements to nuclei.
 1782 This will provide an alternative look at the universality of the Collins effect in hadron-
 1783 production by dramatically increasing the color flow options of the sort that have been
 1784 predicted to break factorization for TMD PDFs like the Sivers effect [160, 161]. This will
 1785 also explore the spin dependence of the hadronization process in cold nuclear matter. STAR
 1786 collected a proof-of-principle data set during the 2015 p +Au run that is currently under
 1787 analysis. Those data will provide a first estimate of medium-induced effects. However, the
 1788 small nuclear effects seen by STAR for forward inclusive π^0 A_N (see Fig. 30) indicate that
 1789 greater precision will likely be needed. Figure 51 shows the projected Run-15 and Run-24
 1790 statistical uncertainties for the p +Au Collins asymmetry measurement at $\sqrt{s_{NN}} = 200$ GeV,
 1791 compared to those for the pp at the same energy.

1792 Ultra-peripheral Collisions

1793

1794

1795

1796

1797

1798

1799

1800

1801

1802

1803

1804

The formalism of generalized parton distributions (GPDs) provides a theoretical framework which addresses some of the above questions [183–186]. Constraints on GPDs have mainly been provided by exclusive reactions in DIS, e.g. deeply virtual Compton scattering. RHIC, with its unique capability to collide transversely polarized protons at high energies, has the opportunity to measure A_N for exclusive J/Ψ production in ultra-peripheral collisions (UPCs) [187]. In such a UPC process, a photon emitted by the opposing beam particle (p or A) collides with the polarized proton. The measurement is at a fixed $Q^2 \sim M_{J/\psi}^2 \approx 10 \text{ GeV}^2$ and $10^{-4} < x < 10^{-1}$. A nonzero asymmetry would be the first signature of a nonzero GPD E_g for gluons, which is sensitive to spin-orbit correlations and is intimately connected with the orbital angular momentum carried by partons in the nucleon and thus with the proton spin puzzle.

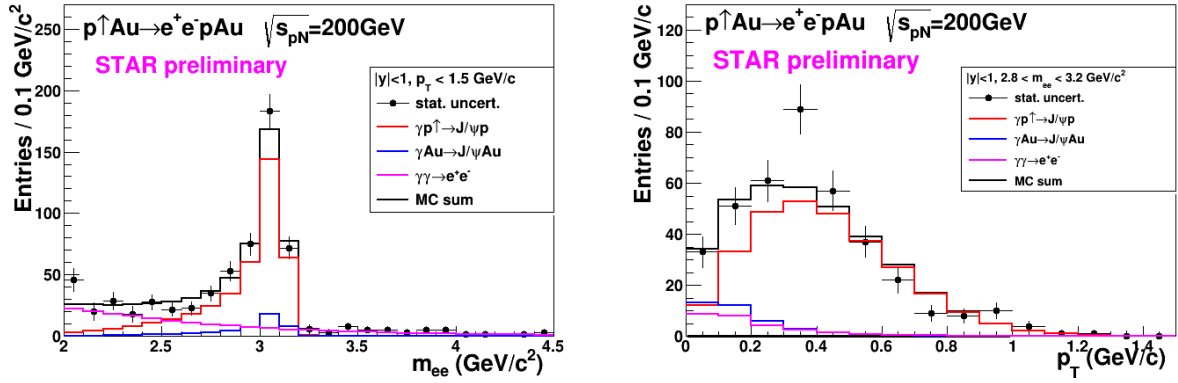


Figure 58: Mass distribution of selected e^+e^- pairs (left), and p_T distribution of the J/ψ mass peak (right). The colored histograms are the indicated processes modelled by STARlight and the sum fit to the data.

1805

1806

1807

1808

1809

1810

1811

1812

1813

1814

1815

The Run-15 p^\uparrow -Au data allowed a proof-of-principle of such a measurement. A trigger requiring back-to-back energy deposits in the Barrel Electromagnetic Calorimeter selected J/Ψ candidates. The e^+e^- mass distribution after selection cuts is shown in the left of Fig. 58, and the pair p_T distribution of the J/ψ mass peak is shown on the right of that figure. The data are well described by the STARlight model [188] (colored histograms in the figure), including the dominant $\gamma+p^\uparrow \rightarrow J/\psi$ signal process and the $\gamma+Au \rightarrow J/\psi$ and $\gamma+\gamma \rightarrow e^+e^-$ background processes. The left of Fig. 59 shows the STAR preliminary measurement (solid circle marker) of the transverse asymmetry A_N^γ for the J/ψ signal, which have a mean photon-proton center-of-mass energy $W_{\gamma p} \approx 24 \text{ GeV}$. The result is consistent with zero. Also shown is a prediction based on a parameterization of E_g [189]; the present data provide no discrimination of this prediction.

1816

1817

1818

This measurement can be greatly improved with a high statistics transversely polarized p^\uparrow -Au Run-24. The integrated luminosity for the Run-15 measurement was 140 nb^{-1} ; the Run-24 will provide 1.3 pb^{-1} , allowing a sizeable reduction of statistical uncertainty in the

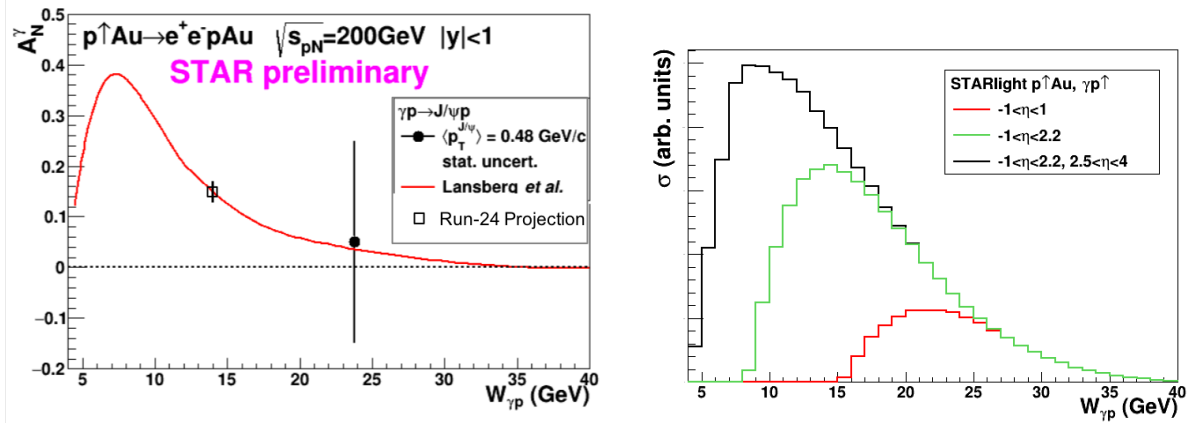


Figure 59: Left: The measured J/ψ transverse asymmetry A_N^γ and a prediction based on a parameterization of E_g . Right: The accepted cross section for $\gamma+p^\dagger \rightarrow J/\psi$ for various detector pseudorapidity η ranges; the black curve shows the result for the full STAR detector with the Forward Upgrade and the iTPC.

1819 same $W_{\gamma p}$ range. However, the Forward Upgrade and iTPC will also provide a significant
 1820 extension of the $W_{\gamma p}$ range of the measurement. The right panel of Fig. 59 shows the
 1821 accepted cross section for $\gamma+p^\dagger \rightarrow J/\psi$ for various detector pseudorapidity ranges. With the
 1822 full detector, the sensitive cross section is a factor of five times the central barrel alone and
 1823 the expected asymmetry is substantially larger. The projected statistical uncertainty on A_N^γ
 1824 as shown in the left of Fig. 59 (open square marker) will be ≈ 0.02 , offering a powerful test of
 1825 a non-vanishing E_g . Also, the accepted region has a lower mean $W_{\gamma p} \approx 14$ GeV. Predictions
 1826 based on E_g parameterizations such as shown in the figure have a larger asymmetry at lower
 1827 $W_{\gamma p}$, with increased possibility of a nonzero result. Alternatively, the increased statistics
 1828 will allow a measurement of A_N^γ in bins of $W_{\gamma p}$.

1829 The UPC cross section scales with Z^2 of the the nucleus emitting the photon; for protons
 1830 this is $1/79^2$ relative to Au nuclei, which makes analogous measurements in pp collisions
 1831 extremely luminosity-hungry. Therefore, the p +Au run is important for this measurement.

1832 2.2.2 Physics Opportunities with Unpolarized proton-Nucleus Collisions

1833 Our quest to understand QCD processes in Cold Nuclear Matter (CNM) centers on the
 1834 following fundamental questions:

- 1835 • Can we experimentally find evidence of a novel universal regime of non-linear QCD
 1836 dynamics in nuclei?
- 1837 • What is the role of saturated strong gluon fields, and what are the degrees of freedom
 1838 in this high gluon density regime?
- 1839 • What is the fundamental quark-gluon structure of light and heavy nuclei?

- Can a nucleus, serving as a color filter, provide novel insight into the propagation, attenuation and hadronization of colored quarks and gluons?

Various aspects of these questions have been addressed by numerous experiments and facilities around the world, most of them at significantly lower center-of-mass energies and kinematic reach than RHIC. Deep inelastic scattering on nuclei addresses some of these questions with results from, for instance, HERMES at DESY [190–192], CLAS at JLab [193], and in the future from the JLab 12 GeV. This program is complemented by hadron-nucleus reactions in fixed target $p+A$ at Fermilab (E772, E886, and E906) [194] and at the CERN-SPS.

In the following we propose a measurement program unique to RHIC to constrain the initial state effects in strong interactions in the nuclear environment. We also highlight the complementarity to the LHC p -Pb program and stress why RHIC data are essential and unique in the quest to further our understanding of nuclei. The uniqueness of the RHIC program is based on the flexibility of the RHIC accelerator to run collisions of different particle species at very different center-of-mass energies. This in combination with the enhanced STAR detector capabilities in Run-24 allows to disentangle nuclear effects in the initial and final state as well as leading twist shadowing from saturation effects in a kinematic regime where all these effects are predicted to be large. Most of the discussed measurements critically rely on the Forward Upgrade.

The Initial State of Nuclear Collisions

Nuclear parton distribution functions: A main emphasis of the Run-15 and later $p+A$ runs is to determine the initial conditions of the heavy ion nucleus before the collision to support the theoretical understanding of the A-A program both at RHIC and the LHC. In the following, the current status of nPDFs will be discussed, including where the unique contributions of RHIC lie, in comparison to the LHC and the future EIC.

Our current understanding of nuclear parton distribution functions (nPDFs) is still very limited, in particular, when compared with the rather precise knowledge of PDFs for free protons collected over the past 30 years. Figure 60 shows an extraction of nPDFs from available data, along with estimates of uncertainties. All results are shown in terms of the nuclear modification ratios, i.e., scaled by the respective PDF of the free proton. The yellow bands indicate regions in x where the fits are not constrained by data [195] and merely reflect the freedom in the functional form *assumed* in the different fits. Clearly, high precision data at small x and for various different values of Q^2 are urgently needed to better constrain the magnitude of suppression in the x region where non-linear effects in the scale evolution are expected. In addition, such data are needed for several different nuclei, as the A-dependence of nPDFs cannot be predicted from first principles in pQCD and, again, currently relies on assumptions. Note that the difference between DSSZ [196] and EPS09 for the gluon modification arise from the different treatment of the PHENIX midrapidity $\pi^0 R_{dAu}$ data [197], which in the EPS09 [198] fit are included with an extra weight of 20. The

1880 $\pi^0 R_{dAu}$ data are the only data, which can probe the gluon in the nucleus directly, but these
 1881 data also suffer from unknown nuclear effects in the final state (see [199]). Therefore, it is
 1882 absolutely critical to have high precision data only sensitive to nuclear modification in the
 1883 initial state over a wide range in x and intermediate values of Q^2 (away from the saturation
 1884 regime) to establish the nuclear modification of gluons in this kinematic range.

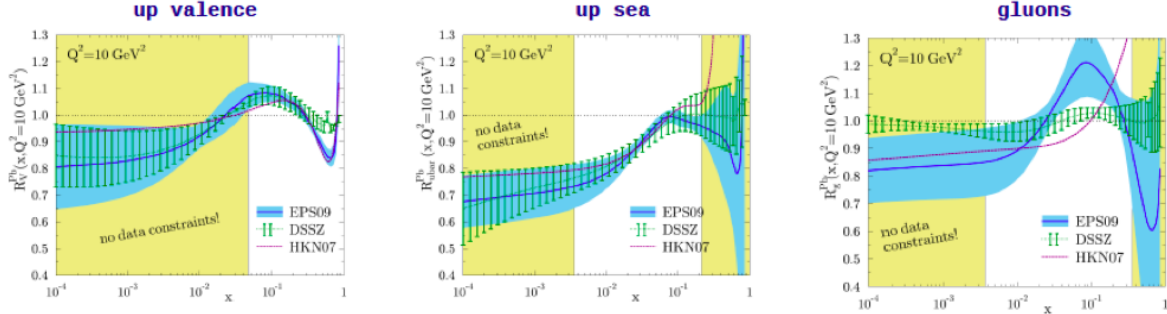


Figure 60: Summary of the most recent sets of nPDFs. The central values and their uncertainty estimates are given for the up valence quark, up sea quark, and the gluon. The yellow bands indicate regions in x where the fits are not constrained by any data (taken from Ref. [195]).

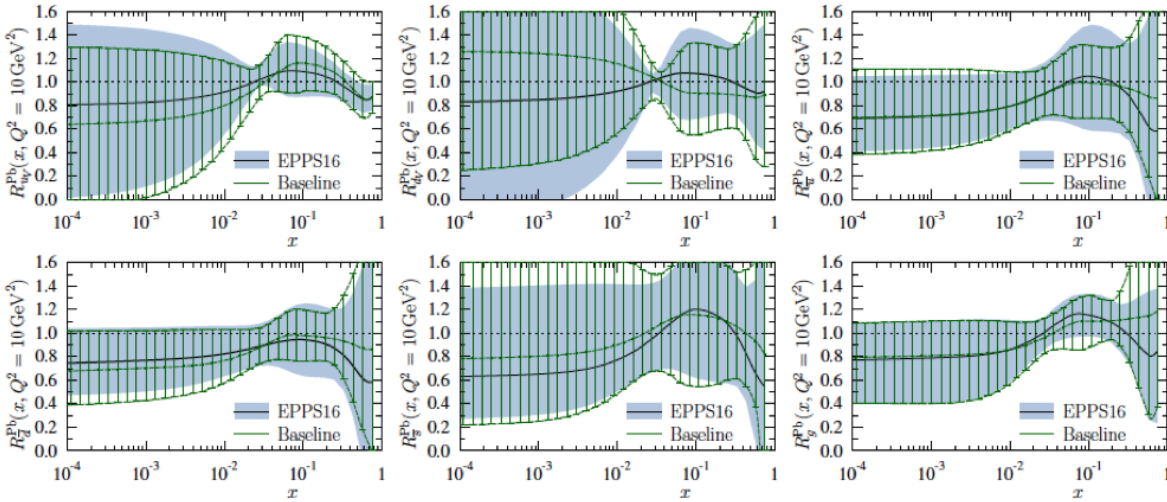


Figure 61: The nuclear modifications at $Q^2 = 10 \text{ GeV}^2$ from the EPPS-16 fit (black central line and light-blue bands) compared with the Baseline fit (green curves with hatching) which uses only the data included in the EPS09 fit.

1885 It is important to realize that the measurements from RHIC are compelling and essential
 1886 even when compared to what can be achieved in p -Pb collisions at the LHC. Due to the
 1887 higher center-of-mass system energy most of the LHC data have very high Q^2 , where the
 1888 nuclear effects are already reduced significantly by evolution and are therefore very difficult
 1889 to constrain. Two recent articles [200, 201] assessed the impact of the available LHC Run-
 1890 I p +Pb data on determinations of nPDFs. The rather moderate impact of these data is

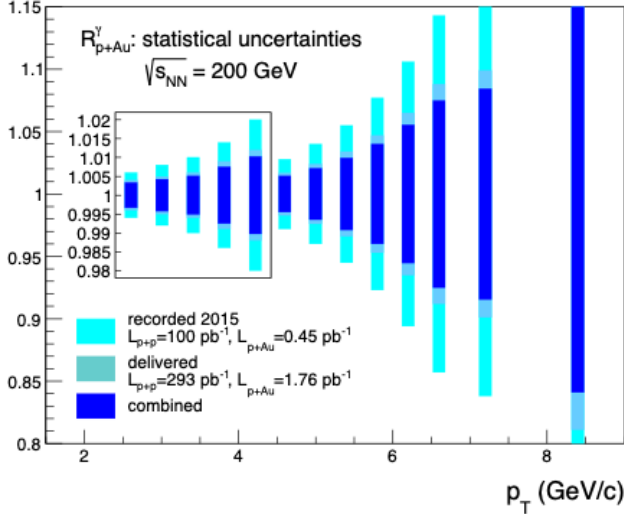


Figure 62: Projected statistical uncertainties for R_{pA} for direct photons in Run-15 (light blue) and Run-24 (blue) and the sum of both (dark blue). The recorded luminosity for Run-15 was $L_{pAu} = 450 \text{ nb}^{-1}$ and $L_{pp} = 100 \text{ pb}^{-1}$. The delivered luminosity for Run-24 is assumed to be $L_{pAu} = 1.8 \text{ pb}^{-1}$ and $L_{pp} = 300 \text{ pb}^{-1}$.

1891 illustrated in Fig. 61. Note that the extra weight factor of 20 for the PHENIX midrapidity
 1892 $\pi^0 R_{dAu}$ data [197] in the original EPS09 [198] fit was removed in all of the new fits, leading
 1893 to a much smaller nuclear modification factor for gluons, especially at medium to high x .

1894 RHIC has the *unique* capability to provide data in a kinematic regime (moderate Q^2 and
 1895 medium-to-low x) where the nuclear modification of the sea quark and the gluon is expected
 1896 to be sizable and currently completely unconstrained. In addition, and unlike the LHC,
 1897 RHIC has the potential to vary the nucleus in $p+A$ collisions and as such also constrain the
 1898 A -dependence of nPDFs.

1899 Extraction of this information is less ambiguous if one uses processes in which strong
 1900 (QCD) final-state interactions can be neglected or reduced. Such golden channels would
 1901 include: a measurement of R_{pA} for Drell-Yan production at forward pseudo-rapidities with
 1902 respect to the proton direction ($2.5 < \eta < 4$) to constrain the nuclear modifications of sea-
 1903 quarks; and of R_{pA} for direct photon production in the same kinematic regime to constrain
 1904 the nuclear gluon distribution. Data for the first measurement of R_{pA} for direct photon
 1905 production have already been taken during the $p+Au$ and $p+Al$ Run-15, with recorded
 1906 luminosities by STAR of $L_{pAu} = 0.45 \text{ pb}^{-1}$ and $L_{pAl} = 1 \text{ pb}^{-1}$, respectively. The anticipated
 1907 statistical precision for $p+Au$ runs in Run-15 and projections for the Run-24 are shown
 1908 in Fig. 62. The Forward Upgrade with its tracking at forward rapidities will also provide
 1909 the possibility to measure R_{pA} for positive and negatively charged hadrons. Approximately
 1910 equal nucleon-nucleon luminosities for pp and $p+Au$ are important for the optimization of
 1911 R_{pA} measurements as they directly compare the same observable—yields—in both collision
 1912 systems.

1913 Figure 63 (left) shows the significant impact of the Run-15 and Run-24 R_{pA} for direct
 1914 photon production on the corresponding theoretical expectations and their uncertainties
 1915 obtained with the EPPS-16 set of nPDFs. The uncertainty bands are obtained through a
 1916 re-weighting procedure [202] by using the projected data shown in Fig. 62 and randomizing
 1917 them according to their expected statistical uncertainties around the central values obtained

1918 with the current set of EPPS-16 nPDFs. Figure 63 (right) shows how these measurements
 1919 will help significantly in further constraining the nuclear gluon distribution in a broad range
 1920 of x that is roughly correlated with accessible transverse momenta of the photon, i.e., few
 1921 times $10^{-3} < x < \text{few times } 10^{-2}$. The relevant scale Q^2 is set by $\sim p_T^2$ and ranges from 6
 1922 GeV^2 to about 40 GeV^2 . Like all other inclusive probes in pp and $p+A$ collisions, e.g., jets,
 1923 no access to the exact parton kinematics can be provided event-by-event but global QCD
 1924 analyses easily account for that. After the $p+Au$ Run-24, the statistical precision of the
 1925 prompt photon data will be sufficient to contribute to a stringent test of the universality
 1926 of nuclear PDFs when combined with the expected data from the EIC (see Figure 2.22 and
 1927 2.23 in Ref [203]).

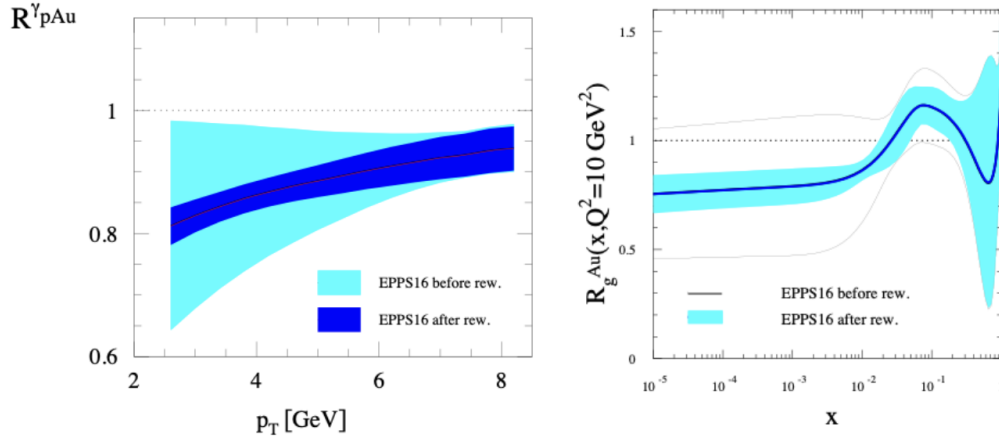


Figure 63: (left) The impact of the direct photon R_{pA} data measured in Run-15 (blue band) and for the anticipated statistics for the future $p+Au$ Run-24 (dark blue band) compared with the current uncertainties (cyan band) from EPPS-16. (right) The impact of the direct photon R_{pA} data measured in Run-15 and for the anticipated statistics for the future Run-24 $p+Au$ run on EPPS-16. The impact is shown on the nuclear suppression factor R_g of nPDF to the proton PDF, the grey bands represent the uncertainties before including the RHIC pseudo data.

1928 Figure 64 shows the kinematic coverage in $x-Q^2$ of past, present, and future experiments
 1929 capable of constraining nuclear parton distribution functions. The shown experiments pro-
 1930 vide measurements that access the initial state parton kinematics on an event-by event basis
 1931 (in a leading order approximation) while remaining insensitive to any nuclear effects in the
 1932 final state. Some of the LHC experiments cover the same x -range as DY at forward pseudo-
 1933 rapidities at RHIC but at a much higher scale Q^2 , where nuclear modifications are already
 1934 significantly reduced [201, 204, 205]. At intermediate Q^2 , DY at STAR will extend the low- x
 1935 reach by nearly one decade compared to EIC.

1936 The biggest challenge of a DY measurement is to suppress the overwhelming hadronic
 1937 background: the total DY cross-section is about 10^{-5} to 10^{-6} smaller than the corresponding
 1938 hadron production cross-sections. Therefore, the probability of misidentifying a hadron
 1939 track as a lepton has to be suppressed to the order of 0.1% while maintaining reasonable
 1940 electron detection efficiencies. To that end, we have studied the combined electron/hadron

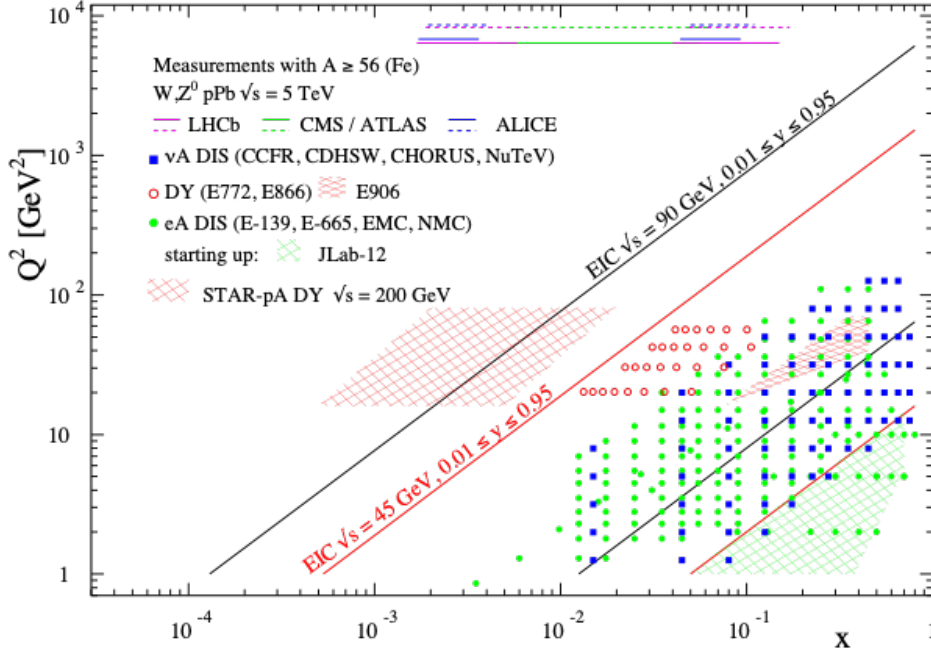


Figure 64: The kinematic coverage in $x - Q^2$ of past, present and future experiments constraining nPDFs with access to the exact parton kinematics event-by-event and no fragmentation in the final state.

1941 discriminating power of the Forward Upgrade. It was found that by applying multivariate
 1942 analysis techniques to the features of EM/hadronic shower development and momentum
 1943 measurements we can achieve hadron rejection powers of 200 to 2000 for hadrons of 15 GeV
 1944 to 50 GeV with 80% electron detection efficiency.

1945 The same procedure as for the direct photon R_{pA} was used to study the potential impact
 1946 of the DY R_{pA} data for the EPPS-19 sets of nPDFs. We expect again a significant impact
 1947 on the uncertainties of R_{pA} DY upon including the projected and properly randomized data.
 1948 Clearly, the DY data from RHIC will be instrumental in reducing present uncertainties in
 1949 nuclear modifications of sea quarks. Again, these data will prove to be essential in testing the
 1950 fundamental universality property of nPDFs in the future when EIC data become available.

1951 STAR's unique detector capabilities will provide the first data on J/Ψ -production in
 1952 ultra-peripheral collisions. This measurement provides access to the spatial gluon distri-
 1953 bution by measuring the t -dependence of $d\sigma/dt$. As follows from the optical analogy, the
 1954 Fourier-transform of the square root of this distribution yields the source distribution of the
 1955 object probed. To study the gluon distribution in the gold nucleus, events need to be tagged
 1956 where the photon is emitted from the proton. For both observables a measurement with
 1957 different nuclei is required to pin down the A-dependence of nPDFs. The J/Ψ -production
 1958 in ultra-peripheral collisions requires significantly more statistics than accumulated to date.

1959 Gluon Saturation

1960

1961 Our understanding of the proton structure and of the nuclear interactions at high energy
 1962 would be advanced significantly with the definitive discovery of the saturation regime [206–
 1963 212]. Saturation physics would provide an infrared cutoff for perturbative calculations,

1964 the saturation scale Q_s , which grows with the atomic number of the nucleus A and with
 1965 decreasing value of x . If Q_s is large it makes the strong coupling constant small, $\alpha_s(Q_s^2) \ll$
 1966 1 allowing for perturbative QCD calculations to be under theoretical control.

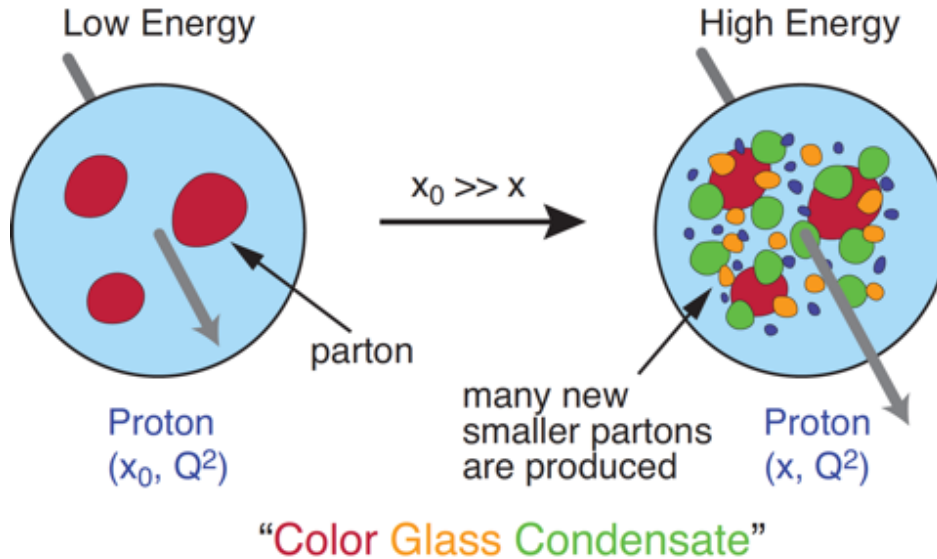


Figure 65: Proton wave function evolution towards small- x .

1967 It is well known that PDFs grow at small- x . If one imagines how such a high number of
 1968 small- x partons would fit in the (almost) unchanged proton radius, one arrives at the picture
 1969 presented in Fig. 65: the gluons and quarks are packed very tightly in the transverse plane.
 1970 The typical distance between the partons decreases as the number of partons increases, and
 1971 can get small at low- x (or for a large nucleus instead of the proton). One can define the
 1972 saturation scale as the inverse of this typical transverse inter-parton distance. Hence Q_s
 1973 indeed grows with A and decreasing x .

1974 The actual calculations in saturation physics start with the classical gluon fields (as gluons
 1975 dominate quarks at small- x) [213–219], which are then evolved using the nonlinear small- x
 1976 BK/JIMWLK evolution equations [220, 221, 221–229]. The saturation region can be well-
 1977 approximated by the following formula: $Q_s^2 \sim (A/x)^{1/3}$. Note again that at small enough
 1978 x the saturation scale provides an IR cutoff, justifying the use of perturbative calculations.
 1979 This is important beyond saturation physics, and may help us better understand small- x
 1980 evolution of the TMDs.

1981 While the evidence in favor of saturation physics has been gleaned from the data col-
 1982 lected at HERA, RHIC and the LHC, the case for saturation is not sealed and alternative
 1983 explanations of these data exist. The EIC is slated to provide more definitive evidence for
 1984 saturation physics [230]. To help the EIC complete the case for saturation, it is mandatory to
 1985 generate higher-precision measurements in p +Au collisions at RHIC. These higher-precision
 1986 measurements would significantly enhance the discovery potential of the EIC as they would
 1987 enable a stringent test of universality of the CGC. We stress again that a lot of theoretical

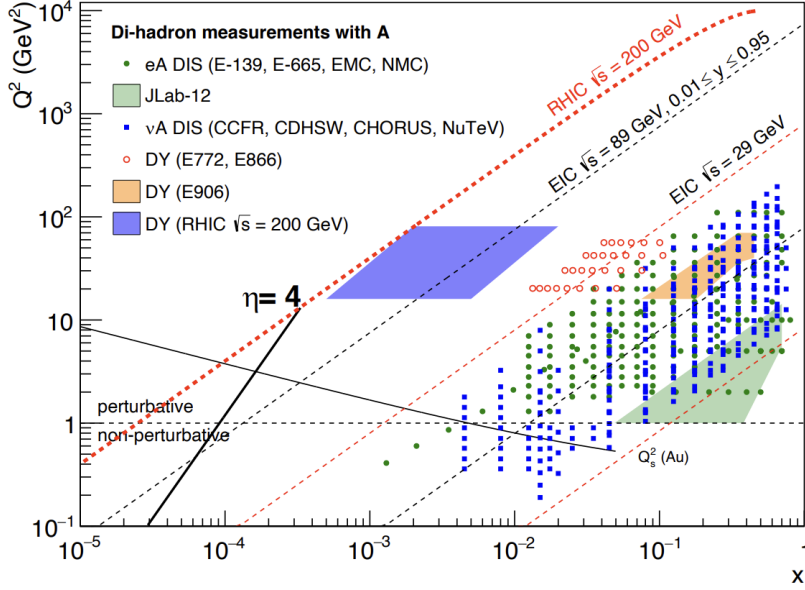


Figure 66: Kinematic coverage in the $x - Q^2$ plane for $p+A$ collisions at RHIC, along with previous $e+A$ measurements, the kinematic reach of an electron-ion collider, and estimates for the saturation scale Q_s in Au nucleus and the line illustrating the range in x and Q^2 covered with hadrons at rapidity $\eta = 4$.

1988 predictions and results in the earlier Sections of this document would greatly benefit from
 1989 saturation physics: the small- x evolution of TMDs in a longitudinally or transversely polarized
 1990 proton, or in an unpolarized proton, can all be derived in the saturation framework [231]
 1991 in a theoretically better-controlled way due to the presence of Q_s . Hence saturation physics
 1992 may help us understand both the quark and gluon helicity PDFs as well as the Sivers and
 1993 Boer-Mulders functions.

1994 The saturation momentum is predicted to grow approximately like a power of energy,
 1995 $Q_s^2 \sim E^{\lambda/2}$ with $\lambda \sim 0.2 - 0.3$, as phase space for small- x (quantum) evolution opens up.
 1996 The saturation scale is also expected to grow in proportion to the valence charge density at
 1997 the onset of small- x quantum evolution. Hence, the saturation scale of a large nucleus should
 1998 exceed that of a nucleon by a factor of $A^{1/3} \sim 5$ (on average over impact parameters). RHIC
 1999 is capable of running $p+A$ collisions for different nuclei to check this dependence on the mass
 2000 number. This avoids potential issues with dividing say p -Pb collisions in N_{part} classes [232].
 2001 Figure 66 shows the kinematic coverage in the $x - Q^2$ plane for $p+A$ collisions at RHIC, along
 2002 with previous $e+A$ measurements and the kinematic reach of an EIC. The saturation scale
 2003 for a Au nucleus is also shown. To access at RHIC a kinematic regime sensitive to saturation
 2004 with $Q^2 > 1$ GeV² requires measurements at forward rapidities. For these kinematics the
 2005 saturation scale is moderate, on the order of a few GeV², so measurements sensitive to the
 2006 saturation scale are by necessity limited to semi-hard processes.

2007 Until today the golden channel at RHIC to observe strong hints of saturation has been
 2008 the angular dependence of two-particle correlations, because it is an essential tool for testing
 2009 the underlying QCD dynamics [232]. In forward-forward correlations facing the $p(d)$ beam
 2010 direction one selects a large- x parton in the $p(d)$ interacting with a low- x parton in the
 2011 nucleus. For $x < 0.01$ the low- x parton will be back-scattered in the direction of the large-
 2012 x parton. Due to the abundance of gluons at small x , the backwards-scattered partons

2013 are dominantly gluons, while the large- x partons from the $p(d)$ are dominantly quarks.
 2014 The measurements of di-hadron correlations by STAR and PHENIX [233, 234], have been
 2015 compared with theoretical expectations using the CGC framework based on a fixed saturation
 2016 scale Q_s and considering valence quarks in the deuteron scattering off low- x gluons in the
 2017 nucleus with impact parameter $b = 0$ [235, 236]. Alternative calculations [237] based on both
 2018 initial and final state multiple scattering, which determine the strength of this transverse
 2019 momentum imbalance, in which the suppression of the cross-section in d+Au collisions arises
 2020 from cold nuclear matter energy loss and coherent power corrections have also been very
 2021 successful to describe the data.

2022 The p +Au Run-15 at RHIC has provided unique opportunities to study this channel in
 2023 more detail at STAR. The high delivered integrated luminosities allow one to vary the trigger
 2024 and associated particle p_T from low to high values and thus crossing the saturation boundary
 2025 as shown in Fig. 66 and reinstate the correlations for central p +A collisions for forward-
 2026 forward π^0 's. Studying di-hadron correlations in p +A collisions instead of d+A collisions has
 2027 a further advantage. In reference [238], the authors point out that the contributions from
 2028 double-parton interactions to the cross-sections for $dA \rightarrow \pi^0\pi^0 X$ are not negligible. They
 2029 find that such contributions become important at large forward rapidities, and especially in
 2030 the case of d+A scattering. Figure 34 shows the results for the di-hadron correlations for π^0
 2031 from the 2015 pp and p +Au run. Shown is the ratio of the area, the width and the level of
 2032 pedestal of the backward peak for p +Au and pp as function of the p_T of the trigger and the
 2033 associated π^0 and the activity in the collision as measured by the BBC.

2034 The results show basically no change in the width of the backward peak and the back-
 2035 ground/pedestal the peak is sitting on shows only up to a 20% increase in p +Au to pp .
 2036 However, the area of the backward peak shows a large suppression with increasing activity
 2037 in the collision. For fixed activity the biggest suppression is observed for the smallest trigger
 2038 p_T in combination with the smallest p_T for the associated π^0 . This behaviour is consistent
 2039 with different calculations based on the CGC formalism. This result is the first clean ob-
 2040 servable, which cannot yet be explained in a different framework than CGC and as such a
 2041 clear hint for non-linear effects.

2042 It is important to note that for the measurements to date in $p(d)$ -A collisions both initial
 2043 and final states interact strongly, leading to severe complications in the theoretical treatment
 2044 (see [240, 241], and references therein). As described in detail in the Section above in p +A
 2045 collisions, these complications can be ameliorated by removing the strong interaction from
 2046 the final state, by using photons and Drell-Yan electrons. The Run-15 p +A run will for the
 2047 first time provide data on R_{pA} for direct photons and therefore allow one to test CGC based
 2048 predictions on this observable as depicted in Fig. 67 (taken from Ref. [239]). The higher
 2049 delivered integrated luminosity for the upcoming p +Au Run-24 together with the Forward
 2050 Upgrade will enable one to study more luminosity hungry processes and/or complementary
 2051 probes to the di- π^0 correlations, i.e. di-hadron correlations for charged hadrons, photon-jet,
 2052 photon-hadron and di-jet correlations, which will allow a rigorous test of the calculation
 2053 in the CGC formalism. It is important to stress that the comparison of these correlation
 2054 probes in pp and p +Au requires approximately equal nucleon-nucleon luminosities for these

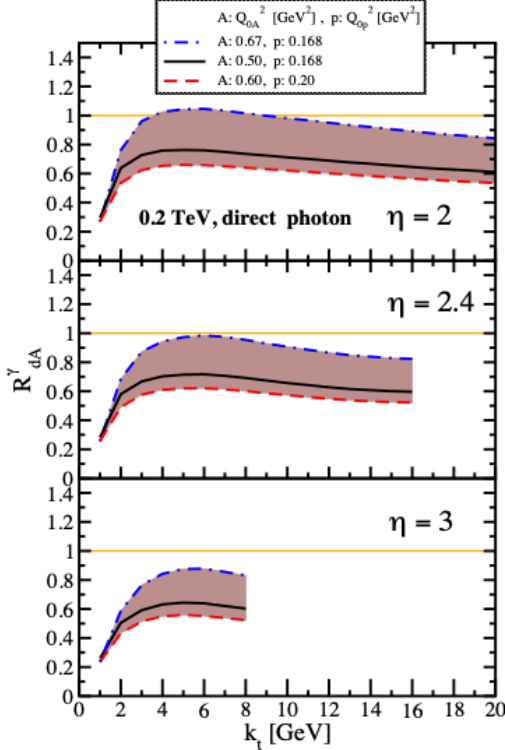


Figure 67: Nuclear modification factor for direct photon production in $p(d)$ - A collisions at various rapidities at RHIC $\sqrt{s} = 200$ GeV. The curves are the results obtained from Eq. (12) in Ref. [239] and the solution to rcBK equation using different initial saturation scales for a proton Q_{op} and a nucleus Q_{oA} . The band shows our theoretical uncertainties arising from allowing a variation of the initial saturation scale of the nucleus in a range consistent with previous studies of DIS structure functions as well as particle production in minimum-bias pp , $p+A$ and A - A collisions in the CGC formalism, see Ref. [239] for details.

2055 two collision systems for optimal measurements. It is noted that these results are crucial for
 2056 the equivalent measurements at an EIC, which are planned at close to identical kinematics,
 2057 because only if non-linear effects are seen with different complementary probes, i.e., ep and
 2058 $p+A$ one can claim a discovery of saturation effects and their universality.

2059 We use direct photon plus jet (direct γ +jet) events as an example channel to indicate what
 2060 can be done in Run-24. These events are dominantly produced through the gluon Compton
 2061 scattering process, $g+q \rightarrow \gamma+q$, and are sensitive to the gluon densities of the nucleon and
 2062 nuclei in pp and $p+A$ collisions. Through measurements of the azimuthal correlations in
 2063 $p+A$ collisions for direct γ +jet production, one can study gluon saturation phenomena at
 2064 small- x . Unlike di-jet production that is governed by both the Weizsäcker-Williams and
 2065 dipole gluon densities, direct γ +jet production only accesses the dipole gluon density, which
 2066 is better understood theoretically [239, 242]. On the other hand, direct γ +jet production
 2067 is experimentally more challenging due to its small cross-section and large background con-
 2068 tribution from di-jet events in which photons from fragmentation or hadron decay could be
 2069 misidentified as direct photons. The feasibility to perform direct γ +jet measurements with
 2070 the Forward Upgrade in unpolarized pp and $p+Au$ collisions at $\sqrt{s_{NN}} = 200$ GeV has been
 2071 studied. PYTHIA-8.189 [243] was used to produce direct γ +jet and di-jet events. In order
 2072 to suppress the di-jet background, the leading photon and jet are required to be balanced
 2073 in transverse momentum, $|\phi^\gamma - \phi^{jet}| > 2\pi/3$ and $0.5 < p_T^\gamma/p_T^{jet} < 2$. Both the photon and
 2074 jet have to be in the forward acceptance $1.3 < \eta < 4.0$ with $p_T > 3.2$ GeV/ c in 200 GeV
 2075 pp collisions. The photon needs to be isolated from other particle activities by requiring the
 2076 fraction of electromagnetic energy deposition in the cone of $\Delta R = 0.1$ around the photon

2077 is more than 95% of that in the cone of $\Delta R = 0.5$. Jets are reconstructed by an anti- k_T
 2078 algorithm with $\Delta R = 0.5$. After applying these selection cuts, the signal-to-background
 2079 ratio is around 3:1 [244]. The expected number of selected direct γ +jet events is around
 2080 1.0M/0.9M at $\sqrt{s_{NN}} = 200$ GeV in p +Au collisions for the proposed Run-24. We conclude
 2081 that a measurement of direct photon-jet correlation from p +Au collisions is feasible, which is
 2082 sensitive to the gluon density in $0.001 < x < 0.005$ in the Au nucleus where parton saturation
 2083 is expected.

2084 The Final State

2085

2086 **Nuclear fragmentation functions:** In spite of the remarkable phenomenological suc-
 2087 cesses of QCD, a quantitative understanding of the hadronization process is still one of the
 2088 great challenges for the theory. Hadronization describes the transition of a quark or gluon
 2089 into a final state hadron. It is a poorly understood process even in elementary collisions.
 2090 RHIC's unique versatility will make it possible to study hadronization in vacuum and in the
 2091 nuclear medium, and additionally with polarized beams (see Sect. 2.2.1 for the latter).

2092 It has long been recognized that the hadron distributions within jets produced in pp
 2093 collisions are closely related to the fragmentation functions that have typically been measured
 2094 in e^+e^- collisions and SIDIS. The key feature of this type of observable is the possibility to
 2095 determine the relevant momentum fraction z experimentally as the ratio of the hadron to
 2096 the jet transverse momentum. Recently [245] a quantitative relationship has been derived in
 2097 a form that enables measurements of identified hadrons in jets in pp collisions to be included
 2098 in fragmentation function fits on an equal footing with e^+e^- and SIDIS data. Furthermore,
 2099 hadrons in pp jets provide unique access to the gluon fragmentation function, which is poorly
 2100 determined in current fits [246], in part due to some tension found in the inclusive high
 2101 p_T pion yields measured by the PHENIX and ALICE collaborations. Here, the proposed
 2102 measurements can provide valuable new insight into the nature of this discrepancy.

2103 This development motivated STAR to initiate a program of identified particle fragmen-
 2104 tation function measurements using pp jet data at 200 and 500 GeV from Run-11, Run-12,
 2105 and Run-15. Figure 68 shows the precision that is anticipated for identified π^+ and π^- in
 2106 200 GeV pp collisions for three representative jet p_T bins after the existing data from Run-12
 2107 and Run-15 are combined with future 200 GeV pp data from Run-24. Identified kaon and
 2108 (anti)proton yields will also be obtained, with somewhat less precision, over a more limited
 2109 range of hadron z . Once the Run-17 data are fully analyzed, the uncertainties for 510 GeV
 2110 pp collisions will be comparable to that shown in Fig. 68 at high jet p_T , and a factor of \sim
 2111 2 larger than shown in Fig. 68 at low jet p_T . Identified hadron yields will also be measured
 2112 multi-dimensionally vs. j_T , z , and jet p_T , which will provide important input for unpolarized
 2113 TMD fits.

2114 Data from the HERMES experiment [190, 192, 247] have shown that production rates
 2115 of identified hadrons in semi-inclusive deep inelastic e -A scattering differ from those in ep
 2116 scattering. These differences cannot be explained by nuclear PDFs, as nuclear effects of

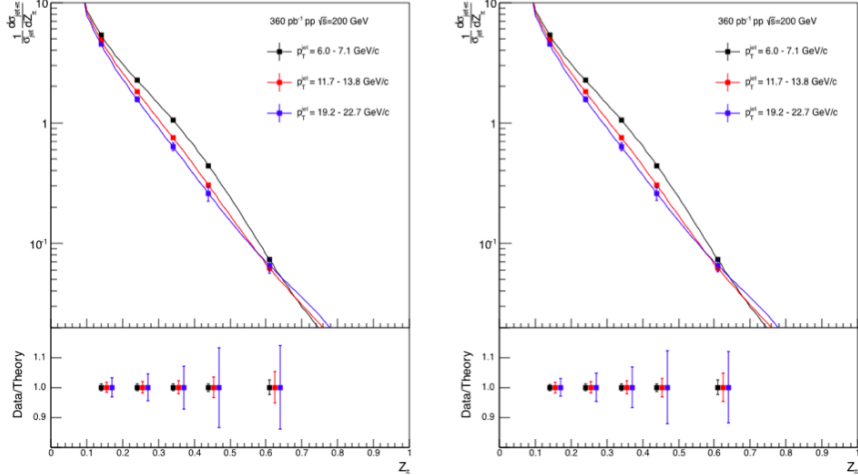


Figure 68: Anticipated precision for identified π^+ (left) and π^- (right) within jets at $|\eta| < 0.4$ in 200 GeV pp collisions for three representative jet p_T bins. The data points are plotted on theoretical predictions based on the DSSV14 pion fragmentation functions [245, 246]. Kaons and (anti)protons will also be measured, over the range from $z < 0.5$ at low jet p_T to $z < 0.2$ at high jet p_T , with uncertainties a factor of ~ 3 larger than those for pions.

2117 strong interactions in the initial state should cancel in this observable. Only the inclusion of
 2118 nuclear effects in the hadronization process allows theory to reproduce all of the dependencies
 2119 (z , x , and Q^2) of R_{eA} seen in SIDIS, as shown in Fig. 69.

2120 It is critical to see if these hadronization effects in cold nuclear matter persist at the higher
 2121 \sqrt{s} and Q^2 accessed at RHIC and EIC – both to probe the underlying mechanism, which is
 2122 not understood currently, and to explore its possible universality. The combination of pp jet
 2123 data from RHIC and future SIDIS data from EIC will also provide a much clearer picture of
 2124 modified gluon hadronization than will be possible with EIC data alone. Using the Run-15
 2125 200 GeV p +Au data, STAR will be able to make a first opportunistic measurement of these
 2126 hadron-jet fragmentation functions in nuclei, but the precision will be limited. Additional pp
 2127 and p +Au data will be needed in Run-24 in order to provide a sensitive test for universality,
 2128 as shown in Fig. 70.

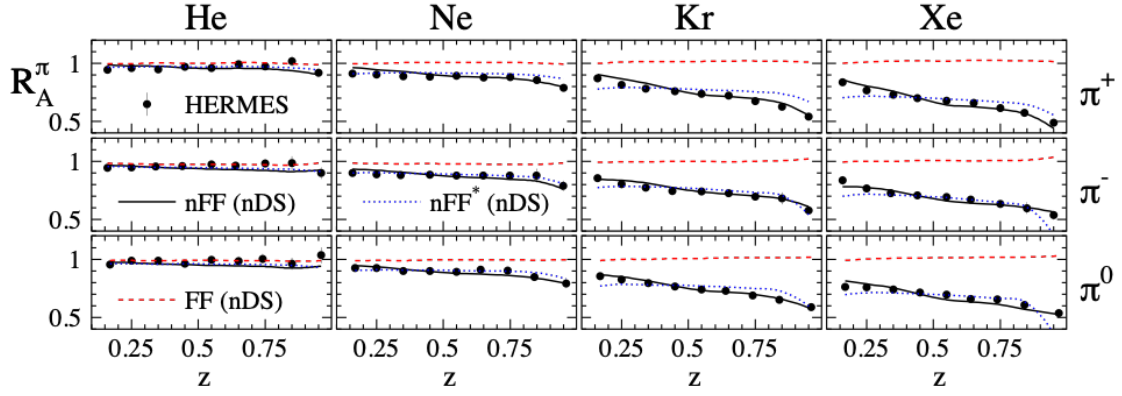


Figure 69: R_{eA} in SIDIS for different nuclei in bins of z as measured by HERMES [190, 192, 247]. The solid lines correspond to the results using effective nuclear FF [199] and the nDS medium modified parton densities [248]. The red dashed lines are estimates assuming the nDS medium modified PDFs but standard DSS vacuum FFs [249, 250] and indicate that nPDFs are insufficient to explain the data

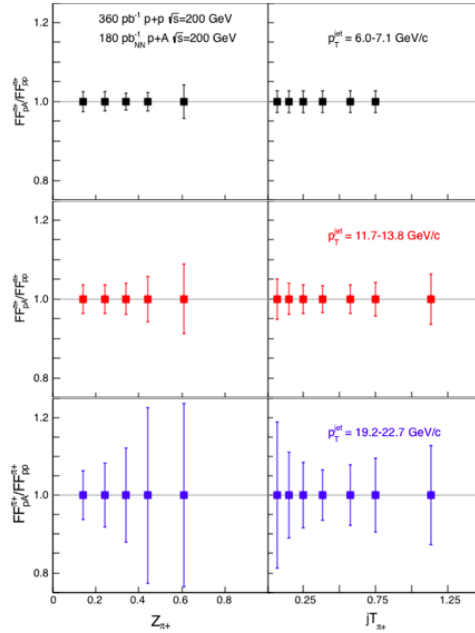


Figure 70: Anticipated precision for measurements of π^+ fragmentation functions in $p+A$ pp at $|\eta| < 0.4$ vs. z and j_T in Run-24 for three representative jet p_T bins. Uncertainties for π^- will be similar to those shown here for π^+ , while those for kaons and (anti)protons will be a factor of ~ 3 larger. Note that, to be species independent, the nucleon-nucleon equivalent luminosity is specified for $p+Au$.

2129 **2.2.3 Novel QGP Droplet Substructure in p+A Collisions**

2130 In addition to cold QCD effects, a high-statistics measurement of p+Au collisions will be
 2131 highly valuable to explore novel fluid configurations that have recently been predicted [251].
 2132 In particular, the data is needed to discover vortex rings or tubes at midrapidity, included
 2133 by shear in the asymmetric initial state.

2134 **Physical Effect and Observable**

2135 It has been suggested [252] that p+A collisions at RHIC form the "smallest QGP droplets."
 2136 This claim is often based on anisotropic yields, which resemble those from A+A collisions
 2137 that are attributed to hydrodynamic collective flow. Indeed, with well-chosen initial condi-
 2138 tions and tuned parameters, three-dimensional viscous hydro calculations can reproduce the
 2139 measured anisotropies from small, asymmetric collisions [138] at RHIC. However, a claim of
 2140 QGP formation in such small systems would be much more compelling if it were based on
 2141 more than one observable, especially since other, non-hydrodynamic mechanisms contribute
 2142 to v_n in these systems, e.g. [17].

2143 As Helmholtz observed more than 150 years ago [253], vortex rings are ubiquitous in
 2144 hydrodynamic systems subject to initial conditions characterized by a "push down the mid-
 2145 dle," such as a smoker blowing a ring. Clear observation of this novel phenomenon would
 2146 constitute important evidence that the smallest systems at RHIC truly do form a fluid sys-
 2147 tem.

2148 This signature probes aspects of particular and fundamental importance to the RHIC
 2149 program, as well. The vortex ring structure is sensitive to the degree and timescale of equi-
 2150 libration in these small systems, as well as the extreme shear fields in the initial state [254].
 2151 Fluctuations in the vortical fields probe hydrodynamic structures at the smallest possible
 2152 scales, as they arise directly from rotational derivatives in the "surface" of the flux tube.

2153 The experimental signature of toroidal vortex structure is the so-called "ring param-
 2154 eter" [251]:

$$\overline{\mathcal{R}}_{\Lambda}^z \equiv \left\langle \frac{\vec{S}'_{\Lambda} \cdot (\hat{z} \times \vec{p}'_{\Lambda})}{|\hat{z} \times \vec{p}'_{\Lambda}|} \right\rangle, \quad (3)$$

2155 where $+\hat{z}$ is the direction of the proton beam, and the average is taken over all particles and
 2156 events. This is the average polarization relative to the hyperon production plane. Rings will
 2157 be most clear for central collisions, but the detailed centrality dependence of the effect is
 2158 currently under investigation [254]. We focus on 0-10% centrality.

2159 Figure 71 shows $\overline{\mathcal{R}}_{\Lambda}^z$ calculated [251] for completely central Au+Au and p+Au collisions at
 2160 $\sqrt{s_{NN}} = 200$ GeV. Calculations were done with MUSIC [255], a three-dimensional relativistic
 2161 viscous hydrodynamics simulation that locally conserves baryon number, and calculation of
 2162 the thermal vorticity along the freezeout hypersurface.

2163 Initial condition (a) corresponds to the usual Bjorken "boost-invariant" flow profile used
 2164 in most A+A simulations, whereas condition (b) features strong shear fields generated in
 2165 the initial condition, leading to observable vortex toroids. Both initial conditions generate
 2166 identical $dN/d\eta$ distributions, but the latter is argued [251] to be more natural.

2167 **Statistics required**

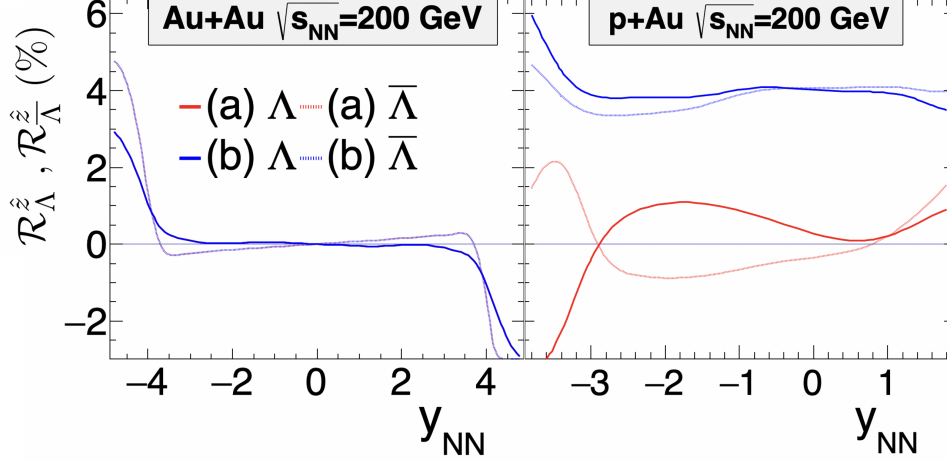


Figure 71: The "ring parameter" $\overline{\mathcal{R}}_{\Lambda}^z$ for $b = 0$ Au+Au and p+Au collisions at top RHIC energy. Blue (red) curves correspond to a scenario in which a toroidal vortex structure is (is not) generated by shear forces in the initial state. Solid (dashed) curves correspond to Λ ($\overline{\Lambda}$; note that baryon current is locally conserved in these collisions, so small differences between Λ and $\overline{\Lambda}$ are expected at finite baryon density. From [251].

2168 The statistical requirement to discover these toroidal vortex structures may be estimated
 2169 by STAR's previous hyperon polarization measurements. The uncertainty on global polar-
 2170 ization measurements $\delta\overline{P}_{\Lambda} \propto N_{\Lambda}^{-1/2} \cdot R_{\text{EP}}^{-1}$, where N_{Λ} is the total number of hyperons in
 2171 the analysis, and R_{EP} is the event plane resolution [103]. Because there is no event plane
 2172 involved in the production plane polarization, on the other hand, the uncertainty on the
 2173 ring observable goes as $\delta\overline{\mathcal{R}}_{\Lambda}^z \propto N_{\Lambda}^{-1/2}$. For the same-magnitude signal, then, $\overline{\mathcal{R}}_{\Lambda}^z$ enjoys an
 2174 effective R_{EP}^{-2} "statistical advantage" over \overline{P}_{Λ} . Since STAR measured [256] $\overline{P}_{\Lambda} \approx 1\%$ at
 2175 $\sqrt{s_{\text{NN}}} = 11$ GeV with 3.5σ significance, with the same number of hyperons in the analysis,
 2176 we should be able to measure $\overline{\mathcal{R}}_{\Lambda}^z \sim 1\%$ with 7σ significance. The 11-GeV analysis involved
 2177 6M Λ s, and we estimate 0.02 Λ s per central (0 – 10%) p+Au collision at $\sqrt{s_{\text{NN}}} = 200$ GeV.
 2178 Therefore, the 7σ measurement will require $6M/0.02 = 300M$ central p+Au collisions.

2179 The need for both field configurations

2180 Also crucial to this measurement is that data must be collected with both polarities
 2181 of STAR's magnetic field. This is because of large and highly nontrivial decay-topology-
 2182 dependent detector effects, which will give a "false" production plane polarization signal.
 2183 The magnitude of the artifact is an order of magnitude larger than the physical signal of
 2184 interest, and it is highly sensitive to momentum, PID, and topological cuts. We could not
 2185 feel confident applying such large and complex "correction factors" based solely on detector
 2186 simulations, if we claim a completely novel signature with far-reaching physical implications.
 2187 Fortunately, the sign of this artifact flips with the magnetic field polarity.

2188 Figure 72 illustrates these points. Au+Au collisions at $\sqrt{s_{\text{NN}}} = 27$ GeV were recorded
 2189 by STAR using opposite polarities of the magnetic field. For Λ s, the quantity $\hat{p}_{\text{p}} \cdot (\hat{p}_{\Lambda} \times \hat{z})$,
 2190 where \hat{p}_{p} is the daughter proton momentum, is proportional to $\overline{\mathcal{R}}_{\Lambda}^z$. For $\overline{\Lambda}$ s, the quantity

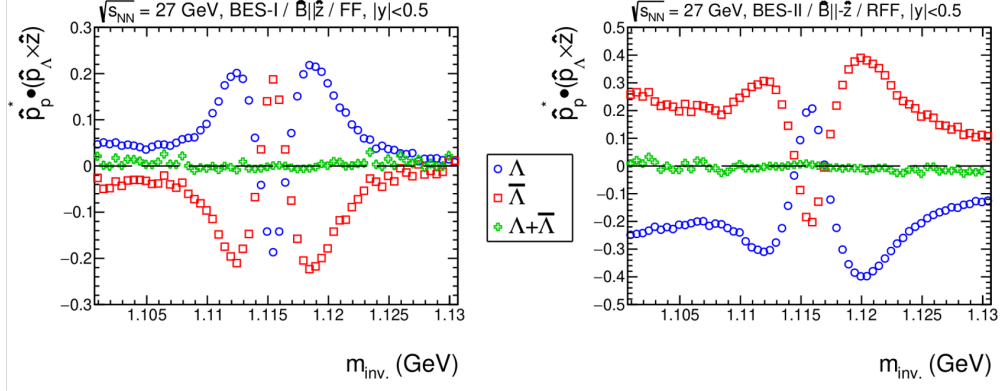


Figure 72: Production-plane polarization (modulo an overall scaling by $\frac{8\pi}{\alpha_\Lambda}$) for Λ (blue) and $\bar{\Lambda}$ (red) candidates, as a function of invariant mass. The data comes from STAR measurements of Au+Au collisions at $\sqrt{s_{NN}}$ in the BES-I (left) and BES-II (right) campaigns. STAR's solenoidal magnetic field was directed to the West and East, respectively, for these two datasets. For the BES-I data, hyperon candidates were identified with "standard" topological cuts, whereas the candidates shown in BES-II were identified using the new KFPARTICLE package.

2191 $\hat{p}_{\bar{p}} \cdot (\hat{p}_{\bar{\Lambda}} \times \hat{z})$, where $\vec{p}_{\bar{p}}$ is the daughter proton momentum, is proportional to $-\overline{\mathcal{R}}_{\bar{\Lambda}}^z$.

2192 A rapidity cut symmetric about midrapidity ($|y| < 0.5$ was used; for a symmetric system,
2193 the physical production plane polarization vanishes by symmetry— any nonvanishing value
2194 results purely from topologically-sensitive efficiency effects.

2195 Consider first the Λ curve from BES-I, the blue points in the left panel. Clearly, the effect
2196 has a nontrivial dependence on invariant mass; note even the asymmetry about $m_{\text{inv}} = m_\Lambda$.
2197 Equally clearly, it is large, corresponding to values $\overline{\mathcal{R}}_{\Lambda}^z = \frac{8}{\pi\alpha_\Lambda} \hat{p}_{\bar{p}} \cdot (\hat{p}_{\Lambda} \times \hat{z}) \approx 50\%$, an order
2198 of magnitude larger than the predicted value of physical effect of interest.

2199 In terms of topologically-sensitive efficiency effects, substituting $\Lambda \rightarrow \bar{\Lambda}$ is equivalent to
2200 flipping the sign of the magnetic field. The red datapoints in the left panel are a perfect
2201 mirror image to the blue points in that panel, as indicated by the vanishing green points,
2202 which are the sum. Further note that naive interpretation of the data in the left panel would
2203 suggest that the vortical ring values for the hyperons and antihyperons ($\overline{\mathcal{R}}_{\Lambda}^z$ and $\overline{\mathcal{R}}_{\bar{\Lambda}}^z$) would
2204 be identical in magnitude and sign.

2205 The right panel shows the same colliding system, but measured during the BES-II cam-
2206 paign with the opposite orientation of STAR's magnetic field. As expected from the above
2207 discussion, $\overline{\mathcal{R}}_{\Lambda}^z = -\overline{\mathcal{R}}_{\bar{\Lambda}}^z$. The shape and magnitude of the artifact is different from the BES-I
2208 case, however, because a different method has been used to identify hyperon candidates.
2209 This illustrates the cut-dependence of the artifact.

2210 In short, for reliable extraction of the ring vorticity measure, STAR must measure p+Au
2211 collisions with both field orientations, in order to cancel the complex efficiency-driven arti-
2212 facts. Finally, we point out that this sort of cancellation is not unique to this observable.
2213 Indeed, there is an analogous effect for the global polarization, which precludes extracting
2214 the *first*-order azimuthal dependence of \overline{P}_Λ ; there, the artifact is of order 100%, compared
2215 to the physical and measured value of $\sim 2\%$ [257].

2216 **Distinction from other effects**

2217 For symmetric collisions (e.g. Au+Au), the quantity $\overline{\mathcal{R}}_\Lambda^z$ must be antisymmetric about
2218 midrapidity. However, at very forward/backward rapidities, circular vorticity has been re-
2219 ported in hydrodynamic [258–262] and transport [15, 263–268]. This effect, also visible in
2220 the left panel in figure 71, arises from strong temperature gradients and edge effects in
2221 three-dimensional space. It is of very different origin than the ring vorticity of interest here.

2222 Finally, production plane polarization at large x_F has been observed (primarily) in p+p
2223 and (in some) p+A collisions [269–274] at energies up to $\sqrt{s_{NN}} = 41$ GeV. This effect,
2224 which is believed to be completely hadronic in origin but remains incompletely understood, is
2225 distinguishable from the hydrodynamically-driven ring vorticity discussed here by its rapidity
2226 dependence, which is strongly forward-focused, as well as the fact that $\overline{\Lambda}$ s do not display
2227 production plane polarization at all. Thus, in addition to double-checking topologically-
2228 dependent efficiency artifacts (discussed above), it is important that STAR will measure
2229 the effect both for hyperons and antihyperons to distinguish hydrodynamic from hadronic
2230 phenomena.

2231 3 Exploring the Microstructure of the QGP (Run-23 and 2232 Run-25 Au+Au)

2233 The completion of RHIC’s scientific mission involves the two central goals of (i) mapping out
2234 the phase diagram of the QCD, and (ii) probing the inner workings of the QGP by resolving
2235 its properties at short length scales [275]. The complementarity of the RHIC and LHC
2236 facilities to study the latter is scientifically as essential as having more than one experiment
2237 independently study the microstructure of the QGP. With several years of operating the
2238 iTPC upgrade and the soon-to-be installation and operation of the forward detectors, the
2239 STAR collaboration will be in an excellent position to take advantage of its vastly improved
2240 detection capabilities. Combine this with the prospect of a substantial increase in beam
2241 luminosities and RHIC will be uniquely positioned to fully engage in a detailed exploration
2242 of the QGP’s microstructure. Through careful discussions in its physics working groups,
2243 the STAR collaboration has identified a number of topics that together make a compelling
2244 case to take data during Runs 23-25 alongside sPHENIX, and successfully complete RHIC’s
2245 scientific mission. In this section, we present a selection of those topics that will take full
2246 advantage of both STAR and RHIC’s unique capabilities and address the following important
2247 questions about the inner workings of the QGP.

- 2248 • What is the precise temperature dependence of the shear η/s , and bulk ζ/s viscosity?
- 2249 • What is the nature of the 3-dimensional initial state at RHIC energies? How does
2250 a twist of the event shape break longitudinal boost invariance and decorrelate the
2251 direction of an event plane?
- 2252 • How is global vorticity transferred to the spin angular momentum of particles on such
2253 short time scales? And, how can the global polarization of hyperons be reconciled with
2254 the spin alignment of vector mesons?
- 2255 • What is the precise nature of the transition near $\mu_B = 0$, and where does the sign-
2256 change of the susceptibility ratio χ_6^B/χ_2^B take place?
- 2257 • What is the electrical conductivity, and what are the chiral properties of the medium?
- 2258 • What can we learn about confinement and thermalization in a QGP from charmonium
2259 measurements?
- 2260 • What are the underlying mechanisms of jet quenching at RHIC energies? What do jet
2261 probes tell us about the microscopic structure of the QGP as a function of resolution
2262 scale?

2263 The event statistics projections that are used in this section will rely on the CAD’s
2264 recently update 2023E and 2025E Au+Au luminosities [276] and are listed in Table 9. For
2265 each year we presume 24 weeks of RHIC operations, and based on past run operations
2266 an overall average of $85\% \times 60\%$ (STAR×RHIC) uptime, respectively. The minimum-bias

2267 rates assume a conservative 1.5 kHz DAQ rates which will allow sufficient bandwidth for
 2268 specialized triggers which are listed as integral luminosities. In order to achieve the projected
 2269 luminosities, the collaboration will look into optimizing the interaction rates at STAR by
 2270 allocating low and high luminosity periods within fills. Such periods, in which low interaction
 2271 rates are sampled in the early part of a fill and high interaction rates typically in the later
 2272 part, will allow us to collect clean, low pile-up, minimum bias events, while at the same
 2273 time not burn beam luminosities that could affect interaction rates for sPHENIX. Clean
 2274 minimum bias events will improve tracking efficiencies which in turn are expected to benefit
 2275 many of the proposed correlation analyses. Optimization of the available bandwidth for
 2276 high- p_T triggers would allow us to push for lower p_T thresholds, thus further reducing biases.
 2277 The impact of such an optimization will lead to some reduction in the projected rates, while
 2278 still enabling a significant improvement in the precision and kinematic reach of current STAR
 2279 measurements, and making important measurements that are yet more differential possible.

year	minimum bias [$\times 10^9$ events]	high- p_T int. luminosity [nb^{-1}]		
		all vz	$ \text{vz} < 70\text{cm}$	$ \text{vz} < 30\text{cm}$
2014 2016	2	27	19	16
2023 2025	20	63	56	38

Table 9: STAR minimum bias event statistics and high- p_T luminosity projections for the 2023 and 2025 Au+Au runs. For comparison the 2014/2016 event statistics and luminosities are listed as well.

2280 At RHIC it is possible to build detectors that can span from mid-rapidity to beam
 2281 rapidity – with the two recent upgrades STAR is able to achieve this unique capability.
 2282 STAR’s BES-II upgrade sub-systems comprised of the inner Time Projection Chamber
 2283 (iTPC, $1.0 < |\eta| < 1.5$), endcap Time Of Flight (eTOF, $1 < \eta < 1.5$) and Event Plane
 2284 Detector (EPDs, $2.1 < |\eta| < 5.1$), that are all commissioned and fully operational since the
 2285 beginning of 2019 [103, 277, 278]. As will be discussed in Section 4, the STAR collaboration
 2286 is constructing a forward rapidity ($2.5 < \eta < 4$) upgrade that will include charged particle
 2287 tracking and electromagnetic/hadronic calorimetry [279]. For charge particle tracking the
 2288 aim is to construct a combination of silicon detectors and small strip thin gap chamber de-
 2289 tectors. The combination of these two tracking detectors will be referred to as the forward
 2290 tracking system (FTS). The FTS will be capable of discriminating the hadron charge sign.
 2291 It should be able to measure transverse momentum of charged particles in the range of $0.2 <$
 2292 $p_T < 2$ GeV/ c with 20 – 30% momentum resolution. In what follows, we will refer to the
 2293 combination of the existing TPC ($|\eta| < 1$) and the iTPC upgrade as iTPC ($|\eta| < 1.5$) for
 2294 simplicity.

2295 The impetus for running STAR during the year of 2023-2025 in terms of bulk correlation
 2296 measurements in Au+Au 200 GeV collisions comes from gains via: i) extended acceptance
 2297 and ii) enhanced statistics. In the first subsections, we briefly describe how these two op-

2298 opportunities can be exploited to perform correlations measurements that are unique to the
 2299 physics goals of the RHIC heavy-ion program.

2300 Next, thanks to a reduced material budget between the beam and the iTPC, STAR will
 2301 be uniquely positioned to perform dielectron measurements with which we propose to probe
 2302 degrees of freedom of the medium and its transport properties. For that we will use the
 2303 high precision dilepton excess yield, i.e. l^+l^- invariant mass distribution after subtraction
 2304 of dilepton sources produced after freeze-out, and contributions from the initial collisions
 2305 such as Drell-Yan and correlated charm-anticharm pairs. Furthermore, we propose to study
 2306 the virtuality, Wigner function and final-state magnetic field in the QGP. For the latter
 2307 photon-photon collisions in ultra-peripheral, peripheral, and midcentral reactions and $p+A$
 2308 (all centralities) in both channels e^+e^- , $\mu^+\mu^-$ will be measured with high accuracy.

2309 In the last subsections, we address our proposed charmonium measurements and motivate
 2310 the importance of STAR's proposed program of precise jet measurements to explore the
 2311 micro-structure of the QGP.

2312 Figure 82 shows the kinematic projection plot for the STAR past (until 2015), current,
 2313 and with Run23+25 hard probes measurements. The corresponding STAR measurements
 2314 are compared with the LHC (published) measurements.

2315 3.1 Correlation Measurements Utilizing Extended Acceptance

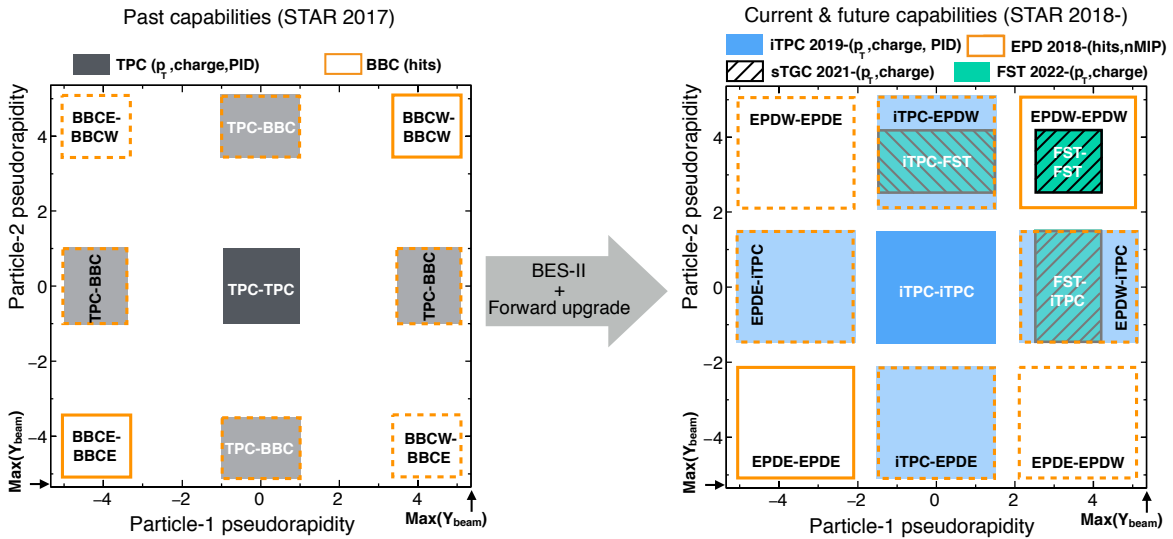


Figure 73: A visual representation of two-particle phase space in pseudorapidity covered by STAR detectors with respect to the region allowed by maximum beam rapidity ($Y_{beam}=5.36$ at 200 GeV Au+Au collisions) of RHIC. Left and right panels show the capabilities before and after BES-II and forward upgrades of the STAR detector, respectively. Note that in addition to a larger pair acceptance, the EPD granularity is over an order of magnitude larger than that of the BBC, and individual EPD tiles are shown to be separable into 1, 2, 3 MIP responses.

2316 Figure 73 demonstrates how STAR, with the BES-II and forward upgrades, will extend
 2317 the two-particle phase-space (in terms of η_1 and η_2 with respect to beam rapidity) many
 2318 times enabling us to perform correlation measurements over a wide window of relative pseu-
 2319 dorapidity. Since many of the important correlation measures are based on two-particle
 2320 correlations, this enhanced phase-space will provide STAR with many advantages: 1) an in-
 2321 crease in the number of pairs resulting in better precision, 2) a reduction in different sources of
 2322 the non-flow backgrounds by increasing the pseudorapidity separation. Many multi-particle
 2323 correlations will also benefit from the increase in triplets, quadruplets and so on due to the
 2324 overall increased acceptance. With this unique extended pseudorapidity reach our goal is
 2325 to perform correlation measurements to enable a deeper understanding of the largely unex-
 2326 plored three-dimensional structure of the initial state, and further improve the extraction of
 2327 temperature dependent transport properties of the subsequent fluid-like medium produced
 2328 in heavy ion and small system collisions at RHIC through data-model comparison such as
 2329 the Bayesian analysis performed in Ref [280].

2330 Two key sets of measurements are of interests: 1) the pseudorapidity dependence of
 2331 azimuthal correlations, 2) the pseudorapidity dependence of global hyperon polarization.

2332 **Pseudorapidity-dependent Azimuthal Correlations to Tightly Constrain the Tem-** 2333 **perature Dependence of Viscosity**

2334 The idea of tightly constraining the temperature dependent viscosity of the QGP was envi-
 2335 sioned in the 2015 Long Range Plan for Nuclear Science [275]. The QCD matter formed at
 2336 RHIC shows nearly perfect fluidity characterized by the smallest viscosity to entropy ratio
 2337 η/s known in nature. One major aim is to perform precision measurements to constrain the
 2338 temperature dependence of the shear η/s (T) and bulk ζ/s (T) viscosities. Recent state-
 2339 of-the-art Bayesian analyses of flow and spectra data within sophisticated event-by-event
 2340 hydrodynamics models has show strong evidence for temperature dependence of η/s and
 2341 ζ/s [280–282], but the uncertainties are still quite large. On the other hand, hydrodynamic
 2342 simulations have demonstrated that since the temperature of the produced fireball in HICs
 2343 vary with the rapidity, the measurement of the rapidity dependence of flow harmonics can
 2344 provide additional constraint on the η/s (T) and ζ/s (T) [283]. For this, RHIC measure-
 2345 ments have an advantage over the LHC since the smaller beam rapidity at RHIC provides
 2346 stronger variations of the temperature with rapidity. The beam energy scan at RHIC pro-
 2347 vides an additional handle on temperature to map η/s (T), and ζ/s (T) over a wide range of
 2348 temperatures. Indeed, the hydrodynamic simulation of Ref. [283] indicates that η/s (T) at
 2349 lower temperatures, near its possible minimum ($T = T_c$), can be better constrained by RHIC
 2350 measurements. Results from such simulations are shown in Fig. 74. In this simulation, a
 2351 number of QCD-motivated parameterizations of the temperature dependence of the shear
 2352 viscosity were assumed, as shown in Fig. 74 (left).

2353 Existing data from the PHOBOS collaboration suffer from large uncertainties, therefore
 2354 only limited constraints on the temperature dependence of the transport parameters can
 2355 be achieved. The BES-II upgrade (with iTPC) and the forward upgrade (FTS) of STAR
 2356 will provide precise estimations of different azimuthal correlation observables: $v_n(\eta)$ and

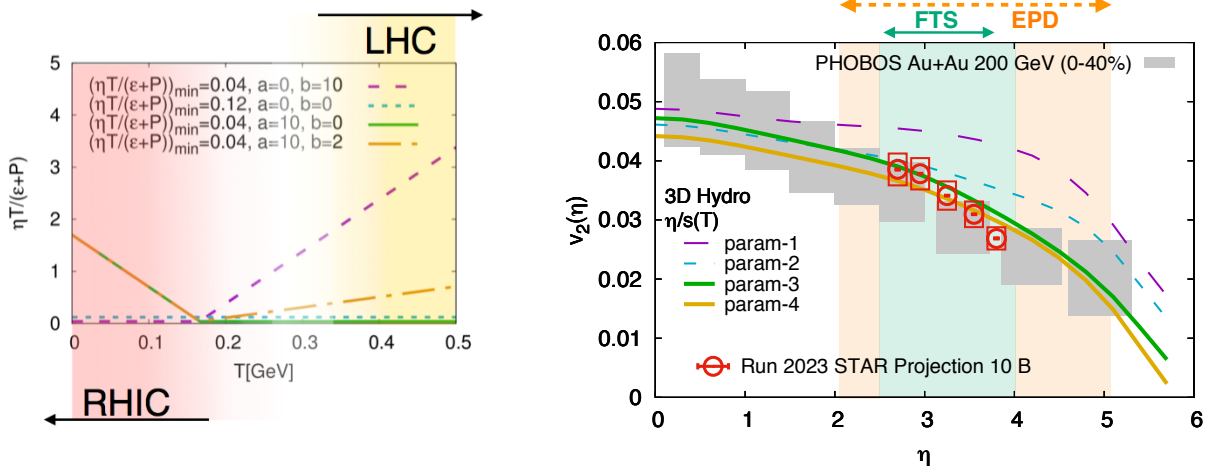


Figure 74: (Left) Different parameterizations of the temperature dependence of the shear viscosity to entropy η/s (T) (at zero chemical potential) used in the hydrodynamical simulation of Ref. [283]. Interestingly, it has been demonstrated in Ref. [284] that the region of lowest η/s is the one that can be probed at RHIC. (Right) Effects on the elliptic flow co-efficient v_2 due to different parameterizations of the viscosity parameter, indicating better constraints on η/s (T) can only be performed by measurements at forward rapidities at RHIC. The interpretation of the existing PHOBOS data is limited by the large uncertainties. Projections for STAR measurements are shown on the same plot.

2357 other higher-order ($n > 2$) flow coefficients $v_n(\eta)$, its fluctuations $\sigma(v_n)/v_n$ that have never
 2358 been measured at forward rapidity, are essential in terms of constraining η/s (T) near its
 2359 possible minimum. These quantities previously measured at mid-rapidity with previous
 2360 data are not enough for discriminating different parameterization of η/s (T) as shown in the
 2361 hydrodynamic simulation of Ref. [283]. While transverse momentum integrated quantities
 2362 at forward rapidity can constrain the shear viscosity, measurement of the p_T of particles at
 2363 forward rapidity (i.e. forward tracking) is essential to constrain the bulk viscosity ζ/s – in
 2364 particular the information of $\langle p_T \rangle$ is needed to constrain $\zeta/s(T)$. With the forward tracking
 2365 systems it will be possible to measure the p_T dependence of v_n in Au–Au collisions in 2023.

2366 Pseudorapidity-dependent Azimuthal Correlations to Constrain the Longitudi- 2367 nal Structure of the Initial State

2368

2369 Initial-state longitudinal fluctuations and the fluid dynamical response of the medium
 2370 formed in heavy ion collisions can lead to de-correlations of the direction of the reaction
 2371 planes Ψ_n (which determines the orientation of the harmonic anisotropies) with pseudora-
 2372 pidity (see Fig. 75). Such effects are often referred to as a torque or twist of the event
 2373 shape [287–289] that eventually leads to a breaking of longitudinal/boost/rapidity invari-
 2374 ance. The magnitude of the de-correlation is determined by the details of the dynam-
 2375 ics of initial state, and the distribution of nucleons and partons inside the colliding nu-

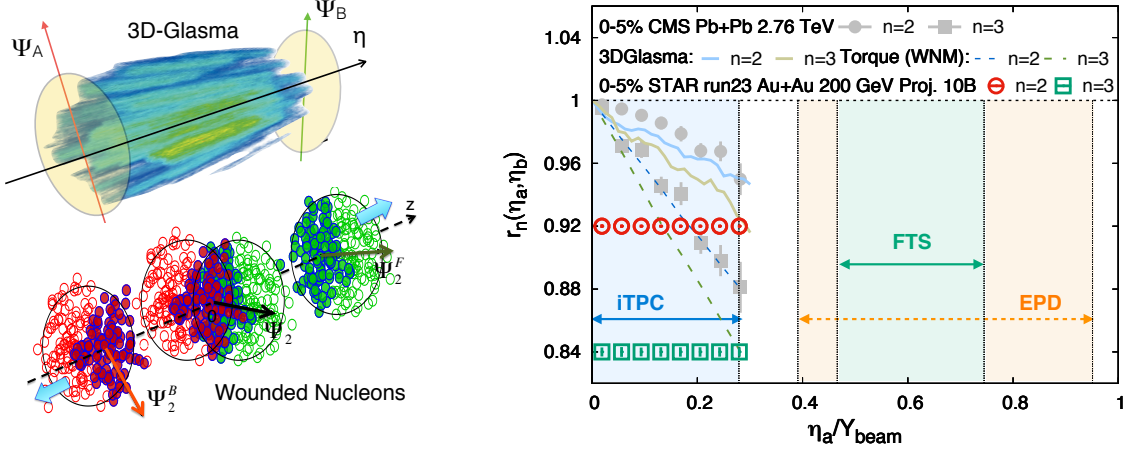


Figure 75: (Left) Cartoon to demonstrate the de-correlation of event planes in the longitudinal direction of a collision from a gluon saturation based 3D-Glasma model [285] and a wounded nucleon model (WNM) [286, 287]. (Right) The longitudinal de-correlation of the elliptic anisotropy plane as a function of pseudorapidity in units of beam rapidity. CMS results are compared to predictions from two models in the left with STAR projection for Run-23 (using preliminary Run-19 results) from an anticipated 10 B min-bias events. The colored regions show that the current and future capabilities at STAR (with iTPC+EPD+FTS) can extend such measurements with good precision by covering a large fraction of the beam rapidity at 200 GeV – this demonstrates the unique strength to STAR to study the physics of 3D initial state.

2376 clei. Several promising observables have been proposed to study this effect, Fig. 75 shows
 2377 one which can be expressed as $r_n(\eta_a, \eta_b) = V_{n\Delta}(-\eta_a, \eta_b)/V_{n\Delta}(\eta_a, \eta_b)$, where $V_{n\Delta}(\eta_a, \eta_b)$ is
 2378 the Fourier coefficient calculated with pairs of particles taken from three different pseu-
 2379 dorapidity regions $-\eta_a$, η_a and η_b . The observable $r_n(\eta_a, \eta_b)$ was originally introduced
 2380 and measured by CMS collaboration in Ref. [290] and also been measured by the AT-
 2381 LAS collaboration in [291]. An observable using three-particle correlations that is sensi-
 2382 tive to this effect is the relative pseudorapidity dependence of the three-particle correlator
 2383 $C_{m,n,m+n}(\eta_a, \eta_b, \eta_c) = \langle \cos(m\phi_1(\eta_a) + n\phi_2(\eta_b) - (m+n)\phi_3(\eta_c)) \rangle$ [292]. Another, very similar
 2384 to r_n in terms of design but involving four-particle correlations, is: $R_{n,n|n,n}(\eta_a, \eta_b)$ [293]. As
 2385 shown in Fig. 75, CMS measurements of r_n show strong de-correlation ($\sim 16\%$ for $n=3$,
 2386 $\sim 8\%$ for $n=2$) in central events within the range of their acceptance. In the 3D-Glasma
 2387 model of initial state, the breaking of boost invariance is determined by the QCD equations
 2388 which predict the evolution of gluons in the saturation regime with Bjorken-x. At the LHC
 2389 such models predict weaker de-correlation as compared to when the initial state is described
 2390 by wounded nucleon models. The 3D-Glasma model does a good job in explaining the r_2
 2391 data from CMS [285] but over-predicts the r_3 results. One expects the nature of the ini-
 2392 tial state to change from LHC to RHIC, in particular the region of Bjorken-x probed is
 2393 very different. It is therefore extremely important to utilize the enhanced acceptance of
 2394 the STAR detector with a Au+Au 200 GeV run to study this effect. In Fig. 75 STAR's
 2395 projections using preliminary Run-19 results to estimate the uncertainties for 10 B events

2396 are shown for the measurement of r_n within the acceptance $|\eta| < 1.5$. The colored regions
 2397 show that the current and future capabilities at STAR (with iTPC+EPD+FTS) can extend
 2398 such measurements using observables $r_n, C_{m,n,m+n}, R_{n,n|n,n}$ with good precision by covering
 2399 either an equal (iTPC only) or larger (iTPC+FTS+EPDs) fraction of the beam rapidity
 2400 at 200 GeV compared to the LHC measurements. This unique measurement capability will
 2401 help pin down the nature of the 3-D initial state of heavy ion collisions. It will also help
 2402 constrain different models of QCD that predict the rapidity (or Bjorken-x) dependence of
 2403 valance quark and gluon distributions inside colliding nuclei as has been demonstrated by
 2404 theoretical calculations in Ref. [285, 294].

2405 **Search for Collectivity in Photo-nuclear ($\gamma + Au$) Processes**

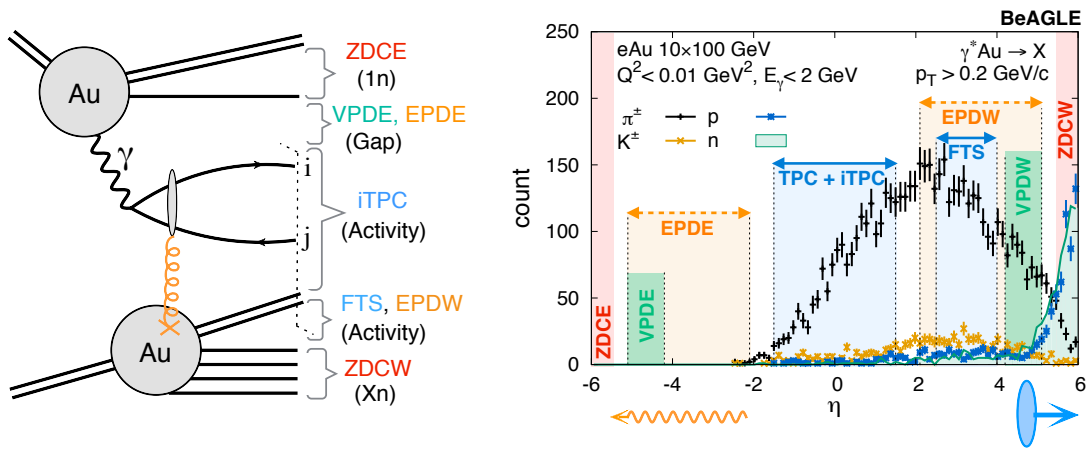


Figure 76: (Left) $\gamma + Au$ process in ultra-peripheral heavy ion collisions associated with a large rapidity asymmetry; the large acceptance of the STAR detector can be used to trigger these events to study bulk observables and search for collectivity, the same can be done in low virtuality e+Au collisions to search for collectivity at the EIC.(Right) Pseudorapidity distribution of different particles using the state-of-the-art BeAGLE [295, 296] event generator for EIC in e+Au events. By restricting virtuality and energy of the photon (γ^*) we try to mimic the kinematics of a $\gamma + Au$ (Au+Au UPC) event. The purpose of this plot is to demonstrate how different STAR detectors will be used to identify such UPC processes at the kinematics similar to that at EIC.

2406

2407 Until the EIC at BNL is built, high-energy photoproduction processes (low virtuality limit
 2408 of deep inelastic scattering) as shown in Fig.76, can be studied using ultra-peripheral ion
 2409 collisions (UPCs) that occur when two heavy ion interact at large impact parameters. Such
 2410 collisions can be considered as $\gamma+A$ collisions but unlike at the EIC, the photons involved
 2411 in UPCs are quasi-real. Do we expect to see collectivity in such collisions? If observed,
 2412 this will address an important question. Origin of collectivity in small collision systems
 2413 has been argued to be driven by the formation of a medium that evolves hydrodynamically.
 2414 However, due to the phenomenon of saturation, intrinsic correlations for gluons in the
 2415 colliding hadrons/nuclei have been shown by theoretical models such as color glass conden-

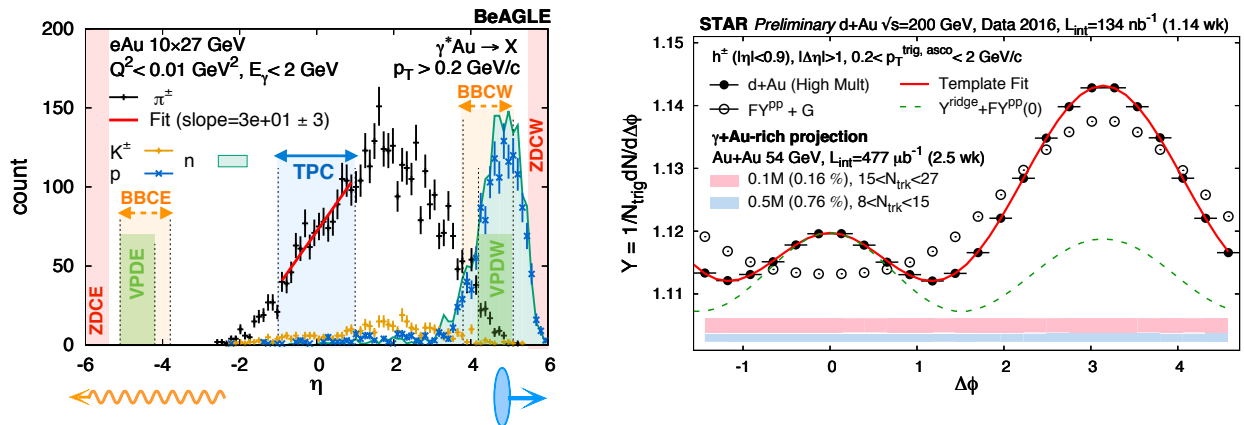


Figure 77: (Left) $\gamma + Au$ processes simulated using BeAGLE event generator in the low virtuality limits ($Q^2 < 0.01 \text{ GeV}^2$) of DIS by restricting the energy of photons to be $E_\gamma < 2 \text{ GeV}$ and ion energy to be 27 GeV. The pseudorapidity distributions thus produced is used to apply cuts on detectors in STAR to identify $\gamma + Au$ candidates in 54 GeV Au+Au collisions. (Right) STAR preliminary data on per-trigger yield estimated using di-hadron correlations in d+Au (hadronic) 200 GeV collisions. The correlation function in pp collisions (open circle) is used as a template to fit the same in relatively higher multiplicity d+Au collisions (solid circle) and to extract the long-range ridge-like component. The red and blue band show projections for $\gamma + Au$ enriched events for two different multiplicity bins. The aim is to use the correlation function from the low multiplicity $\gamma + Au$ to perform template fit in the high multiplicity bin. Our exploratory analysis with 54 GeV data indicates about 0.16-0.76% of minbias events are $\gamma + Au$ events. With the anticipated 20 Billion Au+Au 200 GeV events collected in Run-23 and Run-25, about 300 times more $\gamma + Au$ candidates can be collected, implying a reduction of the red and blue bands by a factor of 17.

2416 sate (CGC) to contribute to collectivity – experimentally such contributions have not been
 2417 decisively established. The general consensus is that correlations predicted by both hydro-
 2418 dynamics and CGC contribute to collectivity – although no experimental measurement has
 2419 been proposed that can disentangle the contribution from the two effects. No studies have
 2420 convincingly demonstrated that in $\gamma + A$ collisions a hydrodynamic medium can be formed.
 2421 Observation of collectivity in $\gamma + Au$ (or future e+A), therefore, may very well be the first
 2422 evidence of purely initial-state gluon driven contribution to such phenomenon as argued in
 2423 the theoretical work of ref [297]. This will be an important step to understanding the role
 2424 of gluon saturation or color coherence in driving collectivity, and also pioneer several new
 2425 measurements in this direction at the BNL EIC.

2426 The search for collectivity in ultra-peripheral (UPC) 5.02 TeV Pb+Pb collisions, by trig-
 2427 gering $\gamma + A$ events, has recently been initiated by the ATLAS collaboration at the LHC
 2428 where interesting hints of long-range ridge like correlations have been observed [298]. How-
 2429 ever, RHIC has similar ion energies when compared to the future EIC. This gives STAR
 2430 the necessary motivation to propose a program to search for the collectivity in $\gamma + A$ events
 2431 at RHIC. This is interesting as $\gamma + A$ UPC events have much synergy with low virtuality
 2432 events in e+A collisions at the EIC and in many ways this provides a chance to better un-

2433 derstand the origin of collectivity. It must be noted the proposed program with STAR will
 2434 have several unique strengths to both complement and extend such a search for collectivity
 2435 at lower collision energies due to: a wider acceptance compared to beam rapidity (Y_{beam}),
 2436 better momentum resolution to measure the soft part of the spectrum, and better particle
 2437 identification capabilities. As shown in Fig.76, our goal is to trigger on the $\gamma + Au$ process in
 2438 ultra-peripheral heavy ion collisions associated with a large rapidity asymmetry. The figure
 2439 also demonstrates how the combination of the inner Time Projection Chamber (iTPC), the
 2440 new highly granular Event-Plane Detectors (EPD) and the forward tracking system (FTS)
 2441 and Zero-Degree Calorimeters (ZDC) can be used isolate $\gamma + Au$ events from peripheral
 2442 Au+Au events (symmetric in η with no gaps). By triggering on these events our aim will
 2443 be to study bulk observables ($dN/dydp_T(\pi^\pm, K^\pm, p/\bar{p})$) and long range ridge-like azimuthal
 2444 correlations to search for collectivity.

2445 A handful of datasets exist on the disk with the appropriate event trigger selection for
 2446 such a process. For example, Fig.77 show a feasibility study using the dataset of Au+Au
 2447 collisions at 54 GeV (year 2017) and 200 GeV (year 2019). In order to mimic the kinematics
 2448 of Fig.77(left) we apply asymmetric cuts on the energy deposition of neutrons in ZDCs
 2449 (1nXn). For example, if the ZDC east is restricted to have a single neutron hit, while no
 2450 restriction is placed on the ZDC west we trigger on $\gamma + Au$ candidates with east going
 2451 photons, and vice versa. We also apply similar asymmetric cuts in the BBCs to get purer
 2452 samples. After collecting $\gamma + Au$ -rich candidates we study di-hadron correlations in such
 2453 events and compare with the same from hadronic events with same activities. We select two
 2454 such windows of event activity based on cuts on numbers of tracks in TPC ($15 < N_{trk}^{|\eta| < 0.5} < 27$
 2455 and $1 < N_{trk}^{|\eta| < 0.5} < 8$). According to our estimates the percentage of possible $\gamma + Au$ candidates
 2456 are about 0.17% and 0.83% of min-bias events in those two windows of multiplicity. Fig.77
 2457 shows STAR preliminary data on the per-trigger yield in di-hadron correlations in d+Au
 2458 events where a clear ridge can be seen after template fitting. On the same plot we show
 2459 projections of uncertainties for the di-hadron correlations in possible $\gamma + Au$ -rich events
 2460 using Au+Au 54 GeV data. With the new forward detector capability and new datasets
 2461 in the future Au+Au 200 GeV (year 2023 and 2025) run of RHIC with a dedicated trigger
 2462 selection, we should be able to make measurements at the kinematics similar to that at EIC
 2463 as shown in Fig.77. Based on the feasibility studies with 54 GeV data, we estimate about
 2464 0.16 – 0.76% of minbias candidates to be potential $\gamma + Au$ candidates (purity of such events
 2465 are still under investigation). Therefore, event without any dedicated trigger, 20 Billion
 2466 minbias Au+Au events can already give us 32-152 Million potential $\gamma + Au$ candidates. This
 2467 will significantly reduce the uncertainties shown by the red and blue projection bands in
 2468 Fig.77. This will enable us to perform differential measurements of di-hadron correlations
 2469 with different combinations of trigger and associated transverse momenta.

2470 Pseudorapidity Dependence of Global Hyperon polarization

2471

2472 The global polarization of hyperons produced in Au+Au collisions has been observed
 2473 by STAR [256]. The origin of such a phenomenon has hitherto been not fully understood.

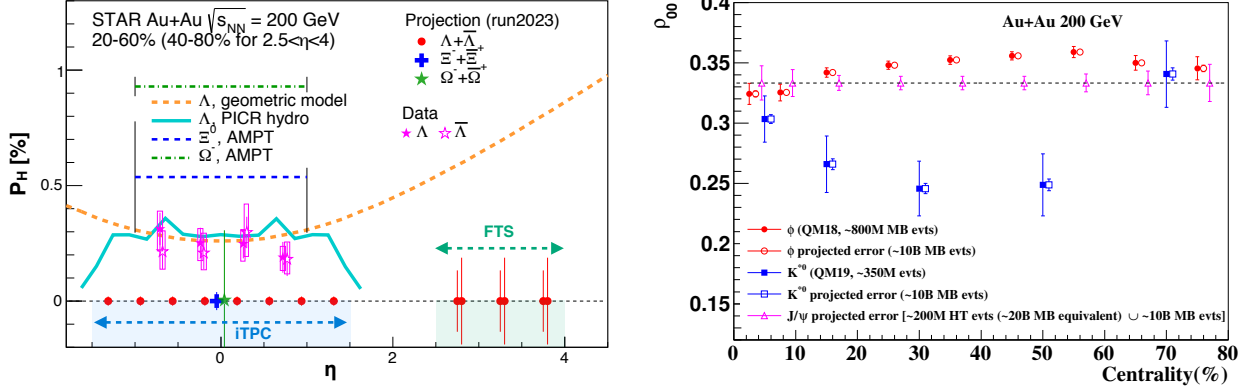


Figure 78: (Left) Projections (along with preliminary data) for differential measurements of Λ ($\bar{\Lambda}$) polarization over the extend range of pseudorapidity with the iTPC and FTS detectors of STAR that will help resolve tension between different theoretical model predictions (shown by curves) of polarization with η . In addition, projections for the measurements of spin-1/2 Ξ and spin-3/2 Ω particles are also shown. (Right) Spin alignment co-efficient ρ_{00} as a function of centrality, with projected errors based on ~ 10 billion minimum bias events. The enhanced statistics Run-23, combined with the excellent dilepton capabilities of STAR, will enable us to measure J/ψ alignment along with increasing the significance of the ϕ and K^{*0} measurements.

2474 Several outstanding questions remain. How exactly is the global vorticity dynamically transferred to the fluid-like medium on the rapid time scales of a collision? Then, how does the
2475 local thermal vorticity of the fluid gets transferred to the spin angular momentum of the
2476 produced particles during the process of hadronization and decay? In order to address these
2477 questions one may consider measurement of the polarization of different particles that are
2478 produced in different spatial parts of the system, or at different times. A concrete proposal
2479 is to: 1) measure the Λ ($\bar{\Lambda}$) polarization as a function of pseudorapidity and 2) measure it for
2480 different particles such as Ω and Ξ . Both are limited by the current acceptance and statistics
2481 available as recently published by STAR [299]. However, as shown in Fig. 78 with the addi-
2482 tion of the iTPC and FTS, and with high statistics data from Run-23 it will be possible to
2483 perform such measurements with a reasonable significance. iTPC (+TPC) has excellent PID
2484 capability to measure all these hyperons. Although the FTS has no PID capability we can
2485 do combinatorial reconstruction of Λ ($\bar{\Lambda}$) candidates via displaced vertices. A similar analysis
2486 was performed and published by STAR using the previous FTPC [300]. In order to make
2487 a conservative projection we assume similar momentum resolution of 10 – 20% for single
2488 charged tracks, similar overall tracking efficiency, charge state identification capability for
2489 the FTS and FTFC (see the forward upgrade section for exact numbers). We also assume
2490 the FTS, with it's novel-tracking framework, will be able to measure a minimum separation
2491 of 20 cm between the all pairs of one positive and one negative track (a possible decay vertex)
2492 from the main vertex of the event. This will give rise to about 5% efficiency of Λ ($\bar{\Lambda}$) recon-
2493 struction with about 15 – 20% background contribution from $K_S^0 \rightarrow \pi^+ + \pi^-$ [300]. With
2494 this we can make projections for a polarization measurement in Au+Au 200 GeV 40 – 80%
2495 assuming 10 Billion minimum-bias events as shown in Fig. 78. The two different error bars
2496

2497 correspond to lower and upper limits considering current uncertainties on the efficiency of
 2498 charged track reconstruction and the final efficiency of Λ reconstruction. Currently theoret-
 2499 cal models predict contradictory trends for the pseudorapidity dependence of Λ polarization.
 2500 If the initial local orbital angular momentum driven by collision geometry [301] plays a dom-
 2501 inant role it will lead to increases of polarization with pseudorapidity. On the other hand
 2502 if the local thermal vorticity and hydrodynamic evolution [302] play a dominant role it will
 2503 predict decreasing trend or weak dependence with pseudorapidity. Such tensions can be
 2504 easily resolved with the future proposed measurement during Run-23.

2505 3.2 Correlation Measurements Utilizing the Enhanced Statistics

2506 Over the past years the STAR collaboration has pursued dedicated measurements of Au+Au
 2507 collisions at $\sqrt{s_{NN}} = 200$ GeV that have major discovery potential but are intrinsically
 2508 statistics hungry. Attempts have been made to combine datasets from several years to
 2509 increase the significance of such measurements. This can result in run-to-run variations and
 2510 systematics in detector responses that sometimes are tedious to correct. A single stable long
 2511 run with similar detector conditions, as anticipated during Run-23, can avoid such issues.
 2512 In the following section, and also in section 1.2.7, we propose correlation measurements that
 2513 will utilize the enhanced statistics from Run-23 and can lead to high-impact results. To
 2514 start we assume STAR will collect data at the rate of 1.5 kHz and a combined RHIC×STAR
 2515 uptime of 50% (12 hour/day) for 24 weeks of running during Run-23. This will lead to the
 2516 accumulation of about $24 \times 7 \times 86400 \times 0.5 \times 1500 \approx 10$ billion events.

2517 Global Spin Alignment of J/ψ

2518 Surprisingly large signals of global spin alignment of vector mesons such as $\phi(1020)$ and
 2519 $K^{*0}(892)$ have been measured via the angular distribution of one of their decay products.
 2520 These experimental observations of vector meson spin alignment have yet to be interpreted
 2521 satisfactorily by theory calculations. It has been realized that the mechanism driving the
 2522 global polarization of hyperons can have its imprint on vector meson spin alignments albeit
 2523 the observed strength of signals for the two measurements cannot be reconciled. In fact
 2524 the large quantitative difference between the measurements of $\phi(1020)$ and $K^{*0}(892)$ spin
 2525 alignment as shown in Fig. 78 (right) cannot be simultaneously explained by conventional
 2526 mechanisms of spin-orbit coupling, driven by angular momentum, without invoking strong
 2527 force fields. It is argued that the strong force field makes a dominant contribution to the
 2528 spin-alignment coefficient ρ_{00} of ϕ , while for K^{*0} , the contribution is diminished due to the
 2529 mixing of quark flavors (averaging-out of different meson fields) [303, 304]. Therefore, the
 2530 current preliminary experimental data from STAR (Fig. 78, showing $\rho_{00}(\phi) > \rho_{00}(K^{*0})$)
 2531 support the role of strong force field as a key mechanism that leads to global spin alignment.
 2532 However, a stringent test of such a prediction can be performed by measuring the spin
 2533 alignment of J/ψ . This is because similar arguments apply for both ϕ and J/ψ , i.e. like s
 2534 and \bar{s} , the strong field component also couples to c and \bar{c} quarks leading to larger ρ_{00} for J/ψ .
 2535 In Fig. 78(right) we present the projected uncertainties for ρ_{00} of J/ψ estimated for various

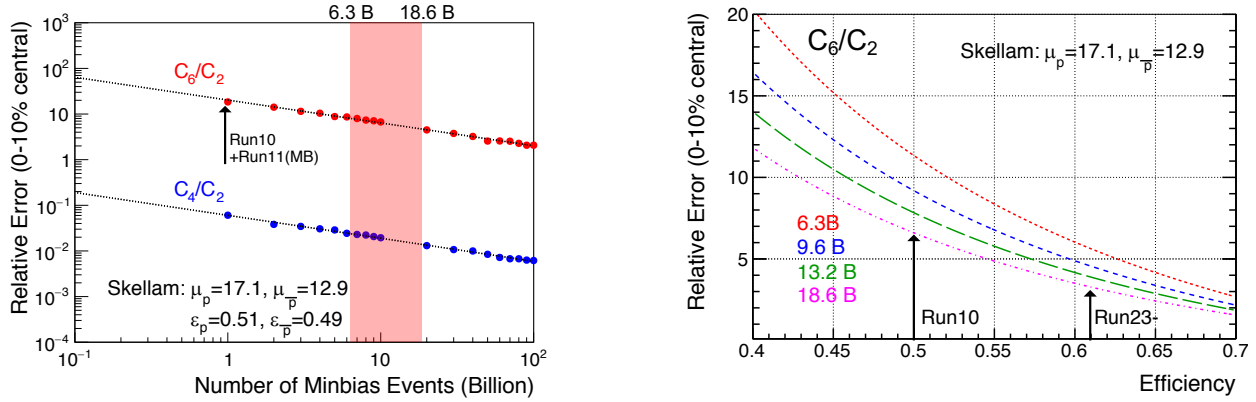


Figure 79: Projection for measurement of ratio of sixth order over second order cumulants of net-proton distribution.

2536 centralities assuming: 1) 10 billion min-bias events for low p_T J/ψ measurements and, 2)
 2537 200 million events implementing High Tower (HT) triggers with the Barrel Electromagnetic
 2538 Calorimeter for the high p_T J/ψ . Both assume 24 weeks running anticipated in Run-23.
 2539 It is worth to mention that apart from J/ψ spin alignment, such a large statistics dataset
 2540 will also allow addition differential study of global spin alignment of ϕ and K^{*0} and help to
 2541 further elucidate the mechanism behind vector meson spin alignment.

2542 Sixth Order Cumulant of Net-proton Distributions

2543 LQCD calculations [5, 305] predict a sign change of the susceptibility ratio χ_6^B/χ_2^B with
 2544 temperature (T at $\mu_B = 0$) taking place in the range of 145-165 MeV. The observation of
 2545 this ratio going from positive to negative values is considered to be a signature of a crossover
 2546 transition. Interestingly, as shown in Section 1.1.1, values of net-proton C_6/C_2 are found
 2547 to be negative systematically from peripheral to central Au+Au 200 GeV collisions within
 2548 large statistical uncertainties. The observation of negative C_6/C_2 is intriguing and so far
 2549 only hinted at in the 200 GeV data, the current result has less than 2.3σ significance for 30-
 2550 40% centrality in terms of statistical uncertainties. The current systematic uncertainty is of
 2551 similar order as the statistical uncertainty and if based off of combining datasets from Run-10
 2552 and Run-11. As shown in the projection plot of Fig. 79 it is possible to establish definitive
 2553 observation of negative C_6/C_2 at 200 GeV with nearly 10 billion minimum-bias events to be
 2554 collected during the Run-23 with 15% increase in the reconstruction efficiency and enhanced
 2555 acceptance of the iTPC detector upgrade. A similar measurement can be performed at the
 2556 LHC for vanishing baryon chemical potential, while only STAR measurements can explore
 2557 the finite μ_B region. Our measurement at $\sqrt{s_{NN}}=200$ GeV has the potential to establish the
 2558 first experimental observation of QCD chiral crossover transition at $\mu_B \approx 20$ MeV.

2559 Strong Interaction Measurements

2560 The strong interaction between baryons leads to a residual force; the most common example
 2561 is NY . The same force is responsible for binding $n - p$ into d . So far, understanding the

2562 strong interaction has been limited to the effective theories related to nucleons and the
 2563 scattering experiments, which are very challenging due to the short lifetime of resonances
 2564 (a few cm decay length). One of the current challenges is to evaluate the strong interaction
 2565 between hyperons, as experimentally still very little is known about NY and YY interactions.
 2566 Hypernuclei (a hyperon bound inside an atomic nucleus) are proof of a positive, attractive
 2567 interaction of NY . Measurements of NN and NY interactions have crucial implications for
 2568 the possible formations of bound states. Studies of the strong interaction potential via two-
 2569 particle correlations in momentum space measured in relativistic heavy-ion and elementary
 2570 collisions have proven to be useful to gain access to the interactions between exotic and rare
 2571 particles. Possible combinations can be: $p\Lambda$, $p\Sigma$, $p\Omega$, $p\Xi$, $\Lambda\Lambda$, $\Xi\Xi$. In contrast to $p\Lambda$, the
 2572 nature of $p\Sigma$, $p\Omega$, $\Lambda\Lambda$ still need experimental verification. Even if scattering experiments are
 2573 available, they are not very conclusive.

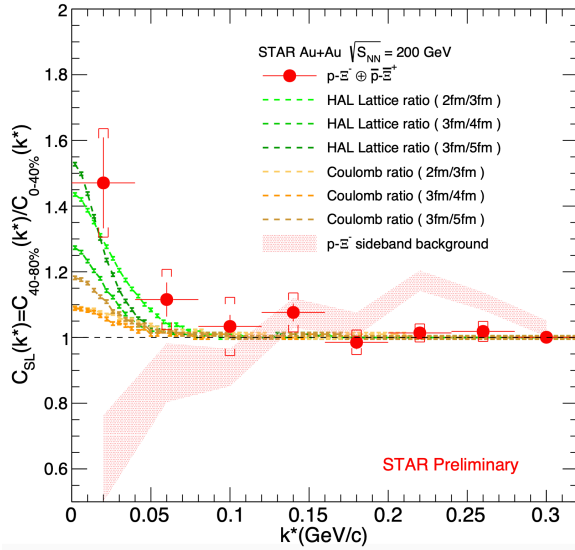


Figure 80: Solid circles represent the ratio (R) of the small system (40-80% collisions) to the large system (0-40% collisions) for proton- Ξ and \bar{p} - Ξ correlations. The bars correspond to the statistical uncertainties. The shaded area represents R for background candidates from the side-band of the Ξ invariant mass. Coulomb-induced R are shown in yellow and orange colors. HAL Lattice predictions of R are shown in green.

2574 Figure 80 shows the preliminary $p\Xi$ correlations function. All available statistics, 3 billion
 2575 events accumulated over all previous runs, were used for the $p\Xi$ and $p\Omega$ cases. Combining
 2576 such datasets leads to the run-to-run variations resulting in larger total systematic uncertain-
 2577 ties in the detector responses. A single stable long run with similar detector settings during
 2578 the Run-23 will avoid such issues. Statistical uncertainties of the current measurements re-
 2579 main high, and the number of points that build the correlation function is minimal. This
 2580 means that the current results are not conclusive enough to study in detail the parameters
 2581 of the strong interaction. Since the effect of the Coulomb interaction, seen via two-particle

2582 correlation, is expected to cancel in the ratio of two correlation functions, the extraction
2583 of the strong interaction parameters can be performed with larger datasets by measuring
2584 the correlation signal for central and mid-central+peripheral collisions. The collection of
2585 10 billion events from Run-23 will make possible the construction of correlation functions
2586 of the $p\Xi$ case with double the number of points and smaller statistical uncertainties than
2587 the current measurement. The $p\Omega$ system is more statistics hungry, and we expect that we
2588 will require 20 billion events, from combining Run-23 and Run-25, before we can double of
2589 the number of points that build the correlation signal. Previous STAR measurements of
2590 $p\Omega$ correlations show that the parameters of the strong interaction can be studied. How-
2591 ever, with higher data collections, more precise and detailed studies would be possible. The
2592 description of the $\Lambda\Lambda$ interaction is still an open issue. Such a description is fundamental
2593 since it plays a decisive role in understanding the nature of hyperons that appear in neutron
2594 stars. If many hyperons appear close to each other and their fraction becomes significant,
2595 the YY interactions are expected to play an essential role in describing the equation of state
2596 of the dense system. An alternative way to study hypernuclei is two-particle momentum
2597 correlations of $\Lambda\Lambda$ pairs produced in hadron-hadron collisions thanks to femtoscopy. Figure
2598 81 shows primary $\Lambda\Lambda$ (left) and $\Xi\Xi$ (right) correlation functions. For current $\Lambda\Lambda$ and $\Xi\Xi$
2599 systems also data from all previous runs were combined. Due to differences between indi-
2600 vidual runs, a significant source of systematic uncertainties exist now, and it will disappear
2601 with all 10 billion events collected during the Run-23 for the $\Lambda\Lambda$ case. More critical seems
2602 to be the increased statistics for the $\Xi\Xi$ case, and having 20 billion events from Run-23 and
2603 Run-25 enables the reduction of statistical uncertainties significantly and makes it possible
2604 to determine parameters of the strong interaction with higher precision. Having combined
2605 data from the Run-23 and Run-25 will also allow the hypotheses about possible bound states
2606 to be verified.

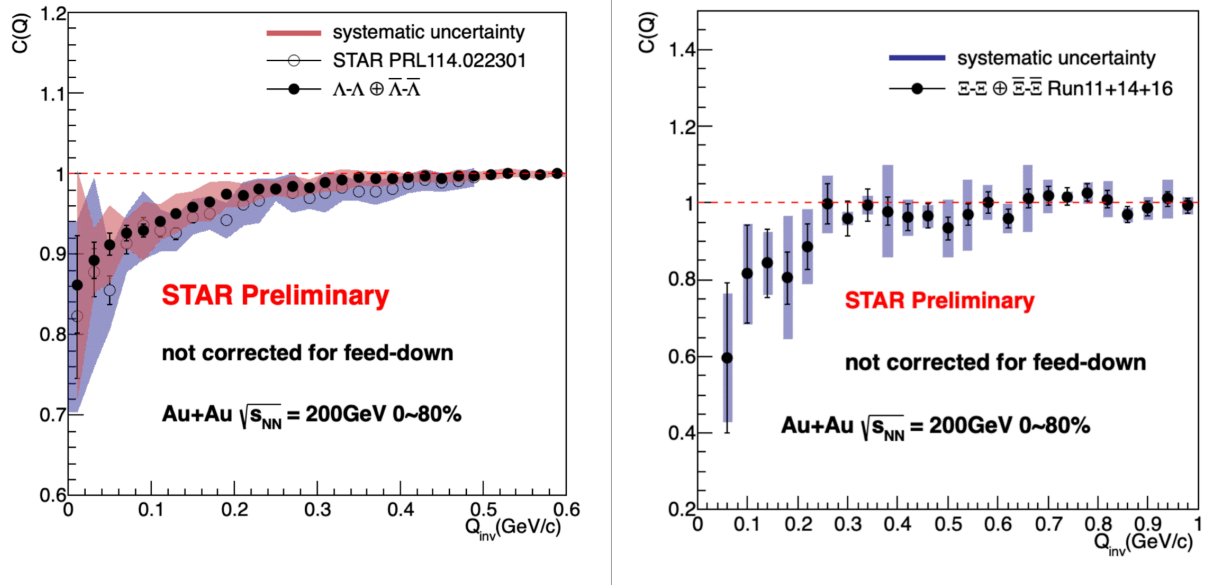


Figure 81: Left: combined $\Lambda\Lambda$ and $\bar{\Lambda}\bar{\Lambda}$ preliminary correlation functions with systematic uncertainties compared with already published previous STAR results. Right: combined $\Xi\Xi$ and $\bar{\Xi}\bar{\Xi}$ correlation functions with systematic uncertainties.

2607 **3.3 Hard Probes: Jets and Heavy Flavor**

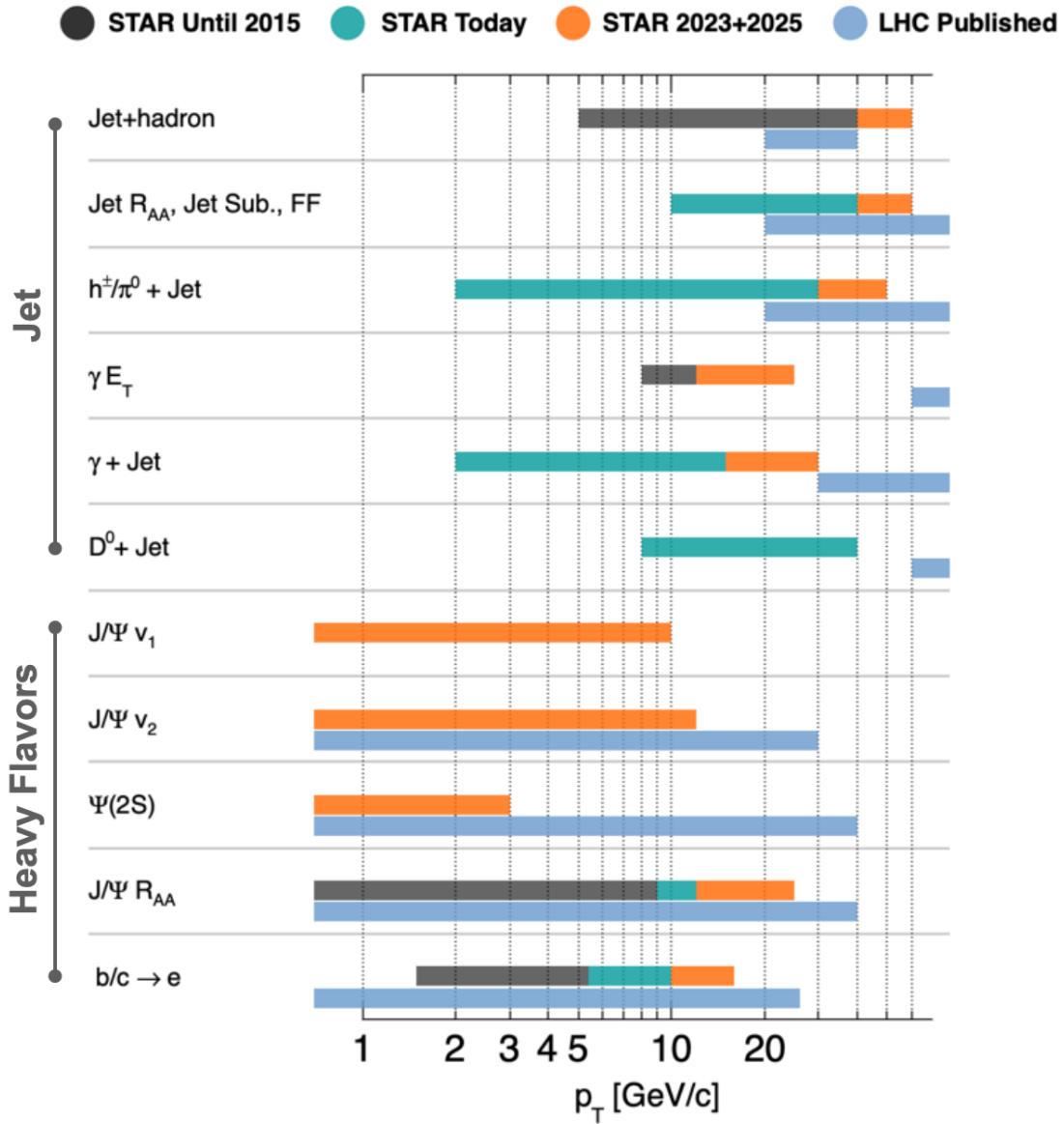


Figure 82: The kinematic coverage of the STAR Hard Probes measurements (past, current, and future projection) are shown with the corresponding comparison to the LHC (published) measurements. The details on the projection for precision measurements can be found in section. 3.3.

2608 Measurements of fully reconstructed jets and heavy flavor particles over a broad kinematic
 2609 range at RHIC are essential to meet the goal outlined in the NSAC 2015 Long Range Plan
 2610 (LRP), to “probe the inner workings of the QGP” [275].

2611 A diagrammatic representation of STAR’s kinematic coverage for various measurements

2612 related to hard probes is shown in Figure 82. The different colored horizontal bars show-
 2613 case STAR measurements that were available at the time of the 2015 NSAC-LRP (black),
 2614 ongoing measurements and recently released results (green) and projections for future data-
 2615 taking in years 2023 and 2025 (orange). The current high statistics STAR Au+Au collision
 2616 datasets available were recorded in 2014 and 2016, the integrated luminosities sampled by
 2617 STAR’s BEMC triggers are shown in Table 9. STAR’s capabilities are compared with the
 2618 corresponding LHC (light blue) published measurements. This overview reveals our ability
 2619 to investigate the QGP over a wide range of temperatures and medium properties produced
 2620 in heavy-ion collisions. Some of the flagship measurements are listed along the different rows
 2621 grouped into two topics related to ‘Jets’ and ‘Heavy Flavors’, where the x-axis represents a
 2622 p_T scale. The Run-23+25 RHIC heavy-ion runs will enable an expanded kinematic range of
 2623 fully reconstructed jets and open heavy flavor measurements through the semi-leptonic decay
 2624 channel, providing an overlap with the LHC data. They will also facilitate measurements
 2625 of low transverse momentum J/ψ elliptic flow (v_2) to study the recombination mechanism
 2626 in more detail, J/ψ directed flow (v_1) that will allow us to study the initial tilt of the bulk
 2627 medium and suppression of the loosely bounded $\psi(2S)$ state to explore the temperature
 2628 profile of the medium.

2629 The dependence of jet energy loss on the jet p_T and/or resolution or angular scale tagged
 2630 by jet substructure observables, are key tools in discriminating various jet quenching mech-
 2631 anisms [306–309]. In addition, the measurement of jet acoplanarity is a sensitive probe of
 2632 transverse momentum broadening and medium-induced radiative effects [310], particularly
 2633 for jets at low p_T which are accessible at STAR by selecting a given momentum transfer
 2634 via a photon trigger. Such a measurement is also minimally affected by background arising
 2635 from vacuum Sudakov radiation at RHIC energies [311, 312], potentially enabling a precise
 2636 extraction of in-medium jet scattering.

2637 Measurements of open heavy flavor and quarkonium production in heavy-ion collisions
 2638 provide important information about the properties of the created medium. Production of
 2639 open heavy flavor hadrons, J/ψ and Υ mesons in Au+Au collisions at RHIC was found to be
 2640 suppressed compared to the production in pp collisions. The suppression of open heavy flavor
 2641 production at high p_T is due to energy loss of heavy quarks in the QGP, while the suppression
 2642 of quarkonium states is due to a screening of the $Q\bar{Q}$ potential by the medium color charges.
 2643 In addition, J/ψ production can be affected by recombination of charm quarks in a later
 2644 stage of the collision evolution. The regeneration mechanism is expected to contribute mostly
 2645 at the low J/ψ transverse momentum range. Furthermore, recent theoretical calculations
 2646 suggest that measurements of the directed flow of heavy flavors particles can be used to shed
 2647 light on the initial geometry and the magnetic field information created during heavy-ion
 2648 collisions [313, 314].

2649 STAR’s unique geometry allows collection of events over a wide range of vertex positions
 2650 along the beam direction (v_z) for jet and heavy flavor analyses, thereby efficiently sampling
 2651 the provided RHIC luminosity. Optimization of the v_z range used in the various analyses
 2652 involves a balance between statistical precision and complexity of corrections, with the latter
 2653 predominantly contributing to the systematic uncertainties of the measurement. Recent

2654 STAR jet measurements in Au+Au collisions have employed two classes of z-vertex cuts: the
2655 inclusive charged-particle jet analysis [315] utilizes $|vz| < 30$ cm, whereas the $\gamma_{\text{dir}}+\text{jet}$ analysis
2656 utilizes $|vz| < 70$ cm. With the $\gamma_{\text{dir}}+\text{jet}$ measurement successfully utilizing the broad vz range
2657 with controlled systematic precision, we are exploring similar event selections maximizing
2658 the available statistics for future jet measurements, including the inclusive/differential jet
2659 analyses. In Section 3 we present the sampled integrated luminosity in 2023 and 2025 for
2660 both the 30 cm and 70 cm vz cuts. The following physics performance projections are based
2661 on the 70 cm cut, using the cumulative sampled integrated luminosity for Run-14, Run-16,
2662 and 2023 and 2025 together. For $|vz| < 70$ cm, this total is 53.3 nb^{-1} , which is roughly a
2663 factor 7 increase in trigger statistics relative to the current analyses based on Run-14 data.

2664 The following paragraphs in this section will highlight some of these measurements in
2665 greater detail.

2666 3.3.1 Precision Jet Measurements to Study the QGP Micro-Structure

2667 To quantify the effect of the marked increase in integrated luminosity, we utilize two mature
2668 jet measurements currently in progress and discuss their expected improvement with en-
2669 hanced integrated luminosity. These analyses are the semi-inclusive distribution of charged-
2670 particle jets recoiling from a high- E_T direct-photon trigger ($\gamma_{\text{dir}} + \text{jet}$); and the differential
2671 measurement of energy loss for jet populations selected by varying a substructure metric.
2672 Since these analyses are mature, their analysis methodologies and correction schemes are
2673 optimized, so that their projections based on increased statistics are meaningful. We do
2674 not imply that these will be the only flagship measurements that STAR will make with
2675 the 2023/2025 datasets; we will additionally continue to focus, for instance, on fully re-
2676 constructed jets and utilizing substructure observables, including those not yet developed.
2677 However, these analyses are most mature at present, and therefore provide the most accurate
2678 projections of gain in precision.

2679 Semi-inclusive $\gamma_{\text{dir}} + \text{jet}$ Measurements

2680

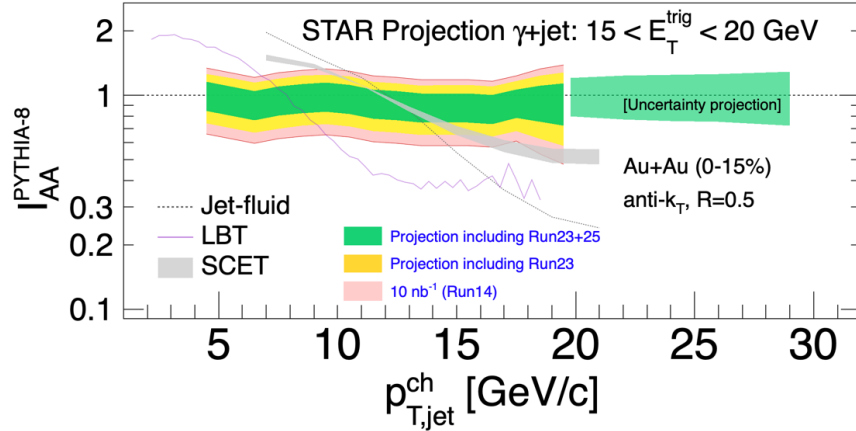


Figure 83: Projections for the I_{AA} for semi-inclusive anti- k_T , $R = 0.5$ jets recoiling from a direct-photon trigger with $15 < E_T < 20$ GeV for central (0-15%) Au+Au collisions at $\sqrt{s_{NN}} = 200$ GeV. The colored bands show the cumulative uncertainty for the current analysis and projections for future analysis with the higher statistics datasets.

2681 Figure 83 shows I_{AA} for fully-corrected semi-inclusive distributions of charged-particle
 2682 jets (anti- k_T , $R = 0.5$) recoiling from a direct-photon trigger with $15 < E_T < 20$ GeV in
 2683 central Au+Au collisions at $\sqrt{s_{NN}} = 200$ GeV, for the current analysis based on 10 nb^{-1} [316]
 2684 within $|vz| < 70$ cm. The projected uncertainties for Run-23 and Run-25 (75 nb^{-1} including
 2685 the previous years and Run-23 and Run-25) are shown in the yellow and green colored
 2686 bands respectively. Significant reduction in the uncertainty band is seen to result from the
 2687 increase in integrated luminosity, together with a significant increase in kinematic reach.
 2688 An additional Run-25 not only reduces the uncertainty but also improves the precision
 2689 measurement of high jet $p_{T,jet}$ as evident by the extended green band along the x-axis.

2690 The revised luminosity projection of 75 nb^{-1} reduces the systematic uncertainty band
 2691 by a factor of $1/\sqrt{7.5}$ from the current measurement since systematic uncertainty of this
 2692 measurement, dominated by the unfolding procedure, is correlated with the statistical pre-
 2693 cision. Due to this correlation, the improvement shown in Fig. 83 should be regarded as a
 2694 conservative estimate of the improvement in precision of this measurement channel with the
 2695 projected integrated luminosity increase.

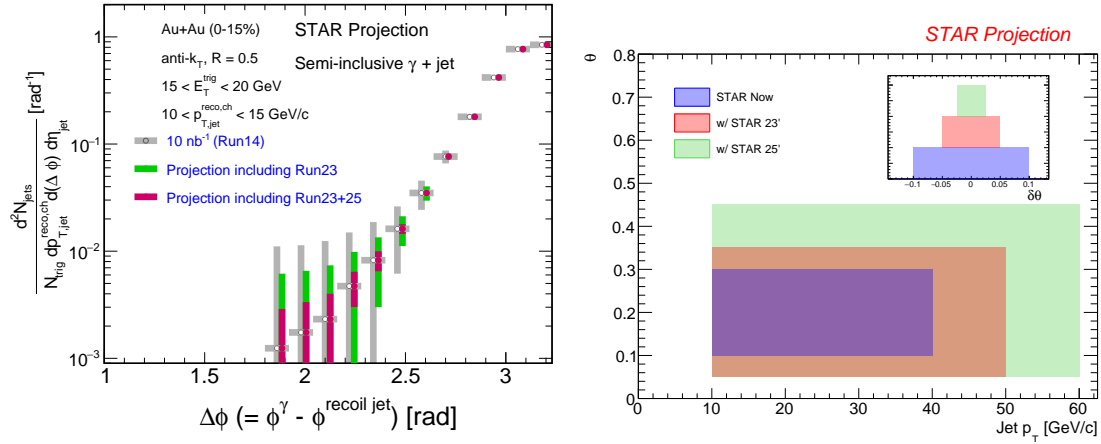


Figure 84: Left: Projections for the acoplanarity for semi-inclusive anti- k_T , $R = 0.5$ jets recoiling from a direct-photon trigger with $15 < E_T < 20$ GeV for central (0-15%) Au+Au collisions at $\sqrt{s_{NN}} = 200$ GeV. The colored bands show the cumulative uncertainty for the current analysis and projections for future analysis with the higher statistics datasets. Right: The subjet opening angle as a function of jet $p_{T,jet}$ in 0-20% central Au+Au collisions for various scenarios of data-taking. The inset is the corresponding resolution of θ . Blue, red, and green represent current (10nb^{-1}), with Run-23, and with Run-23+Run-25, respectively.

2696 The p_T broadening due to medium effects not only modifies the shape but also introduces
 2697 a decorrelation between the di-jet angular distributions. The vacuum QCD process (Sudakov
 2698 radiation) makes such measurements challenging in heavy-ion collisions, although at RHIC
 2699 the Sudakov effect is smaller than at the LHC as it depends on the virtuality Q^2 [311,
 2700 312]. A detailed study is needed to understand both these effects (medium-induced and
 2701 vacuum radiation) at a wide range of jet $p_{T,jet}$ both at RHIC and the LHC energies. Such
 2702 measurements are crucial to probe \hat{q} and/or quest for the predicted large-angle jet scattering
 2703 off of quasi-particles in the QGP [317].

2704 In this direction, STAR is undertaking a preliminary study using $\gamma_{dir} + \text{jet}$ and $\pi^0 + \text{jet}$ with
 2705 $11 < E_T < 15$ GeV and a charged-particle jet (anti- k_T , $R = 0.2$ and 0.5) with $10 <$
 2706 $p_{T,jet}^{ch} < 15$ GeV/c. The analysis techniques pertaining to this measurement are being studied
 2707 extensively to achieve precision on systematic uncertainty. Such measurements with higher
 2708 energy triggers (γ_{dir} and π^0) E_T^{trig} and $p_{T,jet}$ are crucial to study the inner working of the
 2709 QGP. This is limited by the current statistics, particularly to study recoil jets at a large $\Delta\phi$
 2710 angle. A similar study at the LHC is also ongoing using h+jet measurements [318].

2711 The left plot of Fig. 84 shows the semi-inclusive distribution of the azimuthal separation
 2712 between a direct-photon trigger with $15 < E_T < 20$ GeV and a charged-particle jet (anti- k_T ,
 2713 $R = 0.5$) with $10 < p_{T,jet}^{ch} < 15$ GeV/c, in central Au+Au collisions at $\sqrt{s_{NN}} = 200$ GeV with
 2714 only statistical uncertainties. The azimuthal smearing of this observable due to uncorrelated
 2715 background is small, and such acoplanarity measurements are therefore strongly statistics-
 2716 dominated [319, 320]. The grey points are from the current preliminary measurement based
 2717 on 10nb^{-1} , whereas the green and red points correspond to including Run-23 and Run-

2718 23+25 (75 nb^{-1}), respectively. A marked increase in measurement precision is projected,
2719 with corresponding qualitative increase in physics impact.

2720 **Differential Measurements of Energy Loss Tagged with a Substructure Metric**

2721

2722 Systematic exploration of parton energy loss controlled for variations in the jet shower
2723 forms an integral part of the jet program at STAR. Since parton showers are inherently
2724 probabilistic, a jet population contains patterns of radiation varying in both angle and mo-
2725 mentum fraction which can be extracted via jet substructure measurements designed with
2726 jet constituents' angle and/or momentum via algorithms or correlations. By selecting jets
2727 based on their substructure, STAR can differentially measure jet-medium interactions for
2728 various types of energy loss e.g. color coherence, dead cone, etc. In other words, the STAR
2729 jet program for Run-23+Run-25 will focus on jet substructure as a jet-tagger.

2730 Theory calculations show significant differences between energy loss signatures for jets
2731 perceived by the medium as a single or multiple color charges [308]. The integrated luminosity
2732 from the Run-23+Run-25 datasets not only provide a substantial increase in statistics in the
2733 current measurements of jet substructure, they also increase the available phase space for
2734 rare processes such as wide angle emissions from high- p_T jets. This enables STAR to extend
2735 our current measurements of differential energy loss, with a resolution of $\delta\theta = 0.1$ to finer
2736 resolution $\delta\theta \approx 0.025$ in the jet opening angle, measured via reconstructed subjets as shown
2737 in Fig. 84 (right) and also extend to jets of higher momenta. By extending to high energy
2738 splittings within jets, at varied opening angles, we can probe earlier formation times whereby
2739 vacuum-like emissions and medium induced radiations are expected to occur.

2740 Given the unique nature of jet-medium interactions at RHIC, with the jet and sub-jet
2741 scales sufficiently closer to the medium scale, the aforementioned measurements bolster the
2742 importance of the STAR jet program with the goal of extracting the microscopic properties
2743 of the QGP as outlined in the 2015 LRP.

2744 **3.3.2 Deconfinement and Thermalization With Charmonia Measurements**

2745 An important observable for studying the properties of the deconfined medium is the second
2746 order flow harmonic of the Fourier expansion of the azimuthal distribution of the produced
2747 hadrons, the elliptic flow coefficient v_2 . As in the case of light hadrons, a positive v_2 of
2748 D -mesons and electrons from heavy-flavor hadron decays was observed at RHIC energies
2749 of 54.4 and 200 GeV. Which suggests that charm quarks may (partially) thermalize and
2750 participate in the bulk medium collective evolution. On the other hand, the v_2 of heavier
2751 J/ψ reported by STAR based on the 2010 Au+Au 200 GeV data sample was found to be
2752 consistent with zero, albeit within large statistical uncertainties and systematic uncertainties
2753 due to non-flow effects. The precision of the measurement was also not enough to distinguish
2754 between theoretical model calculations that assume only primordial J/ψ production and ones
2755 that include additional J/ψ production via recombination. This calls for a larger sample of
2756 heavy-ion data at 200 GeV, as will be provided by RHIC in 2023 and 2025, in order to
2757 observe a possible non-zero J/ψ v_2 at RHIC energies and put more constraints on the J/ψ

2758 production models especially regarding its regeneration. Particularly important for these
 2759 studies is STAR's potential to measure low transverse momentum J/ψ with a very good
 2760 precision. This excellent low- p_T performance at STAR can be achieved thanks to its low
 2761 material budget and great particle identification capabilities.

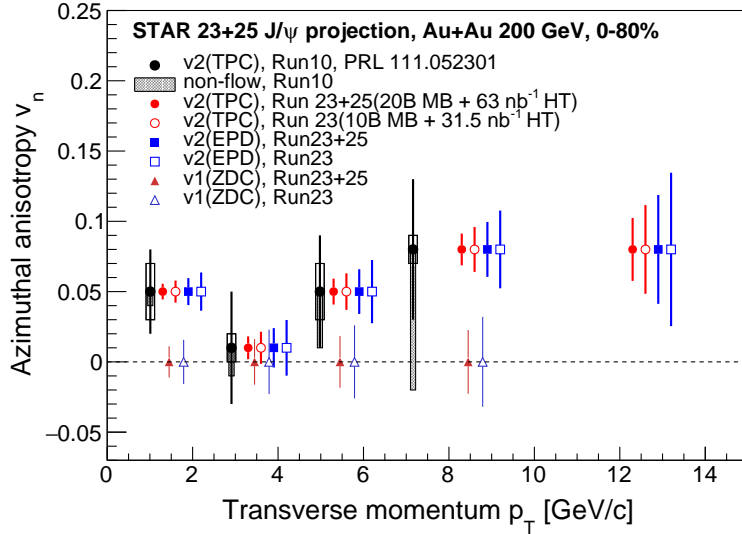


Figure 85: Projections for the J/ψ ($J/\psi \rightarrow e^+e^-$) directed (v_1) and elliptic (v_2) flow vs J/ψ p_T in 0-80% Au+Au collisions at 200 GeV, assuming 20 B MB events and HT triggered events corresponding to an integrated luminosity of 63 nb^{-1} with $|V_Z| < 30 \text{ cm}$.

2762 Moreover, the second order Event Plane (EP) can be reconstructed using the new Event
 2763 Plane Detectors (EPD) installed before Run-18. It is expected that using the forward EPD
 2764 will significantly decrease the contribution from the non-flow effects and consequently the
 2765 measurement's systematic uncertainties. Also, an inverse of the EP resolution enters di-
 2766 rectly the J/ψ v_2 uncertainty calculation. Thanks to the EPD, the resolution of the EP
 2767 reconstruction at forward rapidity for the J/ψ v_2 measurement at STAR will improve. Fig-
 2768 ure 85 presents statistical projections for the J/ψ v_2 measurement in 0-80% central Au+Au
 2769 collisions assuming 20 B MB events and HT triggered events corresponding to an integrated
 2770 luminosity of 63 nb^{-1} . Both cases of the second order EP reconstruction, using the for-
 2771 ward EPD and mid-rapidity TPC detectors, are considered and shown. A clear significant
 2772 improvement in the precision of the J/ψ v_2 can be seen across the whole experimentally
 2773 accessible J/ψ p_T coverage of the previous measurement. In addition, the new larger dataset
 2774 would allow to extend the measured p_T range beyond 10 GeV/ c .

2775 Studies of the directed flow, v_1 , as a function of rapidity provide crucial information to
 2776 understand the initial tilt of the medium produced in heavy-ion collision [313, 314]. Heavy
 2777 quarks are produced in the early stage of a heavy-ion collision and thus are of particu-
 2778 lar interest for the medium initial asymmetry studies. STAR recently reported the first
 2779 measurement of D-meson v_1 in Au+Au collisions at 200 GeV where the magnitude of the
 2780 heavy-flavor meson v_1 is about 25 times larger than the v_1 for charged kaons. With the

2781 2023-2025 data, STAR would have a unique opportunity to also study the v_1 of a bound
 2782 $c\bar{c}$ state, the J/ψ mesons, for which even larger directed flow can be expected [321]. In
 2783 addition to STAR's excellent capability to reconstruct low- p_T J/ψ , as discussed above, the
 2784 iTPC detector completed in 2018 will improve the momentum resolution and extend the
 2785 pseudorapidity coverage. This will provide better precision for the slope extraction of the v_1
 2786 vs y measurement, that quantifies the strength of directed flow. The expected precision of a
 2787 J/ψ v_1 measurement vs p_T at STAR in 2023-2025, assuming 20 B MB events and HT trig-
 2788 gered events corresponding to an integrated luminosity of 63 nb^{-1} , in 0-80% central Au+Au
 2789 collisions at 200 GeV is shown in Fig. 85. Together with the J/ψ v_2 measurements, v_1 would
 2790 provide a more complete picture of the J/ψ production mechanism as well as the medium
 2791 properties in heavy-ion collisions at RHIC.

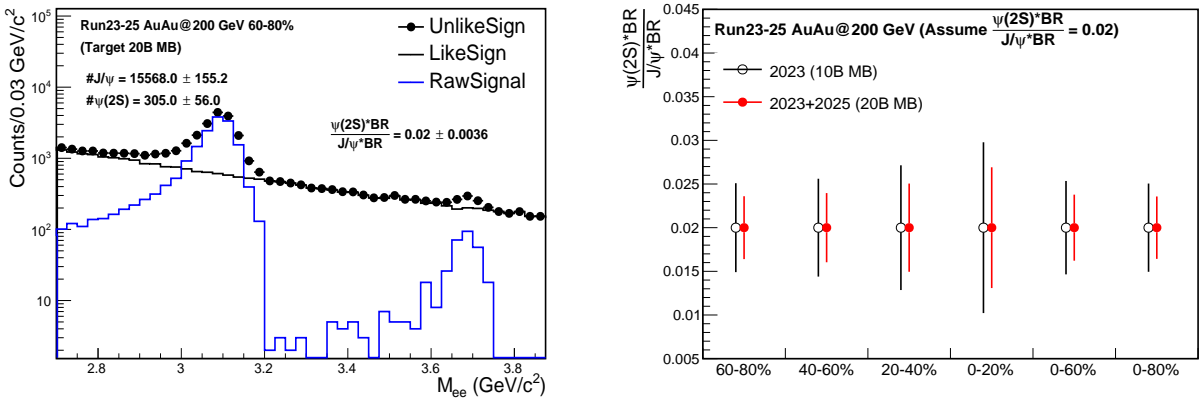


Figure 86: Projections for the J/ψ and $\psi(2S)$ signals in 60-80% Au+Au collisions at 200 GeV and the yield ratio in various centrality bins. The improvement of momentum and dE/dx resolution thanks to the iTPC upgrade have not been taken into account.

2792 $\psi(2S)$ is the most loosely bounded quarkonium state currently accessible to heavy-ion
 2793 collision experiments. Its dissociation temperature is predicted to be around, or below, the
 2794 critical temperature, and is much less than that of J/ψ and Υ states. It is therefore more
 2795 likely to be dissociated in the early stage and in the core of the fireball, and those $\psi(2S)$
 2796 that are measured may have significant contributions from regeneration at a later stage in
 2797 the evolution of the fireball. The relative suppression of $\psi(2S)$ and J/ψ is sensitive to the
 2798 temperature profile of the fireball produced in heavy-ion collisions and its space-time evolu-
 2799 tion. It is also argued that the charmonium formation process from a $c\bar{c}$ pair may be affected
 2800 by both the QGP and the initial strong external magnetic field, altering the relative yields
 2801 among different charmonium states [322, 323]. The measurement of $\psi(2S)$ is much more
 2802 difficult than that of J/ψ due to a much smaller production cross-section and dilepton decay
 2803 branching ratio, resulting in a very low signal-to-background ratio. The ALICE Collabora-
 2804 tion successfully measured the relative suppression of $\psi(2S)$ and J/ψ in Pb+Pb collisions
 2805 at forward rapidity [324], and the ATLAS and CMS Collaborations published the relative
 2806 suppression in Pb+Pb collisions at mid-rapidity and high p_T [325, 326]. Attempts to measure

2807 $\psi(2S)$ suppression in heavy-ion collisions at RHIC have not been successful to date. The low
 2808 material budget and excellent particle identification capability of STAR together with the
 2809 combined large data sample in 2023 and 2025 will provide a unique opportunity to measure
 2810 the suppression of $\psi(2S)$ at low p_T and mid-rapidity in heavy-ion collisions. Figure 86 shows
 2811 the projections of $\psi(2S)$ signal and the yield ratio of $\psi(2S)$ and J/ψ from 20 B MB events
 2812 in Au+Au collisions. Here the $\psi(2S)/J/\psi$ ratio is assumed to be 0.02, and the performance
 2813 of detectors from existing data before STAR iTPC upgrade is used for the projection. As
 2814 shown in the figure, the $\psi(2S)$ signal significance will be around 3σ level in the 0-20% cen-
 2815 trality bin. This significance could become even smaller depending on the level of further
 2816 suppression for $\psi(2S)$ compared to J/ψ . Despite the improvement of momentum and dE/dx
 2817 resolution thanks to the STAR iTPC upgrade, it is crucial to have both the 2023 and 2025
 2818 data for a significant $\psi(2S)$ measurement.

2819 3.4 Electromagnetic Probes and Ultra-peripheral collisions

2820 3.4.1 Probing the degrees of freedom of the medium and its transport proper- 2821 ties:

2822 At $\mu_B \sim 0$ Lattice QCD works and can be directly tested against experimental results.
 2823 In case the measured in-medium spectral function merges into the QGP description this
 2824 would indicate a transition from hadrons into a structure-less quark-antiquark continuum,
 2825 thus providing the manifestation of chiral symmetry restoration. We will continue to search
 2826 for a direct signature of chiral symmetry restoration via chiral ρ - a_1 mixing. The signal is
 2827 predicted to be detectable in the dilepton intermediate mass range. Difficulties are related
 2828 to the fact that correlated charm-anticharm and QGP saturate the invariant mass region
 2829 of 1.1 — 1.3 GeV/ c^2 . Therefore an accurate measurement of the excess dilepton yield, i.e.
 2830 dilepton yield after subtraction of the cocktail of contributions from final-state decays, Drell-
 2831 Yan and those from correlated heavy-flavor decays, up to invariant mass of 2.5 GeV/ c^2 is
 2832 required. The challenging analysis on charmed-decayed dielectron is ongoing from the data
 2833 sets taken with the Heavy Flavor Tracker at STAR [327]. Thus deeper understanding of
 2834 origin of thermal radiation in Au+Au collisions at $\sqrt{s_{NN}} = 200$ GeV from \sim zero mass up
 2835 to 2.5 GeV/ c^2 will become possible with rigorous theoretical efforts and improved dielectron
 2836 measurements. Figure 87 shows the expected statistical and systematic uncertainties of the
 2837 dielectron excess mass spectrum with all the detector upgrades and for the anticipated total
 2838 Run-23/Run-25 statistics of 20×10^9 events.

2839 Another application of dileptons is to use them to measure transport coefficients. The
 2840 electrical conductivity can be directly obtained as the low-energy limit of the EM spectral
 2841 function. We aim to extract such information by studying excess dielectron yields at the low-
 2842 energy regime of the dilepton spectra and the conductivity peak at small invariant masses,
 2843 i.e. at low invariant mass and low p_T^{ee} . Low field run could be profitable, however already
 2844 now leptons with p_T^e down to 60 MeV/ c could be measured. Measurement of Drell-Yan in
 2845 p +A collisions at low p_T would provide an important reference to constrain the dilepton
 2846 cocktail.

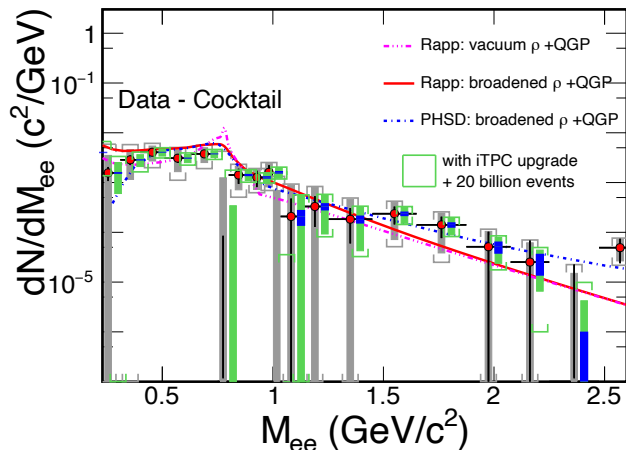


Figure 87: The expected statistical and systematic uncertainties on the dielectron excess mass spectrum with the iTPC upgrade compared to the current TPC case. The data are from our measurements in $\sqrt{s_{NN}} = 200$ GeV Au+Au collisions [328]. Model comparisons are also shown. The boxes represent systematic uncertainties from data and the brackets represent the total systematic uncertainties including those from cocktails. The grey ones are for the current case while the green ones are for the Run-23+Run-25 case. The blue bands represent statistical uncertainties from 20 billion minimum-bias events with the iTPC upgrade.

2847 To gain a deeper understanding of the microscopic origin of the excess radiation, we will

2848 • separate early from later time radiation by measuring dilepton elliptic flow (v_2) as a
2849 function of dilepton mass;

2850 • identify the source of dilepton radiation by studying dilepton polarization versus in-
2851 variant mass (helicity angle);

2852 • measure precisely the lifetime of the interacting fireball. As an observable we will use
2853 integrated low-mass yield but also compare explicit model calculations with various
2854 $\mathcal{T}_{fireball}$;

2855 • extract an average radiating source temperature from the fit of a Boltzmann distribu-
2856 tion to the invariant mass slope in the range 1.1 - 2.5 GeV/ c^2 spectrum. The higher
2857 the invariant mass, the stronger the QGP contribution to the spectrum, the higher the
2858 chance to measure temperature of the QGP.

2859 Last, but not least, concerning direct-photon emission, the existing difference, on the
2860 order of a factor of two, between the low momentum spectra from PHENIX and STAR in
2861 200 GeV Au+Au collisions, has to be resolved. In order to clarify the direct photon puzzle
2862 we will measure with precision the direct virtual photon yield as well as its elliptic flow
2863 coefficient. We will particularly focus on low p_T η measurement which might be instrumental
2864 in clarifying this long standing question.

2865 **3.4.2 Studying the Photon Wigner Function and Final-state Magnetic Fields**
 2866 **in the QGP**

2867
 2868 The unsuccessful description of STAR data by the STARLight model led to the attribution
 2869 of the broadening to the possible residual magnetic field trapped in an electrically conducting
 2870 QGP [329]; which is key information to the study of the chiral magnetic effect.

2871 Similarly, ATLAS quantified the effect via the acoplanarity of lepton pairs in contrast
 2872 to the measurements in UPC and explained the additional broadening by multiple electro-
 2873 magnetic scatterings in the hot and dense medium [330], which is analogous to the medium
 2874 P_{\perp} -broadening effects for jet quenching.

2875 These descriptions of the broadening in hadronic collisions are based on the assumption
 2876 that there is no impact parameter dependence of the transverse momentum distribution for
 2877 the electromagnetic production. Recent lowest-order QED calculations, in which the impact
 2878 parameter dependence is recovered, could reasonably describe the broadening observed by
 2879 STAR and ATLAS without any in-medium effect. To solve the puzzle, we propose to precisely
 2880 study the initial P_{\perp} -broadening for the dilepton pair in ultra-peripheral collisions. Different
 2881 neutron emission tags serve as the centrality definition, and will allow us to explore the
 2882 broadening baseline variation with impact parameter. Furthermore, the differential spectrum
 2883 as a function of pair P_{\perp} , rapidity, and mass enable us to study the Wigner function of the
 2884 initial electromagnetic field, which provide the information to extract the momentum and
 2885 space correlation of EM field.

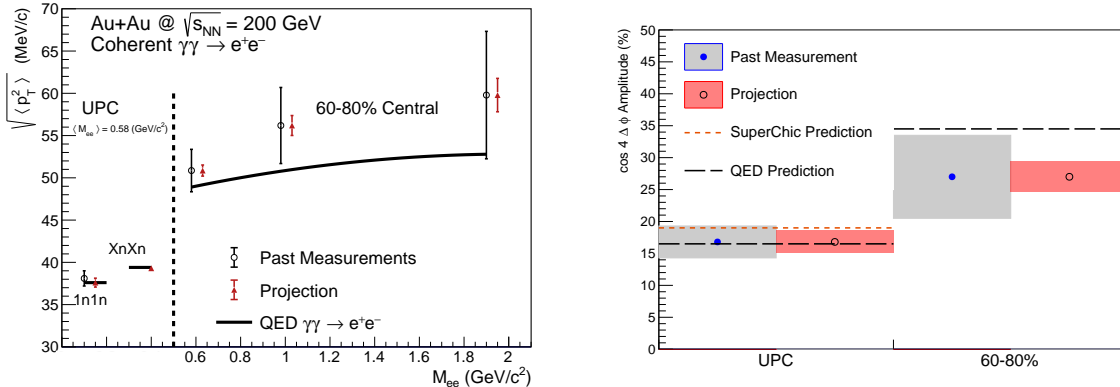


Figure 88: (Color online) Projections for measurements of the $\gamma\gamma \rightarrow e^+e^-$ process in peripheral and ultra-peripheral collisions. Left: The $\sqrt{\langle p_{\perp}^2 \rangle}$ of di-electron pairs within the fiducial acceptance as a function of pair mass, M_{ee} , for 60–80% central and ultra-peripheral Au+Au collisions at $\sqrt{s_{\text{NN}}} = 200$ GeV. Right: The projection of the $\cos 4\Delta\phi$ measurement for both peripheral (60–80%) and ultra-peripheral collisions.

2886 As shown in Fig. 88, comparing with the latest QED calculation, there still exists addi-
 2887 tional broadening in peripheral collisions, although the significance is only about 1σ , which
 2888 still leave room for the medium effect. In Run-23 and Run-25, as projected in the figure, we

2889 could judge the existence of additional broadening with much higher precision and further
2890 constrain the strength of final-state magnetic field in the QGP.

2891 Precision measurement of the amplitude of the recently observed $\cos 4\Delta\phi$ modulation of
2892 the $\gamma\gamma \rightarrow e^+e^-$ process will allow precision mapping of the photon Wigner function and
2893 provide additional constraints on possible final-state effects, thereby complementing the P_\perp
2894 broadening measurement. Figure 88 right panel shows the projected precision for a mea-
2895 surement of the $\cos 4\Delta\phi$ modulation in Run-23+25. The modulation is a direct result of
2896 the mismatch in initial and final spin configuration of the $\gamma\gamma \rightarrow e^+e^-$ process. Any final-
2897 state effect that modifies the P_\perp will necessarily reduce the amplitude of the modulation.
2898 Assuming the same central value as previously measured, evidence for suppression of the
2899 $\cos 4\Delta\phi$ modulation will be visible at the $> 3\sigma$ level (stat. & syst. uncertainty). Preci-
2900 sion measurement of the $\cos 4\Delta\phi$ modulation in Run-23+25 may also allow a first direct
2901 experimental measurement of the impact parameter dependence of this new observable (by
2902 comparing UPC and 60 – 80%). Assuming the same central values as previously measured,
2903 the improved precision will provide evidence for impact parameter dependence at the $> 3\sigma$
2904 level (stat. & syst. uncertainty). Assuming the central value predicted by QED would lead
2905 to a $> 5\sigma$ difference between the UPC case and the 60 – 80% case.

2906 3.4.3 Ultra-peripheral Au+Au Collisions: Probe Gluon Distribution Inside the 2907 Nucleus

2908
2909 STAR recently observed a significant $\cos 2\Delta\phi$ azimuthal modulation in $\pi^+\pi^-$ pairs from
2910 photonuclear ρ^0 and continuum production. The structure of the observed modulation as
2911 a function of the $\pi^+\pi^-$ pair transverse momentum, P_\perp , appears related to the diffractive
2912 pattern. Recent theoretical calculations [331], which implemented linearly polarized pho-
2913 tons interacting with the saturated gluons inside a nucleus, have successfully described the
2914 qualitative features of the observed modulation(see Fig. 89), and indicate that the detailed
2915 structure of the $\cos 2\Delta\phi$ modulation vs. P_\perp is sensitive to the nuclear geometry and gluon
2916 distribution. Data from Run-23+25 would allow the additional statistical reach needed to
2917 perform multi-differential analysis, providing stronger theoretical constraints. Specifically,
2918 multi-differential analysis of the $\cos 2\Delta\phi$ modulation with respect to pair rapidity and pair
2919 mass are needed. Multi-differential analysis with respect to pair mass is needed to separate
2920 the ρ^0 production from the continuum Drell-Soding production. Multi-differential analysis
2921 with respect to the pair rapidity is needed to quantitatively investigate how the double-slit
2922 interference mechanism effects the structure of the observed azimuthal modulation. Addi-
2923 tional statistical precision is also needed for measurement of the higher harmonics. Similar
2924 measurements with $J/\Psi \rightarrow e^+e^-$ can be performed and such measurements at higher mass
2925 provide better comparison with more reliable QCD calculation.

2926 Ultraperipheral Å collisions, where photons generated by the Lorentz-boosted electro-
2927 magnetic field of one nucleus interact with the gluons inside the other nucleus, can provide
2928 certain 3D gluonic tomography measurements of heavy ions, even before the operation of
2929 the future EIC. STAR has performed experimental measurements of the photoproduction

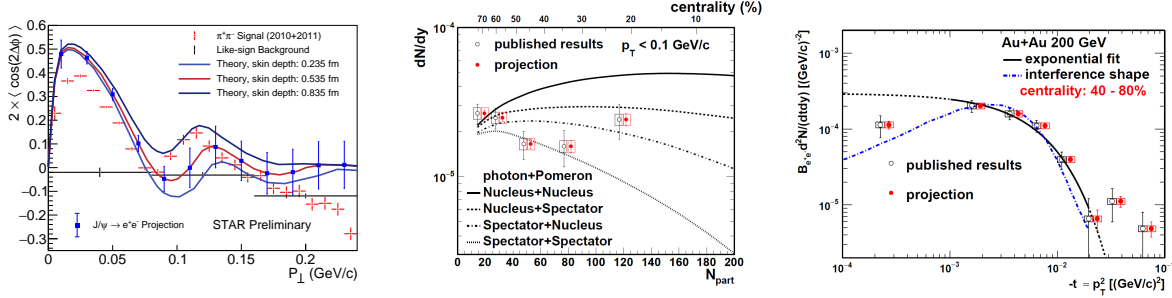


Figure 89: Left: Measurement of the $\cos 2\Delta\phi$ modulation of $\pi^+\pi^-$ pairs from photonuclear ρ^0 and continuum production compared to theoretical predictions [331]. Projections are shown for a similar measurement of the azimuthal modulation of e^+e^- pairs from photonuclear production of the J/ψ . Center: Projection of the dN/dy of photoproduced J/ψ in non-UPC events vs. the event centrality (N_{part}) compared to various theoretical production scenarios. Right: Projection of the t spectra of photoproduced J/ψ in 40 – 80% central collisions.

2930 of J/ψ at low transverse momentum in non-UPC heavy-ion collisions [332], accompanying
 2931 the violent hadronic collisions. A detailed study with p_T distributions has shown that the
 2932 $|t|$ distribution in peripheral collisions is more consistent with the coherent diffractive pro-
 2933 cess than the incoherent process. Although models [333, 334] incorporating different partial
 2934 coherent photon and nuclear interactions could explain the yields, it remains unclear how
 2935 the coherent process happens and whether final-state effects play any role [335]. Resolving
 2936 this puzzle with high statistical data and detailed $|t|$ distributions at different centralities
 2937 at RHIC as projected for Run-23+25 in Fig. 89 may be important for understanding what
 2938 defines the coherentness of the photoproduction, how vector mesons are formed in the pro-
 2939 cess and how exclusive the similar process has to be in future EIC experiments with forward
 2940 neutron veto/tagging.

4 Forward Upgrade

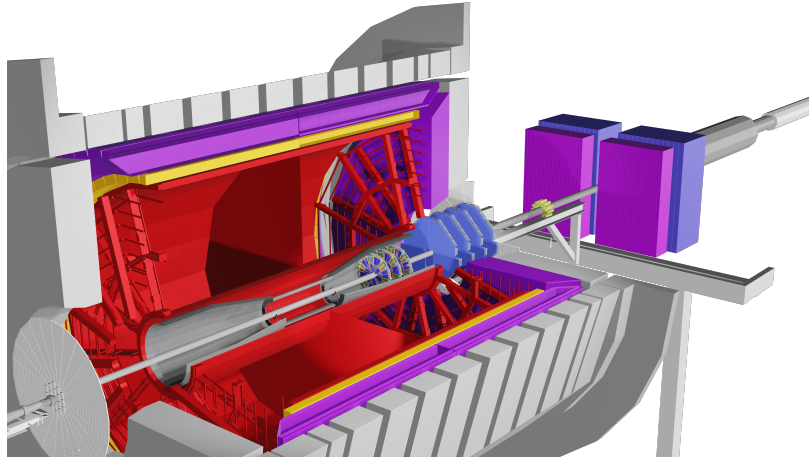


Figure 90: A view of the detectors comprising the STAR forward upgrade, rendered by simulation.

2942

STAR is finalizing construction of the forward detector system, realized by combining tracking with electromagnetic and hadronic calorimeters, in preparation for first data taking in Run-22. It will have superior detection capability for neutral pions, photons, electrons, jets, and leading hadrons within the pseudorapidity range $2.5 < \eta < 4$.

2946

The design of the Forward Calorimeter System (FCS) was driven by consideration of detector performance, integration into STAR, and cost optimization. For the electromagnetic calorimeter, components of the refurbished PHENIX sampling EMCAL were used, while the hadronic calorimeter has been newly constructed as a sandwich iron/scintillator plate sampling type, based on extensive STAR Forward Upgrade and EIC Calorimeter Consortium R&D. The existing Event Plane Detector (EPD) will be used as a trigger detector, especially for di-electron triggers. Both calorimeters share the same cost-effective readout electronics, with SiPMs as photo-sensors. The FCS system will have very good electromagnetic ($\sim 10\%/\sqrt{E}$) and hadronic ($\sim 50\%/\sqrt{E} + 10\%$) energy resolution.

2955

In addition, a Forward Tracking System (FTS) is being constructed. The FTS will be capable of discriminating hadron charge sign for transverse spin asymmetry and Drell-Yan measurements in pp and $p+A$ collisions. In heavy ion collisions, measurements of charged-particle transverse momenta over the range $0.2 < p_T < 2$ GeV/ c with 20-30% momentum resolution are required. To keep multiple scattering and photon conversion backgrounds under control, the material budget of the FTS must be small. Hence, the FTS design is based on three Silicon mini-strip detectors that consist of disks with a wedge-shaped design to cover the full azimuth and $2.5 < \eta < 4.0$; they are read out radially from the outside to minimize the material. The Si-disks are combined with four small-strip Thin Gap Chamber (sTGC) wheels following the ATLAS design [336, 337]. The three Si mini-strip disks will be located in the region $z = 146.6 - 173.7$ cm, while the four sTGC wheels will be placed 30 cm apart starting from $z = 273$ cm. The Si-Disks readout is based on APV chips and will reuse

2966

2967 the readout chain of the IST, which was part of the STAR HFT. For the sTGC the readout
2968 will be based on the ATLAS VMM3 chip [338].

2969 4.1 Status

2970 Following a successful Director’s Review in November 2018, the FCS consortium submitted
2971 an NSF Major Research Instrumentation (MRI) proposal for construction of the EMCAL
2972 and HCAL and associated electronics. The MRI was approved in Summer 2019 and work
2973 began in earnest on all aspects of the upgrade. In August 2020, another successful Director’s
2974 Review was conducted on the status of the upgrades. No serious issues were found. By the
2975 end of 2020, construction of both the EMCAL and HCAL had been successfully completed;
2976 they are now being commissioned as part of the ongoing Run-21. The Silicon Tracker and
2977 sTGC Tracker systems are expected to finish construction in June 2021, and will be installed
2978 in STAR prior to the start of Run-22.

2979 4.2 Forward Calorimeter System

2980 The platform that supports the HCAL and EMCAL was installed in 2019, followed by
2981 installation and stacking of the refurbished PHENIX EMCAL blocks.

2982 Production of the HCAL absorber blocks at Chapman Lake Instrumentation and Gatto
2983 Industrial Plating was completed in late summer 2020, with all parts delivered to BNL. All of
2984 the 18,200 scintillating tiles have been produced and polished at ACU, Valparaiso, UCLA and
2985 OSU. Front-end electronics boards were designed and tested at Indiana University, sent out
2986 for commercial production, then QA’ed at IU and UKY. Other parts have been fabricated,
2987 tested, and calibrated at Rutgers, Temple, BNL and UCLA. HCAL construction started on
2988 the platform in Fall 2020, and successfully finished by the end of 2020 on schedule despite
2989 following COVID19 restrictions, as seen in Fig. 91.

2990 For both the EMCAL and HCAL, front-end electronics cards with SiPM sensors were
2991 installed, calibrated, and commissioned with very few failures, and are now fully working.
2992 Seventy-eight DEP/ADC readout boards and three DEP/IO boards for trigger processing
2993 have been produced and installed in five crates at STAR. They are connected to DAQ PCs
2994 and are currently being used to take data during Run-21. About 0.5% of channels were
2995 found to have issues, and will be fixed during the upcoming shutdown.

2996 LED systems were also installed for both the EMCAL and HCAL. They are being used
2997 for mapping verification, as shown in Fig. 92, and for short- and long-term gain stability
2998 monitoring, as well as determining temperature compensation for the SiPM voltages. Ra-
2999 diation damage monitoring has started and small increases in the dark current have been
3000 observed, which fall well within the expected range.

3001 A signal splitter for the west EPD has been designed, and two prototype boards were
3002 produced. These were installed in late May 2021 for testing and for timing adjustments
3003 during the remaining weeks of Run-21. A total of 24 boards (plus spares) will be produced
3004 and installed prior to Run-22.

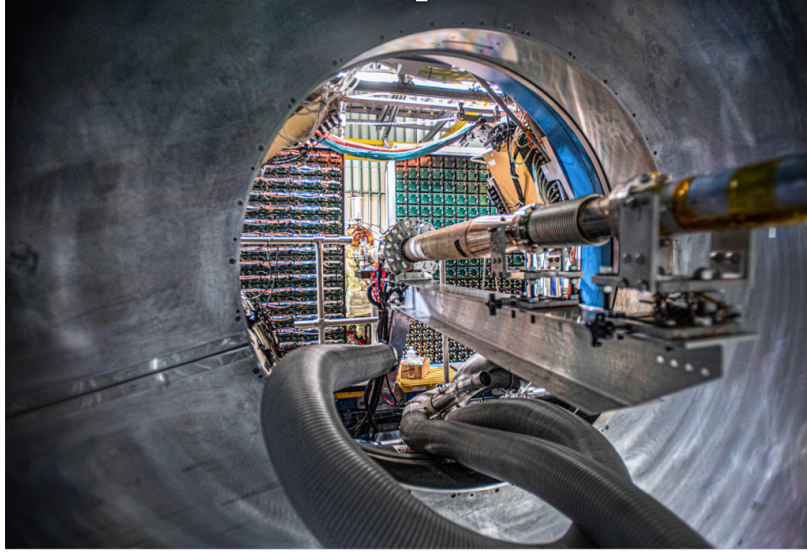


Figure 91: A view of the installed forward EMCAL, with the HCAL behind, left and right of the beam pipe.

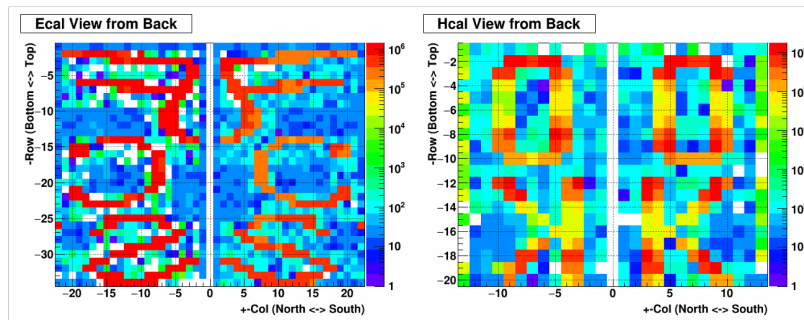


Figure 92: An event display of FCS EMCAL and HCal with voltage patterns loaded for mapping checks.

3005 4.3 Forward Silicon Tracker

3006 The Forward Silicon Tracker (FST) consists of three disks, each with 12 wedge-shaped de-
 3007 tector modules. Each module is separated into two sections along the radial direction, with
 3008 Silicon mini-strip sensors mounted on different sides of the module respectively. These mod-
 3009 ules will be mounted on an aluminum support structure and inserted into the inner cone
 3010 of the STAR TPC. Two prototype detector modules were assembled and their efficiency
 3011 and resolution were verified with cosmic ray (see Figure 93). Mass production of detector
 3012 modules started after a FST production readiness review in Aug. 2020. As of May 2021,
 3013 about 40 detector modules have been fully assembled and tested successfully at Fermilab
 3014 and at the University of Illinois at Chicago. Six of these have arrived at BNL for initial
 3015 installation tests; the rest will be shipped in the first week of June. The support structure
 3016 and its associated installation tooling have been fabricated and assembled in the STAR clean

3017 room. Mounting detector modules onto the support structure has started, together with the
 3018 full set of cabling and cooling tube connections. The cooling and DAQ systems, which were
 3019 used previously for the HFT-IST sub-system, have been incorporated into the FST and their
 3020 performance has been verified. The operation of the entire detector will be verified by run-
 3021 ning the cooling and DAQ systems with the fully assembled detector in the clean room in
 3022 June-July before installation into STAR in August, 2021. Despite all the complications and
 3023 challenges imposed by COVID19, the Forward Silicon Tracker upgrade project has stayed
 3024 on schedule and the detector is expected to be ready for physics data taking in Run-22.

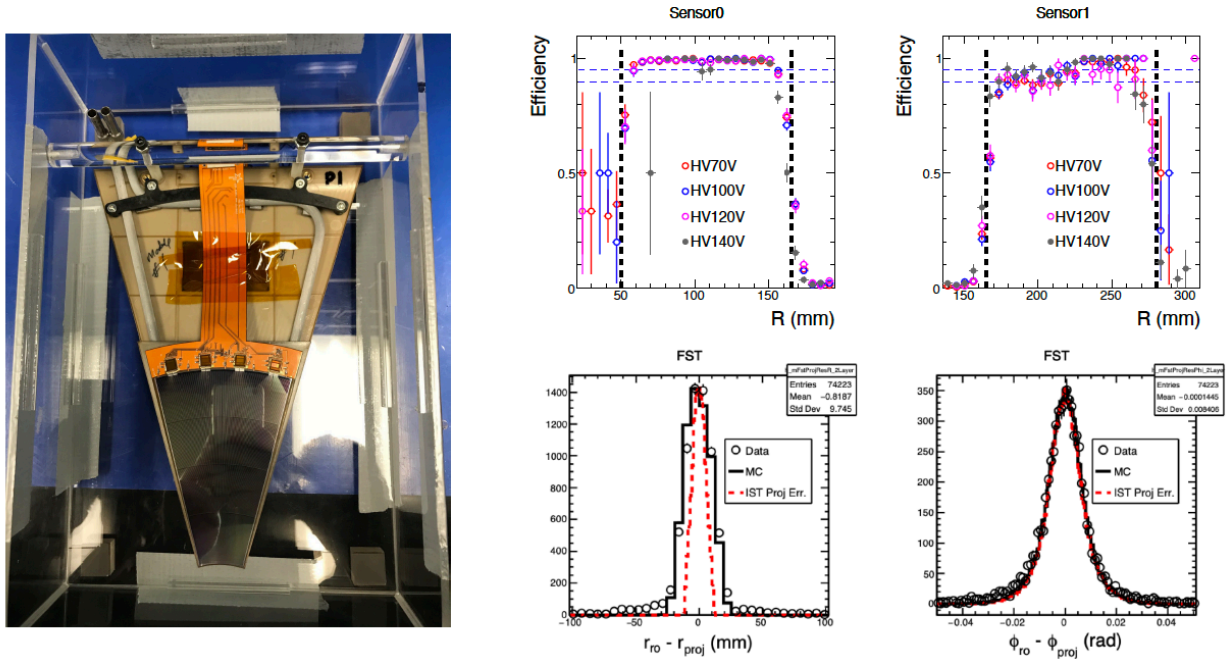


Figure 93: Left: a photograph of a FST detector module in the storage box with the Silicon sensor in the inner section facing up. Right: measured FST detector module performance from cosmic ray testing. Shown on the top are the efficiencies for the inner (left) and outer sensor (right) respectively. Shown in the bottom are the residual distributions between the measured and projected positions in the radial and azimuthal directions, respectively.

3025 4.4 Forward sTGC Tracker

3026 The sTGC system for the forward upgrade has been designed by collaborators from Shandong
 3027 University, who also oversee the mass production and testing of the sTGC modules. A 60×60
 3028 cm^2 sTGC module was produced, and was found to have a position resolution of 140 microns
 3029 and a detector efficiency of 97.3%. This module was shipped to BNL and installed at STAR
 3030 for data taking this year. Due to space constraints around the beam pipe, the final sTGC
 3031 modules have been designed to have a pentagon shape (see Figure 94). Four pentagon
 3032 pre-production modules were assembled in August 2020. Following an sTGC production
 3033 readiness review in Nov. 2020, comments and suggestions received from the review committee

3034 were addressed. Mass production of pentagon modules started in March 2021; 20 pentagon
 3035 sTGC stations have been produced as of mid-May this year.

3036 High detector efficiencies and low leakage currents have been demonstrated for the pro-
 3037 duced stations. Final position resolutions will be measured using the new read-out electron-
 3038 ics, which is based on the ATLAS VMM3a chip developed for a similar detector. The strips
 3039 of each sTGC layer will be read out by 24 Front-End Boards (FEBs), so a total of 96 FEBs
 3040 are needed for the four sTGC layers. The signals are sent to a Readout Board Driver (ROD)
 3041 and interfaced to STAR DAQ. The electronics design and fabrication was carried out by
 3042 USTC. The FEB design is complete and final production is ongoing. RDO construction is
 3043 finished, as is design of the installation and mounting frames. The required n-pentane gas
 3044 system and interlocks have been designed and approved at BNL. The full sTGC system will
 3045 be installed at STAR during the shutdown this summer.

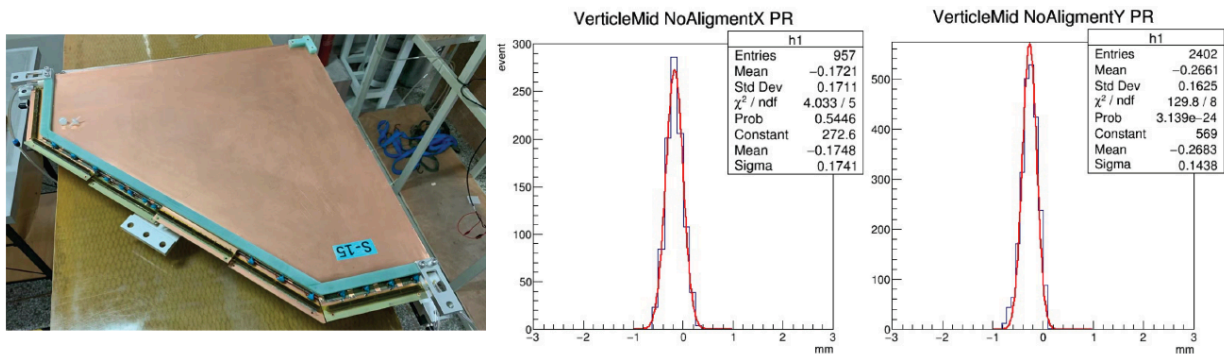


Figure 94: Left: a photograph of a pentagon-shaped sTGC module. Middle and right: residual distributions between the measured and projected positions of the $60 \times 60 \text{ cm}^2$ sTGC prototype in the x and y directions, respectively, from cosmic ray testing.

3046 In order to mitigate the effect of COVID19 and stay on schedule, more engineers for
 3047 module production were hired at Shandong University. However, the delay in procurement
 3048 of necessary materials to build up sTGC mechanical supporting structures and unpredicted
 3049 damages to our first 4 pentagon-shaped sTGC modules in the shipping process make our
 3050 schedule very tight even though we think we can still make our trackers ready for Run-22.

3051 4.5 Software

3052 Much of the software needed for the Forward Calorimeter System has already been developed,
 3053 including DAQ, online monitoring, trigger algorithm simulation and verification, slow control
 3054 and alarming, and recording the detector status to the STAR database. Offline codes for
 3055 fitting pulse shapes, cluster finding, and cluster analysis are working. From test data taken
 3056 with 200 GeV Au+Au collisions during Run-19, π^0 and MIP peaks in the EMCAL were
 3057 successfully reconstructed and identified, as shown in Fig. 95 and Fig. 96. Data have also
 3058 been collected from 200 GeV O+O collisions during the ongoing Run-21 using the fully
 3059 assembled FCS, and are being analyzed to set final calibrations.

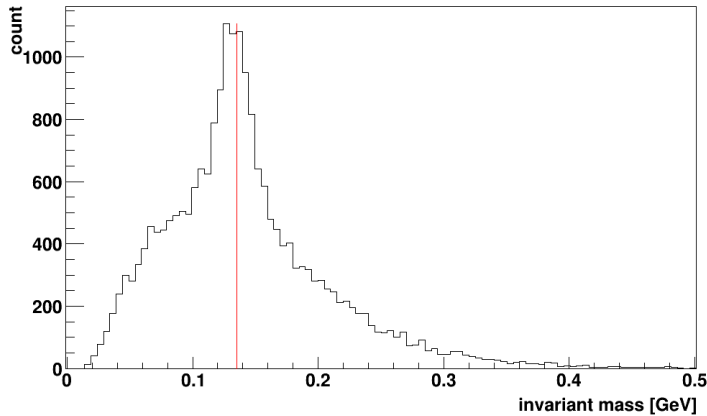


Figure 95: Reconstructed π^0 peak from 200 GeV Au+Au collisions taken during Run-19.

3060 Sets of trigger algorithms for the FCS have been developed, based on simulations per-
 3061 formed by Texas A&M. FPGA codes have been written, loaded to the DEP/IO boards,
 3062 their timing adjusted and verified, and are currently being used for data taking during the
 3063 ongoing Run-21. We will continue to work on refining the algorithms, as it was found that
 3064 more powerful logic is available on the FPGAs than is used in current algorithms.

3065 Preliminary versions of slow control, DAQ, and online monitoring software for the track-
 3066 ing detectors have also been developed and tested. Track reconstruction algorithms utilizing
 3067 hits from the four sTGC planes and the three Si layers have been developed, and good per-
 3068 formance has been demonstrated. The tracking algorithm is based on modern techniques:
 3069 it depends on GENFIT, a general purpose tracking toolkit, and on the iLCSoft KiTrack, a
 3070 Cellular Automata library, which is used to seed track finding. Other components of the
 3071 offline software needed for the tracking detectors are being developed and tested.

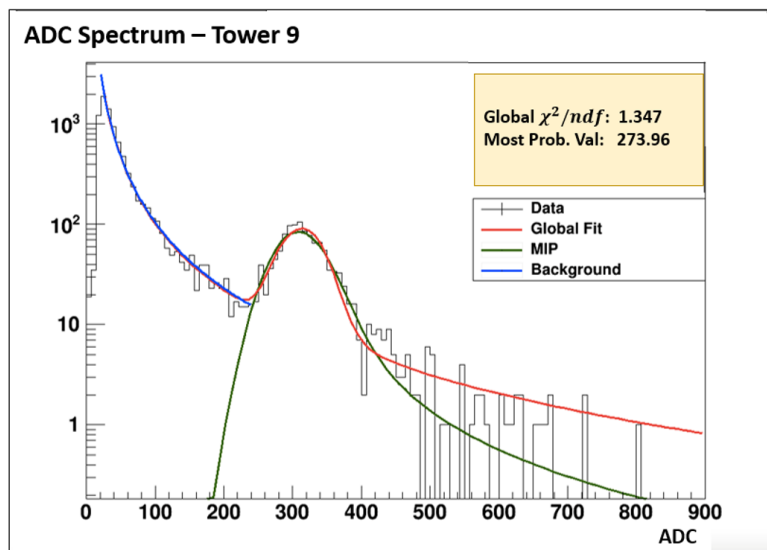


Figure 96: Reconstructed MIP peak from 200 GeV Au+Au collisions taken during Run-19.

5 Future Opportunities

Experience from the BES-II has taught us that the excellent performance from RHIC may allow us to take short opportunistic datasets that enable unique physics programs with minimal extra running time. With this in mind we outlined in Section 1.5 a request for a short d+Au run in Run-21 if time permits. If this is not possible, STAR remains interested in taking this data if the opportunity arrives in 2023-2025. Below we outline two other opportunistic programs, both are of great interest to STAR and the larger nuclear physics community.

5.1 Fixed-target Measurements Using Light Beam and Target Combinations

Although the proposed fixed-target Au+Au energy scan has been completed, if the opportunity exists for further measurements, light beam and target combinations could help to clarify the role and mechanisms of nucleon stopping. Indeed, STAR was recommended to consider installing a beryllium target, that being the lowest Z feasible solid target which could work with the target apparatus. This was not done previously because changing the target requires opening the STAR beampipe and removing the existing target, and that could not be done until the Au+Au energy scan had been completed. Both the collider and STAR have demonstrated that fixed-target runs can be quickly tuned, as the demands on collider operations are modest, and efficiently run, as the collider can control and deliver sufficient intensity to fill the STAR DAQ bandwidth and the experiment can cleanly trigger on these events.

It is possible that fixed-target collisions using light beam and target combinations could also benefit the Space Radiation Protection community. Cosmic rays are a serious concern to astronauts, electronics, and spacecraft. Although 90% of the cosmic ray flux is comprised of energetic protons and another 9% is Helium nuclei, the remaining 1%, which is made up of nuclei from Li to Fe, is not negligible both because the energy loss is proportional to Z^2 and because additional damage is done by the energetic light nuclei (p, d, t, 3He , and 4He) produced through the fragmentation of the target and projectile nuclei. Light ion cross section measurements represent the largest uncertainty in space radiation estimates. The energy spectrum of cosmic rays in the solar system is concentrated at energies below 1 GeV/n. Extensive measurements have been made using the dedicated NSRL facility at the booster, and at other lower energy facilities. However, the Space Radiation Community has recently identified higher energy systems, using beams from 3 to 50 GeV/n on C, Al, and Fe targets as one of the next areas of need. The requirements would be to measure the cross section for light nucleus (p, d, t, 3He , and 4He) production through fragmentation of the target and projectile. STAR has very good particle identification for all of these particle species using both dE/dx and time-of-flight, however the acceptance is only in the target-side of the rapidity distribution. For symmetric systems this is not a problem. For asymmetric systems this would require both light-on-heavy and heavy-on-light combinations. Efforts are underway to determine if the STAR detector has sufficient acceptance in p_T and

3112 y to meet the needs of the Space Radiation Protection community. If it is determined that
 3113 the measurements that could be made at RHIC using the STAR detector would meet those
 3114 needs, STAR is likely to propose brief energy scans using He, Si, and Fe beams on light
 3115 targets in years 23, 24, and 25. Such measurements could not be made in 2022 because the
 3116 timeline to prepare for the Run-22 is very brief and there is not be adequate time to open
 3117 the STAR beampipe and replace the targets.

3118 5.2 Shape Tomography of Atomic Nuclei Using Collective Flow 3119 Measurements

3120 The success of the hydrodynamic framework of heavy-ion collisions permits us today to per-
 3121 form quantitative extractions of the transport properties of the QGP via the state-of-the-art
 3122 multi-system Bayesian analysis approaches [280–282]. Such extractions rely largely on a
 3123 correct description of the initial condition of the QGP prior to the hydrodynamic expansion.
 3124 Recent experimental data in $^{238}\text{U}+^{238}\text{U}$ [16] (see also Figs. 3) and $^{129}\text{Xe}+^{129}\text{Xe}$ [339–341] col-
 3125 lisions, as well as dedicated theoretical studies [31, 342–344], have indicated the importance
 3126 of nuclear deformation on the measured anisotropic flow. However, the effects of nuclear
 3127 deformation are not yet considered in these Bayesian approaches. For a reliable extraction
 3128 of transport properties and initial-state from the flow data, we need to ensure that the
 3129 uncertainty associated with the structure of the colliding ions is under control in the hy-
 3130 drodynamic models, especially since all species for which high statistics of events have been
 3131 collected at RHIC and the LHC are expected to present some deformations in the ground
 3132 state, as indicated in Table 10). Note that the deformation values are often obtained via
 3133 global analysis of nuclear structure data and to some extent are model dependent.

	β_2	β_3	β_4
^{238}U	0.286 [27]	0.078 [345]	0.09 [346]
^{208}Pb	0.05 [27]	0.04 [347]	?
^{197}Au	-(0.13-0.16) [346, 348]	?	-0.03 [346]
^{129}Xe	0.16 [346]	?	?
^{96}Ru	0.05-0.16 [27, 346]	?	?
^{96}Zr	0.08 [27]	?	0.06 [346]

Table 10: Some estimates of the deformation values $\beta_2, \beta_3,$ and β_4 for the large nuclei collided at RHIC and the LHC with references given, mostly based on global analysis of the $B(E_n)$ transition data.

3134 It is straightforward to see why the geometry of heavy-ion collisions is sensitive to nuclear
 3135 deformation. We refer to the cartoon in Figure 97. A nucleus can be modeled through a
 3136 nucleon density of Woods-Saxon form:

$$\rho(r, \theta, \phi) = \frac{\rho_0}{1 + e^{[r-R(\theta, \phi)]/a}}, \quad R(\theta, \phi) = R_0 (1 + \beta_2[\cos \gamma Y_{2,0} + \sin \gamma Y_{2,2}] + \beta_3 Y_{3,0} + \beta_4 Y_{4,0}), \quad (4)$$

3137 where the nuclear surface $R(\theta, \phi)$ includes only the most relevant deformation components,
 3138 $Y_{n,m}(\theta, \phi) = \sqrt{2}(-1)^m \text{Re}[Y_n^m(\theta, \phi)]$, from nuclear structure physics, quadrupole $n = 2$, oc-
 3139 tupole $n = 3$ and hexadecapole $n = 4$. The angle $0 \leq \gamma \leq \pi/3$ controls the triaxiality of the
 3140 quadruple deformation or the three radii R_a, R_b, R_c of the ellipsoid, with $\gamma = 0$ corresponds
 3141 to prolate ($R_a = R_b < R_c$), and $\gamma = \pi/3$ corresponds to oblate ($R_a < R_b = R_c$). In central
 3142 heavy-ion collisions, the shape of the deformed ions determines the geometry of overlap. The
 3143 entire mass distribution is probed simultaneously, and one can use multi-particle correlation
 3144 observables to probe it. This way of probing nuclear densities is very different from the
 3145 standard techniques of low-energy physics, namely $e+A$ collisions which probe the shape
 3146 averaged over orientations, and low energy experiments where β_n is inferred from multipole
 3147 transition probabilities, $B(E_n)$, between low-lying rotational states. The $B(E_n)$ method is
 3148 also sensitive to whether the rotor undergoes rigid or wavelike (irrotational) rotations, while
 3149 heavy ion collisions only care about the spatial distribution of nucleons. Furthermore, the
 3150 time scales involved in high-energy heavy ion collisions are much shorter ($< 10^{-24}\text{s}$), than
 3151 the typical timescale of the EM transition involved in the rotational bands (typically on
 3152 the order of 10^{-21}s). As we shall also argue below, a remarkable question is whether the
 3153 manifestation of nuclear deformation – collective features of the nuclear many-body system
 3154 – is the same across energy scales.

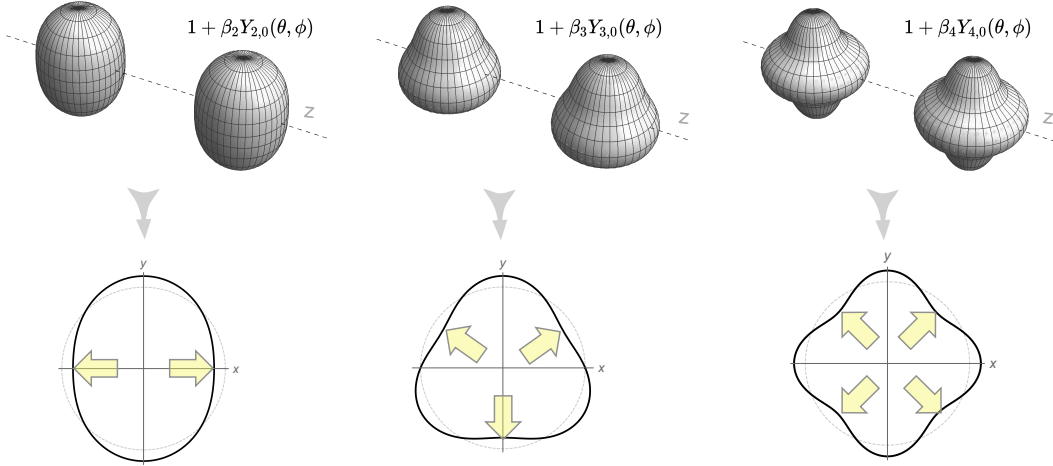


Figure 97: A cartoon of a collision of nuclei with quadrupole (left), octupole (middle) and hexadecapole (right) deformations including only the $Y_{n,0}$ mode and with $\beta_n = 0.25$ (we ignore the large Lorentz contraction in the z -direction). The bottom row shows how the initial condition of the medium formed after the collision looks like in the transverse plane. The yellow arrows indicate the direction of maximum pressure gradients along which the medium expands with the largest velocity, leading to final state harmonic flow v_n with n -fold symmetry.

3155 The presence of multipoles, β_n , in the colliding ions modifies nontrivially the corre-
 3156 sponding spatial anisotropy, ε_n , of the produced QGP, and consequently the final-state flow
 3157 harmonic, v_n . For $n = 2$ both the mean-squared eccentricity and the mean-squared elliptic

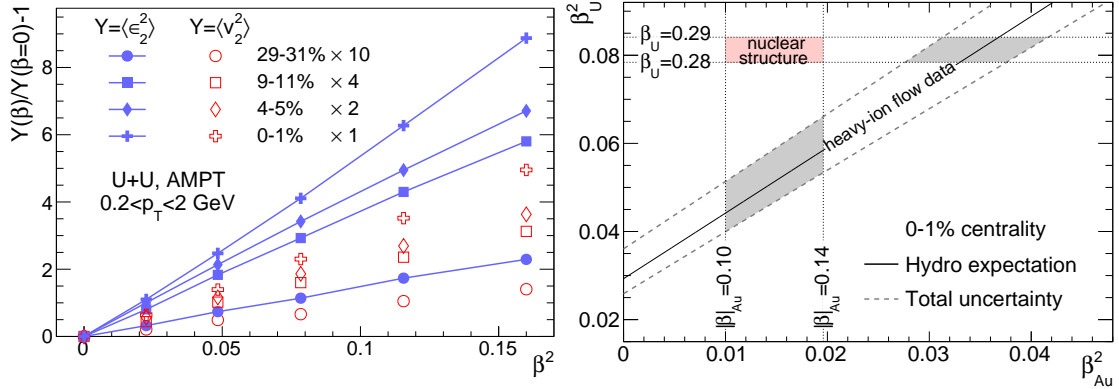


Figure 98: Left panel: $\langle v_2^2(\beta) \rangle / \langle v_2^2(0) \rangle - 1 = b/a \beta_2^2$ (empty symbols) and $\langle \epsilon_2^2(\beta_2) \rangle / \langle \epsilon_2^2(0) \rangle - 1 = b'/a' \beta_2^2$ (full symbols) as a function of β_2^2 in U+U collisions from the AMPT model. Different symbols correspond to different centrality classes. Right panel: $\beta_{2,U}^2$ as a function of $\beta_{2,Au}^2$. The region between the dashed lines is consistent with the hydrodynamic expectation based on Eq. (6) and STAR v_2 data in 0–1% centrality. Figures taken from Ref. [350].

3158 flow are simple functions of the quadrupole deformation parameter [344, 349] (see Fig. 98)

$$\langle \epsilon_2^2 \rangle = a' + b' \beta_2^2, \quad \langle v_2^2 \rangle = a + b \beta_2^2, \quad (5)$$

3159 where the a' and a are mean-squared eccentricity and elliptic flow without deformation,
 3160 $a' = \langle \epsilon_2^2 \rangle|_{\beta_2=0}$ and $a = \langle v_2^2 \rangle|_{\beta_2=0}$, while the b' and b describe the parametric dependence of
 3161 the deformation-enhanced component of eccentricity and elliptic flow, respectively. Interest-
 3162 ingly, the response coefficients for the deformation-independent and deformation-dependent
 3163 components are not the same, i.e. $k_a \equiv a/a' \neq b/b' \equiv k_b$, which opens up the possibility to
 3164 test hydrodynamics using β_2 as a new control variable. The value $b' \approx 0.2$ reflects a simple
 3165 phase space factor accounting for the average over all random orientations, and is found to
 3166 be nearly independent of the colliding systems. The strict quadratic dependence of Eq. 5
 3167 leads to a very robust equation relating the β_2 between any pair of collision systems, X+X
 3168 and Y+Y, that are close in mass number [349]:

$$\beta_{2,Y}^2 = \left(\frac{r_{v_2^2} r_a - 1}{r_Y} \right) + \left(r_{v_2^2} \right) \beta_{2,X}^2, \quad r_{v_2^2} = \langle v_2^2 \rangle_Y / \langle v_2^2 \rangle_X, \quad (6)$$

3169 The ratios r_a and r_Y reflect properties of the initial state geometry and are robust against
 3170 details of final-state effects. This provides a data-driven way to constrain the β_2 . Applied to
 3171 RHIC data, it allows one to derive a constraint on the $\beta_{2,U}$ and $\beta_{2,Au}$, as shown in the right
 3172 panel of Fig. 98. This highlights how, at present, the low-energy nuclear structure model
 3173 calculation and the flow data from high-energy nuclear collisions are fairly inconsistent.
 3174 Relations similar to Eq. 5 can also be written down for v_3 and v_4 , which can be used to
 3175 potentially constrain octupole and hexadecapole deformations.

3176 An additional observable showing large sensitivity to the nuclear quadrupole deforma-
 3177 tion is the Pearson correlation coefficient, $\rho(v_2^2, [p_T])$, between v_2 and the mean transverse
 3178 momentum, $[p_T]$. This observable probes in particular the full quadrupole structure of the

3179 colliding ions [349], i.e., both β_2 and its triaxiality γ in Eq. 4. This observable has been
 3180 measured by the STAR collaboration in U+U and Au+Au collisions (Fig. 3 in Section 1.1.1),
 3181 which established unambiguously the large and dominating influence of the nuclear quadru-
 3182 ple deformation. The large prolate deformation of ^{238}U yields a strong negative contribution
 3183 to the $v_2 - [p_T]$ correlation, enough to make it change sign. Similar effect have further been
 3184 observed in the fluctuations of $[p_T]$ (Fig. 4 in Section 1.1.1). Hydrodynamic models based on
 3185 state-of-the-art initial conditions with deformation values from Table 10 struggle to describe
 3186 quantitatively all these experimental measurements [20, 25, 26]. This suggests that the radial
 3187 flow response of the system to the fluctuations induced by the deformation of the colliding
 3188 ions is poorly captured by the existing models. Collisions of well-deformed ions, and their
 3189 comparisons with the collisions of more spherical species, provide us with a new way to test
 3190 the hydrodynamic description.

3191 We propose thus to collide more species to extract their value of β_2 , and other deforma-
 3192 tion parameters γ , β_3 and β_4 , from flow measurements, with a twofold purpose: 1) provide
 3193 a new handle on the initial state and hydrodynamic response of the QGP, 2) perform stud-
 3194 ies of nuclear structure physics at high energy to complement the information coming from
 3195 lower energies, and so assess the consistency of nuclear phenomena across energy scales. The
 3196 ground state of almost all stable nuclei is deformed (see for example the interactive chart
 3197 in Ref. [351]). RHIC, with its flexibility to collide almost any nuclei from $p+p$ to U+U,
 3198 is a unique facility to perform such studies in the foreseeable future. The best example to
 3199 showcase this capability is the run of isobars performed in 2018, where the two systems,
 3200 Zr+Zr and Ru+Ru, were alternated on a fill-by-fill basis, leading to extremely small sys-
 3201 tematic uncertainties on the final observables [80] (also Section 1.2). This allows one to
 3202 detect minute differences in the physics observables such as multiplicity, $[p_T]$ and v_n in the
 3203 comparison of the two systems. Consequently, even small differences in the values of β_n of
 3204 the colliding systems can be precisely mapped [352]. For each species, we need roughly
 3205 100 million minimum bias and 50 million 0-5% central events. Assuming the standard 50%
 3206 RHIC+STAR up time and 1.5 KHz DAQ rate, same as Au+Au running, we will be able to
 3207 collect 130M minbias events and 64M central events in three days of physics running. This
 3208 is slightly less than the existing U+U dataset taken in 2011, but with comparable statistical
 3209 precision due to the increased acceptance from the iTPC. Adding two days of setup time,
 3210 this leads to about five days of total time for each species.

3211 The system scan we propose can be divided into two steps. Given the tight schedule for
 3212 the next few years, instead of making an explicit proposal on how much running time are
 3213 needed to fully explore these topics, we discuss what can be achieved if we are given certain
 3214 number of days.

- 3215 • **≈ 10 days:** In the first step, we would like to scan two nuclei in the vicinity of the
 3216 most studied species at RHIC, ^{197}Au , to improve the modeling of Au+Au collisions,
 3217 an information which is crucial for the future precision interpretation of high-statistics
 3218 data expected during the operation of sPHENIX. To achieve this, ideal candidates are
 3219 ^{208}Pb and ^{196}Hg (^{198}Hg could be a substitute). Having ^{208}Pb at $\sqrt{s_{\text{NN}}} = 200$ GeV
 3220 provides a crucial bridge with the ^{208}Pb at LHC energies: comparison between ^{208}Pb

3221
3222
3223
3224
3225
3226
3227
3228
3229
3230
3231
3232

measurements at RHIC and the LHC will constrain any possible energy dependence of the initial state effects and pre-equilibrium dynamics. Additionally, ^{208}Pb is nearly spherical, so that Pb+Pb collisions at the same energy will allow us to better understand the impact of the moderate deformation of ^{197}Au in Au+Au collisions. The Hg+Hg collisions would then permit us to understand more deeply the nature of the deformation of ^{197}Au , which, being an odd-mass nucleus, hasn't been determined in low-energy experiments. ^{196}Hg is an oblate nucleus with $|\beta_2| \approx 0.1$, and the observable $\rho(v_2^2, [p_T])$ can be used to quantify whether ^{197}Au is more or less oblate than ^{196}Hg , an information which will gauge more tightly the initial geometry of Au+Au collisions. Adding Hg+Hg collisions will also provide an independent cross-check on the initial state, for example one can setup three relations like Eq.6 from Pb+Pb, Hg+Hg and Au+Au to triangulate the consistency of the three deformation values.

3233
3234
3235
3236
3237
3238
3239
3240
3241
3242
3243
3244
3245
3246
3247
3248
3249
3250
3251
3252

- **Additional time:** In the second step, our proposal is to use hydrodynamics and flow measurements to perform precision cross-check of low-energy nuclear physics by constraining the evolution of the quadrupole deformation along the chain of stable samarium isotopes. It would be useful in particular to collide three isotopes: ^{144}Sm ($\beta_2 = 0.08$, as spherical as ^{208}Pb), ^{148}Sm ($\beta_2 = 0.14$, triaxial much as ^{129}Xe and ^{197}Au), and ^{154}Sm ($\beta_2 = 0.34$ well-deformed like ^{238}U). The evolution of the quadrupole deformation can be mapped precisely at RHIC, thus offering a valuable test of nuclear structure knowledge. If data on $^{154}\text{Sm}+^{154}\text{Sm}$ collisions is available, it would be desirable to also have $^{154}\text{Gd}+^{154}\text{Gd}$ ($\beta_2 = 0.31$) collisions. The comparison between the two well-deformed isobaric systems could potentially yield the most precise information about the relative deformation of two ground states. Theoretical studies further suggest that ground states in the region $Z \sim 56/N \sim 88$ [353] (including the samarium isotopes) may display enhanced octupole correlations, i.e., β_3 values. These would manifest in high-energy collisions as enhanced v_3 , as well as in the correlators $\rho(v_3^2, [p_T])$. Evidence of static octupole moments at low energies is rather sparse, and heavy ion collisions might be a more sensitive approach. The study of octupole deformation is also fundamentally interesting because nuclei with large β_3 provides a stringent test of the electric-dipole moment (EDM) [354]. The exact choice of species is still under refinement, presently we have a preference for ^{154}Sm and ^{148}Sm , followed by ^{154}Gd and ^{144}Sm .

3253
3254
3255
3256

Finally, one should note that the STAR DAQ rate for these moderate-sized systems could be significantly larger, possibly reaching 2KHz. This enhanced DAQ rate will compensate partially the smaller number of charged particles expected in these systems compared to larger systems.

3259 **6 Charge for 2021 NPP PAC**

- 3260 • STAR: Beam Use Requests for Runs 22-25
- 3261 • sPHENIX: Beam Use Requests for Runs 23-25
- 3262 • CeC: Beam Use Requests

3263 The Beam Use Requests should be submitted in written form to PAC by May 14, 2021. The
3264 BURs should be based on the following number of expected cryo-weeks. First number is
3265 minimal expected RHIC run duration and second number is optimal duration:

- 3266 2022: 18 (20)
- 3267 2023: 20 (28)
- 3268 2024: 20 (28)
- 3269 2025: 20 (28)

3270 References

- 3271 [1] STAR, J. Adam *et al.*, Phys. Rev. Lett. **126**, 092301 (2021), 2001.02852.
- 3272 [2] Y. Aoki, G. Endrodi, Z. Fodor, S. D. Katz, and K. K. Szabo, Nature **443**, 675 (2006),
3273 hep-lat/0611014.
- 3274 [3] B. Friman, F. Karsch, K. Redlich, and V. Skokov, Eur. Phys. J. C **71**, 1694 (2011),
3275 1103.3511.
- 3276 [4] A. Bazavov *et al.*, (2020), 2001.08530.
- 3277 [5] S. Borsanyi *et al.*, JHEP **10**, 205 (2018), 1805.04445.
- 3278 [6] Z.-T. Liang and X.-N. Wang, Phys. Rev. Lett. **94**, 102301 (2005), nucl-th/0410079,
3279 [Erratum: Phys.Rev.Lett. 96, 039901 (2006)].
- 3280 [7] S. A. Voloshin, (2004), nucl-th/0410089.
- 3281 [8] STAR, J. Adam *et al.*, Phys. Rev. C **98**, 014910 (2018), 1805.04400.
- 3282 [9] Y. Sun and C. M. Ko, Phys. Rev. C **96**, 024906 (2017), 1706.09467.
- 3283 [10] Y. Xie, D. Wang, and L. P. Csernai, Phys. Rev. C **95**, 031901 (2017), 1703.03770.
- 3284 [11] Y. B. Ivanov, V. D. Toneev, and A. A. Soldatov, Phys. Rev. C **100**, 014908 (2019),
3285 1903.05455.
- 3286 [12] O. Vitiuk, L. V. Bravina, and E. E. Zabrodin, Phys. Lett. B **803**, 135298 (2020),
3287 1910.06292.
- 3288 [13] STAR, B. I. Abelev *et al.*, Phys. Rev. C **76**, 024915 (2007), 0705.1691, [Erratum:
3289 Phys.Rev.C 95, 039906 (2017)].
- 3290 [14] ALICE, S. Acharya *et al.*, Phys. Rev. C **101**, 044611 (2020), 1909.01281.
- 3291 [15] D.-X. Wei, W.-T. Deng, and X.-G. Huang, Phys. Rev. C **99**, 014905 (2019), 1810.00151.
- 3292 [16] STAR, L. Adamczyk *et al.*, Phys. Rev. Lett. **115**, 222301 (2015), 1505.07812.
- 3293 [17] G. Giacalone, B. Schenke, and C. Shen, Phys. Rev. Lett. **125**, 192301 (2020),
3294 2006.15721.
- 3295 [18] P. Bozek, Phys. Rev. C **93**, 044908 (2016), 1601.04513.
- 3296 [19] P. Bozek and H. Mehrabpour, Phys. Rev. C **101**, 064902 (2020), 2002.08832.
- 3297 [20] B. Schenke, C. Shen, and D. Teaney, Phys. Rev. C **102**, 034905 (2020), 2004.00690.

- 3298 [21] G. Giacalone, F. G. Gardim, J. Noronha-Hostler, and J.-Y. Ollitrault, Phys. Rev. C
3299 **103**, 024909 (2021), 2004.01765.
- 3300 [22] S. H. Lim and J. L. Nagle, (2021), 2103.01348.
- 3301 [23] P. Bozek and W. Broniowski, Phys. Rev. C **85**, 044910 (2012), 1203.1810.
- 3302 [24] G. Giacalone, Phys. Rev. Lett. **124**, 202301 (2020), 1910.04673.
- 3303 [25] G. Giacalone, Phys. Rev. C **102**, 024901 (2020), 2004.14463.
- 3304 [26] G. Giacalone, F. G. Gardim, J. Noronha-Hostler, and J.-Y. Ollitrault, Phys. Rev. C
3305 **103**, 024910 (2021), 2004.09799.
- 3306 [27] S. Raman, C. W. G. Nestor, Jr, and P. Tikkanen, Atom. Data Nucl. Data Tabl. **78**, 1
3307 (2001).
- 3308 [28] C. Nepali, G. Fai, and D. Keane, Phys. Rev. C **73**, 034911 (2006).
- 3309 [29] M. R. Haque, Z.-W. Lin, and B. Mohanty, Phys.Rev. **C85**, 034905 (2012), 1112.2340.
- 3310 [30] V. Bairathi, M. R. Haque, and B. Mohanty, Phys. Rev. C **91**, 054903 (2015),
3311 1504.04719.
- 3312 [31] U. W. Heinz and A. Kuhlman, Phys.Rev.Lett. **94**, 132301 (2005), nucl-th/0411054.
- 3313 [32] A. J. Kuhlman and U. W. Heinz, Phys. Rev. C **72**, 037901 (2005), nucl-th/0506088.
- 3314 [33] A. Kuhlman, U. W. Heinz, and Y. V. Kovchegov, Phys. Lett. B **638**, 171 (2006),
3315 nucl-th/0604038.
- 3316 [34] D. Molnar and S. A. Voloshin, Phys. Rev. Lett. **91**, 092301 (2003), nucl-th/0302014.
- 3317 [35] R. J. Fries, B. Muller, C. Nonaka, and S. A. Bass, Phys. Rev. Lett. **90**, 202303 (2003),
3318 nucl-th/0301087.
- 3319 [36] I. Takashi, I. G. Noriyoshi, A. Sinya, and D. Takumi, Prog. Theor. Phys **124**, 591
3320 (2010), 1007.3559v1.
- 3321 [37] B. Abelev *et al.*, Science **328**, 58 (2010), 1003.2030v1.
- 3322 [38] J. Adam *et al.*, Phys. Lett. B **790**, 490 (2019), 1808.02511.
- 3323 [39] L. Adamczyk *et al.*, Nature **527**, 345 (2015), 1507.07158.
- 3324 [40] S. Acharya *et al.*, Nature **588**, 232 (2020), 2005.11495.
- 3325 [41] I. Takashi, I. G. Noriyoshi, A. Sinya, and D. Takumi, Nucl. Phys. A **881**, 28 (2012),
3326 1112.5926v2.

- 3327 [42] M. Kenji, O. Akira, E. Faisal, and H. Tetsuo, Phys. Rev. C **94** (2016), 1605.06765.
- 3328 [43] R. Jaffe, Phys. Rev. Lett **38**, 617 (1977).
- 3329 [44] N. Shah, Y. Ma, J. Chen, and S. Zhang, Phys. Lett. B **754**, 6 (2016).
- 3330 [45] S. Marzani, G. Soyez, and M. Spannowsky *Looking inside jets: an introduction to jet*
3331 *substructure and boosted-object phenomenology* Vol. 958 (Springer, 2019), 1901.10342.
- 3332 [46] A. J. Larkoski, S. Marzani, G. Soyez, and J. Thaler, JHEP **05**, 146 (2014), 1402.2657.
- 3333 [47] A. J. Larkoski, S. Marzani, and J. Thaler, Phys. Rev. D **91**, 111501 (2015), 1502.01719.
- 3334 [48] STAR, J. Adam *et al.*, Phys. Lett. B **811**, 135846 (2020), 2003.02114.
- 3335 [49] STAR, M. Abdallah *et al.*, (2021), 2103.13286.
- 3336 [50] Z.-B. Kang, K. Lee, X. Liu, and F. Ringer, Phys. Lett. B **793**, 41 (2019), 1811.06983.
- 3337 [51] A. Majumder and J. Putschke, Phys. Rev. C **93**, 054909 (2016), 1408.3403.
- 3338 [52] Z.-B. Kang, K. Lee, and F. Ringer, JHEP **04**, 110 (2018), 1801.00790.
- 3339 [53] T. Auye, Unfolding algorithms and tests using RooUnfold, in *PHYSTAT 2011*, Geneva,
3340 2011, CERN, 1105.1160.
- 3341 [54] F. A. Dreyer, L. Necib, G. Soyez, and J. Thaler, JHEP **06**, 093 (2018), 1804.03657.
- 3342 [55] STAR, J. Adam *et al.*, Phys. Rev. D **101**, 052004 (2020), 1912.08187.
- 3343 [56] STAR, J. Adam *et al.*, Phys. Rev. D **102**, 092009 (2020), 2007.04732.
- 3344 [57] STAR, J. Adam *et al.*, (2021), 2101.11793.
- 3345 [58] STAR, L. Adamczyk *et al.*, Phys. Lett. B **771**, 13 (2017), 1607.07517.
- 3346 [59] STAR, J. Adam *et al.*, Phys. Lett. B **797**, 134917 (2019), 1905.13669.
- 3347 [60] PHENIX, A. Adare *et al.*, Phys. Rev. C **87**, 034904 (2013), 1204.0777.
- 3348 [61] J.-P. Lansberg and H.-S. Shao, Eur. Phys. J. C **77**, 1 (2017), 1610.05382.
- 3349 [62] Y. Ma and R. Vogt.
- 3350 [63] E. G. Ferreira, F. Fleuret, J. P. Lansberg, N. Matagne, and A. Rakotozafindrabe, Few
3351 Body Syst. **53**, 27 (2012), 1201.5574.
- 3352 [64] K. Zhou, N. Xu, Z. Xu, and P. Zhuang, Phys. Rev. C **89**, 054911 (2014).
- 3353 [65] X. Zhao and R. Rapp, Phys. Rev. C **82**, 064905 (2010).

- 3354 [66] NA50, M. C. Abreu *et al.*, Phys. Lett. B **477**, 28 (2000).
- 3355 [67] L. Kluberg, Eur. Phys. J. C **43**, 145 (2005).
- 3356 [68] ALICE, B. B. Abelev *et al.*, Phys. Lett. B **734**, 314 (2014), 1311.0214.
- 3357 [69] ALICE, X. Bai, Nucl. Phys. A **1005**, 121769 (2021), 2001.11925.
- 3358 [70] STAR, J. Adam *et al.*, Phys. Lett. B **808**, 135663 (2020), 2003.12136.
- 3359 [71] D. Kharzeev and R. D. Pisarski, Phys.Rev. **D61**, 111901 (2000), hep-ph/9906401.
- 3360 [72] D. Kharzeev, Phys.Lett. **B633**, 260 (2006), hep-ph/0406125.
- 3361 [73] S. A. Voloshin, Phys. Rev. Lett. **105**, 172301 (2010), 1006.1020.
- 3362 [74] W.-T. Deng, X.-G. Huang, G.-L. Ma, and G. Wang, Phys. Rev. C **97**, 044901 (2018),
3363 1802.02292.
- 3364 [75] B. Schenke, C. Shen, and P. Tribedy, Phys. Rev. **C99**, 044908 (2019), 1901.04378.
- 3365 [76] H.-J. Xu *et al.*, Phys. Rev. Lett. **121**, 022301 (2018), 1710.03086.
- 3366 [77] J. Hammelmann, A. Soto-Ontoso, M. Alvioli, H. Elfner, and M. Strikman, (2019),
3367 1908.10231.
- 3368 [78] STAR 2017 BUR [https://drupal.star.bnl.gov/STAR/system/files/STAR_BUR_](https://drupal.star.bnl.gov/STAR/system/files/STAR_BUR_Run1718_v22_0.pdf)
3369 [Run1718_v22_0.pdf](https://drupal.star.bnl.gov/STAR/system/files/STAR_BUR_Run1718_v22_0.pdf).
- 3370 [79] STAR, P. Tribedy, J. Phys. Conf. Ser. **1602**, 1 (2020), 2009.01230.
- 3371 [80] STAR, J. Adam *et al.*, (2019), 1911.00596.
- 3372 [81] STAR, J. Zhao, (2020), 2002.09410.
- 3373 [82] CMS, A. M. Sirunyan *et al.*, Phys. Rev. **C97**, 044912 (2018), 1708.01602.
- 3374 [83] H.-j. Xu *et al.*, Chin. Phys. **C42**, 084103 (2018), 1710.07265.
- 3375 [84] S. A. Voloshin, Phys. Rev. **C98**, 054911 (2018), 1805.05300.
- 3376 [85] J. Zhao, H. Li, and F. Wang, Eur. Phys. J. C **79**, 168 (2019), 1705.05410.
- 3377 [86] STAR, J. Adam *et al.*, (2020), arXiv:2006.05035.
- 3378 [87] STAR, P. Tribedy, Nucl. Phys. A **967**, 740 (2017), 1704.03845.
- 3379 [88] STAR, J. Adam *et al.*, (2020), arXiv:2006.04251.
- 3380 [89] STAR, Y. Lin, Nucl. Phys. A **1005**, 121828 (2021), 2002.11446.

- 3381 [90] N. Magdy, S. Shi, J. Liao, N. Ajitanand, and R. A. Lacey, Phys. Rev. C **97**, 061901
3382 (2018), 1710.01717.
- 3383 [91] A. H. Tang, Chin. Phys. C **44**, 054101 (2020), 1903.04622.
- 3384 [92] S. A. Voloshin, Phys. Rev. **C70**, 057901 (2004), hep-ph/0406311.
- 3385 [93] N. N. Ajitanand, R. A. Lacey, A. Taranenko, and J. M. Alexander, Phys. Rev. **C83**,
3386 011901 (2011), 1009.5624.
- 3387 [94] S. Choudhury *et al.*, (2021), 2105.06044.
- 3388 [95] S. Shi, Y. Jiang, E. Lilleskov, and J. Liao, Annals Phys. **394**, 50 (2018), 1711.02496.
- 3389 [96] Y. Jiang, S. Shi, Y. Yin, and J. Liao, Chin. Phys. C **42**, 011001 (2018), 1611.04586.
- 3390 [97] S. Shi, H. Zhang, D. Hou, and J. Liao, Phys. Rev. Lett. **125**, 242301 (2020), 1910.14010.
- 3391 [98] H. Song, S. A. Bass, U. Heinz, T. Hirano, and C. Shen, Phys. Rev. Lett. **106**, 192301
3392 (2011), 1011.2783, [Erratum: Phys.Rev.Lett. 109, 139904 (2012)].
- 3393 [99] M. Bleicher *et al.*, J. Phys. G **25**, 1859 (1999), hep-ph/9909407.
- 3394 [100] S. A. Bass *et al.*, Prog. Part. Nucl. Phys. **41**, 255 (1998), nucl-th/9803035, [Prog.
3395 Part. Nucl. Phys.41,225(1998)].
- 3396 [101] W.-T. Deng, X.-G. Huang, G.-L. Ma, and G. Wang, Phys. Rev. C **94**, 041901 (2016),
3397 1607.04697.
- 3398 [102] L. Finch and S. Murray, Phys. Rev. C **96**, 044911 (2017), 1801.06476.
- 3399 [103] J. Adams *et al.*, Nucl. Instrum. Meth. A **968**, 163970 (2020), 1912.05243.
- 3400 [104] STAR, M. Abdallah *et al.*, (2021), 2103.05571.
- 3401 [105] STAR, L. Adamczyk *et al.*, Phys. Rev. D **95**, 071103 (2017).
- 3402 [106] D. de Florian, R. Sassot, M. Stratmann, and W. Vogelsang, Phys. Rev. Lett. **113**,
3403 012001 (2014), 1404.4293.
- 3404 [107] NNPDF, E. R. Nocera, R. D. Ball, S. Forte, G. Ridolfi, and J. Rojo, Nucl. Phys.
3405 **B887**, 276 (2014), 1406.5539.
- 3406 [108] STAR, J. Adam *et al.*, Phys. Rev. D. **98**, 032011 (2018).
- 3407 [109] STAR, J. Kwasizur, Longitudinal Double-Spin Asymmetries for Dijet Production at
3408 Intermediate Pseudorapidity in Polarized Proton-Proton Collisions at $\sqrt{s} = 510$ GeV,
3409 in *APS Division of Nuclear Physics Meeting*, 2020.

- 3410 [110] STAR, Y. Xu, Longitudinal and Transverse Spin Transfer of Λ and $\bar{\Lambda}$ Hyperons in
3411 Polarized $p+p$ Collisions at $\sqrt{s} = 200$ GeV at RHIC-STAR, in *XXVIII International*
3412 *Workshop on Deep-Inelastic Scattering and Related Subjects, Stony Brook University,*
3413 2021, <https://indico.bnl.gov/event/9726/contributions/46261/>.
- 3414 [111] J. Adam *et al.*, Phys. Rev. D **98**, 112009 (2018).
- 3415 [112] STAR, B. Pokhrel, Transverse Spin Dependent Azimuthal Correlations of Charged
3416 hadrons in Collisions at $\sqrt{s} = 200$ GeV, in *XXVIII International Workshop on Deep-*
3417 *Inelastic Scattering and Related Subjects*, 2021.
- 3418 [113] STAR, B. Pokhrel, Transverse Spin Dependent Azimuthal Correlations of Charged
3419 hadrons(s) in $p \uparrow p$ Collisions at $\sqrt{s} = 200$ GeV, in *XXVIII International Work-*
3420 *shop on Deep-Inelastic Scattering and Related Subjects, Stony Brook University*, 2021,
3421 <https://indico.bnl.gov/event/9726/contributions/46262/>.
- 3422 [114] STAR, J. Adam *et al.*, Phys. Rev. D **103**, 072005 (2021), 2012.07146.
- 3423 [115] STAR, J. Adam *et al.*, accepted by Phys. Rev. D (2020), 2012.11428.
- 3424 [116] U. D’Alesio, F. Murgia, and C. Pisano, Phys. Lett. B **773**, 300 (2017), 1707.00914.
- 3425 [117] Z.-B. Kang, X. Liu, F. Ringer, and H. Xing, JHEP **11**, 068 (2017), 1705.08443.
- 3426 [118] Z.-B. Kang, A. Prokudin, F. Ringer, and F. Yuan, Phys. Lett. B **774**, 635 (2017),
3427 1707.00913.
- 3428 [119] U. D’Alesio, F. Murgia, and C. Pisano, Phys. Rev. D **83**, 034021 (2011), 1011.2692.
- 3429 [120] STAR, J. Adam *et al.*, Phys. Rev. D **98**, 091103(R) (2018), 1808.08000.
- 3430 [121] Q. Xu, Z. Liang, and E. Sichtermann, Phys. Rev. D **73**, 077503 (2006), 0511061.
- 3431 [122] Jefferson Lab Angular Momentum, J. Cammarota *et al.*, Phys. Rev. D **102**, 054002
3432 (2020).
- 3433 [123] STAR, J. Adam *et al.*, Phys. Rev. D **103**, 012001 (2021), 2011.04708.
- 3434 [124] NuSea, R. S. Towell *et al.*, Phys. Rev. **D64**, 052002 (2001), hep-ex/0103030.
- 3435 [125] SeaQuest, J. Dove *et al.*, Nature **590**, 561 (2021), 2103.04024.
- 3436 [126] STAR, J. Nam, Measurements of W and Z/γ^* cross sections and their
3437 ratios in pp collisions at STAR, in *XXVIII International Workshop on*
3438 *Deep-Inelastic Scattering and Related Subjects, Stony Brook University*, 2021,
3439 <https://indico.bnl.gov/event/9726/contributions/46577/>.
- 3440 [127] STAR, D. Kalinkin, Measurement of Mid-rapidity Inclusive Jet Cross Section in pp
3441 Collisions at $\sqrt{s} = 200$ GeV, in *APS Division of Nuclear Physics Meeting*, 2020.

- 3442 [128] STAR, D. Kalinkin, Measurement of Mid-rapidity Inclusive Jet Cross Section in pp
3443 Collisions at $\sqrt{s} = 200$ GeV, in *XXVIII International Workshop on Deep-Inelastic*
3444 *Scattering and Related Subjects*, 2021.
- 3445 [129] STAR, X. Chu, Di-hadron correlations in p+p, p+Au and p+Al collisions at
3446 STAR, in *2020 Fall Meeting of the APS Division of Nuclear Physics, online*, 2020,
3447 https://meetings.aps.org/Meeting/DNP20/APS_epitome.
- 3448 [130] J. L. Albacete, G. Giacalone, C. Marquet, and M. Matas, Phys. Rev. D **99**, 014002
3449 (2019), 1805.05711.
- 3450 [131] CMS, V. Khachatryan *et al.*, JHEP **09**, 091 (2010), 1009.4122.
- 3451 [132] CMS, S. Chatrchyan *et al.*, Phys. Lett. B **718**, 795 (2013), 1210.5482.
- 3452 [133] ALICE, B. Abelev *et al.*, Phys. Lett. B **719**, 29 (2013), 1212.2001.
- 3453 [134] ATLAS, G. Aad *et al.*, Phys. Rev. Lett. **110**, 182302 (2013), 1212.5198.
- 3454 [135] PHENIX, A. Adare *et al.*, Phys. Rev. Lett. **115**, 142301 (2015), 1507.06273.
- 3455 [136] PHENIX, A. Adare *et al.*, Phys. Rev. Lett. **114**, 192301 (2015), 1404.7461.
- 3456 [137] STAR, L. Adamczyk *et al.*, Phys. Lett. B **747**, 265 (2015), 1502.07652.
- 3457 [138] PHENIX, C. Aidala *et al.*, Phys. Rev. C **95**, 034910 (2017), 1609.02894.
- 3458 [139] PHENIX, C. Aidala *et al.*, Nature Phys. **15**, 214 (2019), 1805.02973.
- 3459 [140] J. L. Nagle *et al.*, Phys. Rev. Lett. **113**, 112301 (2014), 1312.4565.
- 3460 [141] STAR, R. A. Lacey, Nucl. Phys. A **1005**, 122041 (2021), 2002.11889.
- 3461 [142] J.-w. Qiu and G. F. Sterman, Phys. Rev. D **59**, 014004 (1999), hep-ph/9806356.
- 3462 [143] K. Kanazawa, Y. Koike, A. Metz, and D. Pitonyak, Phys. Rev. D **89**, 111501 (2014).
- 3463 [144] L. Bland *et al.*, Physics Letters B **750**, 660 (2015).
- 3464 [145] STAR, H. Liu, Measurement of transverse single-spin asymmetries for dijet production
3465 in polarized p+p collisions at $\sqrt{s} = 200$ GeV at STAR, in *Nuclear Physics Seminar,*
3466 *Brookhaven National Laboratory*, 2020, <https://indico.bnl.gov/event/8633/>.
- 3467 [146] M. Boglione *et al.*, Phys. Lett. B **815**, 136135 (2021), 2101.03955.
- 3468 [147] L. Gamberg, Z.-B. Kang, and A. Prokudin, Phys. Rev. Lett. **110**, 232301 (2013).
- 3469 [148] STAR, B. Abelev *et al.*, Phys. Rev. Lett. **99**, 142003 (2007), 0705.4629.

- 3470 [149] M. Bury, A. Prokudin, and A. Vladimirov, Phys. Rev. Lett. **126**, 112002 (2021),
3471 2012.05135.
- 3472 [150] STAR, L. Adamczyk *et al.*, Phys. Rev. Lett. **116**, 132301 (2016), 1511.06003.
- 3473 [151] J. P. Ralston and D. E. Soper, Nuclear Physics B **152**, 109 (1979).
- 3474 [152] R. Jaffe and X.-D. Ji, Nucl. Phys. B **375**, 527 (1992).
- 3475 [153] P. Mulders and R. Tangerman, Nucl. Phys. B **461**, 197 (1996), hep-ph/9510301,
3476 [Erratum: Nucl.Phys.B 484, 538–540 (1997)].
- 3477 [154] D. Sivers, Nuovo Cim. C **035N2**, 171 (2012), 1109.2521.
- 3478 [155] C. Alexandrou *et al.*, Phys. Rev. D **98**, 091503 (2018).
- 3479 [156] R. Jaffe and X.-D. Ji, Phys. Rev. Lett. **67**, 552 (1991).
- 3480 [157] J. C. Collins, S. F. Heppelmann, and G. A. Ladinsky, Nucl. Phys. B **420**, 565 (1994),
3481 hep-ph/9305309.
- 3482 [158] L. Adamczyk *et al.*, Phys. Lett. B **780**, 332–339 (2018).
- 3483 [159] M. Radici and A. Bacchetta, Phys. Rev. Lett. **120**, 192001 (2018), 1802.05212.
- 3484 [160] J. Collins and J.-W. Qiu, Phys. Rev. D **75**, 114014 (2007).
- 3485 [161] T. C. Rogers and P. J. Mulders, Phys. Rev. D **81**, 094006 (2010).
- 3486 [162] X. Liu, F. Ringer, W. Vogelsang, and F. Yuan, Factorization and its breaking in dijet
3487 single transverse spin asymmetries in pp collisions, 2020, 2008.03666.
- 3488 [163] Z.-B. Kang, K. Lee, D. Y. Shao, and J. Terry, The sivers asymmetry in hadronic dijet
3489 production, 2020, 2008.05470.
- 3490 [164] F. Yuan, Phys. Rev. Lett. **100**, 032003 (2008).
- 3491 [165] F. Yuan, Phys. Rev. D **77**, 074019 (2008).
- 3492 [166] STAR, L. Adamczyk *et al.*, Phys. Rev. D **97**, 032004 (2018), 1708.07080.
- 3493 [167] M. Anselmino *et al.*, Phys. Rev. D **73**, 014020 (2006), hep-ph/0509035.
- 3494 [168] M. Anselmino *et al.*, Phys. Rev. D **75**, 054032 (2007).
- 3495 [169] J. Soffer, Phys. Rev. Lett. **74**, 1292 (1995).
- 3496 [170] U. D'Alesio, F. Murgia, and C. Pisano, Phys. Lett. B **773**, 300–306 (2017).

- 3497 [171] CJ, S. Park, CJ15 global PDF analysis with new electroweak data, in *XXVIII In-*
3498 *ternational Workshop on Deep-Inelastic Scattering and Related Subjects, Stony Brook*
3499 *University*, 2021, <https://indico.bnl.gov/event/9726/contributions/46569/>.
- 3500 [172] H1, ZEUS, F. Aaron *et al.*, *Eur. Phys. J. C* **72**, 2175 (2012), 1207.4864.
- 3501 [173] CMS, V. Khachatryan *et al.*, *Phys. Rev. D* **92**, 012003 (2015), 1503.08689.
- 3502 [174] S. L. Bultmann *et al.*, *Phys. Lett. B* **579**, 245 (2004), nucl-ex/0305012.
- 3503 [175] S. Bultmann *et al.*, *Phys. Lett. B* **632**, 167 (2006), nucl-ex/0507030.
- 3504 [176] pp2pp, S. Bultmann *et al.*, *Phys. Lett. B* **647**, 98 (2007), nucl-ex/0610022.
- 3505 [177] STAR, L. Adamczyk *et al.*, *Phys. Lett. B* **719**, 62 (2013), 1206.1928.
- 3506 [178] T. Sjöstrand *et al.*, *Comput. Phys. Commun.* **191**, 159 (2015), 1410.3012.
- 3507 [179] I. Helenius, Recent pythia 8 developments: Hard diffraction, colour reconnection and
3508 $\gamma\gamma$ collisions, in *7th International Workshop on Multiple Partonic Interactions at the*
3509 *LHC*, 2015, <http://indico.ictp.it/event/a14280/session/266/contribution/1042/>.
- 3510 [180] STAR, C. Dilks, *PoS DIS2016*, 212 (2016), 1805.08875.
- 3511 [181] A. Airapetian *et al.*, *Phys. Lett. B* **693**, 11–16 (2010).
- 3512 [182] C. Adolph *et al.*, *Phys. Lett. B* **744**, 250–259 (2015).
- 3513 [183] D. Müller, D. Robaschik, B. Geyer, F.-M. Dittes, and J. Hořejší, *Fortsch. Phys.* **42**,
3514 101 (1994), hep-ph/9812448.
- 3515 [184] X.-D. Ji, *Phys. Rev. Lett.* **78**, 610 (1997), hep-ph/9603249.
- 3516 [185] A. Radyushkin, *Phys. Lett. B* **380**, 417 (1996), hep-ph/9604317.
- 3517 [186] M. Burkardt, *Phys. Rev. D* **62**, 071503 (2000), hep-ph/0005108, [Erratum: *Phys. Rev. D*
3518 **66**, 119903 (2002)].
- 3519 [187] S. Klein and J. Nystrand, Photoproduction of J / psi and Upsilon in pp and anti-p p
3520 collisions, in *5th Workshop on Small x and Diffractive Physics*, 2003, hep-ph/0310223.
- 3521 [188] S. R. Klein, J. Nystrand, J. Seger, Y. Gorbunov, and J. Butterworth, *Comput. Phys.*
3522 *Commun.* **212**, 258 (2017), 1607.03838.
- 3523 [189] J. Lansberg, L. Massacrier, L. Szymanowski, and J. Wagner, *Phys. Lett. B* **793**, 33
3524 (2019), 1812.04553.
- 3525 [190] HERMES, A. Airapetian *et al.*, *Phys. Lett. B* **577**, 37 (2003), hep-ex/0307023.

- 3526 [191] HERMES, A. Airapetian *et al.*, Nucl. Phys. B **780**, 1 (2007), 0704.3270.
- 3527 [192] HERMES, A. Airapetian *et al.*, Phys. Lett. B **684**, 114 (2010), 0906.2478.
- 3528 [193] W. Brooks and H. Hakobyan, Nucl. Phys. A **830**, 361C (2009), 0907.4606.
- 3529 [194] NuSea, M. Vasilev *et al.*, Phys. Rev. Lett. **83**, 2304 (1999), hep-ex/9906010.
- 3530 [195] H. Paukkunen, The LHC p+Pb run from the nuclear PDF perspective, in *XXII*
 3531 *International Workshop on Deep-Inelastic Scattering and Related Subjects*, 2014,
 3532 <https://indico.cern.ch/event/258017/contributions/1588381>.
- 3533 [196] D. de Florian, R. Sassot, P. Zurita, and M. Stratmann, Phys. Rev. D **85**, 074028
 3534 (2012), 1112.6324.
- 3535 [197] PHENIX, S. Adler *et al.*, Phys. Rev. Lett. **98**, 172302 (2007), nucl-ex/0610036.
- 3536 [198] K. Eskola, H. Paukkunen, and C. Salgado, Nucl. Phys. A **855**, 150 (2011), 1011.6534.
- 3537 [199] R. Sassot, M. Stratmann, and P. Zurita, Phys. Rev. D **81**, 054001 (2010), 0912.1311.
- 3538 [200] K. J. Eskola, P. Paakkinen, H. Paukkunen, and C. A. Salgado, Eur. Phys. J. C **77**,
 3539 163 (2017), 1612.05741.
- 3540 [201] N. Armesto, H. Paukkunen, J. M. Penín, C. A. Salgado, and P. Zurita, Eur. Phys. J.
 3541 C **76**, 218 (2016), 1512.01528.
- 3542 [202] H. Paukkunen and P. Zurita, JHEP **12**, 100 (2014), 1402.6623.
- 3543 [203] E. Aschenauer *et al.*, (2014), 1409.1633.
- 3544 [204] H. Paukkunen, K. J. Eskola, and C. Salgado, Nucl. Phys. A **931**, 331 (2014), 1408.4563.
- 3545 [205] K. J. Eskola, H. Paukkunen, and C. A. Salgado, JHEP **10**, 213 (2013), 1308.6733.
- 3546 [206] L. Gribov, E. Levin, and M. Ryskin, Phys. Rept. **100**, 1 (1983).
- 3547 [207] E. Iancu and R. Venugopalan, The Color glass condensate and high-energy scattering
 3548 in QCD, in *In *Hwa, R.C. (ed.) et al.: Quark gluon plasma* 249-3363*, 2003, hep-
 3549 ph/0303204.
- 3550 [208] H. Weigert, Prog. Part. Nucl. Phys. **55**, 461 (2005), hep-ph/0501087.
- 3551 [209] J. Jalilian-Marian and Y. V. Kovchegov, Prog. Part. Nucl. Phys. **56**, 104 (2006),
 3552 hep-ph/0505052.
- 3553 [210] F. Gelis, E. Iancu, J. Jalilian-Marian, and R. Venugopalan, Ann. Rev. Nucl. Part. Sci.
 3554 **60**, 463 (2010), 1002.0333.

- 3555 [211] G. Giuliani, H. Zheng, and A. Bonasera, *Prog. Part. Nucl. Phys.* **76**, 116 (2014),
3556 1311.1811.
- 3557 [212] Y. V. Kovchegov and E. Levin *Quantum chromodynamics at high energy* Vol. 33 (Cam-
3558 bridge University Press, 2012).
- 3559 [213] A. H. Mueller and J.-w. Qiu, *Nucl. Phys. B* **268**, 427 (1986).
- 3560 [214] L. McLerran and R. Venugopalan, *Phys. Rev. D* **49**, 2233 (1994).
- 3561 [215] L. McLerran and R. Venugopalan, *Phys. Rev. D* **49**, 3352 (1994).
- 3562 [216] L. McLerran and R. Venugopalan, *Phys. Rev. D* **50**, 2225 (1994).
- 3563 [217] Y. V. Kovchegov, *Phys. Rev. D* **54**, 5463 (1996).
- 3564 [218] Y. V. Kovchegov, *Phys. Rev. D* **55**, 5445 (1997).
- 3565 [219] J. Jalilian-Marian, A. Kovner, L. McLerran, and H. Weigert, *Phys. Rev. D* **55**, 5414
3566 (1997).
- 3567 [220] A. H. Mueller, *Nucl. Phys.* **B415**, 373 (1994).
- 3568 [221] A. H. Mueller and B. Patel, *Nucl. Phys. B* **425**, 471 (1994), hep-ph/9403256.
- 3569 [222] I. Balitsky, *Nucl. Phys.* **B463**, 99 (1996), hep-ph/9509348.
- 3570 [223] I. Balitsky, *Phys. Rev. D* **60**, 014020 (1999), hep-ph/9812311.
- 3571 [224] Y. V. Kovchegov, *Phys. Rev. D* **60**, 034008 (1999), hep-ph/9901281.
- 3572 [225] Y. V. Kovchegov, *Phys. Rev. D* **61**, 074018 (2000), hep-ph/9905214.
- 3573 [226] J. Jalilian-Marian, A. Kovner, and H. Weigert, *Phys. Rev. D* **59**, 014015 (1998),
3574 hep-ph/9709432.
- 3575 [227] J. Jalilian-Marian, A. Kovner, A. Leonidov, and H. Weigert, *Phys. Rev. D* **59**, 014014
3576 (1998), hep-ph/9706377.
- 3577 [228] E. Iancu, A. Leonidov, and L. D. McLerran, *Phys. Lett. B* **510**, 133 (2001), hep-
3578 ph/0102009.
- 3579 [229] E. Iancu, A. Leonidov, and L. D. McLerran, *Nucl. Phys.* **A692**, 583 (2001), hep-
3580 ph/0011241.
- 3581 [230] A. Accardi *et al.*, *Eur. Phys. J. A* **52**, 268 (2016), 1212.1701.
- 3582 [231] Y. V. Kovchegov and M. D. Sievert, *Nucl. Phys. B* **903**, 164 (2016), 1505.01176.

- 3583 [232] CMS, S. Chatrchyan *et al.*, Eur. Phys. J. C **74**, 2951 (2014), 1401.4433.
- 3584 [233] STAR, E. Braidot, Nucl. Phys. A **854**, 168 (2011), 1008.3989.
- 3585 [234] PHENIX, A. Adare *et al.*, Phys. Rev. Lett. **107**, 172301 (2011), 1105.5112.
- 3586 [235] C. Marquet, Nucl. Phys. A **796**, 41 (2007), 0708.0231.
- 3587 [236] J. L. Albacete and C. Marquet, Phys. Rev. Lett. **105**, 162301 (2010), 1005.4065.
- 3588 [237] Z.-B. Kang, I. Vitev, and H. Xing, Phys. Rev. D **85**, 054024 (2012), 1112.6021.
- 3589 [238] M. Strikman and W. Vogelsang, Phys. Rev. D **83**, 034029 (2011), 1009.6123.
- 3590 [239] J. Jalilian-Marian and A. H. Rezaeian, Phys. Rev. D **86**, 034016 (2012), 1204.1319.
- 3591 [240] J. L. Albacete and C. Marquet, Nucl. Phys. A **854**, 154 (2011), 1009.3215.
- 3592 [241] K. J. Eskola, H. Paukkunen, and C. A. Salgado, JHEP **07**, 102 (2008), 0802.0139.
- 3593 [242] A. H. Rezaeian, Phys. Rev. D **86**, 094016 (2012), 1209.0478.
- 3594 [243] T. Sjostrand, S. Mrenna, and P. Z. Skands, Comput. Phys. Commun. **178**, 852 (2008),
3595 0710.3820.
- 3596 [244] Di-jet production from pythia8.189 is scaled down due to its overestimation of inclusive
3597 π_0 yields compared to those reported by BRAHMS in phys. rev. lett. 98 (2007) 252001
3598 and STAR in phys. rev. lett. 97 (2006) 152302.
- 3599 [245] T. Kaufmann, A. Mukherjee, and W. Vogelsang, Phys. Rev. D **92**, 054015 (2015),
3600 1506.01415, [Erratum: Phys.Rev.D 101, 079901 (2020)].
- 3601 [246] D. de Florian, R. Sassot, M. Epele, R. J. Hernández-Pinto, and M. Stratmann, Phys.
3602 Rev. D **91**, 014035 (2015), 1410.6027.
- 3603 [247] A. Khouaja *et al.*, Nucl. Phys. A **780**, 1 (2006).
- 3604 [248] D. de Florian and R. Sassot, Phys. Rev. D **69**, 074028 (2004), hep-ph/0311227.
- 3605 [249] D. de Florian, R. Sassot, and M. Stratmann, Phys. Rev. D **75**, 114010 (2007), hep-
3606 ph/0703242.
- 3607 [250] D. de Florian, R. Sassot, and M. Stratmann, Phys. Rev. D **76**, 074033 (2007),
3608 0707.1506.
- 3609 [251] M. A. Lisa *et al.*, (2021), 2101.10872.
- 3610 [252] J. L. Nagle and W. A. Zajc, Ann. Rev. Nucl. Part. Sci. **68**, 211 (2018), 1801.03477.

- 3611 [253] H. Helmholtz, The London, Edinburgh, and Dublin Philosophical Magazine and Jour-
3612 nal of Science **33**, 485 (1867), <https://doi.org/10.1080/14786446708639824>.
- 3613 [254] C. Shen *et al.*, In preparation.
- 3614 [255] B. Schenke, S. Jeon, and C. Gale, Phys. Rev. **C82**, 014903 (2010), 1004.1408.
- 3615 [256] STAR, L. Adamczyk *et al.*, Nature **548**, 62 (2017), 1701.06657.
- 3616 [257] I. Upsal, *Global Polarization of the $\Lambda/\bar{\Lambda}$ system in the STAR BES*, Ph.D. thesis, The
3617 Ohio State University, 2018.
- 3618 [258] Y. B. Ivanov and A. Soldatov, Phys. Rev. C **95**, 054915 (2017), 1701.01319.
- 3619 [259] Y. B. Ivanov and A. Soldatov, Phys. Rev. C **97**, 044915 (2018), 1803.01525.
- 3620 [260] Y. B. Ivanov, V. Toneev, and A. Soldatov, Phys. Atom. Nucl. **83**, 179 (2020),
3621 1910.01332.
- 3622 [261] Y. B. Ivanov, V. Toneev, and A. Soldatov, J. Phys. Conf. Ser. **1435**, 012012 (2020).
- 3623 [262] B. Fu, K. Xu, X.-G. Huang, and H. Song, (2020), 2011.03740.
- 3624 [263] M. Baznat, K. Gudima, A. Sorin, and O. Teryaev, Phys. Rev. C **88**, 061901 (2013),
3625 1301.7003.
- 3626 [264] O. Teryaev and R. Usubov, Phys. Rev. C **92**, 014906 (2015).
- 3627 [265] M. I. Baznat, K. K. Gudima, A. S. Sorin, and O. Teryaev, Phys. Rev. C **93**, 031902
3628 (2016), 1507.04652.
- 3629 [266] W.-T. Deng and X.-G. Huang, Phys. Rev. C **93**, 064907 (2016), 1603.06117.
- 3630 [267] X.-L. Xia, H. Li, Z.-B. Tang, and Q. Wang, Phys. Rev. C **98**, 024905 (2018),
3631 1803.00867.
- 3632 [268] A. Zinchenko, A. Sorin, O. Teryaev, and M. Baznat, J. Phys. Conf. Ser. **1435**, 012030
3633 (2020).
- 3634 [269] G. Bunce *et al.*, Phys. Rev. Lett. **36**, 1113 (1976).
- 3635 [270] COSY-TOF, F. Hauenstein *et al.*, Eur. Phys. J. A **52**, 337 (2016), 1607.06305.
- 3636 [271] F. Abe *et al.*, Phys. Rev. D **34**, 1950 (1986).
- 3637 [272] B. Lundberg *et al.*, Phys. Rev. D **40**, 3557 (1989).
- 3638 [273] HERA-B, I. Abt *et al.*, Phys. Lett. B **638**, 415 (2006), hep-ex/0603047.

- 3639 [274] HADES, G. Agakishiev *et al.*, Eur. Phys. J. A **50**, 81 (2014), 1404.3014.
- 3640 [275] A. Aprahamian *et al.*, Reaching for the horizon: The 2015 long range plan for
3641 nuclear science, 2015, The 2015 Long Range Plan for Nuclear Science “Reach-
3642 ing for the Horizon” [http://science.energy.gov/~media/np/nsac/pdf/2015LRP/](http://science.energy.gov/~media/np/nsac/pdf/2015LRP/2015_LRPNS_091815.pdf)
3643 [2015_LRPNS_091815.pdf](http://science.energy.gov/~media/np/nsac/pdf/2015LRP/2015_LRPNS_091815.pdf).
- 3644 [276] RHIC luminosity projection [https://www.rhichome.bnl.gov//RHIC/Runs/](https://www.rhichome.bnl.gov//RHIC/Runs/RhicProjections.pdf)
3645 [RhicProjections.pdf](https://www.rhichome.bnl.gov//RHIC/Runs/RhicProjections.pdf).
- 3646 [277] SN0619 : A Proposal for STAR Inner TPC Sector Upgrade (iTPC) [https://drupal.](https://drupal.star.bnl.gov/STAR/starnotes/public/sn0619)
3647 [star.bnl.gov/STAR/starnotes/public/sn0619](https://drupal.star.bnl.gov/STAR/starnotes/public/sn0619).
- 3648 [278] STAR, CBM eTOF Group, The CBM Collaboration eTOF Group, (2016), 1609.05102.
- 3649 [279] The STAR Forward Calorimeter System and Forward Tracking System beyond
3650 BES-II [https://drupal.star.bnl.gov/STAR/files/Proposal.ForwardUpgrade.](https://drupal.star.bnl.gov/STAR/files/Proposal.ForwardUpgrade.Nov_.2018.Review.pdf)
3651 [Nov_.2018.Review.pdf](https://drupal.star.bnl.gov/STAR/files/Proposal.ForwardUpgrade.Nov_.2018.Review.pdf).
- 3652 [280] JETSCAPE, D. Everett *et al.*, Phys. Rev. C **103**, 054904 (2021), 2011.01430.
- 3653 [281] J. E. Bernhard, J. S. Moreland, S. A. Bass, J. Liu, and U. Heinz, Phys. Rev. C **94**,
3654 024907 (2016), 1605.03954.
- 3655 [282] G. Nijs, W. van der Schee, U. Gürsoy, and R. Snellings, (2020), 2010.15130.
- 3656 [283] G. Denicol, A. Monnai, and B. Schenke, Phys. Rev. Lett. **116**, 212301 (2016),
3657 1512.01538.
- 3658 [284] H. Niemi, G. S. Denicol, P. Huovinen, E. Molnar, and D. H. Rischke, Phys. Rev. **C86**,
3659 014909 (2012), 1203.2452.
- 3660 [285] B. Schenke and S. Schlichting, Phys. Rev. **C94**, 044907 (2016), 1605.07158.
- 3661 [286] W. Li, Nucl. Phys. A **967**, 59 (2017), 1704.03576.
- 3662 [287] P. Bozek, W. Broniowski, and J. Moreira, Phys. Rev. **C83**, 034911 (2011), 1011.3354.
- 3663 [288] J. Jia and P. Huo, Phys. Rev. **C90**, 034915 (2014), 1403.6077.
- 3664 [289] L.-G. Pang, H. Petersen, G.-Y. Qin, V. Roy, and X.-N. Wang, Eur. Phys. J. **A52**, 97
3665 (2016), 1511.04131.
- 3666 [290] CMS, V. Khachatryan *et al.*, Phys. Rev. C **92**, 034911 (2015), 1503.01692.
- 3667 [291] ATLAS, M. Aaboud *et al.*, Eur. Phys. J. C **78**, 142 (2018), 1709.02301.
- 3668 [292] STAR Collaboration, L. Adamczyk *et al.*, Manuscript under preparation (2016).

- 3669 [293] A. Behera, M. Nie, and J. Jia, Phys. Rev. Res. **2**, 023362 (2020), 2003.04340.
- 3670 [294] C. Shen and B. Schenke, Phys. Rev. **C97**, 024907 (2018), 1710.00881.
- 3671 [295] BeAGLE: a Tool to Refine Detector Requirements for eA Collisions EIC R&D; Project
3672 eRD17 E. Aschenauer, M. Baker, W. Chang, J. Lee, Z. Tu et al. [https://wiki.bnl.](https://wiki.bnl.gov/eic/index.php/BeAGLE)
3673 [gov/eic/index.php/BeAGLE](https://wiki.bnl.gov/eic/index.php/BeAGLE).
- 3674 [296] Z. Tu *et al.*, Phys. Lett. B **811**, 135877 (2020), 2005.14706.
- 3675 [297] Y. Shi, L. Wang, S.-Y. Wei, B.-W. Xiao, and L. Zheng, Phys. Rev. D **103**, 054017
3676 (2021), 2008.03569.
- 3677 [298] ATLAS, G. Aad *et al.*, (2021), 2101.10771.
- 3678 [299] STAR, J. Adam *et al.*, Phys. Rev. Lett. **126**, 162301 (2021), 2012.13601.
- 3679 [300] STAR, B. Abelev *et al.*, Phys. Rev. C **76**, 064904 (2007), 0706.0472.
- 3680 [301] Z.-T. Liang, J. Song, I. Upszal, Q. Wang, and Z.-B. Xu, (2019), 1912.10223.
- 3681 [302] Y. Xie, D. Wang, and L. P. Csernai, Eur. Phys. J. C **80**, 39 (2020), 1907.00773.
- 3682 [303] X.-L. Sheng, L. Oliva, and Q. Wang, Phys. Rev. D **101**, 096005 (2020), 1910.13684.
- 3683 [304] X.-L. Sheng, Q. Wang, and X.-N. Wang, (2020), 2007.05106.
- 3684 [305] A. Bazavov *et al.*, Phys. Rev. D **95**, 054504 (2017), 1701.04325.
- 3685 [306] S. Cao, G.-Y. Qin, and S. A. Bass, Phys. Rev. C **92**, 024907 (2015).
- 3686 [307] JETSCAPE, A. Kumar *et al.*, Nucl. Phys. A **1005**, 122009 (2021), 2002.07124.
- 3687 [308] Y. Mehtar-Tani and K. Tywoniuk, Phys. Rev. D **98**, 051501 (2018), 1707.07361.
- 3688 [309] Y. Mehtar-Tani and K. Tywoniuk, Nucl. Phys. A **979**, 165 (2018), 1706.06047.
- 3689 [310] B. G. Zakharov, Eur. Phys. J. C **81**, 57 (2021), 2003.10182.
- 3690 [311] L. Chen, G.-Y. Qin, S.-Y. Wei, B.-W. Xiao, and H.-Z. Zhang, Phys. Lett. B **773**, 672
3691 (2017), 1607.01932.
- 3692 [312] A. H. Mueller, B. Wu, B.-W. Xiao, and F. Yuan, Phys. Lett. B **763**, 208 (2016),
3693 1604.04250.
- 3694 [313] S. K. Das *et al.*, Phys. Lett. B **768**, 260 (2017), 1608.02231.
- 3695 [314] S. Chatterjee and P. Bożek, Phys. Rev. Lett. **120**, 192301 (2018), 1712.01189.
- 3696 [315] STAR, J. Adam *et al.*, (2020), 2006.00582.

- 3697 [316] STAR, N. R. Sahoo, Measurement of γ +jet and π^0 +jet in central Au+Au collisions
3698 at $\sqrt{s_{NN}} = 200$ GeV with the STAR experiment, 2020, 2008.08789.
- 3699 [317] F. D’Eramo, K. Rajagopal, and Y. Yin, JHEP **01**, 172 (2019), 1808.03250.
- 3700 [318] ALICE, J. Norman, Jet acoplanarity via hadron+jet measurements in Pb-Pb collisions
3701 at $\sqrt{s_{NN}} = 5.02$ TeV with ALICE, in *10th International Conference on Hard and*
3702 *Electromagnetic Probes of High-Energy Nuclear Collisions: Hard Probes 2020* , 2020,
3703 2009.08261.
- 3704 [319] ALICE, J. Adam *et al.*, JHEP **09**, 170 (2015), 1506.03984.
- 3705 [320] STAR, L. Adamczyk *et al.*, Phys. Rev. C **96**, 024905 (2017), 1702.01108.
- 3706 [321] B. Chen, M. Hu, H. Zhang, and J. Zhao, Phys. Lett. B **802**, 135271 (2020), 1910.08275.
- 3707 [322] X. Guo, S. Shi, N. Xu, Z. Xu, and P. Zhuang, Phys. Lett. B **751**, 215 (2015),
3708 1502.04407.
- 3709 [323] B. Chen, X. Du, and R. Rapp, Nucl. Part. Phys. Proc. **289-290**, 475 (2017),
3710 1612.02089.
- 3711 [324] ALICE, J. Adam *et al.*, JHEP **05**, 179 (2016), 1506.08804.
- 3712 [325] ATLAS, M. Aaboud *et al.*, Eur. Phys. J. C **78**, 762 (2018), 1805.04077.
- 3713 [326] CMS, A. M. Sirunyan *et al.*, Phys. Rev. Lett. **118**, 162301 (2017), 1611.01438.
- 3714 [327] STAR, F. Seck, Nucl. Phys. A **1005**, 122005 (2021).
- 3715 [328] STAR, L. Adamczyk *et al.*, Phys. Rev. Lett. **113**, 022301 (2014), 1312.7397, [Adden-
3716 dum: Phys.Rev.Lett. 113, 049903 (2014)].
- 3717 [329] STAR Collaboration, J. Adam *et al.*, Phys. Rev. Lett. **121**, 132301 (2018).
- 3718 [330] ATLAS Collaboration, M. Aaboud *et al.*, Phys. Rev. Lett. **121**, 212301 (2018).
- 3719 [331] H. Xing, C. Zhang, J. Zhou, and Y.-J. Zhou, The $\cos 2\phi$ azimuthal asymmetry in ρ^0
3720 meson production in ultraperipheral heavy ion collisions, 2020, 2006.06206.
- 3721 [332] STAR, J. the STAR Collaboration, Adam *et al.*, Phys. Rev. Lett. **123**, 132302 (2019),
3722 1904.11658.
- 3723 [333] W. Zha *et al.*, Phys. Rev. C **97**, 044910 (2018).
- 3724 [334] M. B. G. Ducati and S. Martins, Phys. Rev. D **97**, 116013 (2018).
- 3725 [335] W. Shi, W. Zha, and B. Chen, Phys. Lett. B **777**, 399 (2018), 1710.00332.

- 3726 [336] V. Smakhtin *et al.*, Nucl. Instrum. Meth. **A598**, 196 (2009).
- 3727 [337] A. Abusleme *et al.*, Nucl. Instrum. Meth. **A817**, 85 (2016), 1509.06329.
- 3728 [338] Iakovidis, George, EPJ Web Conf. **174**, 07001 (2018).
- 3729 [339] ALICE Collaboration, Phys. Lett. B **784**, 82 (2018), 1805.01832.
- 3730 [340] CMS, A. M. Sirunyan *et al.*, Phys. Rev. C **100**, 044902 (2019), 1901.07997.
- 3731 [341] ATLAS Collaboration, (2019), 1911.04812.
- 3732 [342] Q. Y. Shou *et al.*, Phys. Lett. B **749**, 215 (2015), 1409.8375.
- 3733 [343] G. Giacalone, J. Noronha-Hostler, M. Luzum, and J.-Y. Ollitrault, Phys. Rev. C **97**,
3734 034904 (2018), 1711.08499.
- 3735 [344] G. Giacalone, Phys. Rev. C **99**, 024910 (2019), 1811.03959.
- 3736 [345] S. E. Agbemava, A. V. Afanasjev, and P. Ring, Phys. Rev. C **93**, 044304 (2016),
3737 1603.03414.
- 3738 [346] P. Möller, A. J. Sierk, T. Ichikawa, and H. Sagawa, Atom. Data Nucl. Data Tabl.
3739 **109-110**, 1 (2016), 1508.06294.
- 3740 [347] L. M. Robledo and G. F. Bertsch, Phys. Rev. C **84**, 054302 (2011), 1107.3581.
- 3741 [348] S. Hilaire and M. Girod, Eur. Phys. J. A **33**, 237 (2007).
- 3742 [349] J. Jia, S. Huang, and C. Zhang, (2021), 2105.05713.
- 3743 [350] G. Giacalone, J. Jia, and C. Zhang, (2021), 2105.01638.
- 3744 [351] Chart of Nuclear Quadrupole Deformations, <https://www.nndc.bnl.gov/nudat2/>.
- 3745 [352] G. Giacalone, J. Jia, and V. Somà, (2021), 2102.08158.
- 3746 [353] P. A. Butler, J. Phys. G **43**, 073002 (2016).
- 3747 [354] C. J. Lister and J. Butterworth, Nature **497**, 190 (2013).